Designing of Functional Materials for Proton Conduction and Electrocatalysis

A THESIS

Submitted in partial fulfilment of the
requirements for the award of the degree
of
DOCTOR OF PHILOSOPHY

by

Olivia Basu

School of Chemistry
University of Hyderabad
Hyderabad – 500046, India

May 2023

Dedicated to my

Family

and

Teachers

"It is not failure when you fail,

but when you fail to try."

CONTENTS

Chapter 3. Designing of Flexible Metal-Organic Framework-based Super-protonic Conductors and their Fabrication with a Polymer into Proton Exchange Membranes

Chapter 4. Tuning the Electrochemical and Catalytic ORR Performance of C_{60} by its Encapsulation in ZIF-8: A Solid-State Analogue of Dilute Fullerene Solution

Chapter 5. A 60-electron-reduced {Mo_{132}} POM acting as a sink to accommodate 60 more electrons: a stable heterogeneous HER electrocatalyst

Chapter 5. Concluding Remarks and Future Scope

DECLARATION

I, **Olivia Basu**, hereby declare that the matter embodied in the thesis '***Designing of Functional Materials for Proton Conduction and Electrocatalysis***' is the result of my investigation carried out in School of Chemistry, University of Hyderabad, Hyderabad, India, during the time period of January 2018 to April 2023, under the supervision of **Prof. Samar K. Das.**

In keeping with the general practice of reporting scientific observations, due acknowledgements have been made wherever the work described is based on the findings of other investigators. Any omission, which might have occurred by oversight or error, is regretted. This research work is free from plagiarism. I hereby agree that my thesis can be deposited in Shodhganga / INFLIBNET. A report on plagiarism statistics from the library, University of Hyderabad, is enclosed.

S.K.Das

Prof. Samar K. Das.

(Thesis supervisor)

Prof. Samar K. Das
School of Chemistry
University of Hyderabad
Hyderabad-500 046., INDIA.
skdas@uohyd.ac.in

Olivia Basu

Olivia Basu

(17CHPH51)

प्रतिष्ठित संस्थान
INSTITUTION OF EMINENCE

CERTIFICATE

This is to certify that the work described in this thesis entitled '*Designing of Functional Materials for Proton Conduction and Electrocatalysis*' submitted on 08/05/2023, has been carried out by **Olivia Basu**, bearing registration number 17CHPH51 (Date of joining: January 02, 2018), in partial fulfilment of the requirements for the award of Doctor of Philosophy in the School of Chemistry, University of Hyderabad, is a bonafide work carried out by her under my supervision and guidance. This thesis is free from plagiarism and has not been submitted previously in part or in full, to this or any other University or Institution for the award of any degree or diploma.

Parts of this thesis has been published in the following publications.

1 Basu, O.; Mukhopadhyay, S.; Laha, S.; Das, S. K. *Chem. Mater.* **2022**, *34*, 6734–6743. **(Chapter 2)**
2 Basu, O.; Das, A.; Jana, T.; Das, S. K. *ACS Appl. Energy Mater.* **2022** (DOI: 10.1021/acsaem.2c02972). **(Chapter 3)**
3 Basu, O.; Mukhopadhyay, S.; De, A.; Das, A.; Das, S. K. *Mater. Chem. Front.* **2021**, *5*, 7654–7665. **(Chapter 4)**

The student has made presentation in the following conferences.

Oral presentation

1 International conference on *modern trends in inorganic chemistry* (MTIC-XIX).
2 Chemfest 2022 (Annual in-house symposium) at School of Chemistry, UoH.

Poster presentation

1 International *conference on electrochemistry in advanced materials, corrosion, and radiopharmaceuticals* (CEAMCR-2018).
2 Chemfest 2018 (Annual in-house symposium) at School of Chemistry, UoH.
3 International conference on *modern trends in inorganic chemistry* (MTIC-XVIII).

The student has passed the following courses towards fulfilment of course work.

Sl. No.	Course code	Course name	No. of credits	Grade
1	CY-801	Research Proposal	4	Pass
2	CY-802	Chemistry Pedagogy	4	Pass
3	CY-805	Instrumental Methods A	4	Pass
4	CY-806	Instrumental methods B	4	Pass

04/05/23

Dean
School of Chemistry,
University of Hyderabad,
Hyderabad – 500046, India.

Dean
SCHOOL OF CHEMISTRY
University of Hyderabad
Hyderabad-500 046.

S.K.Das
Prof. Samar K. Das
(Thesis supervisor)

Prof. Samar K. Das
School of Chemistry
University of Hyderabad
Hyderabad-500 046., INDIA.
skdas@uohyd.ac.in

ACKNOWLEDGEMENTS

It was rightly said by one of my teachers that, the journey of PhD is not about publishing papers, but it is an important training period which prepares you for life. Through my days in PhD, I have grown up both as a researcher and as a person. And so, it is a genuine pleasure to take this opportunity and thank all who have directly or indirectly associated with this journey.

Firstly, I express my sincere gratitude to my research supervisor, Prof. Samar K. Das, for guiding me through this journey. His passion for science and knack for hard work has been very inspiring. Apart from science he has been kind enough to discuss his life experiences – both success and failure, which has served as a source of motivation in times of need. I feel truly fortunate to have him as a teacher in my academic career. I am thankful to him for having faith in me and providing complete freedom of work in the lab, which has helped me realize my potential and grow as a researcher. Apart from that, I also thank him for his support, to participate in activities outside lab and work.

I thank the present and former deans of School of Chemistry for providing the facilities required for the research work. I thank all the faculty members of the school for their help at various stages. I am particularly thankful to my doctoral committee members Prof. Samudranil Pal and Prof. K. Muralidharan for their encouragement and valuable suggestions. I thank Prof. Tushar Jana, our scientific collaborator for helping with the works on polymer membranes and providing his valuable suggestions. I am thankful to Prof. Raju Mondal (IACS, Kolkata), and Prof. T. K. Majhi (JNCASR, Bangalore) for their timely help with the research works.

I would also like to acknowledge the contribution of the non-teaching and technical staffs, in our School of Chemistry, who have been very helpful in making my day to day works easier.

I thank DST-SERB, India, and IoE University of Hyderabad, for the much-needed financial assistance for the research works. I thank UGC, India for my fellowship.

Here I must acknowledge that none of this would have been possible without the love and support of my lab mates, who have been my friends and family for the past 5 years. I shall miss our everyday tea-time, our biriyani plans after lab cleaning, our samosa parties, Sir's *pizza parties, our picnics, Sukoon and campus hikes; all of which has helped me to overcome the temporary setbacks in PhD life. We share countless memories which shall forever be a source of joy to me. I thank my lab seniors Pratap anna, Vinod anna, Rajendar anna, pedda Sathish anna, Ramakrishna anna, chinna Sateesh anna, Suresh bhaiya, Thulasi akka, Subha da, Tanmaya da, Chandani di, Joycee di, Pinki di, and Mousami di for their love. I want to specially thank Subha da for teaching me how to work, as well as, how to live through the ups and downs of PhD life. He has been a constant source of motivation throughout my PhD. I am grateful to Rajendar anna for always being there to support me and cheer me up whenever I have been low. I thank Hema, Athira, and Debu, for their insightful discussions, both academic and non-academic, and their enormous support throughout my PhD. I thank Parvathy and Gopika for their joyful companionship in the last days of my PhD. I also thank the newest members of our lab Shalini, Rameswari, Florence, Laxmi, and Sarbani for enriching the lab atmosphere. I thank Karthik for taking care of the lab and for filling our days with fun. I fondly remember my association with Atanu, Gourab, Ahsan and my project students Ankita, Hemalatha, Subhrajyoti, Kinshuk and Jaysri during this journey.*

I feel fortunate to have got a lot of help and support from my friends, colleagues, and seniors in School of Chemistry. I shall always be thankful to Sugata da, Arijit da, Kaushik da, Kallol da, Suriya anna, Anil anna, Manish anna, Chaitanya anna, Sneha di, Tasneem di, Sabari di, Moumita di, Mou di, Sarada di, Alim da, Senthil anna, Divya akka, Sujana akka, Ankit bhaiya, Sameeta di, Sipra di, Soutrik da, Irfan, Anupam, Nilanjan, Somnath, Sumanta, Vinod, Sasikanth, Suman, Sneha, Ajay, Alamgir, Jhansi, and Rani. I am especially thankful to my friend Anupam, for always cheering me up and to never say 'no', whenever I have needed help.

I am glad to have got the company of Tasneem di, Sarada di, and Debika during the difficult times of COVID-19. I shall miss our academic discussions and fun-filled hostel days. I am very thankful to Alam and Sourav for being by my side through happiness and sorrow. I am thankful to my group of 'food mates' – Prasad, Varsha, Raju, and Naresh ji, for their love and good food. A note of thanks to the group members of 'Nairit kon' for making my last few days at the campus, memorable.

My MSc days in University of Hyderabad, have been one of the most memorable days of my life. Here, I had the fortune of associating with some teachers who inspired and *motivated me to pursue research as a career. I thank Prof. A. K. Sahoo for teaching important life lessons, and Prof. S. Mahapatra for always believing in me and guiding me through tough times.*

My roommate Rina has always been by my side through the ups and downs of MSc days. I am thankful to have got the company of Suranjan da, Dayeeta di, Aranya, and Subha da, who have helped me throughout the journey.

My BSc days in Presidency University ignited my love for chemistry and laid the foundation of where I am today. I would forever miss the classes of Prof. Balai Chandra Kundu (BCK), Prof. Dipak K. Mondal (DM), Prof. AKS, Dr. Chandan Saha (CS), Prof. Pradeepta Ghosh (PG), Prof. DPC, and Prof. Arnab Haldar (AH). They are some of my teachers I look up to. It was for them that I realized what it means to be mesmerized and hypnotized, both at the same time, while attending a lecture.

I thank Srijana, Ishita, and Priya for taking care of me and cheering me up whenever I was at my low. I thank my senior Abhijit Sen for inspiring me in those days. I would be ever grateful to Gourab who has been a friend, a teacher, and a constant source of encouragement and motivation.

I sincerely thank the lab members of Prof. Somdutta Ghosh Dey and Prof. Abhishek Dey (IACS, Kolkata), for their love and encouragement. I will be forever in debt of Manas da and Chandradeep da for having faith in me at a time when I did not have any on myself.

I am thankful to my childhood teachers Kaushik Ghosh, and Sibaprasad Kar who have played a major role in moulding the person I am and motivating me throughout my academic career.

I would also like to thank those who did not support me in need, because it is also for them that I found my strength and confidence to overcome my obstacles.

Looking back, I feel lucky to have got the family I have. The love and encouragement I have got from my family, is my biggest strength. They have been my guide to life as well as my dear friends. They have always stood beside me through my whims and sorrow, with love and patience. They are also the ones who taught me the important lessons of life. I have learnt to be independent and live with self-respect, from my mother. My father made me realize the value of honesty and perseverance. The free spirit and will force of my *grandmother, is something I admire, and look up to. I respect my grandfather for his selfless nature. And, I am yet learning the great art of finding happiness amidst worries, from my brother. I am very thankful to Uttam kaka, Mani, Mesho, Babin, Bonnie, Basanti pishi and family, for their love and care.*

My sincere apologies if I have missed anyone. I extend my heartfelt gratitude to everyone who has contributed in one way or the other, for me to complete this journey of PhD.

Lastly, I thank God for filling my life with such amazing people and experiences.

Olivia

University of Hyderabad,
May 2023

SYNOPSIS

of the Thesis entitled

Designing of Functional Materials for Proton Conduction and Electrocatalysis

To be submitted to the
University of Hyderabad

For the Degree of
DOCTOR OF PHILOSOPHY

by

Olivia Basu
(17CHPH51)

School of Chemistry
University of Hyderabad
Hyderabad – 500046, India

May 2023

The doctoral thesis entitled as "**Designing of Functional Materials for Proton Conduction and Electrocatalysis**" contains four working chapters along with a general introduction. This is followed by concluding remarks and future scope. The chapters are titled as (**1**) Introduction to Designing of Functional Materials for Proton Conduction and Electrocatalysis, (**2**) Defect Engineering in a Metal−Organic Framework System to Achieve Super-Protonic Conductivity, (**3**) Designing of Flexible Metal-Organic Framework-based Super-protonic Conductors and their Fabrication with a Polymer into Proton Exchange Membranes (**4**) Tuning the Electrochemical and Catalytic ORR Performance of C_{60} by its Encapsulation in ZIF-8: A Solid-State Analogue of Dilute Fullerene Solution, (**5**) A 60-electron-reduced {Mo_{132}} POM acting as a sink to accommodate 60 more electrons: a stable heterogeneous HER electrocatalyst, (**6**) Concluding Remarks and Future Scope.

The **chapter 1**, that is, Introduction, consists of a general discussion about water splitting, with particular emphasis on hydrogen evolution reaction (HER) catalysis. It also discusses about fuel cells, and ways of improving the technology by developing better proton conductors and oxygen reduction reaction (ORR) electrocatalysts. At the end of the chapter, the motivation of this thesis work is discussed. All other chapters (**Chapter 2–5**) consist of (**a**) brief overview of the work; (**b**) introduction, which includes relevant literature survey and also framing of the problem; (**c**) experimental section, (**d**) results and discussion, and at the end (**e**) conclusion. The compounds, presented in this thesis work, are generally characterized by powder X-ray diffraction (PXRD), FT-IR spectral studies, UV-Visible diffused reflectance spectroscopy (DRS), Raman spectroscopy, X-ray photoelectron spectroscopy, field emission scanning electron microscopy (FESEM), high resolution transmittance electron microscopy (HRTEM), inductively coupled plasmon optical emission spectroscopy (ICP-OES), thermogravimetric studies and, N_2 and water sorption analysis. In addition, further characterization was carried out using ^{1}H-NMR, atomic force microscopy (AFM), dynamic mechanical analyser (DMA), universal testing machine (UTM), dynamic light scattering (DLS) and photoluminescence (PL) spectroscopy, whenever it was required. Proton conductivity studies of MOF powder samples were performed using sample pellets in solid state, using a 2-electrode setup, inside a humidity chamber. Proton conductivity studies of MOF@polymer membranes were performed using a 4-electrode setup, inside a temperature-controlled oven under anhydrous condition. Electrochemical analysis for ORR and HER were carried out in heterogeneous mode, using a 3-electrode setup, in aqueous as well as non-aqueous medium.

Chapter 1

Introduction to Designing of Functional Materials for Proton Conduction and Electrocatalysis

This chapter discusses the world scenario in terms of primary energy consumption, global CO_2 emissions, and the need to move towards sustainable energy harvesting methods and a carbon-neutral economy. Particular emphasis has been given to showcase the benefits and roadblocks to a H_2 fuel technology and the role of contemporary research in fighting these issues. The basics of water-splitting and the reactions involved to produce H_2 have been discussed briefly. The basics to H_2 fuel-cell technology has been discussed along with the ways in which its performance can be improved. The role of proton conducting membrane is particularly important here in governing the efficiency of a fuel cell. Followed by these is an introduction to the materials employed in this thesis work – *metal-organic frameworks (MOFs)*, *polyoxometalates (POMs)*, and *giant POMs*, for developing electrocatalysts and proton conductors. This chapter finally concludes with describing the motivation for this thesis work.

Chapter 2

Defect Engineering in a Metal−Organic Framework System to Achieve Super-Protonic Conductivity

Controlled incorporation of missing-linker defect sites could be achieved in four sister metal-organic frameworks (MOFs) of MOF-808, namely, **MOF-808 A – D** *via* modulated-synthesis**.** An impressive enhancement in proton conductivity is observed in these sister MOFs (increase from 10^{-3} Scm^{-1} to 10^{-1} Scm^{-1}) as compared to a highly crystalline, low-in-defect variant of MOF-808. **MOF-808 C**, having optimized defect density, shows proton conductivity of 2.6×10^{-1} Scm^{-1} at 80 ^{o}C and 98% relative humidity – the highest value reported till date for pure MOF-based proton conductors without extensive structural modifications. The introduction of defects induces super-protonic conductivity by modifying different properties, like porosity, water sorptivity and acidity. Furthermore, an assembly of this super proton-conducting MOF with Pt – a versatile HER catalyst, has been studied with the objective to influence the catalytic activity. This MOF-catalyst assembly was found to have lower overpotential requirements, owing to an increase in local acidity and efficient proton management around the catalyst. A schematic illustration of the idea of missing linker defect in MOF-808, and its correlation between observed proton conductivity for **MOF-808 A – D** (80 ºC, 98% R.H.) and the corresponding average number of BTC linkers per SBU, is provided in Figure 1.

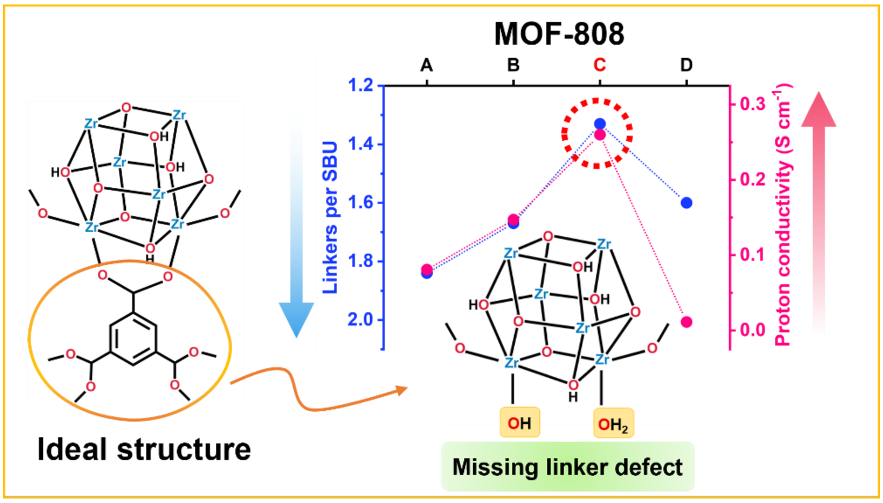

Figure 1. Schematic representation of missing linker defect in MOF-808, and its correlation between observed proton conductivity for **MOF-808 A – D** (80 ºC, 98% R.H.) and the corresponding average number of BTC linkers per SBU.

Chapter 3

Designing of Flexible Metal-Organic Framework-based Super-protonic Conductors and their Fabrication with a Polymer into Proton Exchange Membranes

In this work, we have focused on developing ‘*flexible MOF*’-based proton conductors with **Fe-MIL-53-NH$_2$** and **Fe-MIL-88B-NH$_2$** MOFs and using post-synthetic modification (PSM) as the tool. Taking advantage of the porous nature of these frameworks, we have carried out PSM on the primary amine groups present on the MOFs and converted them to -NH($CH_2CH_2CH_2SO_3H$) groups. The PSM increased the number of labile protons in the channels of the modified MOFs as well as the extent of H-bonded networks inside the framework. The modified **Fe-MIL-53-NH$_2$** and **Fe-MIL-88B-NH$_2$** MOFs, named hereafter as **53-S** and **88B-S**, respectively showed proton conductivity of 1.298×10^{-2} and 1.687×10^{-2} S cm^{-1} at ~80 ºC and 98% relative humidity (R. H), respectively. This is ~10-fold and ~5-fold increment in their proton conductivity than their respective parent MOFs. Since MOFs as such are difficult to be directly made into flexible membranes, that are essential for practical applications as proton conductor, we have incorporated **53-S** and **88B-S** as fillers into a robust imidazole-based polymer matrix namely OPBI [poly(4,4′-diphenylether-5,5′-bibenzimidazole)]. The resulting polymer-MOF mixed matrix membranes (MMMs) after being doped with phosphoric acid (PA) performed as flexible proton exchange membranes (PEMs) above 100 ºC under anhydrous condition and found to be much more efficient and stable than the pristine OPBI membrane (devoid of any filler loading). By optimizing the amount of filler loading in the membrane, we obtained the highest conductivity of 0.304 S cm^{-1} at 160 ºC under anhydrous condition. A graphical representation of post synthetic modification on the linkers of MOFs, **Fe-MIL-53-NH$_2$** and **Fe-MIL-88B-NH$_2$**, and their subsequent fabrication into MOF@polymer mixed matrix membranes (MMMs) is shown in figure 2.

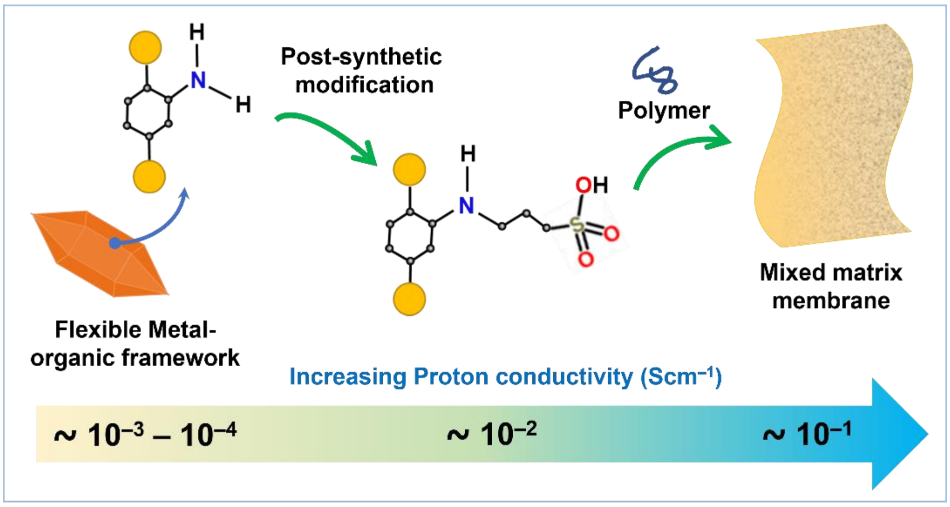

Figure 2. Graphical representation of post synthetic modification on the linkers of MOFs, **Fe-MIL-53-NH$_2$** and **Fe-MIL-88B-NH$_2$**, and their subsequent fabrication into MOF@polymer mixed matrix membranes.

Chapter 4

Tuning the Electrochemical and Catalytic ORR Performance of C_{60} by its Encapsulation in ZIF-8: A Solid-State Analogue of Dilute Fullerene Solution

Metal–organic frameworks (MOFs) with intrinsic electrochemical activity have received significant attention in the last two decades, mainly because of the high density of physically separated active sites. Yet, the potential of chemical tunability, spatial confinement and scope of heterogenization in the electrochemically inactive MOFs have been less explored. Here, we have shown that fullerene C_{60}, well-known for its rich reductive electrochemistry, when encapsulated inside zeolitic imidazolate framework-8 (ZIF-8) to prepare a heterogeneous composite (**C_{60}Z**), can act as a catalyst for the oxygen reduction reaction (ORR) at a lower overpotential with better selectivity than bare C_{60} *per se*. Spectroscopic and electrochemical characterization methods prove significant interactions between the ZIF-8 host and the C_{60} guest, which results in the modification of the electro- chemical behavior of C_{60} inside ZIF-8 and thereby causes an enhanced electrochemical ORR performance of the guest. The mono-confinement of C_{60} inside ZIF-8 also results in spatial separation of C_{60} molecules, which is highly effective for preserving its dilute solution-like behavior in solid-state inside the framework matrix. Furthermore, we have explored the scope of device processability of this solid-state analogue of dilute C_{60} solution *i.e.*, **C_{60}Z**, by its fabrication into a polymer membrane (**C_{60}Z–PVA** thin film) which could retain the physical properties of the **C_{60}Z**. A graphical representation of the encapsulation of C_{60} in ZIF-8 to form **C_{60}Z**, and the electrocatalytic conversion of oxygen to hydrogen peroxide is shown in Figure 3.

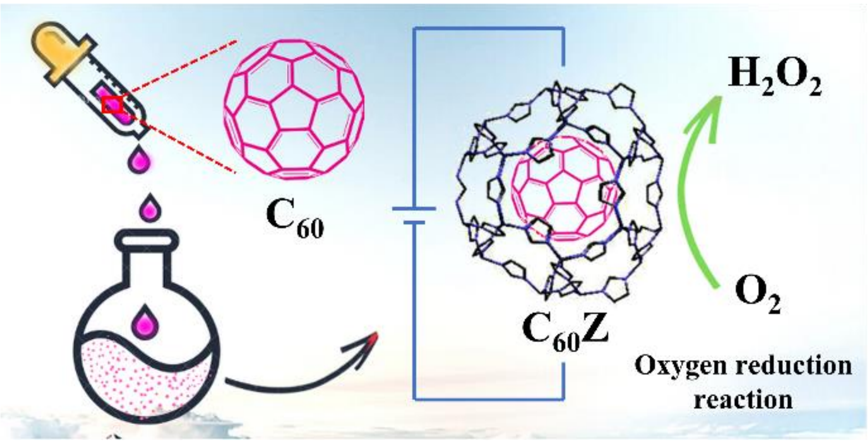

Figure 3. Graphical representation of the encapsulation of C_{60} in ZIF-8 to form **C_{60}Z**, and the electrocatalytic conversion of oxygen to hydrogen peroxide.

Chapter 5

A 60-electron-reduced {Mo_{132}} POM acting as a sink to accommodate 60 more electrons: a stable heterogeneous HER electrocatalyst

Developing an efficient and stable hydrogen evolution reaction (HER) catalyst is of utmost importance nowadays. Polyoxometalates (POMs) are well-known for their reversible redox activity, which make them high-potential materials for energy applications. In this work, we report an 120-electron-reduced heterogeneous electrocatalyst **Mo_{132}-R-ED**, synthesized by the electrochemical reduction of a highly water soluble, 60-electron-reduced giant POM, {Mo_{132}}. Using several characterization techniques and performing redox titration, it was confirmed that, **Mo_{132}-R-ED** contains parent 60-electron-reduced {Mo_{132}} clusters which are further reduced by ~ 60 more electrons. While parent water-soluble-{Mo_{132}} itself is not catalytically active towards HER, **Mo_{132}-R-ED** is found to be a stable and efficient electrocatalyst towards HER, having a hydrogen evolution turn over frequency of ~ 0.52 **s^{-1}** at 1 mA cm^{-2} current density.

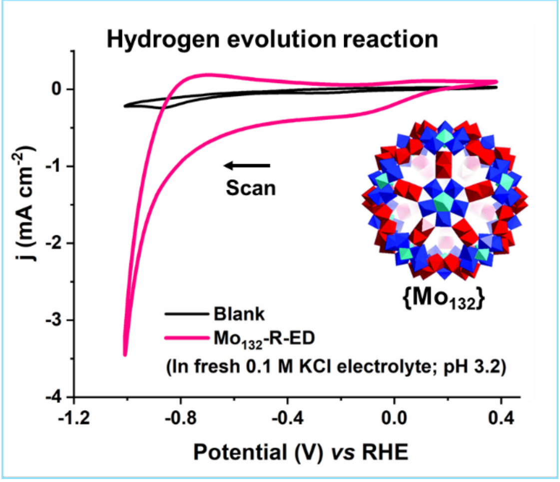

Figure 4. Cyclic voltammogram showing electrocatalytic hydrogen evolution reaction (HER) performed by **Mo_{132}-R-ED**.

Chapter 6

Concluding remarks and Future Scope

At the end of the working chapters of this thesis, conclusion, and future scope of the research work of the thesis has been discussed. This thesis endeavours to design and develop efficient metal-organic framework (MOF) based proton conductors, and electrocatalysts for oxygen reduction reaction (ORR) and hydrogen evolution reaction (HER), by modifying and improving the properties of already known parent materials, using techniques such as defect engineering, post-synthetic modification, host-guest supramolecular interaction, and electrochemical reduction.

The future scope of this work includes further development of functional materials by combining efficient proton conducting MOFs with electrocatalysts for HER, to enhance the overall catalytic properties of the catalyst. MOF@polymer based mixed matrix membranes have a lot of potential in the field of proton exchange membranes for fuel cells, which need to be further explored. Encapsulation of small molecules in the cages of MOFs can be used to design electrochemically and photochemically active functional materials. Polyoxometalates can prove to be potential proton conductors because of their oxygen rich surface and the capacity to form extensive H-bonding with water molecules. The requirement here, is to make POMs such as $\{Mo_{132}\}$, insoluble in water, and there is a scope of finding new strategies for that.

CHAPTER 1

Introduction to Designing of Functional Materials for Proton Conduction and Electrocatalysis

OVERVIEW:

This chapter discusses the world scenario in terms of primary energy consumption, global CO_2 emissions, and the need to move towards sustainable energy harvesting methods and a carbon-neutral economy. Particular emphasis has been given to showcase the benefits and roadblocks to a H_2 fuel technology and the role of contemporary research in fighting these issues. The basics of water-splitting and the reactions involved to produce H_2 have been discussed briefly. The basics to H_2 fuel-cell technology has been discussed along with the ways in which its performance can be improved. The role of proton conducting membrane is particularly important here in governing the efficiency of a fuel cell. Followed by these is an introduction to the materials employed in this thesis work – *metal-organic frameworks (MOFs)*, *polyoxometalates (POMs)*, and *giant POMs*, for developing electrocatalysts and proton conductors. This chapter finally concludes with describing the motivation for this thesis work.

1.1. INTRODUCTION

Our world economy is based on the capitalist system which is always striving for a positive Gross Domestic Product – GDP. With the GDP% increasing every year and the population booming exponentially, the rate of global energy consumption has also shot up in the past 50 years.[1] This rapid and unsustainable growth of our economy is causing depletion of our resources. Unfortunately, even now most of this demand for energy is fulfilled by the use of fossil fuels – oil, gas and coal (Figure 1.1, left). As of the year of 2019 (Figure 1.1, right),

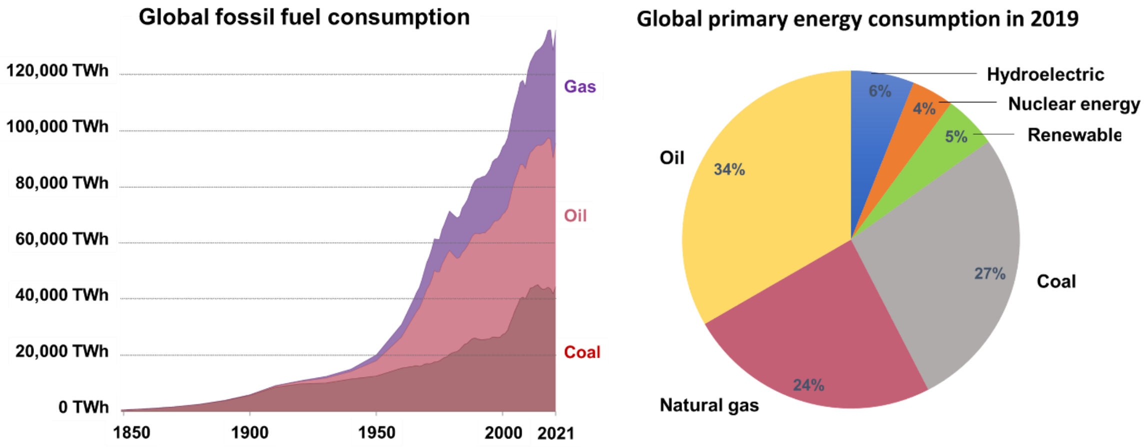

Figure 1.1. Global primary energy consumption by fossil fuel source, measured in terawatt-hours (TWh) (left). Overall distribution of energy resources in 2019 (right).[1]

approximately 84% of the global energy consumption was in fossil fuels, 11% in renewables and remainder by nuclear energy.[2] Here it is important to keep in mind that fossil fuel reserves on our earth are limited, and with the present rate of consumption, these reserves would last only for the next 50 years.[3] So, there is an urgent need to shift our dependencies from fossil fuels to other renewable sources of energy.

Moreover, the extensive combustion of fossil fuels for the past several decades has dramatically increased the pollution and CO_2 levels in the atmosphere, the effects of which can already be experienced in the form of rise in global average temperatures and climate change (Figure 1.2).[2] So, from the perspective of the present global situation, it is imperative that we focus towards developing better sustainable energy harvesting methods and work together to create a carbon-neutral economy.

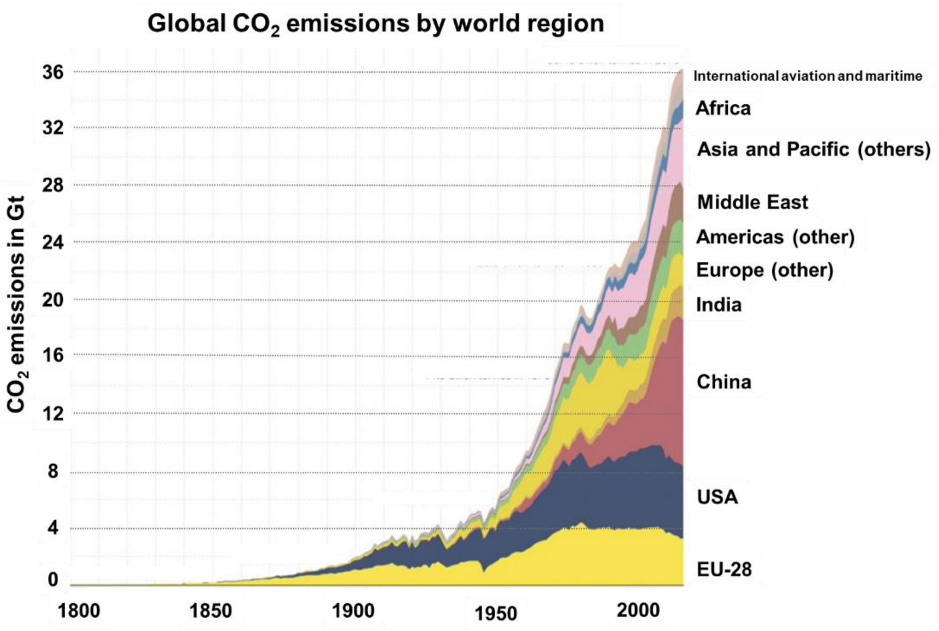

Figure 1.2. Annual carbon dioxide emissions since 1800 to 2015, in billion tonnes (Gt).[1]

Although substantial advancement has been made in developing technology for obtaining electrical energy from renewable sources such as solar energy, wind energy, geothermal energy, and hydropower, among others, but the contribution of renewable energy in global energy consumption is still marginal.[1] One way to change this is by regularizing the availability of renewable energy resources by storing energy in chemical bonds of fuels; and if these fuels have to replace fossil fuels, these must be of high energy density. Keeping all these points into consideration, one of the best methods the scientists have come up with, is to generate hydrogen fuel from electrolysis of water, also known as ‘*water splitting*’. Since splitting of water into H_2 and O_2 ($2H_2O \rightarrow O_2 + 2H_2$) is an energy intensive process, extensive research has been going on worldwide to develop better catalysts, so that the storage of electrical energy into the bond of H_2 can take place with a minimum loss of energy.

The hydrogen fuel thus produced, can be stored, and converted back to electrical energy as and when required, using a fuel cell. Research and innovation are important in this segment as well since it is very important to maximize the efficiency of a fuel cell to be able to convert energy with minimum loss. We shall discuss all these topics in more detail in the following sections.

In the works discussed in this thesis, we have combined different materials like metal-organic frameworks (MOFs), polymers, small inorganic molecules and giant polyoxometalates (POMs) to create diverse materials for application in electrocatalysis [hydrogen evolution reaction (HER), oxygen reduction reaction (ORR)] and proton conduction.

1.2. APPLICATIONS

1.2.1. Water splitting

The splitting of water molecules to produce H_2 can be done by using several methods like, electrolysis, thermolysis, photo-electrolysis, and photochemical charge separation.[4,5] Water electrolysis and photo-electrolysis work by the same principles of splitting water by passing electric current through it, are one of the best methods to obtain pure H_2 at an industrial

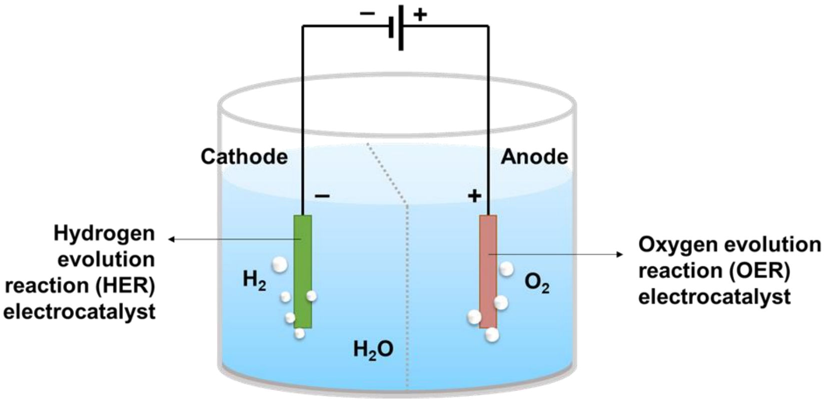

Figure 1.3. A schematic representation of an electrochemical cell showing electrolysis of water.

level without causing any greenhouse gas emissions. But the conversion efficiency of electrical energy to H_2 is still low to make these processes a viable alternative. To enhance the conversion efficiency, and to be able to use these methods industrially, better electrocatalysts need to be designed and developed.

Electrolysis of water takes place by the simultaneous occurrence of hydrogen evolution reaction (HER) at cathode and oxygen evolution reaction (OER) at anode as shown in Figure 1.3.[6]

In aqueous acid:

$$2\,H_2O \rightleftharpoons O_2 + 4\,H^+ + 4\,e^- \qquad E_{anodic} = -1.23\text{ V} + 0.059\text{ (pH) V vs NHE} \quad \ldots (1)$$

$$4\,H^+ + 4\,e^- \rightleftharpoons 2\,H_2 \qquad E_{cathodic} = 0\text{ V} - 0.059\text{ (pH) V vs NHE} \quad \ldots (2)$$

$$2\,H_2O \rightarrow 2\,H_2 + O_2 \qquad E_{reaction} = -1.23\text{ V}$$

In aqueous base:

$$4\,OH^- \rightleftharpoons O_2 + 2\,H_2O + 4\,e^- \qquad E_{anodic} = -\,0.40\text{ V} - 0.059\text{ (pOH) V vs NHE} \ldots (3)$$

$$4\,H_2O + 4\,e^- \rightleftharpoons 2\,H_2 + 4\,OH^- \qquad E_{cathodic} = -\,0.83\text{ V} + 0.059\text{ (pOH) V vs NHE} \ldots (4)$$

$$2\,H_2O \rightarrow 2\,H_2 + O_2 \qquad E_{reaction} = -1.23\text{ V}$$

Scheme 1: Half-cell reactions involved in water splitting in acidic (equation 1 and equation 2) and basic (equation 3 and equation 4) pH solutions.

As can be seen in Scheme 1, the Nernstian potential of overall water splitting is independent of pH, but the potential for individual half-cell reactions is pH dependent. For both acidic and basic media, the thermodynamic potential requirement for OER is much higher than HER due to the presence of several elementary steps and intermediates. Here it is important to note that neither of the reactions, HER or OER, proceed at their thermodynamic potential, due to the presence of kinetic reaction barrier, which is manifested in the form of high overpotential.[7] The term, overpotential can be defined as the additional potential above the thermodynamic potential which needs to be applied, to cross the reaction kinetic barrier and drive the reaction at a given rate. These two factors *i.e.*, high Nernstian potential and high overpotential requirement combined, make the overall process of water oxidation challenging. And therefore, for both these processes, the use of efficient electrocatalysts is important for lowering the overpotentials and driving the overall water splitting at a lower energy expenditure.

1.2.1.1. Hydrogen evolution reaction (HER)

The HER in acidic as well as in alkaline aqueous media, can proceed through three possible steps (Figure 1.4).[8] These can be written as:

(I) electrochemical hydrogen adsorption (Volmer reaction) (eqn. 5 and 6)

$$H_3O^+ + M + e^- \rightleftharpoons M{-}H^* + H_2O \text{ (acidic medium)} \qquad \dots (5)$$

$$H_2O + M + e^- \rightleftharpoons M{-}H^* + OH^- \text{ (alkaline medium)} \qquad \dots (6)$$

(II) electrochemical desorption (Heyrovsky reaction) (eqn. 7 and 8)

$$H^+ + e^- + M{-}H^* \rightleftharpoons H_2 + M \text{ (acidic medium)} \qquad \dots (7)$$

$$H_2O + e^- + M{-}H^* \rightleftharpoons H_2 + OH^- + M \text{ (alkaline medium)} \qquad \dots (8)$$

Or,

(III) chemical desorption (Tafel reaction) (eqn. 9)

$$2\ M{-}H^* \rightleftharpoons H_2 + 2\ M \text{ (both acidic and alkaline mediums)} \qquad \dots (9)$$

[Here M is electrode surface; H* is H-atom adsorbed on the electrode surface]

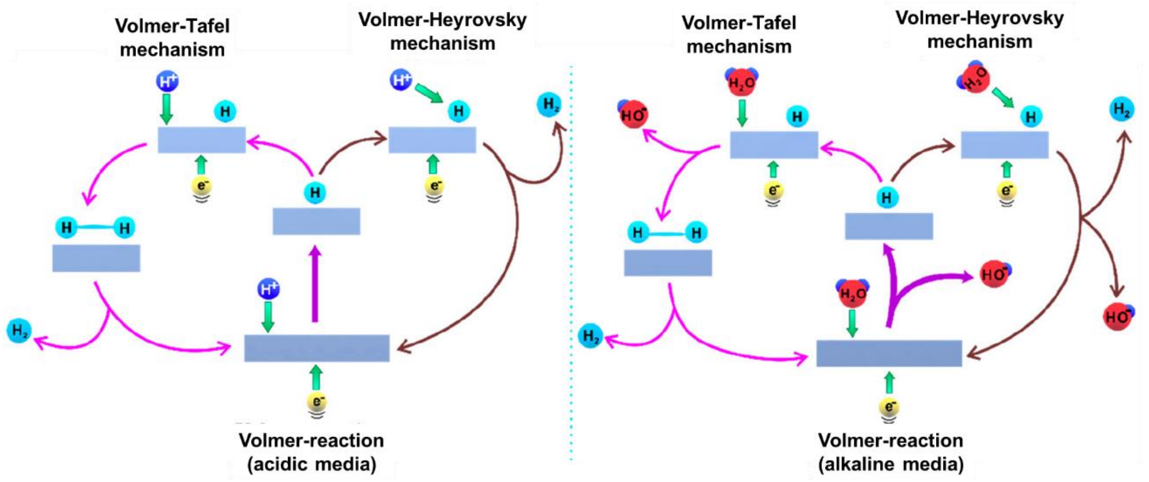

Figure 1.4. A schematic representation of the mechanisms of hydrogen evolution reaction (HER) occurring on an electrode surface in acidic (left) and alkaline (right) media.[8]

Pt group metal-based catalysts and their derivatives are well-known for their catalytic activity towards HER. Some of these are even known to deliver ~100% Faradaic efficiency at very low overpotential. But the high cost of these Pt group metals and their limited reserves on earth make it difficult to scale up the production of these catalysts.

Therefore, last several years, extensive research is being carried out to prepare efficient catalysts using non-noble metals or metal-free earth-abundant elements.[8-11]

1.2.2. Fuel cell

Fuel cells are electrochemical cells which can convert the chemical energy released during oxidation of fuel molecules, directly into electricity. It is the most energy-efficient device to derive power from fuels.

While the report of first fuel cell came in 1838 by Sir William Grove, the first commercial use of one happened only after a century when NASA used a hydrogen-oxygen fuel cell developed by Francis Thomas Bacon, for their space programs.[12] Among the six main types of fuel cells – PEMFC (proton exchange membrane fuel cell), SOFC (solid oxide fuel cell), DMFC (direct methanol fuel cell), PAFC (phosphoric acid fuel cell), MCFC (molten carbonate fuel cell), and AFC (alkaline fuel cell), PEMFC is the preferred one due to its durability and versatility.[13]

A proton exchange membrane fuel cell (PEMFC) transforms the chemical energy liberated during the reaction of hydrogen and oxygen into electrical energy, with only pure water and some heat as by-products. The fuel to electricity conversion efficiency of a PEMFC is ~60%, which is much higher than that of a conventional combustion-based power plant (fuel efficiency 33-35%).[14]

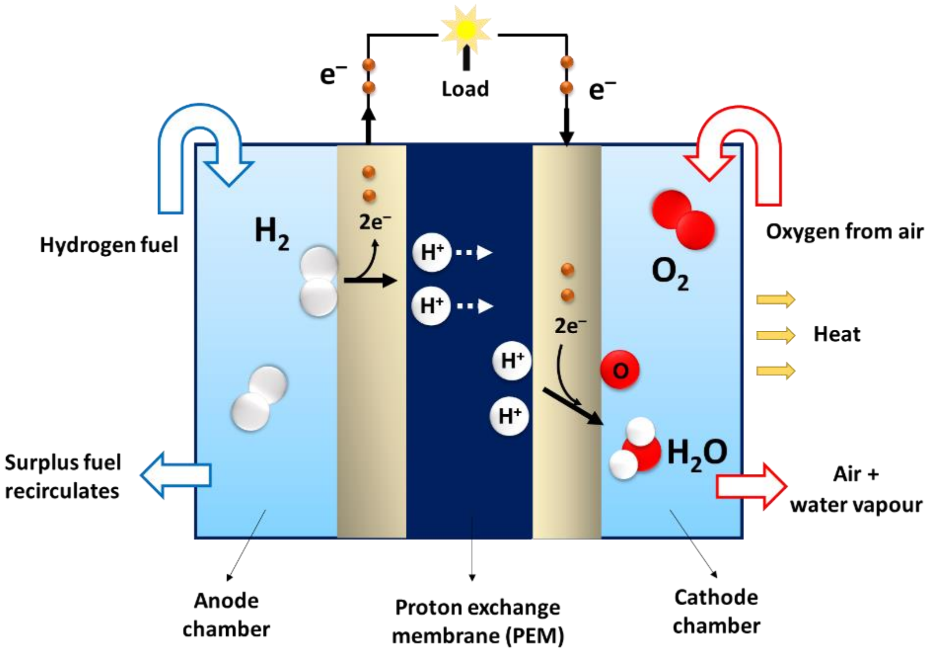

Figure 1.5. A schematic representation of the working of a proton exchange membrane fuel cell (PEMFC).

PEMFC: A fuel cell has two chambers – one connected to anode and the other to cathode (Figure 1.5). These chambers are separated from each other by a proton-exchange membrane (PEM). At the anode, H_2 is separated into H^+ ions and electrons. While the H^+ ions (chemical charge carriers) pass through a membrane to the cathode, the liberated electrons go through an external circuit to cathode. This flow of electrons produced from anode to cathode (the current), is directed through the load, typically an electric motor. At the cathode, O_2 is reduced to H_2O in the presence of an oxygen reduction reaction (ORR) catalyst. The only mode of interaction between H_2 and O_2 in a fuel cell is by means of the PEM. It selectively allows the transport of protons across it and restricts fuel crossover. In fine, the PEM acts like an electrolyte, and therefore also known as solid electrolyte.[15]

Now, for the wide-spread commercialization of fuel cells, the important task is to reduce its manufacturing cost and increase its durability. It can be done by improving the essential components of the fuel cell, like catalysts, proton exchange membrane, bipolar plates, and membrane-electrode assemblies.

1.2.2.1. Oxygen reduction reaction (ORR)

Oxygen reduction reaction (ORR) can proceed through three possible pathways:

(I) direct 4-electron reduction from $O_2 \rightarrow H_2O$

(II) 2-electron reduction from $O_2 \rightarrow H_2O_2$

(III) 1-electron reduction from $O_2 \rightarrow O_2^-$ (less common pathway; occurs in non-aqueous aprotic solvents and/or in alkaline solutions)

Now, the ΔE value for ORR is pH dependent and therefore, the reactions can be written in different ways based on the pH of the medium.[16,17] In acidic medium (at pH = 0, $[H^+_{(aq)}] = 1\ \mathrm{mol\ dm^{-3}}$), the 4-electron and 2-electron pathways of ORR can be written as:

$$O_2 + 4\,H^+ + 4\,e^- \rightarrow 2\,H_2O \qquad E^0 = +1.229\ \mathrm{V} \qquad \ldots (10)$$

$$O_2 + 2\,H^+ + 2\,e^- \rightarrow H_2O_2 \qquad E^0 = +0.670\ \mathrm{V} \qquad \ldots (11)$$

In alkaline medium (at pH = 14, $[OH^-_{(aq)}] = 1\ \mathrm{mol\ dm^{-3}}$), the reactions can be written as:

$$O_2 + 2\,H_2O + 4\,e^- \rightarrow 4\,OH^- \qquad E^0 = +0.401\ \mathrm{V} \qquad \ldots (12)$$

$$O_2 + H_2O + 2\,e^- \rightarrow HO_2^- + OH^- \qquad E^0 = -0.065\ \mathrm{V} \qquad \ldots (13)$$

For application in fuel cells, the direct 4-electron reduction from $O_2 \rightarrow H_2O$ is preferred since it would generate more electricity. In a fuel cell, ORR is also the slowest reaction since it involves the dissociation of O=O → 2 O ($\Delta H° = +498$ kJ mol^{-1}). It means that this activation energy barrier needs to be overcome in order to get high current density at cathode. And therefore, the use of a suitable electrocatalyst is required to lower the activation energy and drive the reaction at a feasible rate. Over the last two decades several efficient electrocatalysts have been developed for the direct reduction of O_2 to H_2O in order to improve the performance of fuel cells.[18-22]

The 2-electron reduction from $O_2 \rightarrow H_2O_2$ represents a green synthetic method for industrial production of H_2O_2, which is becoming increasingly important nowadays.[23] The traditional anthraquinone process of H_2O_2 production is an energy, capital and waste intensive method. Alternatively, the production of H_2O_2 by electrochemical reduction of O_2 has several advantages:

(i) Mild reaction conditions – room temperature and ambient pressure.
(ii) Use of green precursors – water and air.
(iii) Use of electricity (which can be sourced from a renewable energy resource) as the energy source.

While there has been significant advancement with respect to developing electrocatalysts for $O_2 \rightarrow H_2O$ conversion, there are very few electrocatalysts which can convert $O_2 \rightarrow H_2O_2$ with high selectivity.[23-26]

1.2.2.2 Proton conductivity in solid electrolytes

A solid proton conductor can be defined as a solid material which allows the passing of electricity through it by the exclusive movement of protons in it. Such materials can be either crystalline or amorphous. Apart from H^+, the conduction of electricity in a material by movement of other polyatomic protonic species such as H_3O^+, OH^- or NH_4^+, are also regarded as proton conducting materials in contemporary literature.[27]

Now, a proton H^+ which has no electron density of its own, has very small radius, and is never found as it is in solids under equilibrium condition. It strongly interacts with the electron density in its surrounding and is always found covalently bonded with some electronegative atom or ion. Protons are also shared between two atoms by means of H-bonding, for example O─H------O. The movement of a proton in a H-bond (O─H------O ↔ O------H─O) corresponds to the movement of charge as well, which is the key to proton conduction in a material.

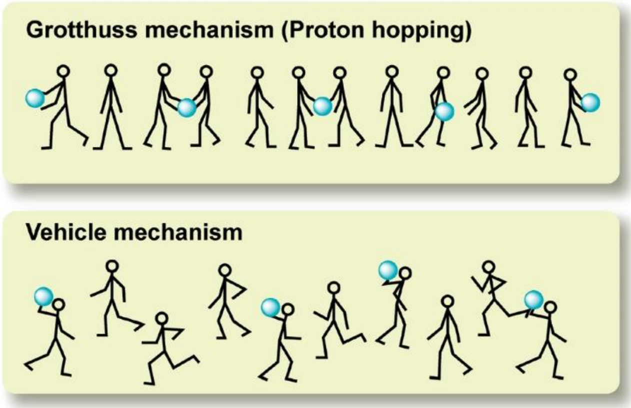

Figure 1.6. Illustration of Grotthuss (top) and vehicular (bottom) proton transport mechanism.[27]

In solution, the transfer rates of proton are very high. Here, the rate determining step is not the bond-making and breaking, but the reorientation of the molecules into the correct position for the transfer to occur. Using this process of making and concomitant breaking of covalent bonds, a proton can travel very fast through a network of H-bonds. This mechanism of proton transport was first proposed by Grotthuss in 1806.

In solids, the nature of proton conduction differs from that in solution, since the H-bonds in solids are more covalent and directional in character. Here, the movement of protons can be described as being analogous to the general acid-base concept.[26] As shown in figure 1.7, if the proton has to move from molecule 1 to molecule 2, the molecule 1 becomes the donor group or an acid, while the molecule 2 accepting the proton becomes the base. Since the reorientation of the molecules in solid is more difficult than that in solution, the energy requirement/activation energy for proton conduction in solid is much higher than that in solution.

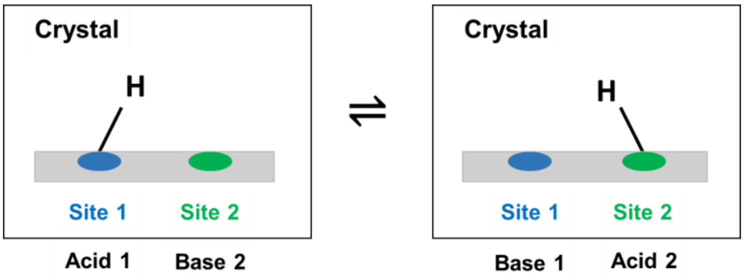

Figure 1.7. Acid-base analogy to proton conduction in solids.

Proton transport in solids can be described by two types of mechanisms - Grotthuss and vehicular (Figure 1.6).[12] The Grotthuss mechanism, is most prevalent in cases of water-assisted proton transport under mild temperatures (< 100 ºC). The activation energy required for this process is typically ≤ 0.4 eV/atom. This mechanism functions with the following sets of acid-base couples, among others:

H_3O^+/H_2O, H_2O/OH^-, $OH^-/[O^{2-}]$

NH_4^+/NH_3, RNH_3^+/RNH_3

$RCOOH/RCOO^-$, RSO_3H/RSO_3^-

In vehicular mechanism, polyatomic protonic species such as H_3O^+, OH^- or NH_4^+ migrate themselves across the bulk material to transport protons, and therefore, requires higher activation energy, typically > 0.4 eV/atom. For this reason, this mechanism is functional mostly at higher temperatures (> 100 ºC). For vehicular mechanism to operate in high efficiency, the solid material should contain wide internal cavities and channels; some zeolites and organic polymers are known to conduct protons using vehicular mechanism. In addition to it, it is preferrable that the migrating polyatomic ions have very less interaction with the molecules constituting the channels and pores, so that they can move faster. This mechanism of proton conduction can function only in materials where the corresponding acid/base partner (elucidated in the previous paragraph) is not present, for example, H_3O^+ without H_2O, or NH_4^+ without NH_3.

Now, for a proton conductor to be used as a solid electrolyte in a fuel cell or electrolyser, it needs to fulfil certain requirements:

(i) Should have proton conductivity ≥ 0.1 S cm^{-1}.
(ii) Should not allow any fuel crossover from anodic chamber to cathodic.
(iii) Should be an electronic insulator.
(iv) Should have high thermal, water, and electrochemical stability.
(v) Its synthesis and fabrication should be cost effective.

1.3. MATERIALS

1.3.1. Metal-organic frameworks (MOFs)

Metal-organic frameworks (MOFs) are a class of crystalline materials consisting of metal ions or clusters (called secondary building unit/SBU) connected by rigid organic ligands (called linkers) to form an infinite extended network.[29] MOFs come under the family of coordination polymers (CPs), but in recent times both the terms are being used interchangeably which is a cause of debate among scientists of inorganic and solid-state chemistry.[30] MOFs are constructed mainly with 3d-block metal ions because of their high

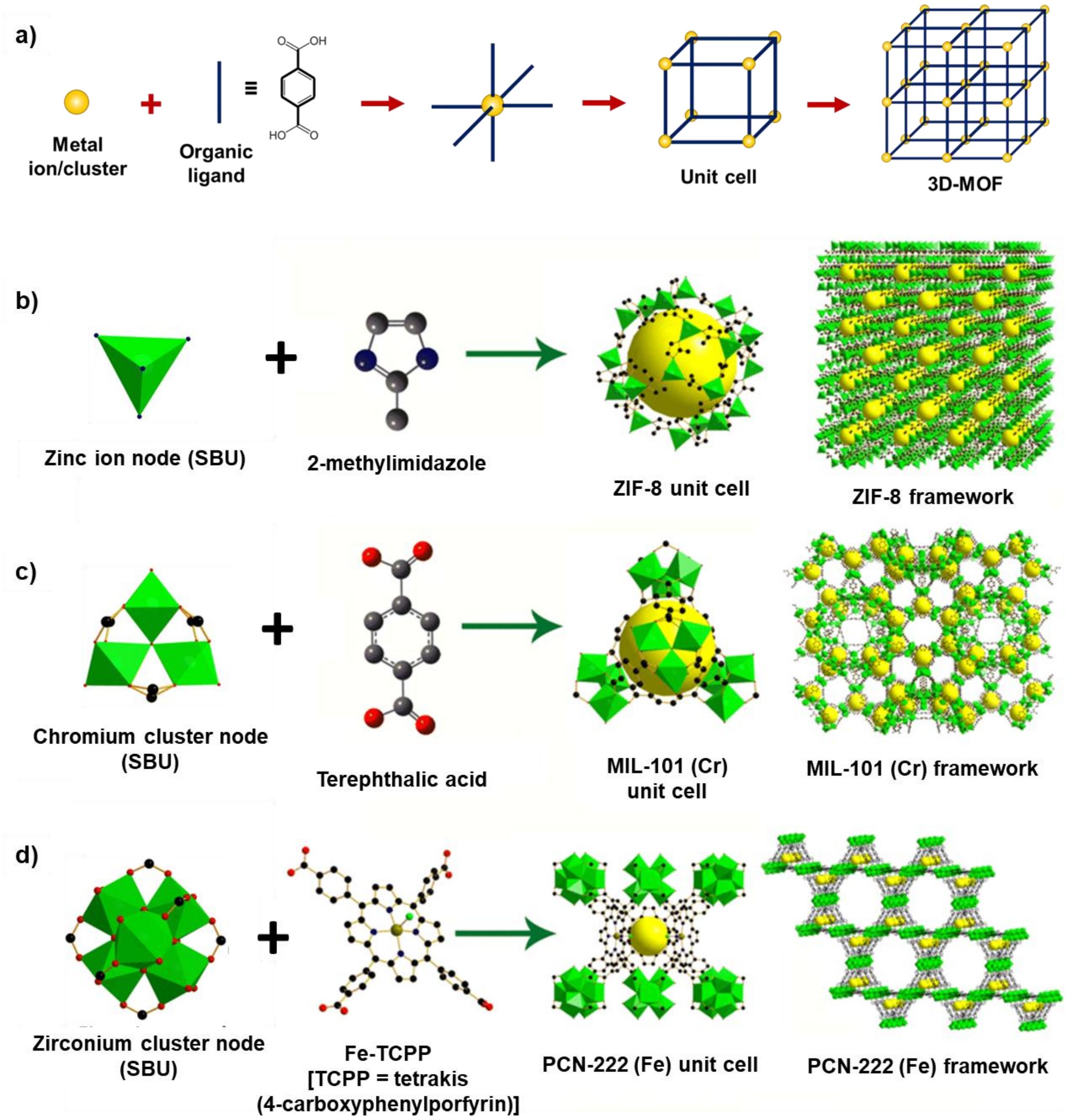

Figure 1.8. (a) Schematic representation of the formation of an arbitrary metal-organic framework (MOF). Illustration of the secondary building unit (SBU), organic linker, and their spatial arrangement in (b) ZIF-8, (c) MIL-101 (Cr) and (d) PCN-222 (Fe) MOFs.[29]

coordination number and ease of availability. Based on the coordination property of the metal ion/cluster and the denticity and size of the organic linker, there can be a wide array of possible frameworks with different pore and channel structures (Figure 1.8). A careful designing of such frameworks is now an active area of research and is called '*reticular synthesis*', as coined by Yaghi.[31,32]

MOFs in general are renowned for their framework stability, porosity, and high surface area. This allows for convenient post-synthetic modification of both the linker and metal node, insertion of small molecules as guest into the framework where the MOF cages act as host.[33-36] Apart from this, MOFs can be easily combined with other materials such as graphene, polymers, metal oxides, metal complexes, etc. to prepare hybrid composites. Figure 1.9 shows some of the possible ways to tune the structure and properties of MOFs, as well as different ways of utilizing MOFs to prepare hybrid-composites. Owing to these characteristics and the ease of tunability of the structure and properties, MOFs have gained huge popularity in the recent past, being used in various fields of applications including catalysis,[37,38] energy conversion,[39,40] molecular sensing,[41,42] optics,[43,44] proton conductivity,[45,46] and gas storage and separation.[47-49]

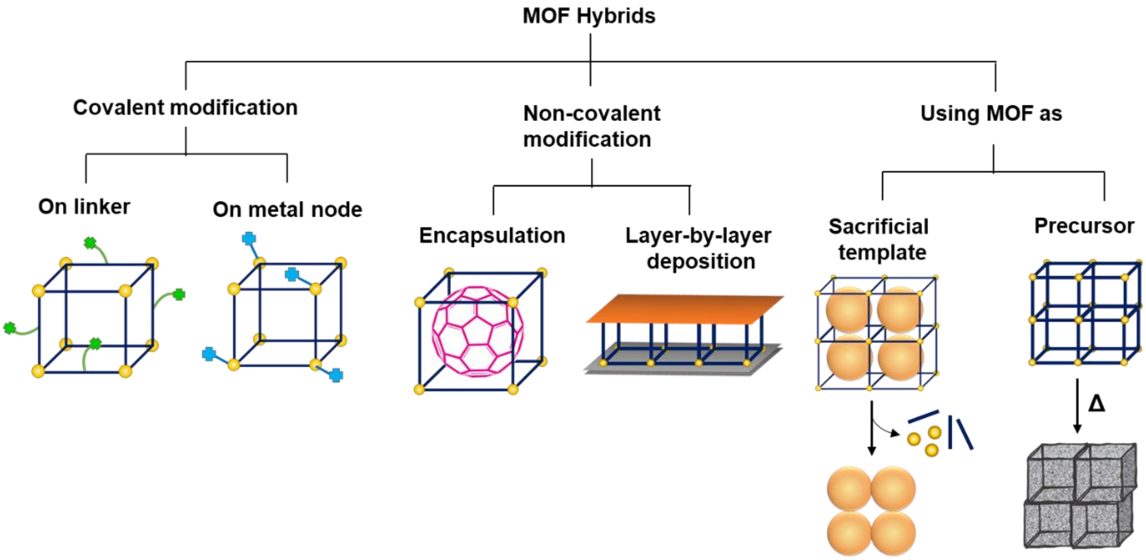

Figure 1.9. Illustration of some of the possible ways of preparing MOF-based hybrid composites.

1.3.2. Polyoxometalates (POMs)

Polyoxometalates are groups of polynuclear metal-oxo clusters. These are mostly anionic in nature. Each discrete unit of a POM consists of several MO_x polyhedra (M = Mo, W, V, Nb, Ta, etc; x = 4-7) units, which get condensed together in a solution upon acidification, to form the polyoxoanion.[50,51] These MO_x polyhedral units are connected to one another by either vertices or edges, and rarely by faces. The metal atoms residing at the surface of the cluster, commonly known as peripheral elements or addenda atoms, need to be able to change their coordination number from 4 in monomeric $\{MO_4)$ to 6 in the polyanion after condensation. And therefore, these addenda atoms are typically in their high oxidation states, with either a d^0 or a d^1 electronic configuration. The terminal O^{2-} ligands in these polyanions are doubly bonded to the metal ion by p_π–d_π interactions.

POMs can be broadly classified as either isopolyanions or heteropolyanions, based on the number of types of metal ions present in it. Isopolyanions, $[M_mO_y]^{q-}$ (M = metal ion) consist of only one type of addenda atoms, while heteropolyanions $[X_rM_mO_y]^{q-}$ (M = metal ion; X = heteroatom) consist of an additional heteroatom around which the condensation of the MO_x polyhedras take place. Now, depending on the coordination number of the heteroatom the structure of a POM can vary. For example, with a 4-coordinated heteroatom having tetrahedral geometry, the POM can form Keggin and Wells-Dawson structures (e.g., PO_4^{3-}, SiO_4^{4-}, and AsO_4^{3-}).[51] With a heteroatom having 6-coordinated octahedral geometry, Anderson-Evans structures can be formed (e.g., $Al(OH)_6^{3-}$ and TeO_6^{6-}); and with a 12-coordinated heteroatom, Silverton $[(UO_{12})Mo_{12}O_{30}]^{8-}$ would be formed. Figure 1.10 shows the generalised structure for some of the most classical POMs in polyhedral representation. Now, if from any of these structures, one or more of the metal-oxo polyhedras go missing, then that POM would be known as ‘lacunary’, owing to the formation of a lacuna in its structure.

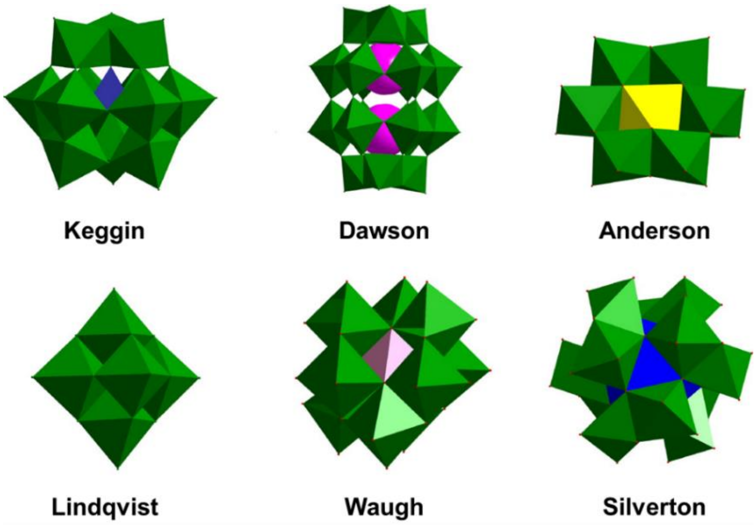

Figure 1.10. Polyhedral representation of some of the common polyoxometalates (POMs).[51]

1.3.2.1. Giant POMs

The Molybdenum Blues and Browns, discovered by Scheele in 1793, are the oldest class of POMs.[52,53] These POMs are known for their giant structures, with some approaching the size of small proteins. The largest amongst them is $\{Mo_{368}\}$, colored blue, shaped as a lemon and having a diameter of ~ 6 nm. Some of the other commonly known Mo-blue POMs are - spherical $\{Mo_{102}\}$ and wheel-shaped $\{Mo_{154}\}$. Another spherical-shaped member of this group of giant POMs is $\{Mo_{132}\}$, which is brown in color.

Most of these giant POMs are constructed using the same structural building block, $\{MoMo_5\}$. At the center of this building block is a pentagonal bipyramidal $\{MoO_7\}$ unit, which is surrounded by five edge-sharing octahedral $\{MoO_6\}$ units along the equator of the bipyramid (Figure 1.11).

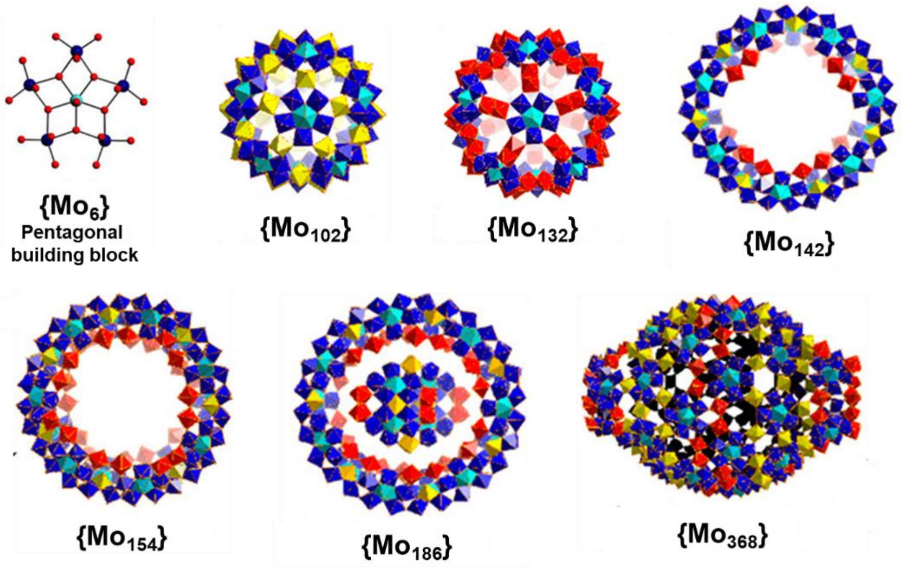

Figure 1.11. Ball and stick representations of the pentagonal building block $\{Mo_6\}$. Polyhedral representation of giant-polyoxometalates.[53]

These giant polyanions contain mixed valence Mo^{V} and Mo^{VI} addenda atoms. An intervalence charge transfer between these Mo^{V} and Mo^{VI} centers gives rise to the rich blue and brown colors of these POMs.[50] This charge transfer is facilitated by the π-orbitals of the bridging oxo ligands. For Mo-brown POMs, the ratio of Mo^{V}/Mo^{VI} is higher than that in Mo-blues.

The well-known Mo-brown giant POM – $\{Mo_{132}\}$, is also known as inorganic super fullerene. It has an icosahedral symmetry with more than 500 atoms constituting the structure. It is shaped like a spherical hollow container and is a characteristic member of Keplerate family of POMs. The sphere consists of a total of 12 $\{Mo_{11}\}$- polyoxomolybdate fragments of fivefold symmetry, born out of the previously mentioned $\{MoMo_5\}$ building blocks. Figure 1.11 shows the polyhedral representation of some of the well-known giant-polyoxometalates.

1.4. MOTIVATION FOR THE THESIS WORK

As has been discussed in the preceding sections, research in the field of '*optimum utilization of renewable energy resources*', is of paramount importance. While development of efficient electrocatalysts and proton conducting materials, has always been of top priority for scientists around the globe, and when we are already witnessing some notable developments in this regard, at this time, the focus should shift towards making these innovations cheaper enough for widespread use in practical applications. In all the works discussed in this thesis, we have tried to focus on developing cheaper yet efficient materials for proton conduction, and electrocatalysis- oxygen reduction reaction (ORR) and hydrogen evolution reaction (HER).

The first part of this thesis work involves designing of MOF based proton conducting material. Since the efficiency of a fuel cell largely depends on the efficiency of the proton exchange membrane (PEM), it is important to develop good yet affordable proton conducting materials. Till now, the most widely commercially used proton conductor is Nafion, which is very costly, and it loses its conducting properties at elevated temperatures. In this regard, designing of MOF-based proton conductors can prove to be beneficial. In **chapter 2**, we have worked with MOF-808 which is well-known for its high water sorptivity, and high surface area and porosity. In this work, we have used a new technique of defect engineering, which is the introduction of a controlled amount of defects in the MOF structure, to tune its physical and chemical properties such as, porosity, water sorptivity and acidity, among others. By using this technique we were able to develop sister MOFs of MOF-808 having much higher proton conductivity. Here it is important to mention that all these MOFs could be prepared in a '*one-pot*' synthesis and therefore, are easy to reproduce.

In **chapter 3**, we have developed two MOF-based proton conductors by using the strategy of post-synthetic modification on two flexible MOFs – Fe-MIL-53-NH_2 and Fe-MIL-88B-

NH_2. The motivation for this work came from one of our previous works on UiO-66 MOF. The reason for choosing flexible MOFs for this study is that these materials undergo dynamic structural transformations in response to host−guest interactions, primarily guided by H-bonds. This feature of these MOFs facilitates them in maintaining high proton conductivity over a wide range of relative humidity (RH). In addition to this, the flexible nature of these frameworks allows easier modification of the pores of the pertinent MOFs. The choice of Fe(III) metal ion for these MOFs is crucial for the possible use of these MOFs for real applications, since Fe is nontoxic in nature. Now, MOFs as such cannot be obtained in the form of a flexible membrane, and therefore MOFs are difficult to be used directly for practical applications, like in a fuel cell or electrolyzers. We have thus investigated, in this work, their applicability by fabricating these functionalized MOFs with organic polymers, resulting in polymer−MOF mixed matrix membranes (MMMs).

Another part of this thesis work focusses on developing electrocatalysts, relevant to energy conversion application. Now, as has been discussed earlier, MOFs are materials of huge potential owing to their ease of structural tunability. They can also be easily combined with various other materials to prepare hybrid composites which can be functional in various types of applications. Since the last several years our research group has been developing MOF-based materials for application in electrocatalysis and proton conduction, and this inspired me further to work with MOFs. In **chapter 4** we have prepared a MOF-based host-guest supramolecular composite where C_{60} molecules (guest) were encapsulated in the cages of ZIF-8 MOF (host) by means of an *in situ* synthetic strategy. ZIF-8 is one of the most easily synthesizable, economical, and stable MOF reported till date. From previous works we had found that catalytically inactive/unstable small molecules often acted as robust and efficient OER electrocatalysts once encapsulated in ZIF-8 MOF cages. In this case as well, the encapsulated C_{60} molecules acted as better ORR electrocatalysts with lower overpotential and higher product selectivity than bare C_{60} as such.

Chapter 5 discusses the synthesis of a HER electrocatalyst by electrochemical reduction of $\{Mo_{132}\}$ solution. As has already been mentioned, giant-POMs like $\{Mo_{132}\}$ are highly reduced polyanions. But in this work, we have successfully been able to reduce it further to generate an extended structure composed of $\{Mo_{132}\}$ balls. And interestingly, this new form of extended structure acts as a very stable and efficient electrocatalyst for HER while the free $\{Mo_{132}\}$ balls in solution were completely inactive towards electrocatalysis.

1.5. REFERENCES

1. Ritchie, H.; Roser, M.; Rosado, P. (2022) - "Energy". Published online at OurWorldInData.org. Retrieved from: 'https://ourworldindata.org/energy' [Online Resource].
2. bp Statistical Review of World Energy 2021.
3. Kuo, G. When Fossil Fuels Run Out, What Then? May 2019. https://mahb.stanford.edu/library-item/fossil-fuels-run/
4. Tahir, M. B.; Batool, A. Chapter 3 - Recent development in sustainable technologies for clean hydrogen evolution: Current scenario and future perspectives. In *Sustainable Materials and Green Processing for Energy Conversion*; Elsevier, 2022; pp 97-130. DOI: 10.1016/B978-0-12-822838-8.00008-9.
5. Wang, S.; Lu, A.; Zhong, C-J. Hydrogen production from water electrolysis: role of catalysts. *Nano Converg*. **2021**, *8*, 4.
6. Hunter, B. M.; Gray, H. B.; Müller., A. M. Earth-Abundant Heterogeneous Water Oxidation Catalysts. *Chem. Rev.* **2016**, *116*, 14120–14136.
7. Blakemore, J. D.; Crabtree. R. H.; Brudvig, G. W. Molecular Catalysts for Water Oxidation. *Chem. Rev.* **2015**, *115*, 12974–13005.
8. Zhu, J.; Hu, L.; Zhao, P.; Lee, L. Y. S.; Wong, K-Y. Recent Advances in Electrocatalytic Hydrogen Evolution Using Nanoparticles. *Chem. Rev.* **2020**, *120*, 851–918.
9. Dubouis, N.; Grimaud, A. The hydrogen evolution reaction: from material to interfacial descriptors. *Chem. Sci*. **2019**,*10*, 9165-9181.
10. Safizadeh, F.; Ghali, E.; Houlachi, G. Electrocatalysis developments for hydrogen evolution reaction in alkaline solutions – A Review. *Int. J. Hydrog. Energy* **2015**, *40*, 256-274.
11. Vesborg, P. C. K.; Seger, B.; Chorkendorff, I. Recent Development in Hydrogen Evolution Reaction Catalysts and Their Practical Implementation. *J. Phys. Chem. Lett.* **2015**, *6*, 951–957.
12. Ramaswamy, P.; Wong, N. E.; Shimizu, G. K. H. MOFs as proton conductors – challenges and opportunities. *Chem. Soc. Rev.* **2014**, *43*, 5913.
13. https://www.chfca.ca/fuel-cells-hydrogen/about-fuel-cells/
14. http://www.hydrogenandfuelcells.energy.gov.
15. Luo, H-B.; Ren, Q.; Wang, P.; Zhang, J.; Wang, L.; Ren, X-M. High Proton Conductivity Achieved by Encapsulation of Imidazole Molecules into Proton-Conducting MOF-808. *ACS Appl. Mater. Interfaces.* **2019**, *11*, 9164−9171.
16. Shimizu, K.; Sepunaru, L.; Compton, R. G. Innovative catalyst design for the oxygen reduction reaction for fuel cells. *Chem. Sci.* **2016**, *7*, 3364-3369.
17. Kulkarni, A.; Siahrostami, S.; Patel, A.; Nørskov, J. K. Understanding Catalytic Activity Trends in the Oxygen Reduction Reaction, *Chem. Rev.* **2018**, *118*, 2302–2312.
18. Stamenkovic, V. R.; Fowler, B.; Mun, B. S.; Wang, G.; Ross, P. N.; Lucas, C. A.; Markovic´, N. M. Improved oxygen reduction activity on $Pt_3Ni(111)$ via increased surface site availability. *Science* **2007**, *315*, 493–497.
19. Strasser, P.; Koh, S.; Anniyev, T.; Greeley, J.; More, K.; Yu, C.; Liu, Z.; Kaya, S.; Nordlund, D.; Ogasawara, H.; Toney, M. F.; Nilsson, A. Lattice-strain control of the activity in dealloyed core-shell fuel cell catalysts. *Nat. Chem*. **2010**, *2*, 454–460.
20. Liang, Y.; Li, Y.; Wang, H.; Zhou, J.; Wang, J.; Regier, T.; Dai, H. Co_3O_4 nanocrystals on graphene as a synergistic catalyst for oxygen reduction reaction. *Nat. Mater.* **2011**, *10*, 780.
21. Wang, J.; Huang, Z.; Liu, W.; Chang, C.; Tang, H.; Li, Z.; Chen, W.; Jia, C.; Yao, T.; Wei, S.; Wu, Y.; Li, Y. Design of N-coordinated dual-metal sites: a stable and active Pt-free catalyst for acidic oxygen reduction reaction. *J. Am. Chem. Soc.* **2017**, *139*, 17281–17284.
22. Wu, G.; More, K. L.; Johnston, C. M.; Zelenay, P. High-performance electrocatalysts for oxygen reduction derived from polyaniline, iron, and cobalt. *Science* **2011**, *332*, 443–447.
23. Jiang, K.; Back, S.; Akey, A. J.; Xia, C.; Hu, Y.; Liang, W.; Schaak, D.; Stavitski, E.; Nørskov, J. K.; Siahrostami, S.; Wang, H. Highly selective oxygen reduction to hydrogen peroxide on transition metal single atom coordination. *Nat. Commun.* **2019**, *10*, 3997.
24. Siahrostami, S.; Verdaguer-Casadevall, A.; Karamad, M.; Deiana, D.; Malacrida, P.; Wickman, B.; Escudero-Escribano, M.; Paoli, E. A.; Frydendal, R.; Hansen, T. W.; Chorkendorff, I.; Stephens, I. E. L.; Rossmeisl, J. Enabling direct H_2O_2 production through rational electrocatalyst design. *Nat. Mater.* **2013**, *12*, 1137–1143.
25. Lee, Y.-H.; Li, F.; Chang, K.-H.; Hu, C.-C.; Ohsaka, T. Novel synthesis of N-doped porous carbons from collagen for electrocatalytic production of H_2O_2. *Appl. Catal. B* **2012**, *126*, 208–214.

26. Lu, Z.; Chen, G.; Siahrostami, S.; Chen, Z.; Liu, K.; Xie, J.; Liao, L.; Wu, T.; Lin, D.; Liu, Y.; Jaramillo, T. F.; Nørskov, J. K.; Cui, Y. High-efficiency oxygen reduction to hydrogen peroxide catalysed by oxidized carbon materials. *Nat. Catal*. **2018**, *1*, 156–162.
27. Poulsen, F. W. (1980). *An introduction to proton conduction in solids*. Risø National Laboratory. Risø-M No. 2244
28. Ueki, T.; Watanabe, M. Macromolecules in Ionic Liquids: Progress, Challenges, and Opportunities. *Macromolecules* **2008**, *41*, 3739–3749.
29. Huo, Y.-p.; Liu, S.; Gao, Z.-x.; Ning, B.-a.; Wang, Y. State-of-the-art progress of switch fluorescence biosensors based on metal-organic frameworks and nucleic acids. *Microchim. Acta* **2021**, *188*, 168.
30. Biradha, K.; Ramanan, A.; Vittal, J. J. Coordination Polymers Versus Metal-Organic Frameworks. *Cryst. Growth Des.* **2009**, *9*, 7.
31. Yaghi, O. M.; O'Keeffe, M.; Ockwig, N. W.; Chae, H. K.; Eddaoudi, M.; Kim, J. Reticular synthesis and the design of new materials. *Nature* **2003**, *423*, 705−714.
32. Jiang, H.; Alezi, D.; Eddaoudi, M. A reticular chemistry guide for the design of periodic solids. *Nat. Rev. Mater.* **2021**, *6*, 466−487.
33. Islamoglu, T.; Goswami, S.; Li, Z.; Howarth, A. J.; Farha, O. K.; Hupp, J. T. Postsynthetic Tuning of Metal-Organic Frameworks for Targeted Applications. *Acc. Chem. Res.* **2017**, *50*, 805−813.
34. Eddaoudi, M.; Sava, D. F.; Eubank, J. F.; Adil, K.; Guillerm, V. Zeolite-like metal-organic frameworks (ZMOFs): design, synthesis, and properties. *Chem. Soc. Rev.* **2015**, *44*, 228−249.
35. Kirchon, A.; Feng, L.; Drake, H. F.; Joseph, E. F.; Zhou, H.-C. From fundamentals to applications: a toolbox for robust and multifunctional MOF materials. *Chem. Soc. Rev.* **2018**, *47*, 8611−8638.
36. Sosa, J. D.; Bennett, T. F.; Nelms, K. J.; Liu, B. M.; Tovar, R. C.; Liu. Y. Metal–Organic Framework Hybrid Materials and Their Applications. *Crystals* **2018**, *8*, 325.
37. Dhakshinamoorthy, A.; Li, Z.; Garcia, H. Catalysis and photocatalysis by metal organic frameworks. *Chem. Soc. Rev.* **2018**, *47*, 8134−8172.
38. Chughtai, A. H.; Ahmad, N.; Younus, H. A.; Laypkov, A.; Verpoort, F. Metal-organic frameworks: versatile heterogeneous catalysts for efficient catalytic organic transformations. *Chem. Soc. Rev.* **2015**, *44*, 6804−6849.
39. Mukhopadhyay, S.; Basu, O.; Nasani, R.; Das, S. K. Evolution of metal organic frameworks as electrocatalysts for water oxidation. *Chem. Commun.* **2020**, *56*, 11735−11748.
40. Qiu, T.; Liang, Z.; Guo, W.; Tabassum, H.; Gao, S.; Zou, R. Metal-Organic Framework-Based Materials for Energy Conversion and Storage. *ACS Energy Lett.* **2020**, *5*, 520−532.
41. Lustig, W. P.; Mukherjee, S.; Rudd, N. D.; Desai, A. V.; Li, J.; Ghosh, S. K. Metal-organic frameworks: functional luminescent and photonic materials for sensing applications. *Chem. Soc. Rev*. **2017**, *46*, 3242−3285.
42. Koo, W.-T.; Jang, J.-S.; Kim, I.-D. Metal-Organic Frameworks for Chemiresistive Sensors. *Chem* **2019**, *5*, 1938−1963.
43. Zheng, Y.; Sun, F.-Z.; Han, X.; Xu, J.; Bu, X.-H. Recent Progress in 2D Metal-Organic Frameworks for Optical Applications. *Adv. Opt. Mater*. **2020**, *8*, 2000110.
44. Horike, S.; Ma, N.; Fan, Z.; Kosasang, S.; Smedskjaer, M. M. Mechanics, Ionics, and Optics of Metal-Organic Framework and Coordination Polymer Glasses. *Nano Lett.* **2021**, *21*, 6382−6390.
45. Lim, D.-W.; Kitagawa, H. Proton Transport in Metal-Organic Frameworks. *Chem. Rev*. **2020**, *120*, 8416−8467.
46. Ye, Y.; Gong, L.; Xiang, S.; Zhang, Z.; Chen, B. Metal-Organic Frameworks as a Versatile Platform for Proton Conductors. *Adv. Mater.* **2020**, *32*, 1907090.
47. Li, B.; Wen, H.-M.; Zhou, W.; Chen, B. Porous Metal-Organic Frameworks for Gas Storage and Separation: What, How, and Why? *J. Phys. Chem. Lett.* **2014**, *5*, 3468−3479.
48. Connolly, B. M.; Madden, D. G.; Wheatley, A. E. H.; Fairen- Jimenez, D. Shaping the Future of Fuel: Monolithic Metal-Organic Frameworks for High-Density Gas Storage. *J. Am. Chem. Soc.* **2020**, *142*, 8541−8549.
49. Dhainaut, J.; Bonneau, M.; Ueoka, R.; Kanamori, K.; Furukawa, S. Formulation of Metal-Organic Framework Inks for the 3D Printing of Robust Microporous Solids toward High-Pressure Gas Storage and Separation. *ACS Appl. Mater. Interfaces* **2020**, *12*, 10983−10992.
50. Gumerova, N. I.; Rompel, A. Synthesis, structures and applications of electron-rich polyoxometalates. *Nat. Rev. Chem*. **2018**, *2*, 0112.
51. Omwoma, S.; Gore, C. T.; Ji, Y.; Hu, C.; Song, Y.-F. Environmentally benign polyoxometalate materials. *Coord. Chem. Rev*. **2015**, *286*, 17–29.
52. Passadis, S.; Kabanos, T. A.; Song, Y-F.; Miras, H. N. Self-Assembly in Polyoxometalate and Metal Coordination-Based Systems: Synthetic Approaches and Developments. *Inorganics* **2018**, *6*, 71.

53. Ng, M. T.-K.; Bell, N. L.; Long, D.-L.; Cronin, L. Facile and Reproducible Electrochemical Synthesis of the Giant Polyoxomolybdates. *J. Am. Chem. Soc.* **2021**, *143*, 20059−20063.

CHAPTER 2

Defect Engineering in a Metal−Organic Framework System to Achieve Super-Protonic Conductivity

OVERVIEW:

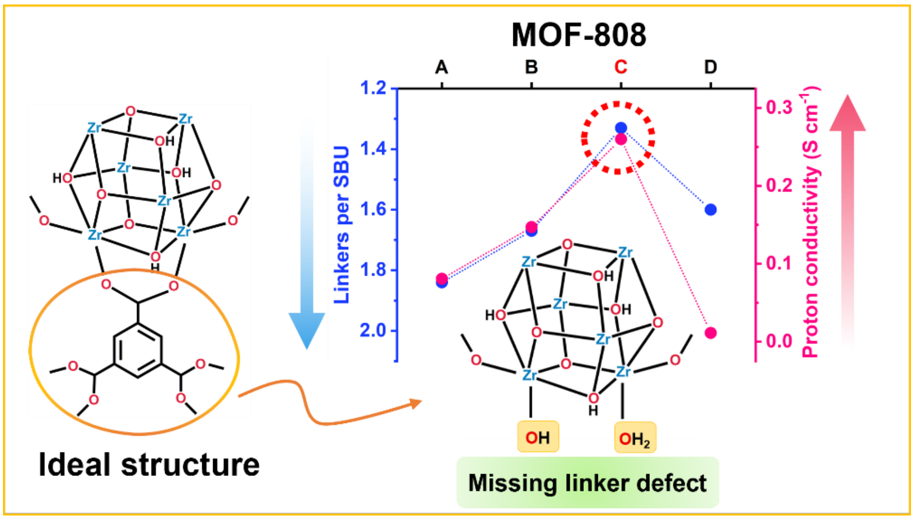

Controlled incorporation of missing-linker defect sites could be achieved in four sister metal-organic frameworks (MOFs) of MOF-808, namely, **MOF-808 A – D** *via* modulated-synthesis**.** An impressive enhancement in proton conductivity is observed in these sister MOFs (increase from 10^{-3} Scm^{-1} to 10^{-1} Scm^{-1}) as compared to a highly crystalline, low-in-defect variant of MOF-808. **MOF-808 C**, having optimized defect density, shows proton conductivity of 2.6×10^{-1} Scm^{-1} at 80 ºC and 98% relative humidity – the highest value reported till date for pure MOF-based proton conductors without extensive structural modifications. The introduction of defects induces super-protonic conductivity by modifying different properties, like porosity, water sorptivity and acidity. Furthermore, an assembly of this super proton-conducting MOF with Pt – a versatile HER catalyst, has been studied with the objective to influence the catalytic activity. This MOF-catalyst assembly was found to have lower overpotential requirements, owing to an increase in local acidity and efficient proton management around the catalyst.

2.1. INTRODUCTION

Metal-organic frameworks (MOFs) have gained huge popularity in the recent past, being used in various fields of applications including catalysis,[1,2] energy conversion,[3,4] molecular sensing,[5,6] optics,[7,8] proton conductivity,[9-13] gas storage and separation.[14-16] Its crystalline structure combined with the scope of reticular synthesis and the wide array of possible post-synthetic modifications has turned MOFs into a material with enormous potential.[17-21] The scope of structural tunability provides us with a convenient way to establish a proper structure-function relationship and modulate the properties of the material as per requirement. The controlled incorporation of structural defects in a MOF to modify its properties or, to say, defect engineering in MOFs, is a relatively new research field that is fast gaining popularity.[22-26] One of the earliest studies on defective MOF was reported by Goodwin and co-workers. who had identified nanoregions of *reo* topology in UiO-66.[27] Since then, UiO-66 has become the ground for studying the effect of defects in a MOF,[28-31] and the different ways of inducing them.[32-37] In one such noteworthy work, Kitagawa and co-workers. had studied the effect of the introduction of defects on the proton-conducting properties of UiO-66.[38] In this work, linker defects helped to enhance the conductivity of the MOF by modifying its porosity, and exposing more Lewis acidic sites – altogether improving the proton mobility. In our present work, controlled defect engineering has been performed on MOF-808 with the aim to enhance and modulate its proton conductivity.

MOF-808 was first reported in 2014 by Yaghi and co-workers.[39,40] The secondary building unit (SBU) of this MOF consists of a hexanuclear zirconium node connected to six tridentate ligands (trimesic acid, H_3BTC) as shown in Figure 2.1. The MOF has lower node connectivity compared to most of the other hexanuclear zirconium node-based MOFs, which in this case, leaves some open metal sites to be occupied by additional six monodentate ligands ($HCOO^-$ and

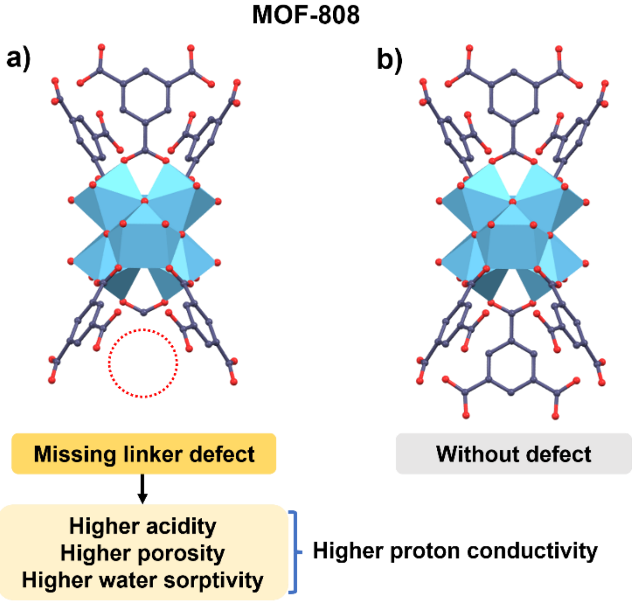

Figure 2.1. Illustration of MOF-808 structure (a) with and (b) without linker defect.

H_2O/OH^-) per SBU for charge balancing.[41] The choice of MOF-808 for this work stemmed from two key factors, that are (a) high water uptake capacity in moderate relative humidity (P/P_0 = 0.3 – 0.9), and (b) Zr_6-oxo nodes having linker connectivity of only six, thus providing adequateaccessible open metal sites, which can be increased further by the introduction of the missing-linker defects. Ever since the first report, the MOF has been mostly explored for heterogeneous catalysis.[42-47] There are only a handful of studies on the proton conductivity of this MOF.[48-53] While the microcrystalline parent MOF shows conductivity of the order of 10^{-3} Scm^{-1} under 99% relative humidity (RH), Luo et al. could enhance the conductivity to the order of 10^{-2} by incorporating imidazole moieties into the framework (Im@MOF-808).[49] In another work, Sharma et al. enhanced the proton transport properties by grafting sulfamate moieties onto the metal clusters of MOF-808.[53] But so far, no attempts have been made to modulate the proton conductivity of MOF-808 using defect engineering. There are a few recent reports on defective MOF-808,[54-56] but no systematic study has been performed yet correlating the structural defects and their effects on the observed proton transport properties. We have contributed to this field by designing four MOFs (**MOF-808 A**, **MOF-808 B**, **MOF-808 C**, and **MOF-808 D**) with varying amounts of missing linker defects and have studied the role of defects in modifying different structural properties of these MOFs and their implication on the proton conductivity. The defects were introduced by coordination modulation method – a versatile approach for controllable synthesis of MOFs.[32,57-61]

The properties of these sister MOFs were studied and compared with those of a MOF-808 sample with low crystal defect (named hereafter as **MOF-808 S**); and it is fascinating to realize that the incorporation of defects by simple twitching of the synthetic conditions, could enhance the protonic conductivity of MOF-808 by ~50 times. Finally, it has been shown that such super-protonic conductors as the defect engineered MOF-808, have the potential to influence electrocatalytic proton-coupled electron transfer reactions (PCETs) positively, when used as a thin layer membrane over a catalyst. Specifically, electrocatalytic hydrogen evolution reaction (HER) performed on Pt disc has been studied as a model system in this regard.

2.2. EXPERIMENTAL SECTION

2.2.1. Materials

All the chemicals were used as received without any further purification. zirconyl chloride octahydrate ($ZrOCl_2.8H_2O$), formic acid - 85% (HCOOH), dimethyl formamide (DMF), benzoic acid, lithium chloride (LiCl) sodium hydroxide (NaOH), and methanol were purchased from Finar chemicals. 1,3,5-benzene tricarboxylic acid (H_3BTC) was purchased from TCI chemicals.

2.2.2. Synthesis

2.2.2.1. Synthesis of MOF-808 S

The synthesis of low-defect **MOF-808 S** was adapted from an earlier report, which yielded octahedral microcrystals.[39] 0.053 g (0.1646 mmol) of $ZrOCl_2.8H_2O$, 0.0366 g (0.1741 mmol) of H_3BTC, 6 mL of DMF and 6 mL of formic acid were taken in a 23 mL Teflon reactor. The reaction mixture was ultrasonicated for 15 minutes and then heated at 100 ^oC for 7 days in a programmable oven, followed by cooling to 30 ^oC in 12 hours. The product was collected by centrifugation and washed with DMF and methanol 3 times each, over the course of 6 days. The product was dried in a hot air oven at 70 °C for 24 hours.

2.2.2.2. Synthesis of MOF-808 A – D

The procedure for preparing the series of defective **MOF-808 (A−D)** variants is based on recently published studies along with some modifications.[40,45] 1.165 g (3.61 mmol) of $ZrOCl_2.8H_2O$, 0.353 g (1.68 mmol) of H_3BTC and 50 mL of DMF were taken in a 200 mL Teflon-capped reaction vessel. To it, varying amounts of formic acid (as specified in Table 2.1) as modulator, was added. The reaction mixture was ultrasonicated for 15 minutes and then heated at 130 ^oC for 20 hours, followed by cooling to 30 ^oC naturally. The product was collected by centrifugation and washed with DMF and methanol for 3 times each, over the course of 6 days. The product was dried in a hot air oven at 70 °C for 24 hours.

In this modulator-mediated synthesis, the formic acid (modulator) acts as a competitor to the framework linker (BTC), since both are having the same carboxylate functionality.[57,58] This, in turn, slows down the reaction rate and aids in the formation of

Table 2.1. Reagent amounts used in the synthesis.

Sample name	$ZrOCl_2.8H_2O$	1,3,5-BTC	HCOOH
MOF-808 S	0.053 g, 0.1646 mmol	0.0366 g, 0.1741 mmol	6 mL, 0.141 mol
MOF-808 A	1.165 g, 3.61 mmol	0.353 g, 1.68 mmol	50 mL, 1.18 mol
MOF-808 B	1.165 g, 3.61 mmol	0.353 g, 1.68 mmol	40 mL, 0.944 mol
MOF-808 C	1.165 g, 3.61 mmol	0.353 g, 1.68 mmol	30 mL, 0.708 mol
MOF-808-D	1.165 g, 3.61 mmol	0.353 g, 1.68 mmol	20 mL, 0.472 mol

highly crystalline materials. Here, the sequential decrease in the concentration of formic acid (**MOF-808 A** > **MOF-808 B** > **MOF-808 C** > **MOF-808 D**) is expected to lead to faster reaction kinetics, allowing for the scope of defect formation.[57] In this series, **MOF-808 A** was found to have a very low defect concentration; in fact lower than **MOF-808 S** (*vide infra*). The properties of all the MOFs in the series have been compared together in the following section, in order to find a trend out of it; a reference has been made to the properties of **MOF-808 S** as and when required.

2.2.2.3. Synthesis of MOF-808 C-benz

MOF-808 C was treated with benzoic acid with an aim to cap the open metal sites originating due to the missing linker defects.

400 mg of **MOF-808 C** was added with 50 mg of benzoic acid and 10 mL of DMF in a 15 mL screw-capped vial. The mixture was heated at 80 °C for 24 hours in a programmable oven. The product (**MOF-808 C-benz**) was separated and heated again at 80 °C with fresh DMF for 20 hours. The washing by DMF to take out additional benzoic acids occupying the MOF pores was repeated four times, followed by washing twice with methanol. The product was dried in a hot air oven at 70 °C for 24 hours.

2.2.2.4. Synthesis of MOF-808 C-Li

MOF-808 C was treated with 0.5 M LiCl with an aim to exchange the acidic protons in the MOF with lithium ions.

Approximately 1 g of **MOF-808 C** was stirred in 20 mL 0.5 M aqueous solution of LiCl for 12 hours. The ion exchanged product was collected by centrifugation and then dispersed in 50 mL of deionized water to wash away the LiCl present inside the pores of the MOF. The washing was repeated thrice and then the collected product was dried in a hot air oven at 70 °C for 48 hours.

2.2.3. Methods

The instrumental details of all the experiments are provided in appendix 1.

2.2.3.1. Electrochemical impedance spectroscopy

Electrochemical impedance measurements for MOF samples were performed using a 2-electrode setup in parallel plate mode. A similar protocol for sample preparation and experimental setup was followed for all the MOF samples.

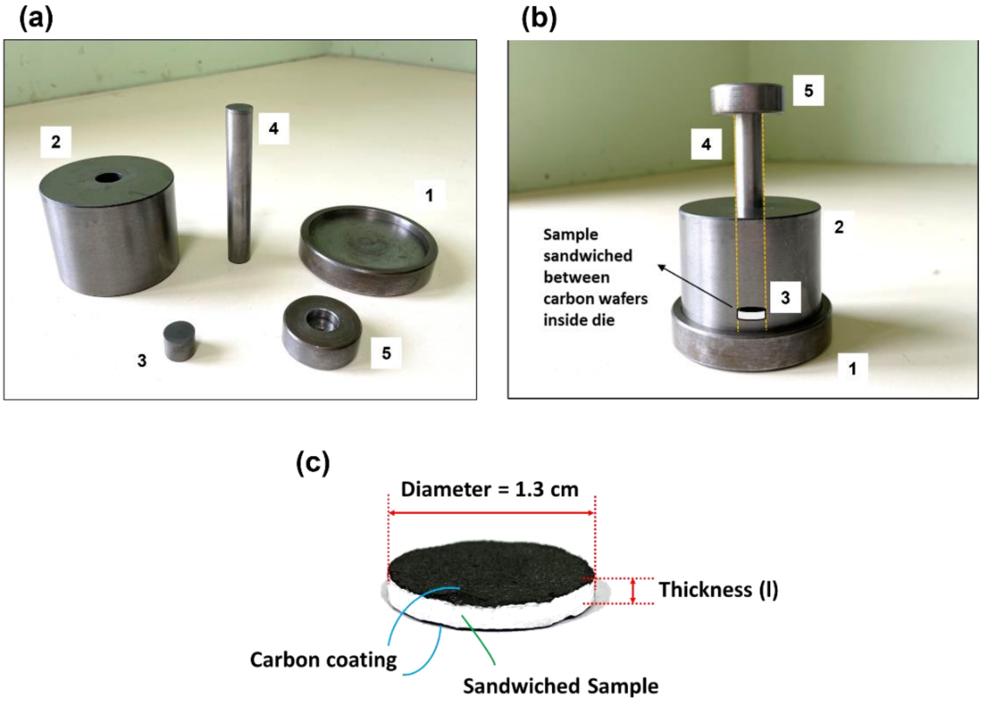

Figure 2.2. Pellet-maker die setup a) showing all the parts separately and b) after assembling the parts together. c) Sample pellet.

The MOF (approximately 400 mg) was powdered and pelletized as a sandwich between two carbon wafers, using a custom-made pellet maker die (Figure 2.2), using a hydraulic pressure of 3 tons for 2 minutes. After the pellets were prepared, they were checked for any cracks or breakage. The thickness of the pellets was then measured carefully using a screw gauze. To determine the thickness of each pellet, three readings from screw gauze were averaged in order to minimize the manual error. The use of pellet maker die ensures that all the pellets have identical diameter. Depending upon the difference in the mass of the MOF in the sample the thickness of the pellet can vary. As the same pellet-maker die and same electrodes were used for all the samples, thus equal surface area of contact between the sample and the electrodes should be achieved. The impedance measurements of these sample pellets were conducted using a stainless-steel 2-electrode setup (Figure 2.3). The pellet was placed between the two electrodes such that, the carbon wafers of the pellet were in contact with each of the stainless-steel plates of the two electrodes.

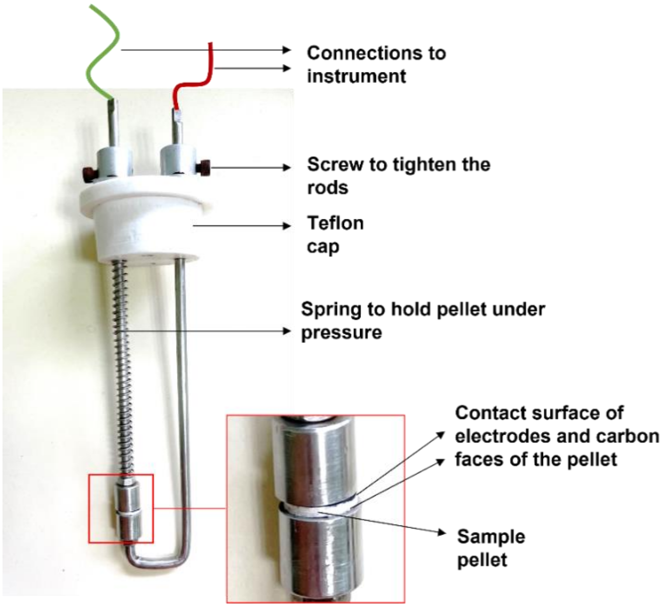

Figure 2.3 2-electrode setup used for impedance measurements.

This electrode setup was then placed in a double-walled incubating chamber maintaining the required humidity and temperature. The inner chamber of the incubator maintains the required temperature by circulating hot air. And the humidity is maintained by a separate flow of water vapour inside this chamber. The circulation of hot air throughout the chamber ensures that the entire electrode setup is uniformly heated during the experiments. Two independent temperature and humidity sensor is placed near the electrode setup to determine if the required conditions are maintained. Due to the presence of a double wall, a temperature gradient is created which helps the excess humidity to condense on the outer wall from where it exits through an outlet.

The impedance spectra were recorded at the open circuit potential for each sample, using a sinusoidal signal of amplitude 5 mV. The frequency was swept from 1 Hz to 10^6 Hz. Before any measurement at a given temperature and relative humidity (R.H.), the sample pellet was kept for four hours to equilibrate.

2.2.3.2. Electrochemical measurements for catalytic HER

The electrochemical measurements for investigating hydrogen evolution reaction (HER) were conducted using a Zahner Zanium electrochemical workstation operated with Thales software. A gas-tight cell with a three-electrode setup was employed. Ag/AgCl electrode was used as the reference electrode, Pt disc as the working electrode, and Pt wire as the counter electrode. All the experiments were done in 0.1 M aqueous solution of KCl at neutral pH under N_2 atmosphere. For coating the MOFs on the Pt disc, a separate coating ink was prepared by mixing 4 mg of the MOFs with 1 mL of 3:2 ethanol/water mixture and 10 µL of 5 wt% Nafion (aq.) as the binder. The mixture was sonicated well to get a homogeneous dispersion. 10 µL of this homogeneous ink was then drop-casted on Pt disc electrode and dried at 60 ^{o}C to obtain **Pt-MOF-808** working electrode. The electrolyte was purged with N_2 for at least 30 minutes before each experiment. Electrochemical responses were recorded at -0.1 V/s scan rate, unless specified otherwise.

2.3. RESULTS AND DISCUSSIONS

2.3.1. Powder X-ray diffraction (PXRD) analysis

The powder X-ray diffraction (PXRD) patterns of all the variants, that is, **MOF-808 A−D** (Figure 2.4) and **MOF-808 S** (Figure A2.1, Appendix 2), matched well with the simulated pattern of MOF-808. It implies that the attempted structural modulation by incorporation of defects does not alter the basic crystal structure of MOF-808 in the case of the sister compounds. However, for **MOF-808 D**, the peaks show a slight broadening. Additionally, a small broad peak at $2\theta = 5.6^{o}$ (marked with an arrow, Figure 2.4) is also observed. It indicates the probable presence of additional missing cluster defects in **MOF-808 D**.[32]

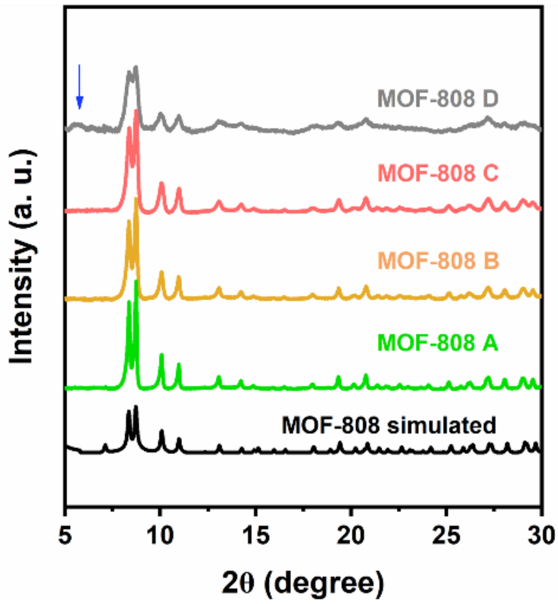

Figure 2.4. Powder X-ray diffraction (PXRD) patterns of simulated MOF-808 and **MOF-808 A – D**.

2.3.2. Determination of defect composition

2.3.2.1. Thermogravimetric analysis (TGA)

A comparison of the ATR-FTIR spectra (Figure A2.2, Appendix 2) of all the MOFs shows similar features and peak positions as reported earlier for MOF-808.[55] The synthetic conditions adapted for **MOF-808 A – D** was expected to result in different defect density in them, or in other words, different structural composition. As inferred from thermogravimetric analysis (TGA), a lower modulator concentration led to a higher density of defects up to an optimum level, which was **MOF-808 C** in this case (Figure 2.5a). The formula for SBU of an ideal MOF-808 is $Zr_6O_4(OH)_4[(C_6H_3)(COO)_3]_2(HCOO)_6$, where for each Zr_6 cluster, there are two BTC linkers, that is, 2 × 3 = 6 out of the 12 coordination sites of each Zr_6 cluster are occupied by BTC linkers. Following previous reports on defect calculations for UiO-66, the average number of linkers per formula unit of MOF-808 was estimated from the TGA analysis. [32] For **MOF-808 A**, **MOF-808 B**, **MOF-808 C** and **MOF-808 D**, the number of BTC linkers as estimated from TGA were 1.94, 1.71, 1.52 and 1.74, respectively per SBU (for details, see appendix 2, section A2.3). The highly crystalline **MOF-808 S** (Figure A2.3, Appendix 2) has also been found to have some inherent crystal defects (1.87 linkers per SBU), similar to earlier reports.[54]

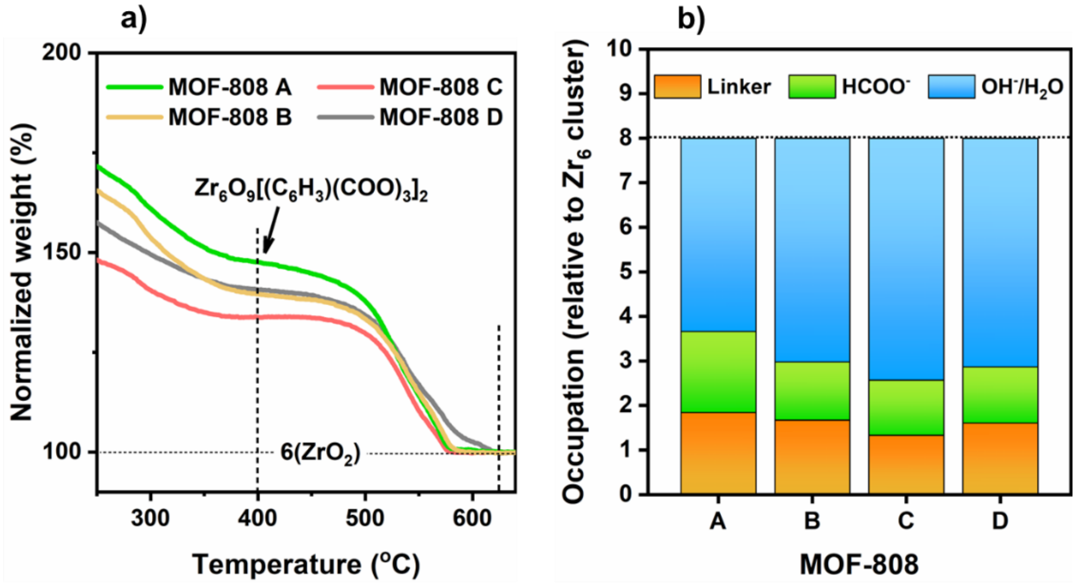

Figure 2.5. a) Thermogravimetric analysis (TGA) of **MOF-808 A – D**; Weight loss is normalized with respect to the residual weight of 6 ZrO_2 after 630 °C; b) Comparison of the MOF composition per SBU, as determined from ^{1}H-NMR and ICP-OES.

2.3.2.2. ^{1}H-NMR and ICP-OES analysis

Furthermore, a combination of ^{1}H-NMR spectroscopy and ICP-OES was used to accurately quantify the defect-density in **MOF-808 A – D**.[62,63] From ^{1}H NMR data, the amount of H_3BTC and formic acid in the structure could be estimated, while from ICP-OES, the amount of Zr in the MOFs could be determined (detailed analysis, calculation and spectra are provided in appendix 2, section A2.4). The number of BTC linkers for **MOF-808 A**, **MOF-808 B**, **MOF-808 C** and **MOF-808 D** as estimated from ^{1}H-NMR were 1.84, 1.67, 1,33 and 1.60, respectively, which matches well with that obtained from TGA (Table A2.1 and Table A2.3, Appendix 2). Figure 2.5b shows a comparison of the MOFs' composition per SBU, as determined from ^{1}H-NMR and ICP-OES.

2.3.3. N_2 sorption analysis

The N_2 sorption isotherms of **MOF-808 A** (Figure 2.6a) and **MOF-808 S** (Figure A2.11, Appendix 2) are type I isotherm (characteristic of microporous sample), with the Brunauer–Emmett–Teller (BET) surface areas of 1351.9 m^2g^{-1} and 1408.6 m^2g^{-1}, respectively. Of note, both **MOF-808 A** and **MOF-808 S** are low in defect density and thus structurally more similar to ideal MOF-808 having microporosity.[40] Isotherms for **MOF-808 B**, **MOF-808 C** and **MOF-808 D** (Figure 2.6a) are similar to **MOF-808 A** in the low relative pressure region showing type I isotherm; but in high relative pressure region, the isotherms resemble type IV isotherm with increasing hysteresis.[37,55-57] The combination of type I and type IV patterns indicates the presence of both micropores and mesopores in **MOF-808 B - D**. The BET surface areas for **MOF-808 B** (1494.5 m^2g^{-1}) and **MOF-808 C** (1423.6 m^2g^{-1}) are higher than that of the low defect sample **MOF-808 A** (1351.9 m^2g^{-1}). Notably, **MOF-808 D** has the lowest surface area of 865.2 m^2g^{-1} among all four sister MOFs. Further insight about the framework structure can be obtained from pore size distribution derived by NLDFT method (Figure 2.6b). The micropores have an average diameter of ~18 Å corresponding to the adamantane cages of the MOF, while the mesopores originating because of missing linker defects have diameters ranging from 23 Å – 44 Å. The relative amount of mesopores increases systematically (**MOF-808 B** < **MOF-808 C** < **MOF-808 D**), with increasing defect density or in other words decreasing modulator concentration in precursor solution. In case of **MOF-808 D**, due to a substantial increase in the amount of mesopores, the porous network reaches a complex situation - a limiting condition of increased defect density. The presence of the high concentration of defects in **MOF-808 D** might have caused the appearance of a new peak at 28 Å in the pore size distribution curve (Figure 2.6b), the broadening of the peaks in the PXRD pattern (Figure 2.4), along with a low BET surface area (Figure 2.6a). Similar observations were earlier reported for UiO-66, a well-known MOF with Zr_6-oxo nodes.[63] The increased defect density in **MOF-808 D** partially disrupts the framework integrity, which results in lowering of its crystallinity as compared to the other MOFs in the series.

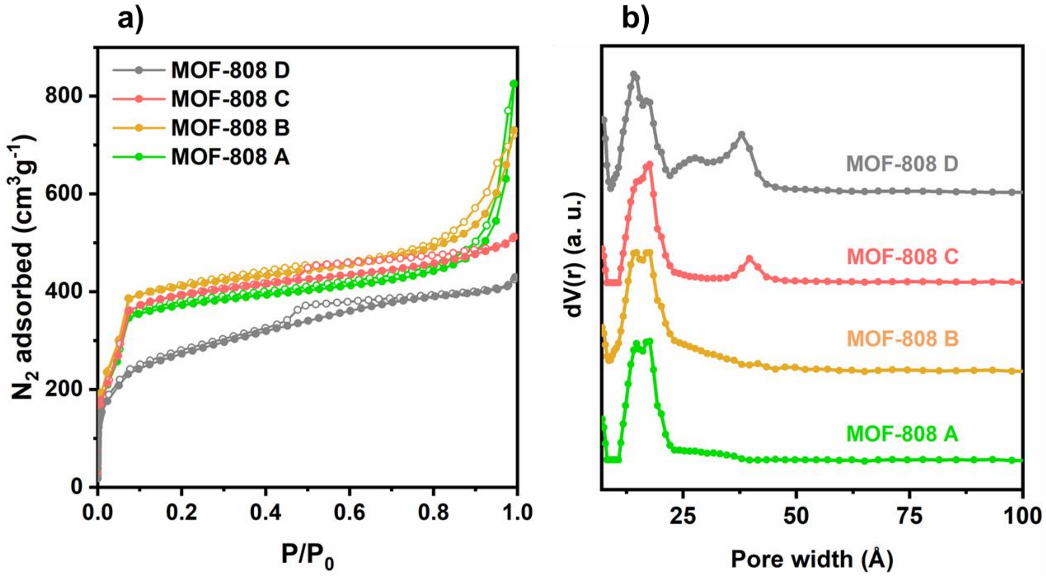

Figure 2.6. a) N_2 sorption isotherms and b) pore size distribution of **MOF-808 A – D**. Filled spheres denote adsorption and hollow spheres denote desorption experimental data points.

2.3.4. X-Ray photoelectron spectral analysis

To understand the changes brought upon **MOF-808 A – D** at a molecular level by defect engineering, X-ray photoelectron spectroscopy was used. The O1s X-ray photoelectron spectra (XPS) of the sister MOFs show signatures of three types of oxygen centered around 530.7 eV, 532 eV and 533.5 eV (Figure 2.7a). The peak centered around 530.7 eV corresponds to the bridging oxygen atoms of Zr_6 cluster (Zr–O–Zr).[63,64] The peak at 532 eV corresponds to the carboxylate linkers including benzenetricarboxylate (R–(C=O)–O–Zr) and formate anions (H–(C=O)–O–Zr) bound to the metal node. A comparison of the relative amounts of oxygen at 532 eV in **MOF-808 A** – **D** series (Figure 2.7b) reveals that the relative number of linkers attached to the Zr_6 node in the MOFs follows a decreasing trend (**A** > **B** > **C** > **D**) with lowering in the concentration of modulator in the precursor solution. The other peak at 533.5 eV originates from the Zr–O–H groups of hydroxide/water moieties coordinated to the Zr_6 node. With variation in the missing linker defect density, the number of open metal sites on the metal node also varies, and so changes the relative abundance of hydroxides/water moieties attached to the metal node. Interestingly, the decreasing trend in the number of coordinated linkers (**A** > **B** > **C** > **D**) is accompanied by a steady increase in the relative amount of Zr_6 node bound OH^-/H_2O (Figure 2.7b) in the MOFs (**A** < **B** < **C** < **D**). Thus, an analysis of the relative abundance of

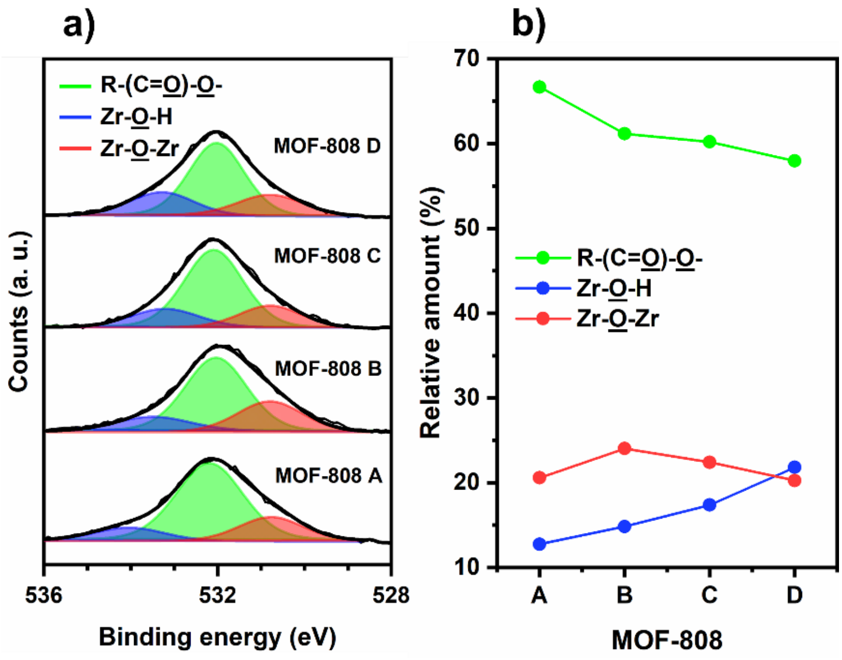

Figure 2.7. a) O1s X-ray photoelectron spectra (XPS) of **MOF-808 A – D**. b) Comparison of relative amount of oxygen in Zr–O–H, R–(C=O)–O–Zr, and Zr–O–Zr for **MOF-808 A – D.**

different types of oxygen species from the O1s XP spectra of the sister MOFs further verifies the increase in the defect density in the order of (**A** < **B** < **C** < **D**).

2.3.5. Water sorption analysis

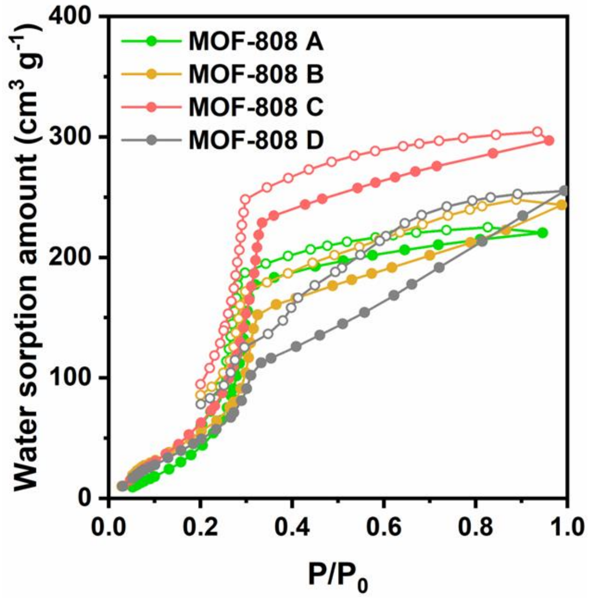

Figure 2.8. Water sorption isotherms.

Now, MOF-808 is well known for its high water sorptivity at moderate to high humidity,[39] and the introduction of missing linker defects in the sister MOFs can influence their water sorptivity, which is one of the notable properties for developing efficient proton conductors performing water assisted proton transport. Other than the available pore volume and surface area, water sorptivity depends largely on presence of hydrophilic functional groups and density of open metal sites.[39] As observed from the water sorption isotherms (Figure 2.8), **MOF-808 C** possesses the highest water sorptivity among its sister MOFs. The water sorption amount (at $p/p_0 = 1$) increases from **MOF-808 A** (220 $cm^3 g^{-1}$) to **MOF-808 B** (243 $cm^3 g^{-1}$) and further to **MOF-808 C** (296 $cm^3 g^{-1}$) and then decreases for **MOF-808 D** (252 $cm^3 g^{-1}$). The lowering of water sorptivity in case of **MOF-808 D** can be a direct consequence of the partial loss in crystallinity because of excessive defect incorporation. Of note, the trend observed with respect to the total amount of water sorbed for **MOF-808 A – D**, matches well with the respective average number of OH^-/H_2O groups coordinated to the open metal sites of Zr_6 metal nodes, as derived from ICP-OES and 1H-NMR analysis (Figure 2.5b). The $-OH/-H_2O$ groups bound to the Lewis acidic Zr_6 nodes are acidic in nature and can help in building extensive H-bonded networks with the sorbed water molecules, hence improving the water sorptivity.[53,54] Thus, an optimum situation could be hypothesized in case of **MOF-808 C**, where the water sorptivity of the MOF is the highest due to the presence of acidic -OH/H_2O groups in abundance because of its high missing linker defect density, while still maintaining the structural integrity of the framework. Furthermore, the water uptake capacity of the sister MOFs in different relative humidity, were compared by dynamic vapour sorption (DVS) measurements (Figure A2.13, Appendix 2). A similar trend of water uptake capacity was observed from the DVS measurements for **MOF-808 A – C**, where **MOF-808 C** was found to have the highest water uptake under medium to high relative humidity.

2.3.6. Acid-base titration

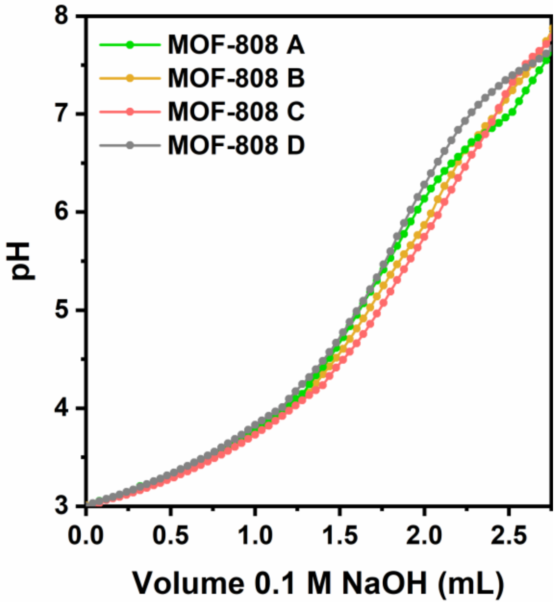

Figure 2.9. Acid-base titration curves for **MOF-808 A – D**.

To obtain further insight on any probable differences in the acidity of the defect engineered MOFs, or in other words, to understand the overall effect of varying amounts of acidic -OH/H_2O in **MOF-808 A – D**, acid-base titrations were performed following the work by Klet *et al.*[65] The detailed methodology is provided in appendix 2 (section A2.8). As determined from the acid-base titration curves (Figure 2.9), **MOF-808 C** was found to have the highest acidity, followed by **MOF-808 B** and **MOF-808 A**. Such increase in the acidity of **MOF-808 C** was expected when compared to its sister MOFs since **MOF-808 C** possesses the highest amount of missing linker defect. High defect density for **MOF-808 C** results in large amount of OH^-/H_2O being coordinated to the Lewis acidic Zr_6-oxo metal nodes, which in turn become highly acidic. Thus, we observed a notable dependence of water sorptivity and inherent acidity of **MOF-808 A – D** on the amount of missing linker defects the MOFs possess. Furthermore, the importance of maintaining a proper balance between the density of missing linker defects and structural integrity of the framework was also established. Of note, water sorptivity and inherent acidity are two important factors that play a crucial role in controlling the efficiency of proton transport following Grotthous mechanism for MOF and similar materials.[53] Considering this, the proton conductivity of the sister MOFs i.e., **MOF-808 A-D** were thoroughly studied.

2.3.7. Proton conductivity studies

Proton conductivity values of all the samples were determined using electrochemical impedance spectroscopy employing a two-electrode setup (parallel plate mode). The detailed methodology is provided in section 2.2.3.1. In brief, the MOF microcrystals were powdered and pelletized between carbon wafers, and the impedance spectra were recorded at different temperatures in the range of 40 – 80 ºC under 98% relative humidity (R.H.). The proton conductivities of the MOFs have been determined from the high-frequency region of corresponding Nyquist plots of impedance measurements, which originate from the intrinsic resistance of the material.[38,66,67] The experimentally obtained Nyquist plots, equivalent circuit and conductivity calculations are provided in appendix 2 (section A2.9).

2.3.7.1. Temperature dependence of proton conductivity

At 80 ºC (98% R.H.), the proton conductivity increased from 8.0×10^{-2} Scm^{-1} in **MOF-808 A** to 1.47×10^{-1} Scm^{-1} in **MOF-808 B**, and further to 2.6×10^{-1} Scm^{-1} in **MOF-808 C**, and then decreased for **MOF-808 D** (1.12×10^{-2} Scm^{-1}). It is noteworthy that all these MOFs (**MOF-808 A – D**) show superior proton conductivity than that shown by **MOF-808 S**, at all temperatures; the best being **MOF-808 C** which has ~50 times enhanced conductivity at 80 ºC and 98% R.H (Figure A2.21, Appendix 2) compared to **MOF-808 S**. To the best of our knowledge, this is also the highest reported proton conductivity for a pure MOF based material, operational at mild conditions. Table 2.13 (Appendix 2) compares **MOF-808 A – D** with some of the important results obtained for pure MOF based proton conductors in recent years. A comparison of the observed proton conductivity of the MOFs (Figure A2.21, Appendix 2) shows that the conductivity increases with increasing density of missing linker defects in the sister MOFs. This trend can be easily identified from figure 2.10 which shows that the optimum defect density could be achieved at **MOF-808 C** - the best proton conducting material among the sister MOFs, where a balance between structural integrity and other chemical properties is maintained. The incorporation of missing linker defects in the **MOF-808 A – D** thus has proved to be impactful in modifying the MOFs' properties in a way which enhances their proton conductivity; this has helped us in designing **MOF-808 C** with the highest reported proton conductivity for a pure MOF based material.

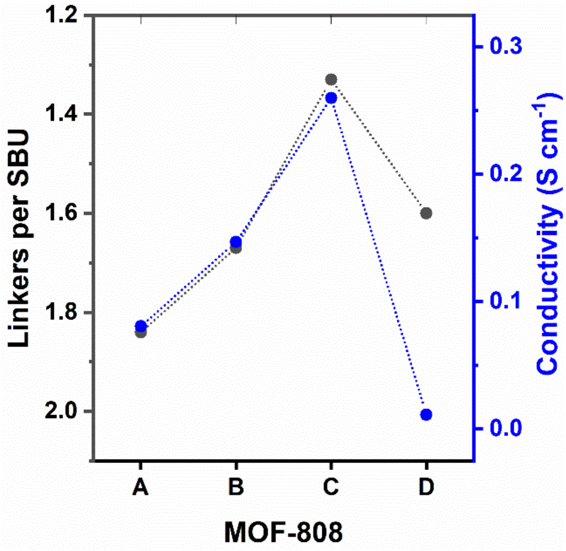

Figure 2.10. a) Water sorption isotherms and b) acid-base titration curves for **MOF-808 A – D**. c) Comparison of the correlation between observed proton conductivity for **MOF-808 A – D** (80 ºC, 98% R.H.) and the corresponding average number of BTC linkers per SBU.

Activation energies (E_a) for proton conduction in **MOF-808 A – D** were calculated by linear fitting of the corresponding Arrhenius plots constructed from the temperature dependence of proton conductivity values (Figure A2.21a, Appendix 2); detailed calculation is provided in appendix 2 (section A2.9). The Arrhenius plots for **MOF-808 A – D** (Figure 2.11) maintained a good linearity in the temperature range of 30 – 70 ºC (coefficient of determination $R^2 = 0.97 – 0.99$). The activation energies for all the MOFs were <0.4 eV/atom, which suggest Grotthuss mechanism being prevalent. However, at higher temperatures (above 70 ºC) the plot of ln(σT) versus 1000/T (Figure A2.21, Appendix 2) was found to deviate from linearity. This deviation could probably be a result of partial contribution in proton conductivity from vehicular mechanism performed by protonated water molecules, such as H_3O^+, $H_5O_2^+$ etc. The large number of acidic -OH/-

H_2O functional groups present on the Zr_6 metal nodes of the MOF, can protonate the water molecules present inside the hydrophilic channels to generate such ions. The vehicular mechanism acts in addition to the Grotthuss mechanism of proton hopping already functional in the MOF. Similar phenomenon has been reported earlier for several porous materials having high concentration of labile protons.[68-73]

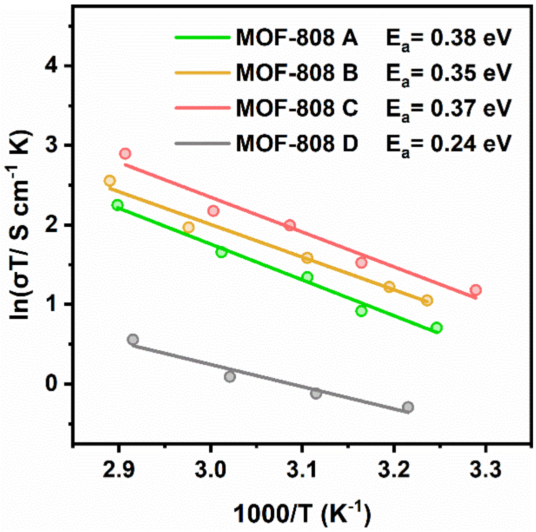

Figure 2.11. Arrhenius plots of proton conductivity for **MOF-808 A – D** at 98% relative humidity (R.H.), along with the corresponding activation energies (E_a).

2.3.7.2. Controlled experiments on MOF-808 C

The proton conductivity of **MOF-808 C** increased rapidly with increasing humidity (Figure A2.23, Appendix 2), which confirms its significant dependence on assistance from water. To better understand the role of adsorbed water molecules and the effect of acidic OH^-/H_2O (attached to the Zr_6 nodes), on the observed proton conduction, a set of controlled experiments were performed: (a) the open metal sites in **MOF-808 C** were capped using benzoic acid (**MOF-808 C-benz**) and (b) the acidic protons of the MOF were exchanged with Li^+ ions (**MOF-808 C-Li**), and thereafter their proton conductivity was studied. Detailed methodology of synthesis (section 2.2.2) and characterizations of these samples (**MOF-808 C-benz** and **MOF-808 C-Li**) are provided with the appendix 2 (section A2.10). As shown in Scheme 2.1, the coordination of benzoic acid should replace the coordinated OH^-/H_2O at the Zr_6 nodes, leading to lowering of the labile proton concentration in the framework. On the other hand, the lithiation should replace most of the labile protons in the framework and form -OLi. Due to the removal of labile protons from the MOF, the water uptake as well as its retention capacity for **MOF-808 C-benz** (Figure A2.26,

Appendix 2) and **MOF-808 C-Li** (Figure A2.30, Appendix 2) was found to be much lowered than their parent **MOF-808 C**.

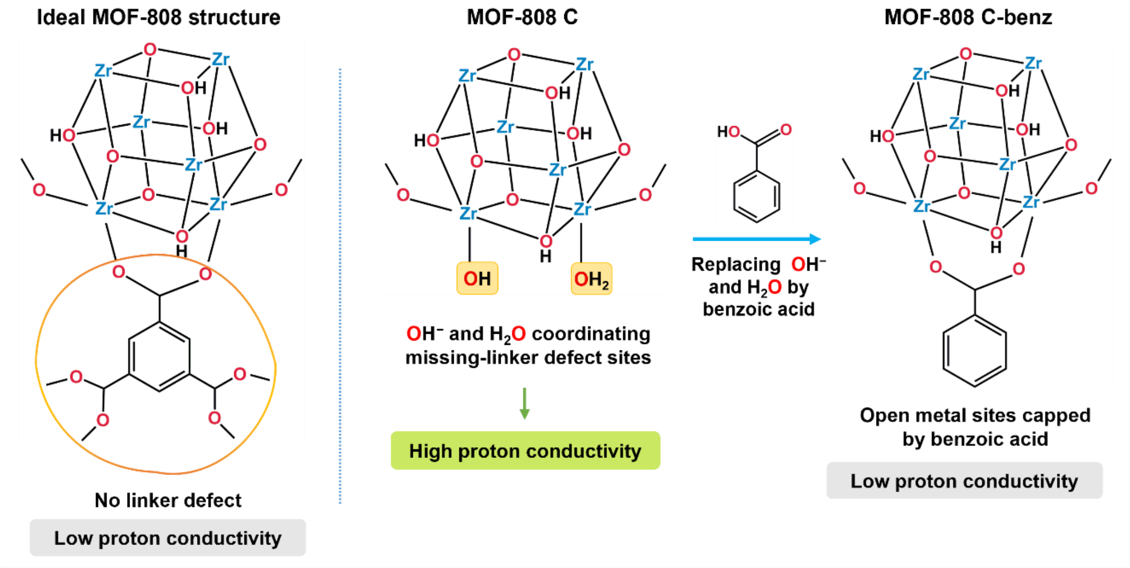

Scheme 2.1. Illustration of the capping of open metal sites in MOF-808 using benzoic acid.

As expected, the proton conductivity of the benzoic acid-modified **MOF-808 C** (i.e., **MOF-808 C-benz**) was found to be considerably lower than that of **MOF-808 C** (Figure A2.28, Appendix 2). In fact, the proton conductivity of the **MOF-808 C-benz** was lower than all the sister MOFs in the series **MOF-808 A – D**. Likewise, for H^+ ion-exchanged **MOF-808 C-Li**, the conductivity was found to be lower than all the MOFs (**MOF-808 A – D**), at all temperatures. This proves that the water assisted high proton conductivity observed in the **MOF-808 A – D** series, depends largely on the amount of acidic protons present in the framework and no evidence could be found signifying any notable contribution from any other factors. The Arrhenius plots for **MOF-808 C-benz** (E_a = 0.36 eV; Figure A2.28, Appendix 2) and **MOF-808 C-Li** (E_a = 0.34 eV; Figure A2.32, Appendix 2) maintained good linearity throughout the temperature range up to 80 °C (coefficient of determination R^2 = 0.98 – 0.99), unlike their parent MOF. This further explains the deviation from the linearity observed in the Arrhenius plots for **MOF-808 A – D** as a probable effect of high concentration of labile protons in them. This means that the significant increase in proton conductivity for **MOF-808 A – D** at high temperatures, is due to the coordinated OH^-/H_2O at the metal nodes. The additional vehicular mechanism operating in these sister MOFs rely on the extent of protonation of the water molecules inside the framework by the labile protons. Since the concentration of labile protons is considerably lowered for both **MOF-808 C-benz** and **MOF-808 C-Li**, the additional contribution in proton conductivity by the vehicular mechanism is diminished, and therefore there is no observable deviation from linearity in the Arrhenius plots.

2.3.7.3. Long term stability test under operational conditions

As for **MOF-808 C**, the pelletized sample retains its conductivity very well during the 84 hours of conductivity measurement at 80 ºC and 98% relative humidity (Figure A2.34, Appendix 2). There was also very negligible loss in conductivity during the 3 cycles of subsequent heating-cooling measurements (Figure A2.37, Appendix 2). To check the stability of **MOF-808 C** during the process of impedance measurement, several physical characterizations e.g., PXRD, FT-IR and FESEM imaging were performed before and after the 84 hours of conductivity measurement. The structural integrity of **MOF-808 A**, **MOF-808 B** and **MOF-808 C** was found to be well maintained during the process (Figure A2.39 – A2.44, Appendix 2). The MOF sample has been found to be stable for over 2 years even when stored in an open-air condition at room temperature (25 ºC) (Figure A2.47, Appendix 2). Altogether, the defect engineered **MOF-808 C** has come about as a robust super-protonic conductor.

The proton conductivity of a material usually depends on two parameters: (a) proton mobility and (b) concentration of labile protons. Modifying either of the parameters by structural modulation of a MOF can result in variation of its proton transport properties. In the case of **MOF-808 C**, we realize that introducing defects has helped in tuning both the parameters. The missing linker defects in **MOF-808 C** enhance the MOF's porosity, acidity and water sorptivity, thereby improving the proton mobility. These inferences concur with an earlier report on the study of defects on UiO-66 MOF by Kitagawa and co-workers.[38] Furthermore, the controlled experiments with **MOF-808 C-benz** and **MOF-808 C-Li** act as a test to this drawn inference. These observations highlight the importance of defect engineering in enhancing the proton conductivity of MOF 808. Table A2.12 in appendix 2 summarizes the major findings of this work together. In a nutshell, it can be said that increasing the missing linker defect density in **MOF 808 A – D** in a controlled manner resulted into (a) increasing the number of labile protons in the proton-transport channel, (b) increasing the surface area and water sorptivity of the MOF and (c) lowering of the crystallinity in extreme case of defect density (**MOF-808 D**). Optimization of the defect density in case of **MOF-808 C** thus led to the highest proton conductivity amongst **MOF 808 A – D**.

2.3.8. Assembly of proton conductors and HER electrocatalyst

Considering the super-proton conducting nature of these MOFs (**MOF-808 A – D**), we have attempted to study the prospect of combining them with a versatile electrocatalyst for hydrogen evolution reaction (HER). Since these MOFs have a controllable efficiency of proton management, an assembly of such MOFs can be expected to have a significant impact on the catalyst's activity towards electrocatalysis involving proton-coupled electron transfer (PCET). The selection of HER as a model reaction stemmed from the fact that HER is a relatively simple reaction involving PCET. Thus it can be expected that the effect of proton management would be manifested easily in the catalytic response.[74] In a recent work it was reported that non-catalytic UiO-66 could influence a catalyst's activity positively, by modifying the microenvironment around the catalyst, when coated as a membrane on it.[63] Here we have analyzed the performance of Pt towards electrocatalytic HER, by coating it with thin layers of proton-conducting **MOF-808 A – D** (detailed methodology provided in section 2.2.3); here the MOFs are non-catalytic towards HER. Efficient proton transport from the bulk to the active site is crucial for the efficient performance of a heterogeneous HER catalyst. Thus, a porous, thin film of a super-proton conducting MOF on a HER electrocatalyst can be expected to influence the catalysis in a positive direction. The MOF-

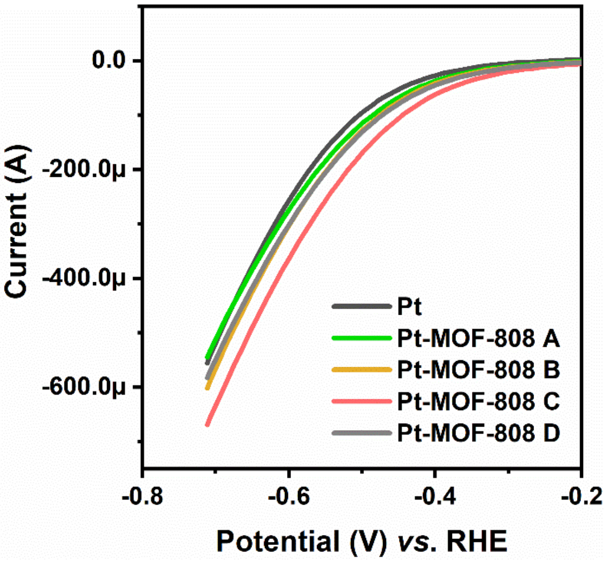

Figure 2.12. Linear sweep voltammograms (LSVs) of bare Pt disc electrode, **Pt-MOF-808 A**, **Pt-MOF-808 B**, **Pt-MOF-808 C** and **Pt-MOF-808 D**. The measurements were recorded in 0.1 M KCl solution at neutral pH and under N_2 atmosphere (scan rate 0.1 Vs^{-1}).

coated Pt disc electrode acted as the working electrode as well as electrocatalyst, while Ag/AgCl and Pt wire were used as the reference and counter electrodes, respectively. All the experiments were done in 0.1 M aqueous solution of KCl at neutral pH, under N_2 atmosphere. The catalytic current of HER for **MOF-808 A** coated Pt (**Pt-MOF-808 A**) is comparable to that of blank Pt (Figure 2.12), while those of **Pt-MOF-808 B** and **Pt-MOF-808 D** are slightly more. Interestingly, the catalytic current for **Pt-MOF-808 C** is markedly higher than Pt electrode itself along with a notable shift in the onset potential. This unique behavior can be reasoned by considering two factors: a) the MOFs helped in the proton management efficiently by virtue of their high proton conductivity. Here, a well-ordered proton transport channel through the MOF to the catalyst might have assisted the catalytic performance. b) The defect containing MOFs are more acidic in nature than the pristine MOF- 808. The performance of a HER catalyst often depends on the local pH of the catalyst; **MOF-808 C** is in fact having the highest acidity in the series. The porous MOF thin film could modify the microenvironment around the Pt disc electrode and create a lower local pH than the bulk solution. It might have played a crucial role in the better catalytic activity of **Pt-MOF-808 C** than the bare Pt. Though a detailed mechanistic study for HER is beyond the scope of this work, it can be unarguably said that proton management with the help of proton conducting MOFs has a lot of scope in electrocatalysis involving PCET.

2.4 CONCLUSIONS

The present work endeavors to design four sister MOFs with controlled concentration of missing linker defects. The presented synthetic procedure yielded defect induced MOF-808 (**MOF-808 A – D**) with superior porosity, water sorptivity and acidity. In this series, **MOF-808 A** was found to have the lowest defect concentration, which then increased through **MOF-808 A → MOF-808 D**. The properties of all these MOFs in the series have been compared together in this work to find a trend out of it. The incorporation of defects was found to have modified several features in these MOFs which has altogether led to super protonic conductivity. The MOF with the optimum defect concentration (**MOF-808 C**) shows a conductivity of 2.6×10^{-1} Scm^{-1}, which is the highest reported proton conductivity to date of a pure MOF based proton conductor without any extensive modification. Such enhancement in proton conductivity of the MOF is a cumulative effect of increased concentration of labile protons as well as an improved mobility of the labile protons; both of which are consequences of the strategic defect engineering. This work highlights the potential of structural tunability in MOFs to develop efficient proton conductors. Systematic design strategies involving defect engineering can broaden the scope further to develop new functional materials from MOFs. As an example, we have extended this work by assembling these title MOF-based proton conductors (**MOF-808 A – D**) with Pt disc electrode to demonstrate electrocatalytic HER. And a considerable increment in the catalytic current for **MOF-808 C** coated Pt electrode (**Pt- MOF-808 C**) was found, as compared to bare Pt electrode. This behaviour is quite unique considering the non-catalytic nature of MOF-808 towards electrocatalytic HER. It can be reasoned by considering the probable effects of a lowering in local pH, along with efficient proton management around the catalyst, by the proton conducting MOF, during electrocatalysis. This work further highlights the importance of the missing linker defects in MOF-808 which helped in modulating its both structural properties and functional behaviour.

Appendix 1: Instrumental details and sample preparation.

Appendix 2: Characterization of MOFs; quantification of defects; details of electrochemical impedance measurements and results obtained; controlled experiments on **MOF-808 C** and stability checks.

2.5 REFERENCES

1. Dhakshinamoorthy, A.; Li, Z.; Garcia, H. Catalysis and photocatalysis by metal organic frameworks. *Chem. Soc. Rev*. **2018**, *47*, 8134—8172.
2. Chughtai, A. H.; Ahmad, N.; Younus, H. A.; Laypkov, A.; Verpoort, F. Metal–organic frameworks: versatile heterogeneous catalysts for efficient catalytic organic transformations. *Chem. Soc. Rev*. **2015**, *44*, 6804−6849.
3. Mukhopadhyay, S.; Basu, O.; Nasani, R.; Das, S. K. Evolution of metal organic frameworks as electrocatalysts for water oxidation. *Chem. Commun.* **2020**, *56*, 11735−11748.
4. Qiu, T.; Liang, Z.; Guo, W.; Tabassum, H.; Gao, S.; Zou, R. Metal−Organic Framework-Based Materials for Energy Conversion and Storage. *ACS Energy Lett.* **2020**, *5*, 520–532.
5. Lustig, W. P.; Mukherjee, S.; Rudd, N. D.; Desai, A. V.; Li, J.; Ghosh, S. K. Metal–organic frameworks: functional luminescent and photonic materials for sensing applications. *Chem. Soc. Rev.* **2017**,*46*, 3242−3285.
6. Koo, W-T.; Jang, J-S.; Kim, I-D. Metal-Organic Frameworks for Chemiresistive Sensors. *Chem* **2019**, *5*, 1938−1963.
7. Zheng, Y.; Sun, F-Z.; Han, X.; Xu, J.; Bu, X-H. Recent Progress in 2D Metal-Organic Frameworks for Optical Applications. *Adv. Opt. Mater*. **2020**, *8*, 2000110.
8. Horike, S.; Ma, N.; Fan, Z.; Kosasang, S.; Smedskjaer, M. M. Mechanics, Ionics, and Optics of Metal–Organic Framework and Coordination Polymer Glasses. *Nano Lett*. **2021**, *21*, 6382–6390.
9. Lim, D-W.; Kitagawa, H. Proton Transport in Metal–Organic Frameworks. *Chem. Rev.* **2020**, *120*, 8416–8467.
10. Chand, S.; Elahi, S. M.; Pal, A.; Das, M. C. Metal–Organic Frameworks and Other Crystalline Materials for Ultrahigh Superprotonic Conductivities of 10^{-2} S cm^{-1} or Higher. *Chem. Eur. J.* **2019**, *25*, 6259–6269.

11. Nagarkar, S. S.; Unni, S. M.; Sharma, A.; Kurungot, S.; Ghosh, S. K. Two-in-One: Inherent Anhydrous and Water-Assisted High Proton Conduction in a 3D Metal–Organic Framework. *Angew. Chem. Int. Ed.* **2014**, *53*, 2638–2642.
12. Zhang, J.; Bai, H-J.; Ren, Q.; Luo, H-B.; Ren, X-M.; Tian, Z-F.; Lu, S. Extra Water- and Acid-Stable MOF-801 with High Proton Conductivity and Its Composite Membrane for Proton-Exchange Membrane. *ACS Appl. Mater. Interfaces* **2018**, *10*, 28656−28663.
13. Ye, Y.; Gong, L.; Xiang, S.; Zhang, Z.; Chen, B. Metal–Organic Frameworks as a Versatile Platform for Proton Conductors. *Adv. Mater*. **2020**, *32*, 1907090.
14. Li, B.; Wen, H-M.; Zhou, W.; Chen, B. Porous Metal–Organic Frameworks for Gas Storage and Separation: What, How, and Why? *J. Phys. Chem. Lett.* **2014**, *5*, 3468–3479.
15. Connolly, B. M.; Madden, D. G.; Wheatley, A. E. H.; Fairen-Jimenez, D. Shaping the Future of Fuel: Monolithic Metal–Organic Frameworks for High-Density Gas Storage. *J. Am. Chem. Soc*. **2020**, *142*, 8541–8549.
16. Dhainaut, J.; Bonneau, M.; Ueoka, R.; Kanamori, K.; Furukawa, S. Formulation of Metal-Organic Framework Inks for the 3D Printing of Robust Microporous Solids toward High-Pressure Gas Storage and Separation. *ACS Appl. Mater. Interfaces* **2020**, *12*, 10983−10992.
17. Yaghi, O. M.; O'Keeffe, M.; Ockwig, N. W.; Chae, H. K.; Eddaoudi, M.; Kim, J. Reticular synthesis and the design of new materials. *Nature* **2003**, *423*, 705–714.
18. Jiang, H.; Alezi, D.; Eddaoudi, M. A reticular chemistry guide for the design of periodic solids. *Nat. Rev. Mater.* **2021**, *6*, 466–487.
19. Islamoglu, T.; Goswami, S.; Li, Z.; Howarth, A. J.; Farha, O. K.; Hupp, J. T. Postsynthetic Tuning of Metal−Organic Frameworks for Targeted Applications. *Acc. Chem. Res.* **2017**, *50*, 805−813.
20. Eddaoudi, M.; Sava, D. F.; Eubank, J. F; Adil, K.; Guillerm, V. Zeolite-like metal–organic frameworks (ZMOFs): design, synthesis, and properties. *Chem. Soc. Rev.* **2015**, *44*, 228−249.
21. Kirchon, A.; Feng, L.; Drake, H. F.; Joseph, E. F.; Zhou, H-C. From fundamentals to applications: a toolbox for robust and multifunctional MOF materials. *Chem. Soc. Rev.* **2018**, *47*, 8611–8638.
22. Cirujano, F. G.; Martin, N.; Wee, L. H. Design of Hierarchical Architectures in Metal–Oganic Frameworks for Catalysis and Adsorption. *Chem. Mater.* **2020**, *32*, 10268–10295.
23. Xiang, W.; Zhang, Y.; Chen, Y.; Liu, C-j.; Tu, X. Synthesis, characterization and application of defective metal–organic frameworks: current status and perspectives. *J. Mater. Chem. A* **2020**, *8*, 21526–21546.
24. Sholl, D. S.; Lively, R. P. Defects in Metal–Organic Frameworks: Challenge or Opportunity? *J. Phys. Chem. Lett.* **2015**, *6*, 3437−3444.
25. Zhang, N.; Gao C.; Xiong, Y. Defect engineering: A versatile tool for tuning the activation of key molecules in photocatalytic reactions. *J. Energy Chem.* **2019**, *37*, 43−57.
26. Jangizehi, A.; Schmid, F.; Besenius, P.; Kremer K.; Seiffert, S. Defects and defect engineering in Soft Matter. *Soft Matter* **2020**, *16*, 10809−10859.
27. Cliffe, M. J.; Wan, W.; Zou, X.; Chater, P. A.; Kleppe, A. K.; Tucker, M. G.; Wilhelm, H.; Funnell, N. P.; Coudert, F-X.; Goodwin, A. L. Correlated defect nanoregions in a metal–organic framework. *Nat. Commun*. **2014**, *5*, 4176.
28. Atzori, C.; Shearer, G. C.; Maschio, L.; Civalleri, B.; Bonino, F.; Lamberti, C.; Svelle, S.; Lillerud, K. P.; Bordiga, S. Effect of Benzoic Acid as a Modulator in the Structure of UiO-66: An Experimental and Computational Study. *J. Phys. Chem. C* **2017**, *121*, 9312–9324.
29. Vos, A. D.; Hendrickx, K.; Voort, P. V. D.; Speybroeck, V. V.; Lejaeghere, K. Missing Linkers: An Alternative Pathway to UiO-66 Electronic Structure Engineering. *Chem. Mater*. **2017**, *29*, 3006–3019.
30. Feng, Y.; Chen, Q.; Jiang, M.; Yao, J. Tailoring the Properties of UiO-66 through Defect Engineering: A Review. *Ind. Eng. Chem. Res.* **2019**, *58*, 17646−17659.
31. Wu, H.; Chua, Y. S.; Krungleviciute, V.; Tyagi, M.; Chen, P.; Yildirim, T.; Zhou, W. Unusual and Highly Tunable Missing-Linker Defects in Zirconium Metal−Organic Framework UiO-66 and Their Important Effects on Gas Adsorption. *J. Am. Chem. Soc.* **2013**, *135*, 10525−10532.
32. Shearer, G. C.; Chavan, S.; Bordiga, S.; Svelle, S.; Olsbye, U.; Lillerud, K. P. Defect Engineering: Tuning the Porosity and Composition of the Metal−Organic Framework UiO-66 via Modulated Synthesis. *Chem. Mater*. **2016**, *28*, 3749−3761.
33. Dissegna, S.; Epp, K.; Heinz, W. R.; Kieslich, G.; Fischer, R. A. Defective Metal-Organic Frameworks. *Adv. Mater*. **2018**, *30*, 1704501.
34. Bueken, B.; Velthoven, N. V.; Krajnc, A.; Smolders, S.; Taulelle, F.; Mellot-Draznieks, C.; Mali, G.; Bennett, T. D.; Vos, D. D. Tackling the Defect Conundrum in UiO-66: A Mixed-Linker Approach to Engineering Missing Linker Defects. *Chem. Mater*. **2017**, *29*, 10478–10486.

35. DeStefano, M. R.; Islamoglu, T.; Garibay, S. J.; Hupp, J. T.; Farha, O. K. Room-Temperature Synthesis of UiO-66 and Thermal Modulation of Densities of Defect Sites. *Chem. Mater.* **2017**, *29*, 1357–1361.
36. Feng, X.; Hajek, J.; Jena, H. S.; Wang, G.; Veerapandian, S. K. P.; Morent, R.; Geyter, N. D.; Leyssens, K.; Hoffman, A. E. J.; Meynen, V.; Marquez, C.; Vos, D. E. D.; Speybroeck, V. V.; Leus, K.; Voort, P. V. D. Engineering a Highly Defective Stable UiO-66 with Tunable Lewis- Brønsted Acidity: The Role of the Hemilabile Linker. *J. Am. Chem. Soc*. **2020**, *142*, 3174–3183.
37. Cai, G.; Jiang, H-L. A Modulator-Induced Defect-Formation Strategy to Hierarchically Porous Metal–Organic Frameworks with High Stability. *Angew. Chem. Int. Ed*. **2017**, *56*, 563 –567.
38. Taylor, J. M.; Dekura, S.; Ikeda, R.; Kitagawa, H. Defect Control to Enhance Proton Conductivity in a Metal−Organic Framework. *Chem. Mater.* **2015**, *27*, 2286−2289.
39. Furukawa, H.; Gándara, F.; Zhang, Y-B.; Jiang, J.; Queen, W. L.; Hudson, M. R.; Yaghi, O. M. Water Adsorption in Porous Metal−Organic Frameworks and Related Materials. *J. Am. Chem. Soc.* **2014**, *136*, 4369−4381.
40. Jiang, J.; Gándara, F.; Zhang, Y-B.; Na, K.; Yaghi, O. M.; Klemperer, W. G. Superacidity in Sulfated Metal−Organic Framework-808. *J. Am. Chem. Soc.* **2014**, *136*, 12844−12847.
41. Aunan, E.; Affolter, C. W.; Olsbye, U.; Lillerud, K. P. Modulation of the Thermochemical Stability and Adsorptive Properties of MOF-808 by the Selection of Non-structural Ligands. *Chem. Mater*. **2021**, *33*, 1471−1476.
42. Moon, S-Y.; Liu, Y.; Hupp, J. T.; Farha. O. K. Instantaneous Hydrolysis of Nerve-Agent Simulants with a Six-Connected Zirconium-Based Metal–Organic Framework. *Angew. Chem. Int. Ed*. **2015**, *54*, 6795 –6799.
43. Rojas-Buzo, S.; García-García. P.; Corma, A. Zr-MOF-808@MCM-41 catalyzed phosgene-free synthesis of polyurethane precursors. *Catal. Sci. Technol.* **2019**, *9*, 146–156.
44. Prasad, R. R. R.; Dawson, D. M.; Cox, P. A.; Ashbrook, S. E.; Wright, P. A.; Clarke, M. L. A Bifunctional MOF Catalyst Containing Metal–Phosphine and Lewis Acidic Active Sites. *Chem. Eur. J.* **2018**, *24*, 15309 – 15318.
45. Zheng, H-Q.; Liu, C-Y.; Zeng, X-Y.; Chen, J.; Lü, J.; Lin, R-G.; Cao, R.; Lin, Z-J.; Su, J-W. MOF-808: A Metal−Organic Framework with Intrinsic Peroxidase-Like Catalytic Activity at Neutral pH for Colorimetric Biosensing. *Inorg. Chem.* **2018**, *57*, 9096−9104.
46. Fu, G.; Bueken, B.; Vos, D. D. Zr-Metal-Organic Framework Catalysts for Oxidative Desulfurization and Their Improvement by Postsynthetic Ligand Exchange. *Small Methods* **2018**, *2*, 1800203.
47. Ly, H. G. T.; Fu, G.; Kondinski, A.; Bueken, B.; Vos, D. D.; Parac-Vogt, T. N. Superactivity of MOF-808 toward Peptide Bond Hydrolysis. *J. Am. Chem. Soc.* **2018**, *140*, 6325−6335.
48. Luo, H-B.; Wang, M.; Liu, S-X.; Xue, C.; Tian, Z-F.; Zou, Y.; Ren X-M. Proton Conductance of a Superior Water-Stable Metal−Organic Framework and Its Composite Membrane with Poly(vinylidene fluoride). *Inorg. Chem.* **2017**, *56*, 4169−4175.
49. Luo, H-B.; Ren, Q.; Wang, P.; Zhang, J.; Wang, L.; Ren X-M. High Proton Conductivity Achieved by Encapsulation of Imidazole Molecules into Proton-Conducting MOF-808. *ACS Appl. Mater. Interfaces* **2019**, *11*, 9164−9171.
50. Meng, X.; Wang, H-N.; Wang, L-S.; Zou, Y-H.; Zhou, Z-Y. Enhanced proton conductivity of a MOF-808 framework through anchoring organic acids to the zirconium clusters by post-synthetic modification. *CrystEngComm*, **2019**, *21*, 3146−3150.
51. Li, X-M.; Wang, Y.; Wu, B.; Zeng, L. Efficient Proton Transport in Stable Functionalized Channels of Zirconium Metal–Organic Frameworks. *ACS Appl. Energy Mater*. **2021**, *4*, 8303–8310.
52. Xin, L.; Zhang, D.; Qu, K.; Lu, Y.; Wang, Y.; Huang, K.; Wang, Z.; Jin, W.; Xu, Z. Zr-MOF-Enabled Controllable Ion Sieving and Proton Conductivity in Flow Battery Membrane. *Adv. Funct. Mater.* **2021**, *31*, 2104629.
53. Sharma, A.; Lim, J.; Jeong, S.; Won, S.; Seong, J.; Lee, S.; Kim, Y. S.; Baek, S. B.; Lah, M. S. Superprotonic Conductivity of MOF-808 Achieved by Controlling the Binding Mode of Grafted Sulfamate. *Angew. Chem. Int. Ed*. **2021**, *60*, 14334 –14338.
54. Hardian, R.; Dissegna, S.; Ullrich, A.; Llewellyn, P. L.; Coulet, M-V.; Fischer, R. A. Tuning the Properties of MOF-808 via Defect Engineering and Metal Nanoparticle Encapsulation. *Chem. Eur. J.* **2021**, *27*, 6804 –6814.
55. Ardila-Suárez, C.; Díaz-Lasprilla, A. M.; Díaz-Vaca, L. A.; Balbuena, P. B.; Baldovino-Medrano, V. G.; Ramírez-Caballero, G. E. Synthesis, characterization, and post-synthetic modification of a micro/mesoporous zirconium– tricarboxylate metal–organic framework: towards the addition of acid active sites. *CrystEngComm* **2019**, *21*, 3014–3030.

56. Ardila-Suárez, C.; V. D. R. M.; Alem, H.; Baldovino-Medrano. V. G.; Ramírez-Caballero, G. E. Synthesis of ordered microporous/microporous MOF-808 through modulator-induced defect formation, and surfactant self-assembly strategies. *Phys. Chem. Chem. Phys.* **2020**, *22*, 12591–12604.
57. Diring, S.; Furukawa, S.; Takashima, Y.; Tsuruoka T.; Kitagawa, S. Controlled Multiscale Synthesis of Porous Coordination Polymer in Nano/Micro Regimes. *Chem. Mater*. **2010**, *22*, 4531–4538.
58. Bonnett, B. L.; Ilic, S.; Flint, K.; Cai, M.; Yang, X.; Cornell, H. D.; Taylor, A.; Morris, A. J. Mechanistic Investigations into and Control of Anisotropic Metal−Organic Framework Growth. *Inorg. Chem*. **2021**, *60*, 10439−10450.
59. Zhao, Y.; Zhang, Q.; Li, Y.; Zhang, R.; Lu, G. Large-Scale Synthesis of Monodisperse UiO-66 Crystals with Tunable Sizes and Missing Linker Defects via Acid/Base Co-Modulation. *ACS Appl. Mater. Interfaces* **2017**, *9*, 15079–15085.
60. Hu, S.; Liu, M.; Guo, X.; Li, K.; Han, Y.; Song, C.; Zhang, G. Effects of Monocarboxylic Acid Additives on Synthesizing Metal–Organic Framework NH_2-MIL-125 with Controllable Size and Morphology. *Cryst. Growth Des.* **2017**, *17*, 6586–6595.
61. Bara, D.; Wilson, C.; Mörtel, M.; Khusniyarov, M. M.; Ling, S.; Slater, B.; Sproules, S.; Forgan, R. S. Kinetic Control of Interpenetration in Fe−Biphenyl-4,4′-dicarboxylate Metal−Organic Frameworks by Coordination and Oxidation Modulation. *J. Am. Chem. Soc*. **2019**, *141*, 8346−8357.
62. Jia, C.; Cirujano, F. G.; Bueken, B.; Claes, B.; Jonckheere, D.; Van Geem, K. M.; Vos, D. D. Geminal Coordinatively Unsaturated Sites on MOF-808 for the Selective Uptake of Phenolics from a Real Bio-Oil Mixture. ChemSusChem **2019**, *12*, 1256–1266.
63. Mukhopadhyay, S.; Shimoni, R.; Liberman, I.; Ifraemov, R.; Rozenberg, I.; Hod, I. Assembly of a Metal–Organic Framework (MOF) Membrane on a Solid Electrocatalyst: Introducing Molecular-Level Control Over Heterogeneous CO_2 Reduction. *Angew. Chem. Int. Ed*. **2021**, *60*, 13423–13429.
64. Wang, Y.; Li, L.; Dai, P.; Yan, L.; Cao, L.; Gu, X.; Zhao, X. Missing-node directed synthesis of hierarchical pores on a zirconium metal–organic framework with tunable porosity and enhanced surface acidity via a microdroplet flow reaction. *J. Mater. Chem. A* **2017**, *5*, 22372–22379.
65. Klet, R. C.; Liu, Y.; Wang, T. C.; Hupp, J. T.; Farha, O. K. Evaluation of Brønsted acidity and proton topology in Zr- and Hf-based metal–organic frameworks using potentiometric acid–base titration. *J. Mater. Chem. A* **2016**, *4*, 1479–1485.
66. Mukhopadhyay, S.; Debgupta, J.; Singh, C.; Sarkar, R.; Basu, O.; Das, S. K. Designing UiO-66-Based Superprotonic Conductor with the Highest Metal−Organic Framework Based Proton Conductivity. *ACS Appl. Mater. Interfaces* **2019**, *11*, 13423−13432.
67. Yang, F.; Xu, G.; Dou, Y.; Wang, B.; Zhang, H.; Wu, H.; Zhou, W.; Li, J-R. Chen, B. A flexible metal–organic framework with a high density of sulfonic acid sites for proton conduction. *Nature Energy* **2017**, *2*, 877–883.
68. Sadakiyo, M.; Yamada, T.; Kitagawa, H. Rational Designs for Highly Proton-Conductive Metal-Organic Frameworks. *J. Am. Chem. Soc.* **2009**, *131*, 9906–9907.
69. Mulfort, K. L.; Farha, O. K.; Stern, C. L.; Sarjeant, A. A.; Hupp, J. T. Post-Synthesis Alkoxide Formation Within Metal-Organic Framework Materials: A Strategy for Incorporating Highly Coordinatively Unsaturated Metal Ions. *J. Am. Chem. Soc.* **2009**, **131**, 3866–3868.
70. Stub, S. Ø.; Vøllestad, E.; Norby, T. Mechanisms of Protonic Surface Transport in Porous Oxides: Example of YSZ. *J. Phys. Chem. C* **2017**, *121*, 12817–12825.
71. Liang, X.; Li, B.; Wang, M.; Wang, J.; Liu, R.; Li. G. Effective Approach to Promoting the Proton Conductivity of Metal–Organic Frameworks by Exposure to Aqua–Ammonia Vapor. *ACS Appl. Mater. Interfaces* **2017**, *9*, 25082–25086.
72. Lim, D-W.; Sadakiyo. M.; Kitagawa, H. Proton transfer in hydrogen-bonded degenerate systems of water and ammonia in metal–organic frameworks. *Chem. Sci.* **2019**, *10*, 16–33.
73. Sadakiyo, M.; Kasai, H.; Kato, K.; Takata, M.; Yamauchi, M. Design and Synthesis of Hydroxide Ion−Conductive Metal−Organic Frameworks Based on Salt Inclusion systems of water and ammonia in metal–organic frameworks. *J. Am. Chem. Soc*. **2014**, *136*, 1702−1705.
74. Bediako, D. K.; Solis, B. H.; Dogutan, D. K.; Roubelakis, M. M.; Maher, A. G.; Lee, C. H.; Chambers, M. B.; Hammes-Schiffer, S; Nocera, D. G. Role of pendant proton relays and proton-coupled electron transfer on the hydrogen evolution reaction by nickel hangman porphyrins. *Proc. Natl. Acad. Sci*. **2014**, *111*, 15001–15006.

CHAPTER 3

Designing of Flexible Metal-Organic Framework-based Super-protonic Conductors and their Fabrication with a Polymer into Proton Exchange Membranes

OVERVIEW:

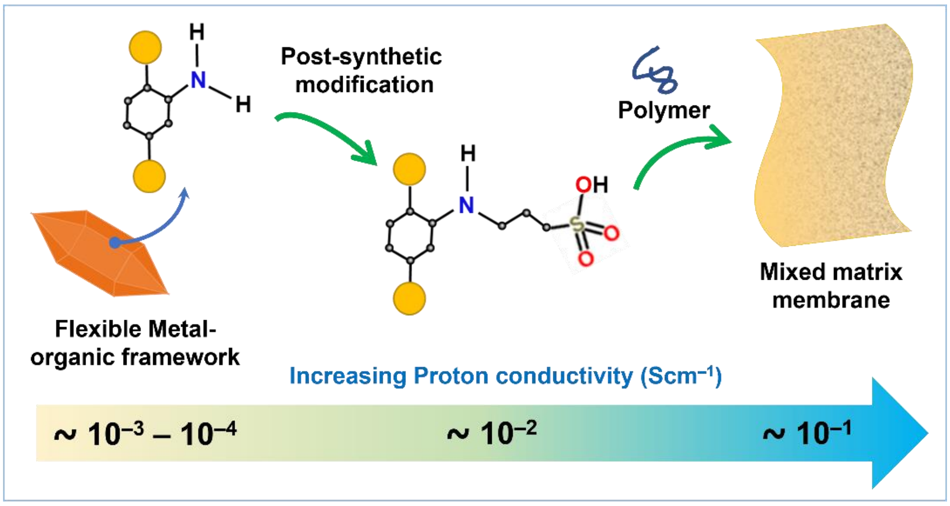

In this work, we have focused on developing '*flexible MOF*'-based proton conductors with **Fe-MIL-53-NH$_2$** and **Fe-MIL-88B-NH$_2$** MOFs and using post-synthetic modification (PSM) as the tool. Taking advantage of the porous nature of these frameworks, we have carried out PSM on the primary amine groups present on the MOFs and converted them to -NH($CH_2CH_2CH_2SO_3H$) groups. The PSM increased the number of labile protons in the channels of the modified MOFs as well as the extent of H-bonded networks inside the framework. The modified **Fe-MIL-53-NH$_2$** and **Fe-MIL-88B-NH$_2$** MOFs, named hereafter as **53-S** and **88B-S**, respectively showed proton conductivity of 1.298×10^{-2} and 1.687×10^{-2} S cm^{-1} at ~80 ^{0}C and 98% relative humidity (R. H), respectively. This is ~10-fold and ~5-fold increment in their proton conductivity than their respective parent MOFs. Since MOFs as such are difficult to be directly made into flexible membranes, that are essential for practical applications as proton conductor, we have incorporated **53-S** and **88B-S** as fillers into a robust imidazole-based polymer matrix namely OPBI [poly(4,4′-diphenylether-5,5′-bibenzimidazole)]. The resulting polymer-MOF mixed matrix membranes (MMMs) after being doped with phosphoric acid (PA) performed as flexible proton exchange membranes (PEMs) above 100 ^{0}C under anhydrous condition and found to be much more efficient and stable than the pristine OPBI membrane (devoid of any filler loading). By optimizing the amount of filler loading in the membrane, we obtained the highest conductivity of 0.304 S cm^{-1} at 160 ^{0}C under anhydrous condition.

3.1. INTRODUCTION

The study of proton conductivity and development of proton conducting materials are of immense importance from the perspective of renewable energy research owing to the widespread use of these materials in fuel cell, electrochemical sensors, electrolyzers and CO_2 convertors, among others.[1,2] The early research works had focused on development of proton conductors from materials such as organic polymers, ceramic oxides, solid acids, intercalation compounds, etc.[3,4] But in the last few years, metal organic frameworks (MOFs) have been explored extensively as proton conductors,[3–11] or as proton exchange membranes (PEMs) in combination with suitable polymers.[12-16] This is due to the crystalline nature, high surface area and the ease of structural tunability in MOFs, which render the material viable for many applications.[17-21] The wide range of metal ions and organic linkers provides us with a plethora of MOFs with different surface functionalities, pore and channel sizes, along with an additional scope of post-synthetic modification.[20]

In this work, we have focused on developing *'flexible MOF'*-based proton conductors using MIL MOFs (MIL: Materials Institute Lavoisier). MIL-MOFs are porous materials composed of trivalent metal cations and carboxylate anion linkers.[22] They are usually known for their huge pores and high hydrothermal stability. The study of MILs as proton conductors have been continuing for the last several years; MIL-101 being the most popular one amongst all.[3-9] But MILs as such do not show much appreciable conductivity and therefore, several methods have been applied to improve their proton conductivity.[23-33] In one such noteworthy work, Ponomareva et al impregnated the MIL-101 framework with non-volatile acids like H_2SO_4 and H_3PO_4, which created a proton conductor operational at low humidity and high temperature.[23] Following this strategy, other MIL MOFs were also treated with acids, to create stable and efficient proton conductors.[6,24] Another common strategy is impregnation of the concerned MOF pores with conducting medium, such as ionic liquids,[25-27] and organic salts.[28] In a work by Kitagawa and coworkers, the proton conductivity in a series of MIL-53 frameworks having different functionalities (–H, $–NH_2$, –OH, –COOH) on the organic linker were studied, and a direct correlation was obtained among the pK_a of the frameworks, their proton conductivity and their activation energy.[29] Since the functional group on a MOF's surface plays an important role in its conductivity, scientists have adopted different methods to modify or incorporate functionalities in MIL MOFs, in order to enhance their proton conductivity.[30-32] Some of these MOF-based proton conductors have also been fabricated into membranes. In an interesting work by Qiu et al, MIL-101 MOF was turned into nanogel for better proton conduction.[33] In all these strategies the one thing which has been common, is the aim to increase the density of H-bonds between the frameworks and proton carriers, which is the key factor to obtaining efficient proton-conducting MOFs.[34,35] In our work, we have chosen two 'Fe(III) and 2-aminoterephthalate (NH_2-BDC)'-based flexible MIL MOFs (MILs) – MIL-53 and MIL-88B, named hereafter as **Fe-MIL-53-NH_2** and **Fe-MIL-88B-NH_2**, respectively, and studied their properties with respect to application as proton conductors. The reason for choosing flexible MOFs for this study is that these materials undergo dynamic structural transformations in response to host-guest interactions, primarily guided by H-bonds.[31] This feature of these MOFs facilitates them in maintaining high proton conductivity over a wide range of relative humidity (RH). In addition to it, the flexible nature of these frameworks allows easier modification of the pores of the pertinent MOFs.

Fe-MIL-53-NH_2 and **Fe-MIL-88B-NH_2** are unique for their structural flexibility; interestingly, even though both these MOFs have been synthesized from the same starting materials, but different reaction conditions lead to different frameworks containing compounds having dissimilar properties. The **Fe-MIL-53-NH_2** framework has one-dimensional chains of corner-sharing Fe(III) octahedra, connected by μ_2-OH and carboxylate groups. These inorganic chains are connected to four neighbouring similar chains by 2-aminoterephthalate linkers. The resulting framework structure contains one-dimensional diamond-shaped channels / pores.[36-40] These channels can partially be occupied with hydrogen-bonded 2-aminoterephthalic acid molecules. From the crystal structure reported by Stock and co-workers, the molecular formula of **Fe-MIL-53-NH_2** was found to be $[Fe(OH)NH_2\text{-}BDC\cdot 0.3NH_2\text{-}H_2BDC]$.[36] While **Fe-MIL-53-$NH_2$** has mono-nuclear metal node, **Fe-MIL-88B-NH_2**, formulated as $[Fe_3O(OH_2)_3Cl(NH_2\text{-}BDC)_3]$, has a tri-nuclear metal node which connects the 2-aminoterephthalate linkers in a cage like fashion giving rise to three dimensional channels.[36, 41-47] Due to these factors, **Fe-MIL-88B-NH_2** possesses exceptionally high framework flexibility. The choice of Fe(III) metal ion for these MOFs is crucial for the possible use of these MOFs for real applications, since Fe is non-toxic in nature. Here, the use of 2-aminoterephthalic acid, over terephthalic acid as the linker, provides us with the additional scope of post-synthetic modification (PSM) of the MOFs, because of the presence of amine functionality. The MOFs **Fe-MIL-88B-NH_2** and **Fe-MIL-53-NH_2** as such, show proton conductivity in the order of 10^{-3} – 10^{-4} S

cm^{-1} (*vide infra*). But with post synthetic modification of the MOFs through 'sulfolactone' reaction of the -NH_2 groups, particularly with 1,3-propane sultone, sulfonic acid pendant groups tethered with dangling side chains ($CH_2CH_2CH_2SO_3H$) could be inserted into the framework, which could greatly enhance the proton conducting properties of the resulting modified MOFs. This strategy of post-synthetic modification has been employed following our previous work on UiO-66 MOF.[48] A schematic representation of the synthetically modified MOFs (abbreviated as **53-S** and **88B-S)** is provided in Scheme 3.1. The comparative studies of the proton conducting properties of these parent MOFs and the modified-MOFs, help us to understand the role of framework flexibility in designing of better MOF-based proton conductors.

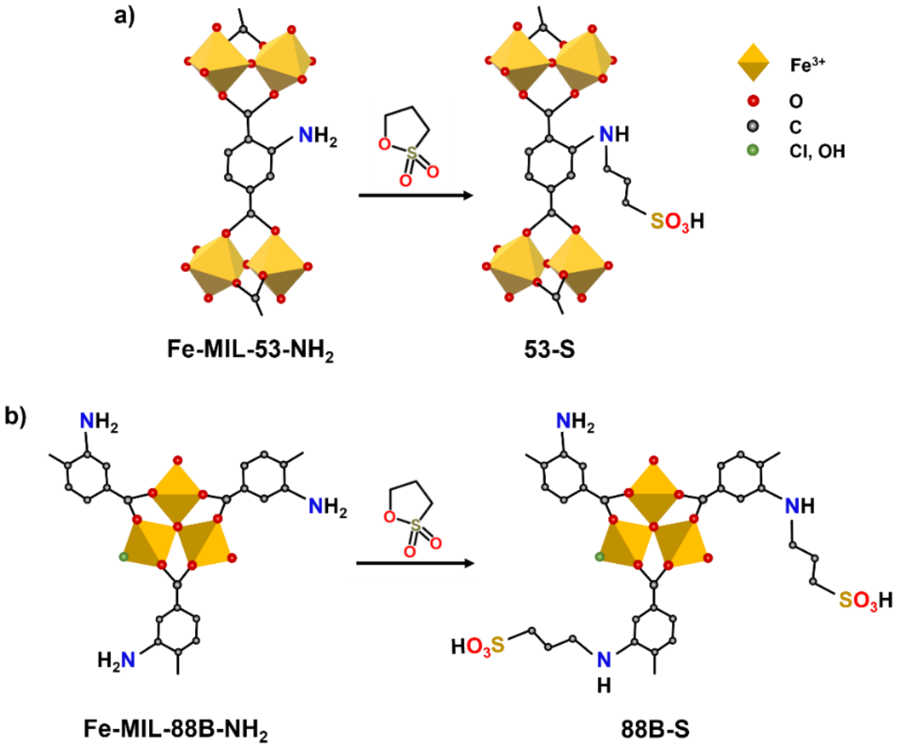

Scheme 3.1. Illustration of the post-synthetic modification of a) **Fe-MIL-53-NH$_2$** and b) **Fe-MIL-88B-NH$_2$** to form **53-S** and **88B-S**, respectively.

Since the proton conducting MOFs as such cannot be obtained in the form of a flexible membrane, MOFs are difficult to be directly used for practical applications, like in fuel cell or electrolyzers. We have thus investigated, in this work, their applicability by fabricating these functionalized MOFs with organic polymers, resulting in polymer-MOF mixed matrix membranes (MMMs). The membranes thus formed by mixing different weight percentage of **53-S** and **88B-S** as nanofillers with OPBI (4,4′-diphenylether-5,5′-

bibenzimidazole) polymer, perform as efficient, flexible, and robust proton exchange membranes (PEMs) above 100°C under anhydrous conditions when doped with phosphoric acid (PA). The developed MMMs, in fact, function as much more efficient and stable PEMs than OPBI polymer as such, and are superior to most of the MOF-based proton conducting MMMs reported till date. [13-15] We have demonstrated that there are significant interfacial interactions among the structural functionalities present in the OPBI polymer (imidazole N−H groups) and in the post synthetically modified **53-S** and **88B-S** MOF nanofillers (primary amines, secondary amines and hydrophilic –SO_3H groups) which has led to their significantly improved performance as PEMs.

3.2. EXPERIMENTAL SECTION

3.2.1. Materials

3,3',4,4'-tetraaminobiphenyl (TAB), 4,4'-oxybis(benzoic acid) (OBA) polyphosphoric acid (115%) (PPA), 2-aminoterephthalic acid (NH_2-H_2BDC, 99%), 1,3-propane sultone (98%), hydrofluoric acid (HF) were purchased from Sigma Aldrich, India. 1,3,5-benzene tricarboxylic acid (H_3BTC) Formic acid (99%) and ortho phosphoric acid (85%) were purchased from Merck India. Sulphuric acid (98%), hydrochloric acid (HCl), N, N-dimethylformamide (DMF), dichloromethane (DCM), ferric chloride ($FeCl_3\cdot 6H_2O$), methanol (MeOH) and glacial acetic acid were purchased from Finar Chemicals. All the chemicals were used as received without any further purification. DDI water was used throughout the project.

3.2.2. Synthesis

The synthesis of parent MOFs: **Fe-MIL-53-NH_2** and **Fe-MIL-88B-NH_2** were adapted from reported literatures with some modifications. [36,41,44,46,49] Poly(4,4′-diphenylether-5,5′-bibenzimidazole) abbreviated as OPBI was synthesized following a modified literature reported synthetic strategy. [16,50]

3.2.2.1. Synthesis of Fe-MIL-53-NH_2

96 mg of H_2BDC-NH_2 was added in 8 mL of H_2O along with 1 mL of 0.2 M HF in a 23 mL autoclave. To it, 0.67 mL of 0.4 M $FeCl_3\cdot 6H_2O$ was added and this mixture was stirred for 15 minutes prior to being heated at 150 °C for 48 hours. On cooling down of the reaction

mixture, the reddish-brown product was separated by centrifugation and washed with H_2O and methanol thrice each. The product was dried in a hot air oven at 70 °C for 24 hours. (Yield with respect to Fe^{3+}: 52%)

3.2.2.2. Synthesis of Fe-MIL-88B-NH_2

1.125 g of BDC-NH_2 was dissolved in 37.5 mL of DMF and 3.375 g of $FeCl_3 \cdot 6H_2O$ was dissolved in 37.5 mL of DMF, separately. These were then added together into a 200 mL screw capped round bottom flask. The reaction mixture was sonicated for 10 minutes and heated at 110 °C for 24 hours. On cooling down of the reaction mixture, the brown product was separated by centrifugation and washed with DMF, H_2O and methanol thrice each. The product was dried in a hot air oven at 70 °C for 24 hours. (Yield with respect to Fe^{3+}: 60%)

3.2.2.3. Synthesis of poly (4,4'-diphenylether-5,5'-bibenzimidazole) (OPBI)

Calculated with respect to 3.5 wt% monomer concentration, equimolar amounts of 3,3'-diaminobenzidine (0.0076 mol, 1.627 g) and 4,4'-oxybis(benzoic acid) (OBA) (0.0076 mol, 1.962 g) along with the required amount of polyphosphoric acid (PPA) (100 ml) were placed in a three-necked RB flask. Then the reaction mixture was subjected to mechanical stirring with an overhead stirrer at 60 rpm in presence of nitrogen gas purging to maintain an inert atmosphere. The polymerization reaction was carried out at 190–220 °C for about 24-26 h. After that, the reaction mixture was poured into distilled water where the polymer melt gets isolated as brown fibrous mass. The fibrous mass was then neutralized with sodium bicarbonate, washed thoroughly with DDI water, and finally dried in a vacuum oven at 100 °C for 24 h to obtain dry **OPBI** (~ 3.0 g) polymer.

3.2.2.4. Synthesis of 53-S and 88B-S

The post-synthetic modification of the MOFs, **Fe-MIL-53-NH_2** and **Fe-MIL-88B-NH_2** was carried out through the reactions of these MOFs with 1,3-propane sultone. Here, the -NH_2 groups of the MOFs react with sultone to form -$NH(CH_2CH_2CH_2SO_3H)$ yielding post synthetically modified systems named hereafter as **53-S** and **88B-S**, respectively as shown in the Scheme 3.1. The synthesized MOFs were activated and characterized prior to post-synthetic modification. The treatment was done following our previous report along with some modifications.[48] In brief, approximately 300 mg of MOF was taken in a screw-capped vial and 5 mL of DCM was added to it along with 0.4 mL of 1,3 propane sultone and stirred for 24 hours. The product was then separated by centrifugation and washed with DCM thrice. The product was dried in a hot air oven at 60 °C for 24 hours.

3.2.2.5. Fabrication of 53-S@OPBI and 88B-S@OPBI Mixed Matrix Membranes

53-S and **88B-S** loaded mixed matrix membranes (MMMs) were fabricated using solution blending technique.[51,52] Firstly, the MOF samples (**53-S**, **88B-S**) were taken in a measured amount [5 mg or 7.5 mg to form respective 5% or 7.5% (with respect to OPBI polymer weight) loaded membranes] in a glass vial and added with 5 ml of formic acid. The mixture was stirred for 15 minutes and added into 5 mL of a 2 wt% solution of OPBI in formic acid [100 mg OPBI in 5 mL FA]. The polymer-MOF mixture was then kept for vigorous stirring in a conical flask at room temperature, to avoid the formation of any lumps and to obtain a homogeneous dispersion (the final concentration of OPBI in the polymer-MOF mixture was 1 wt %). This mixture was then poured into a petri dish and kept inside a heating oven at 60 °C for 12 h for slow evaporation of solvent. After solvent evaporation, flexible MMM was peeled out from the petri dish and kept for drying in a vacuum oven at 100 °C to remove the absorbed moisture and trapped FA. Apart from the preparation of **53-S-5%**, **53-S-7.5%**, **88B-S-5%** and **88B-S-7.5%** MMMs, **88B-7.5%** composite membrane was also prepared using 7.5% of unmodified parent MOF (**Fe-MIL-88B-NH_2**) following similar synthetic protocol for the purpose of comparison. A schematic representation of this MMM fabrication is shown in the Scheme 3.2.

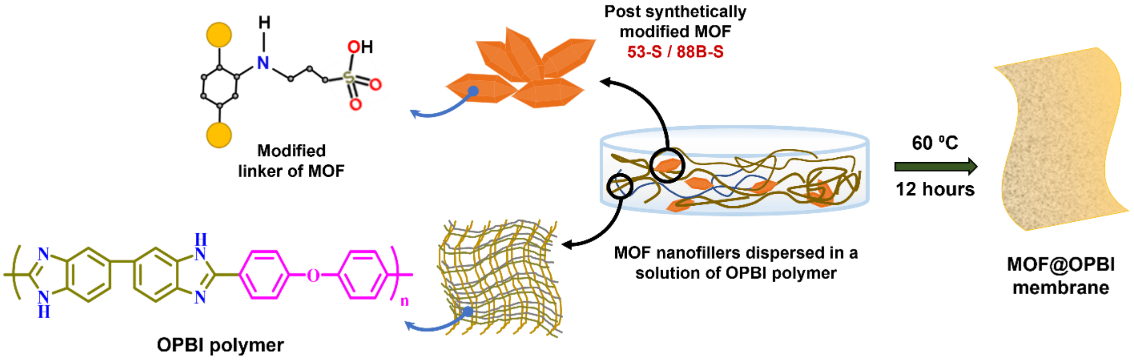

Scheme 3.2. Schematic representation of the fabrication of **53-S@OPBI** and **88B-S@OPBI** MMMs.

3.2.2.6. Phosphoric Acid (PA) Doping of the MOF loaded MMMs

Pristine OPBI membrane and the composite membranes, **53-S-5%**, **53-S-7.5%**, **88B-S-5%**, **88B-S-7.5%** and **88B-7.5%**, were kept for drying at 100 °C for 24 h and then these dried membranes were dipped into 85% PA solution for 5 days to generate PA loaded proton exchange membranes (PEMs). After 5 days, the MMMs were taken out from the PA container, wiped with a blotting paper to remove the excess PA on the surface, and stored in a zip-lock cover for future analysis.

3.2.3. Methods

All the synthesized MOF samples were characterized by powder X-ray diffraction (PXRD) studies, fourier-transformed infrared (FTIR) spectroscopy, field emission scanning electron microscopy (FESEM), thermogravimetric analysis (TGA), inductively coupled plasma-optical emission spectrometry (ICP-OES), N_2 gas sorption and dynamic vapor sorption (DVS) techniques. Proton conductivity studies were done using electrochemical impedance spectroscopy. The MOF loaded MMMs, **53-S-5%**, **53-S-7.5%**, **88B-S-5%**, **88B-S-7.5%** and **88B-7.5%**, developed in this work, were also characterized by FT-IR, PXRD, FESEM, transmission electron microscopy (TEM), atomic force microscopy (AFM), TGA, dynamic mechanical analyser (DMA), and universal testing machine (UTM). The detailed experimental procedures for water uptake (WU), swelling ratio (SWR) in water and in PA, PA doping level, proton conductivity measurement and PA retention analysis of the MMMs are included in the appendix 3.
The instrumental details of all the experiments are provided in appendix 1.

The methodology for electrochemical impedance spectroscopy measurements on MOF powder samples (**Fe-MIL-53-NH$_2$**, **Fe-MIL-88B-NH$_2$**, **53-S**, and **88B-S**) is provided in section 2.2.3.1, Chapter 2.

3.2.3.1. PA doping level, swelling ratio, and water uptake capacity of the membranes

Three similar sized pieces of the **OPBI**, **53-S (-5%** and **-7.5%)** and **88B-S (-5%** and **-7.5%)** membranes (made from formic acid) were immersed in phosphoric acid for 5 days. Then these soaked membranes were taken out, wiped with filter paper, and transferred into 50 ml of water. It was titrated against 0.1 N sodium hydroxide (NaOH). The phosphoric acid content was calculated as the number of PA moles per PBI repeat unit. The length, thickness and width of the dried membranes were measured before dipping in phosphoric acid and after 5 days of the dipping.

Swelling ratio of the membranes in PA were calculated from the following equation.

$$\%\text{Swelling Ratio} = \frac{L_w - L_d}{L_d} \times 100\% \qquad \ldots (1)$$

Where, L_w, and L_d are the length of the wet membranes and dry membranes, respectively.

Similarly, the water uptake and swelling ratio in water for **OPBI** and the fabricated MMMs were obtained by immersing the membranes in water for 5 days. The length, thickness and width of the dried membranes were measured before dipping in water. After 5 days, the membranes were removed from water bath and quickly wiped to remove surface water from the membranes. After this the length, thickness and width of the wet membranes were measured. Water uptake was calculated from the following equation.

$$\%\text{Water Uptake} = \frac{W_w - W_d}{W_d} \times 100\% \qquad \ldots (2)$$

Where, W_w is wet membrane weight and W_d, is dry membrane weight, respectively.

Similarly, swelling ratio in water was measured using equation (1).

3.2.3.2. Ion exchange capacity (IEC) of the membranes

Firstly, the membranes were converted to its protonated form by soaking them in 1 M HCl solution for 48 h. Then the membranes were washed with distilled water and immersed in a 1M NaCl solution for 48 h, to exchange the H^+ ions with Na^+ ions. Then this solution with H^+ ions was titrated with a 0.01 M NaOH solution. The IEC was calculated according to the following equation:

$$\text{IEC} = \frac{V_{NaOH} \times C_{NaOH}}{W_{Dry}} \text{ (meq/g)} \qquad (3)$$

Here, V_{NaOH} and C_{NaOH} are the volume and concentration of NaOH, respectively, and W_{Dry} denotes the weight of the dry membrane.

3.2.3.3. Proton conductivity studies on the membranes

Proton conductivity studies on the membranes were carried out using electrochemical impedance spectroscopy, employing a four-probe setup. During a measurement, the frequency was swept from 1 Hz to 100 KHz. The phosphoric acid doped **53-S@OPBI and 88B-S@OPBI** composite membranes were cut in rectangular shape, and then kept sandwiched between two Teflon plates with four platinum electrodes. Two outer electrodes (1.5 cm apart) supply current to the cell, while the two inner electrodes, 0.5 cm apart on opposite sides of the membrane, measure the potential drop.

First, the surface of the PA doped membranes was wiped out carefully and fitted into conductivity cell. Prior to the conductivity measurements, the conductivity cell was placed in a vacuum oven at 100 °C for 2h to remove any surface adsorbed water and thus avoid the conduction due to the presence of water molecules. After that, the conductivity cell was cooled down to room temperature and kept in a vacuum desiccator until going for its conductivity measurement. The complete conductivity cell set up was kept in a vacuum oven to measure the temperature dependence of proton conduction. The conductivities of the membranes were measured from room temperature to 160 °C at intervals of 20 °C. At every temperature jump, the sample was kept for 30 minutes to attain isothermal equilibrium and then data were recorded. The conductivities of the membranes were calculated from the following equation:

$$\sigma = \frac{D}{RBL} \qquad \ldots (4)$$

Here, D is the distance between the electrodes (here it is 0.5 cm), B is the thickness of the membrane, L is the width of the membrane and R is the bulk resistance obtained from the Nyquist plot.

3.2.3.4. Acid leaching test

The acid doped membranes were taken out from the phosphoric acid bath and excess phosphoric acid was wiped out with a tissue paper. The membranes were then placed in a closed setup under continuous flow of water vapour at 100 °C for a period of three hours. The weight of the membrane (W_t) was recorded in every one hour after wiping the water on the surface. The weight loss ratio of acid in the membranes was calculated by using the following formula:

$$\mathrm{R} = \frac{W_o - W_t}{W_a} \times 100\,\% \qquad \ldots (5)$$

Where, W_o is weight of the PA doped membranes at the initial time of zero hour, W_t is the weight of the PA membrane after acid leaching at different times (t) and W_a is the original weight of PA present in the membranes calculated from the PA doping level of the membranes.

3.3. RESULTS AND DISCUSSIONS

3.3.1. Powder X-ray diffraction (PXRD) analysis

The PXRD patterns of synthesized parent MOFs (**Fe-MIL-53-NH$_2$** and **Fe-MIL-88B-NH$_2$**) and the post-synthetically modified MOFs (**53-S** and **88B-S**) match well with the corresponding simulated patterns (Figures 3.1a and 3.1b). This confirms the successful formation of the parent MOFs and shows that the framework integrity is well-maintained during the post-synthetic modification process for **53-S** and **88B-S**.

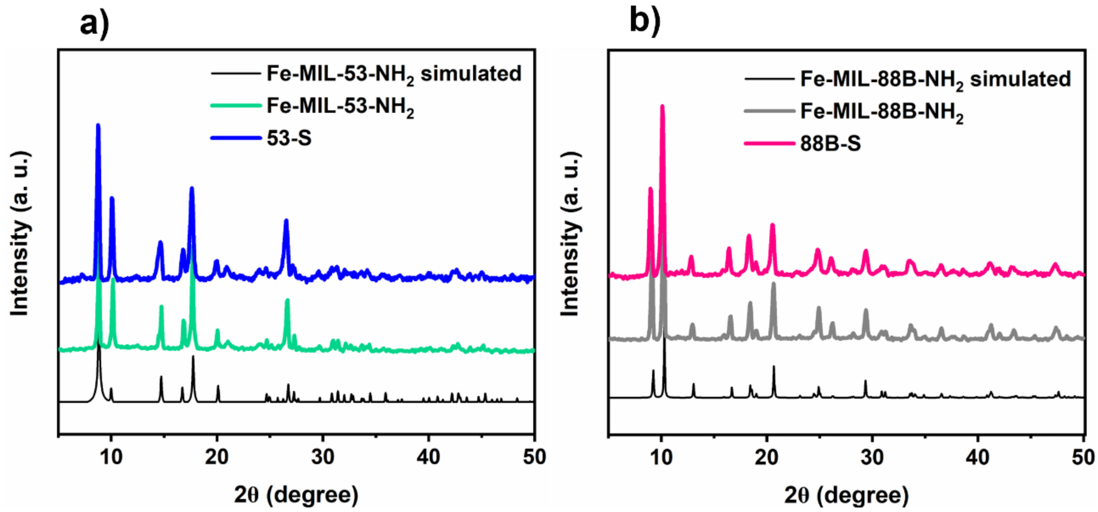

Figure 3.1. a) PXRD patterns of **53-S**, **Fe-MIL-53-NH$_2$**, and simulated PXRD pattern from the crystal data of **Fe-MIL-53-NH$_2$**; b) PXRD patterns of **88B-S**, **Fe-MIL-88B-NH$_2$**, and simulated PXRD pattern from the crystal data of **Fe-MIL-88B-NH$_2$**.

3.3.2. Fourier transformed infrared (FT-IR) spectral analysis

The ATR-FTIR spectra of **Fe-MIL-53-NH$_2$** and **Fe-MIL-88B-NH$_2$** (Figures 3.2a and 3.2a) match well with the reported literature.[36,41,44,46,49] For **Fe-MIL-53-NH$_2$**, the symmetric (γ_s C-O) and asymmetric (γ_{as} C-O) stretching of the carboxylate groups in NH$_2$-BDC are observed at ~1530 cm^{-1} and ~1378 cm^{-1}, respectively. A sharp band at ~1678 cm^{-1} is also found, which originates from the C=O stretching of the H-bonded NH$_2$-H$_2$BDC acid molecules present in the channels of the MOF, a characteristic signal of **Fe-MIL-53-NH$_2$**. From a combination of different techniques like TGA, ^{1}H-NMR and ICP-OES, the number of H-bonded NH$_2$-H$_2$BDC molecules was estimated to be ~0.21, such that the structural formula for **Fe-MIL-53-NH$_2$** becomes [Fe(OH)NH$_2$-BDC·0.21NH$_2$-H$_2$BDC]; the relevant experimental details and results are provided in appendix 3 (Section A3.1 and A3.2). For **Fe-MIL-88B-NH$_2$**, this extra peak is not observed which proves the absence of any free

NH_2-H_2BDC acid in the MOF. The corresponding symmetric (γ_s C-O) and asymmetric (γ_{as} C-O) stretching of the carboxylate groups are observed at ~1580 cm^{-1} and ~1378 cm^{-1}, respectively. For both **MIL-53** and **MIL-88B**, a strong peak at ~760 cm^{-1} is observed, originating from the Csp^2-H bending vibrations of NH_2-BDC aromatic rings, and two small peaks around 3400 cm^{-1} due to primary amines. The ATR-FTIR spectra **53-S** and **88B-S** show several similar features as those of their respective parent MOFs along with the appearance of new peaks at ~1150 cm^{-1} and ~1037 cm^{-1} corresponding to -SO_3H functionality.[48] The post-synthetic treatment with 1,3-propane sultone convert the primary amines -NH_2 in the **Fe-MIL-53-NH₂** and **Fe-MIL-88B-NH₂** MOF framework to -$NH(CH_2CH_2CH_2SO_3H)$, which means that there should be a reduction in the peak intensity of primary amines in the FT-IR spectra, and this is what is observed in the IR spectra of **53-S** and **88B-S**. This is further accompanied by the presence of a broad peak around 3000 cm^{-1}, which is much more prominent for **88B-S** (ranging from 2900 cm^{-1} to 3600 cm^{-1}) due to the formation of extensive H-bonded networks within the MOF. All these observations together indicate the successful modification of the parent MOFs.

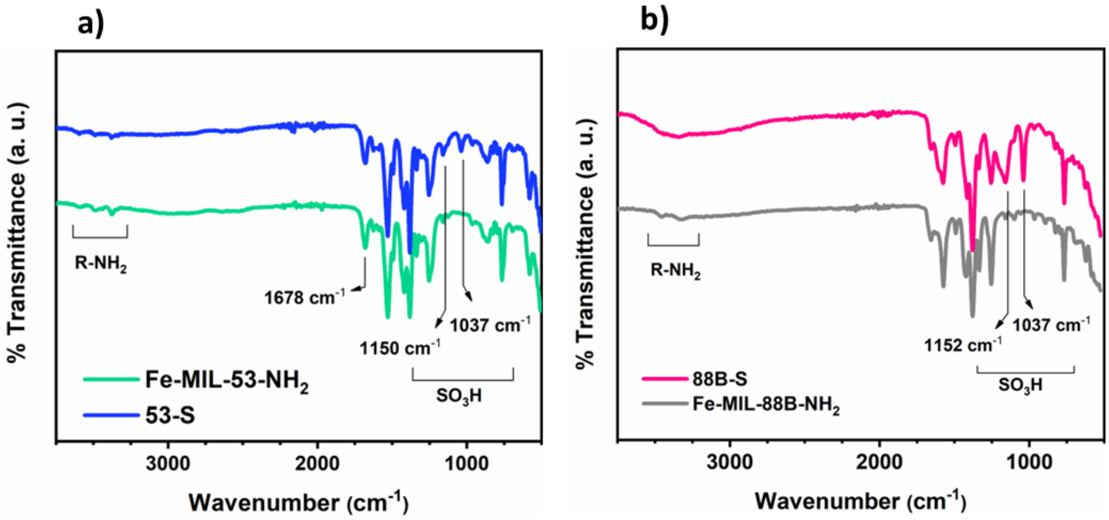

Figure 3.2. a) ATR-FTIR spectra of **53-S** and **Fe-MIL-53-NH₂**; b) ATR-FTIR spectra of **88B-S** and **Fe-MIL-88B-NH₂**.

3.3.3. Determination of extent of post synthetic modification

ICP-OES technique was used to estimate the extent to which the -NH_2 groups of the MOFs are modified. For this, the MOF samples were digested in an aqua regia solution and the iron and sulfur contents, present in the framework, are estimated (detailed methodology and calculation are provided in the Appendix 3; section A3.3). The results show that ~21.6% of the -NH_2 groups in **53-S** and ~57.3% in **88B-S** were modified. Here it is interesting to note that even, with the same post-synthetic treatment for both **Fe-MIL-53-NH_2** and **Fe-MIL-88B-NH_2**, the extent of modification is considerably different. This might be because **Fe-MIL-88B-NH_2** framework is much more flexible in nature than **Fe-MIL-53-NH_2** framework. Higher flexibility would mean easier accommodation of guest species which might have led to higher conversion of -NH_2 to -$NH(CH_2CH_2CH_2SO_3H)$.[42] In addition to it, since the channels of **Fe-MIL-53-NH_2** are already partially occupied by H-bonded disordered NH_2-H_2BDC acid molecules, there would probably be some amount of steric crowding if higher degree of linker modification is to occur.

3.3.4. FESEM image analysis

The FESEM images of **Fe-MIL-53-NH_2** and **Fe-MIL-88B-NH_2**, (Figure A3.4, Appendix 3) show spindle-shaped micro-crystallites having well-developed morphology. The post synthetically modified MOFs, **53-S** and **88B-S** do not show any noticeable changes from their corresponding parent MOFs, with respect to morphology (Figure 3.3). The crystallite sizes for both **53-S** and **88B-S** were comparable to each other as shown in Figure 3.3.

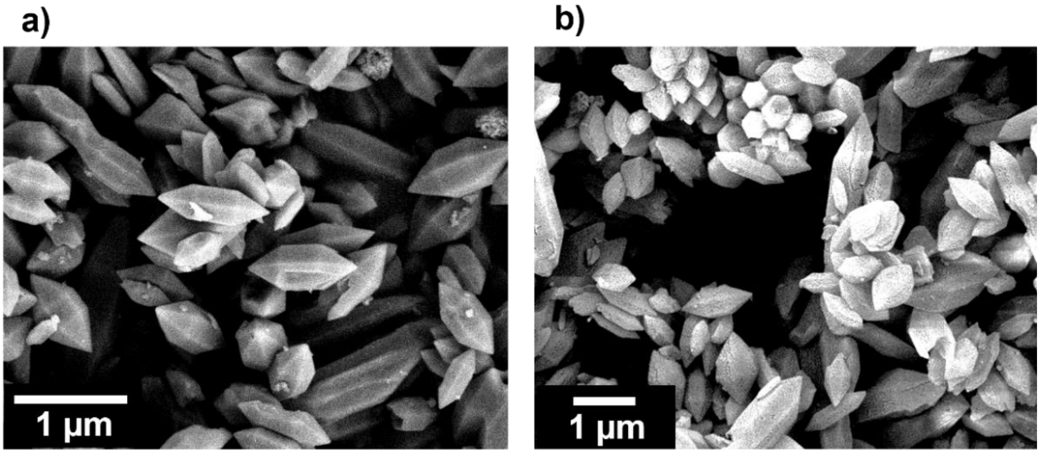

Figure 3.3. FESEM images of a) **53-S** and b) **88B-S**.

3.3.5. Thermogravimetric analysis (TGA)

The thermogravimetric plots for **Fe-MIL-53-NH_2** and **Fe-MIL-88B-NH_2** (Figure A3.5, S6, Appendix 3**)** matched well with those from relevant reported literature.[36] **53-S** displays much higher mass loss (11% weight loss) as compared to that shown by parent MOF **Fe-MIL-53-NH_2** (2% weight loss) in the temperature range of 80 ºC – 250 ºC, probably due to higher amount of adsorbed water molecules. For **88B-S** the amount of weight loss (17% weight loss) in the range of 80 ºC – 250 ºC is comparable to that shown by **Fe-MIL-88B-NH₂** (18.5% weight loss); but while in case of **Fe-MIL-88B-NH₂**, the weight loss primarily occurs in one step at around 100 ºC, for **88B-S**, it took place in two steps at 100 ºC and 200 ºC. This could be an indication that the water molecules present in **88B-S** framework are much more tightly bound than those in the corresponding parent MOF, **Fe-MIL-88B-NH₂**. For all the MOFs, the framework disintegration starts after 300 ºC and for the modified MOFs, the weight loss is slightly higher than that of the parent MOFs due to the higher organic contents in the post synthetically modified frameworks.

3.3.6. N_2 sorption analysis

Now, the side arms -NH($CH_2CH_2CH_2SO_3H$) attached onto the surface of the pores and channels of **53-S** and **88B-S** frameworks due to the post synthetic modification, is expected to increase the steric bulkiness inside the channels of the modified MOFs, as compared to their corresponding parent MOFs.[48] This outcome can be observed in the N_2 sorption isotherms for **53-S** and **Fe-MIL-53-NH₂** (Figure 3.4a), and **88B-S** and **Fe-MIL-88B-NH₂** (Figure 3.4b). The N_2 sorption analysis was performed at 77 K and all the samples were

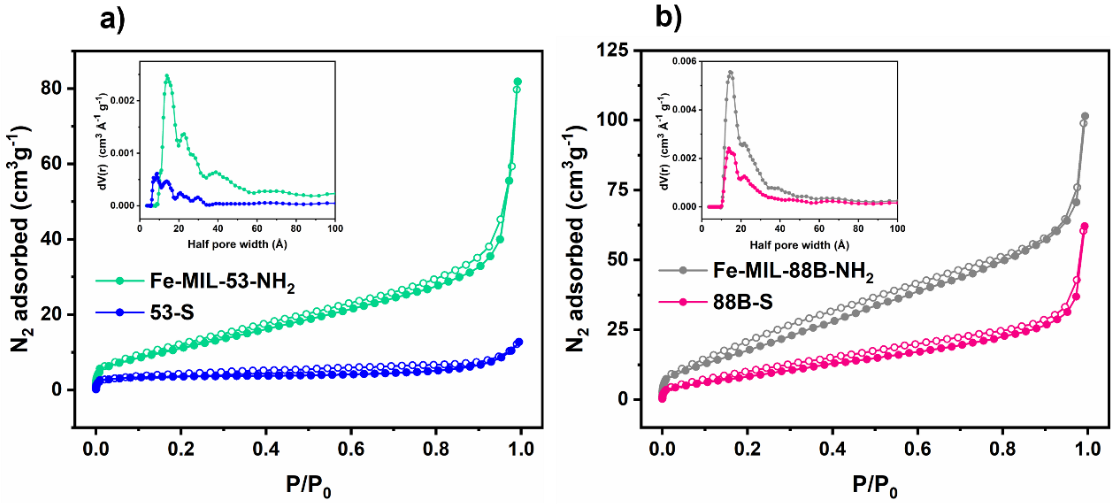

Figure 3.4. N_2 sorption isotherms of a) **53-S** and **Fe-MIL-53-NH₂**, b) **88B-S** and **Fe-MIL-88B-NH₂**; inset of (a) and (b): corresponding pore size distribution curves; filled spheres denote adsorption and hollow spheres denote desorption experimental data points.

kept for activation at 150 ºC under vacuum for 12 hours prior to analysis. For both the parent MOFs, the specific surface area (SSA) observed was found to be of similar order as reported earlier.[38-41,47] For **Fe-MIL-53-NH₂**, the (SSA) was found to be 26.3 m^2g^{-1}, which reduces to 10.1 m^2g^{-1} for **53-S**. The pore size distribution derived by NLDFT method (Figure 3.4a inset) shows a reduction in pore width of the channels along with significant decrease in pore volume for **53-S**. For **Fe-MIL-88B-NH$_2$**, the (SSA) was found to be 35.8 m^2g^{-1}, which decreases to 18.2 m^2g^{-1} for **88B-S**. Here as well a considerable decrease in pore volume is observed for **88B-S** from the pore size distribution (Figure 3.4b inset).

3.3.7. Dynamic vapor sorption analysis (DVS)

As observed from dynamic vapor sorption study (DVS) of **53-S** and **Fe-MIL-53-NH$_2$** (Figure 3.5a), the water uptake capacity of **53-S** has been found to have improved considerably due to the post-synthetic modification. The incorporation of -SO_3H groups in the MOF framework as well as on the H-bonded NH_2-H_2BDC acid molecules, present in the channels of the MOF, would have helped in increasing the hydrophilicity of the framework and thus increase the water uptake capacity of the MOF. For **88B-S**, the total water uptake did not improve as compared to the water uptake of unmodified parent MOF (Figure 3.5b). However, the desorption isotherm for **88B-S** shows a relatively constant hysteresis throughout the humidity range as opposed to **Fe-MIL-88B-NH$_2$**, for which the hysteresis appeared at lower humidity. This shows that the **88B-S** framework has higher water-retention capacity in the high humidity range. But a low water uptake by **88B-S** framework, might be due to the shrinking of the framework and constriction of the pores – a usual characteristic of flexible MIL-88B framework in presence of water, due to the formation of extensive H-bonded networks (as inferred from ATR-FTIR spectra; *vide*

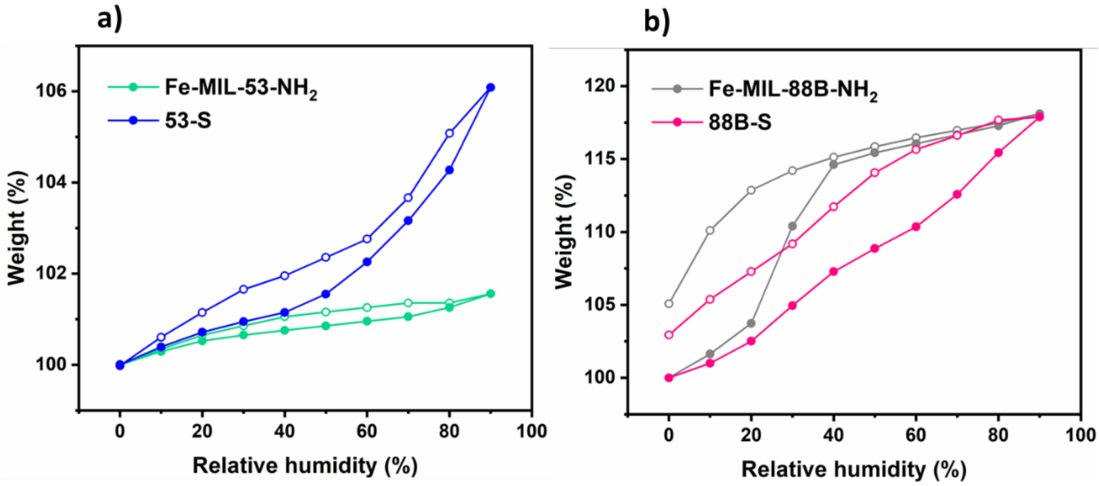

Figure 3.5. Water uptake capacity of a) **53-S** and **Fe-MIL-53-NH$_2$**, b) **88B-S** and **Fe-MIL-88B-NH$_2$** at different relative humidity (R. H.) as determined by dynamic vapor sorption (DVS). Filled spheres denote adsorption and hollow spheres denote desorption experimental data points.

supra).[41-47] The very dissimilar behaviors of two flexible MOFs in similar environments prompted us to study their proton conducting properties in detail.

3.3.8. Proton conductivity studies

Proton conductivity measurements of all the MOF samples (**Fe-MIL-53-NH$_2$**, **53-S**, **Fe-MIL-88B-NH$_2$** and **88B-S**) were performed using electrochemical impedance spectroscopy (EIS) employing a two-electrode setup (parallel plate mode). The detailed methodology including instrument setup and sample preparation is provided in section 2.2.3.1, chapter 2. In brief, the MOF microcrystals were powdered and pelletized between two carbon wafers and the corresponding impedance spectra of the pellet were recorded at different temperatures (40 ºC – 80 ºC) and 98% relative humidity (R.H.). The proton conductivities of the MOFs were determined from the high-frequency region of corresponding Nyquist plots by fitting with a suitable equivalent circuit.[48,53,54] The Nyquist plots for all the samples, equivalent circuit and conductivity calculations are provided in appendix 3 (section A3.6).

3.3.8.1. Temperature dependence of proton conductivity

The proton conductivities of the parent MOFs **Fe-MIL-53-NH$_2$** and **Fe-MIL-88B-NH$_2$** were found in the range of 10^{-3} – 10^{-4} S cm^{-1} (Table A3.2 and Table A3.4, Appendix 3), as determined at various temperatures, while keeping the relative humidity (R.H.) constant at 98%. A comparison of the proton conductivities of these parent MOFs, **Fe-MIL-53-NH$_2$** and **Fe-MIL-88B-NH$_2$** and their post-synthetically modified variants **53-S** and **88B-S**, respectively (Figure 3.6), clearly shows the huge enhancement in proton conductivity as a result of the introduction of SO_3H groups in **53-S** and **88B-S**. For example, in case of **Fe-MIL-53-NH$_2$**, the highest conductivity achieved is 1.51×10^{-3} Scm^{-1} (~80 ºC, 98% R. H.), which has increased to 1.298×10^{-2} Scm^{-1} (~80 ºC, 98% R. H.) for **53-S** (Figure 3.6a; see also Figures A3.7- A3.8 and Tables A3.2- A3.3 in Appendix 3); that is, ~10-fold increase in conductivity. Similarly, for **Fe-MIL-88B-NH$_2$**, the conductivity achieved at ~80 ºC and 98% R. H. is 3.36×10^{-3} Scm^{-1}, while for **88B-S**, it is 1.68×10^{-2} Scm^{-1} (Figure 3.6b; see also Figure A3.9- A3.10 and Tables A3.4- A3.5 in Appendix 3), that is, ~5-fold increase in conductivity.

Activation energies (E_a) for proton conduction in the MOFs have been calculated by linear fitting of the corresponding Arrhenius plots constructed from the temperature

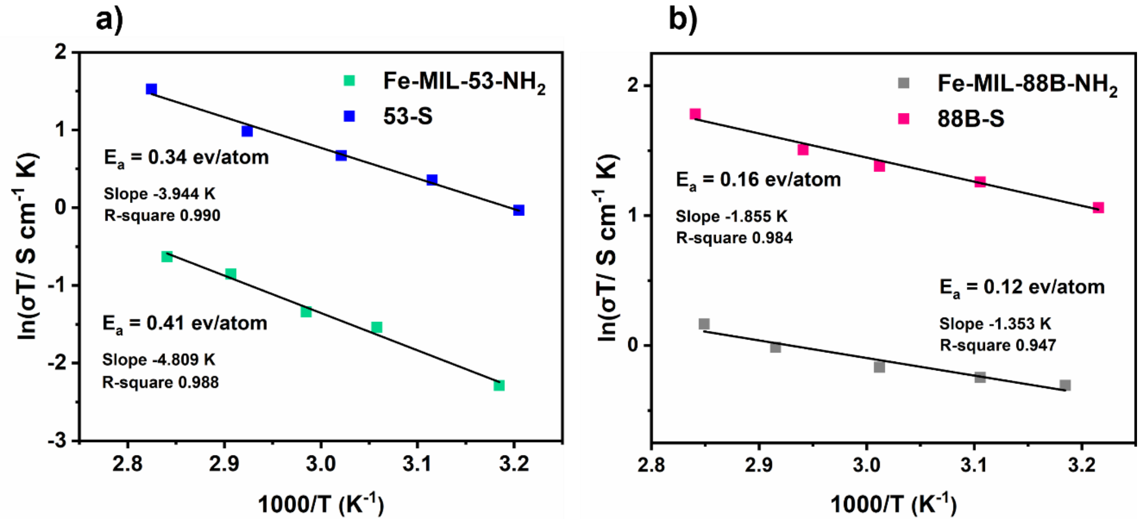

Figure 3.6. Arrhenius plots of proton conductivity for a) **Fe-MIL-53-NH$_2$** and **53-S**, b) **Fe-MIL-88B-NH$_2$** and **88B-S**, at 98% R.H., along with the corresponding activation energies (*E*a), slope of fitted line, and coefficient of determination (R^2).

dependence of proton conductivity values (Figure 3.6); detailed calculation is provided in the appendix 3 (section A3.6). The Arrhenius plots for all the MOFs maintain a good linearity throughout the temperature range of 40 – 80 °C. The corresponding activation energies for **Fe-MIL-53-NH$_2$** (0.41 eV/atom), **53-S** (0.34 eV/atom), **Fe-MIL-88B-NH$_2$** (0.12 eV/atom) and **88B-S** (0.16 eV/atom) show that, proton conduction in all these MOFs occurs by Grotthuss mechanism, predominantly. From Figure 3.6a we find that there is no significant difference in the activation energies for **Fe-MIL-53-NH$_2$** and **53-S**. For **Fe-MIL-88B-NH$_2$** and **88B-S** as well, we find very negligible change in their activation energies (Figure 3.6b). This probably means that the proton conduction pathway in the modified MOFs is similar to that in their corresponding parent MOFs.

3.3.8.2. Humidity dependence of proton conductivity

The proton conductivities of both **53-S** and **88B-S** were found to increase sequentially with increasing humidity (Figure 3.7; Figures A3.11 and A3.12 Appendix 3), which further confirms a water-assisted proton transport in both the MOFs. Of note, the rate of change of conductivity with respect to humidity, is much higher for **53-S** than **88B-S**. This shows that the **88B-S** MOF has higher H-bonded networks than **53-S**, even at a lower humidity, which makes it function as an efficient proton conductor over a wide range of R.H.

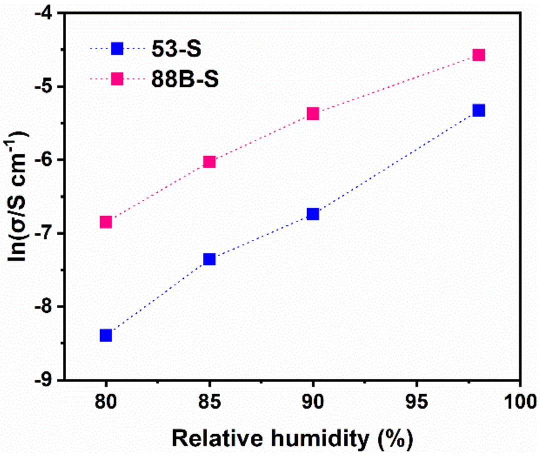

Figure 3.7. Plot of ln(conductivity) versus relative humidity for **53-S** and **88B-S**.

3.3.8.3. *Long term stability test under operational conditions*

Now, for a proton conductor, the efficiency of proton conduction is just as important as the stability of the material under operational conditions. Therefore, we have studied the conductivity of **53-S** (Figure 3.8a**,** see also Figure A3.13) and **88B-S** (Figure 3.8b**,** see also Figure A3.14) pellets for three consecutive heating-cooling cycles, during which, there was very negligible loss in conductivity. After the consecutive heating-cooling cycles, the sample pellets of **53-S** and **88B-S** were powdered and analyzed using PXRD, FT-IR spectroscopy and FESEM. A comparison of the data taken for samples before and after the impedance measurements (Figures A3.15- A3.18, Appendix 3), shows that the structural integrity of the MOFs is well-maintained during the complete process.

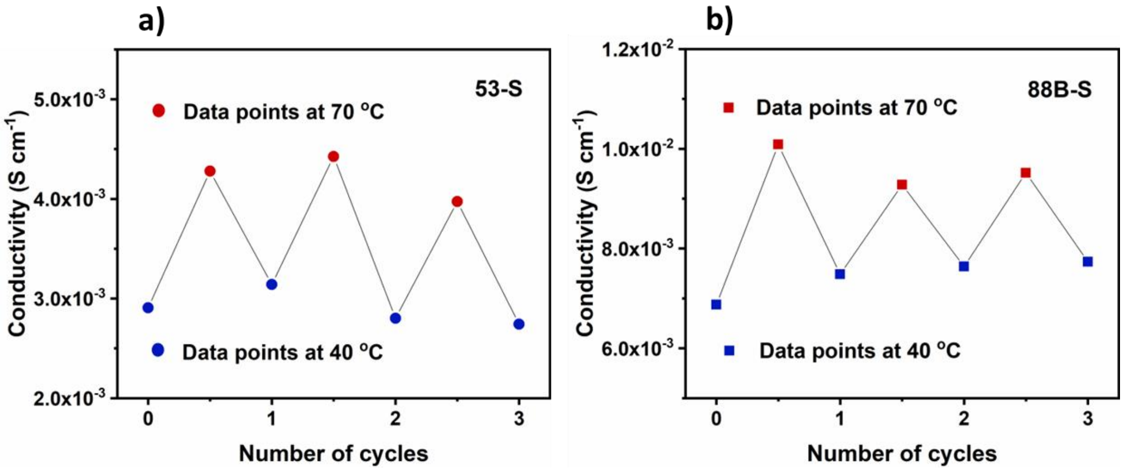

Figure 3.8. Proton conductivity of a) **53-S** and b) **88B-S**, at a constant relative humidity of 98%, during consecutive heating-cooling cycles.

Thus, we find that for both **53-S** and **88B-S**, the post synthetic modification has helped in improving their proton conducting properties to a considerable extent; a 10-fold increase in **53-S** than **Fe-MIL-53-NH$_2$**, and a 5-fold increase in **88B-S** than **Fe-MIL-88B-NH$_2$**. It is important to note in this context that, for **53-S**, the extent of framework modification, or conversion from -NH$_2$ to -NH(CH$_2$CH$_2$CH$_2$SO$_3$H) is only one-third to that of **88B-S**, which means that **53-S** has approximately one-third the number of labile protons in its framework than **88B-S**. But, in spite of it, the extent of enhancement in proton conductivity is much higher than **88B-S**. In the present study, the –SO$_3$H functionalization helps in two-fold ways – a) increasing the number of labile protons in the framework and b) increasing the hydrophilicity of the framework. For **88B-S**, we find that the first factor is dominating, that is, the higher number of labile protons in **88B-S** than **Fe-MIL-88B-NH$_2$** increased its conductivity. Though the **88B-S** MOF has been found to have a more extensive H-bonded network than **Fe-MIL-88B-NH$_2$** (*vide supra*), there has been no improvement with respect to uptake of water molecules in high humidity, probably due to the high flexibility of MOF framework in presence of water molecules. Interestingly, for **53-S**, both the factors played an important role in improving its conductivity. Considering these observations, it can be said that the PSM (post synthetic modification) of the MOFs, **Fe-MIL-53-NH$_2$** and **Fe-MIL-88B-NH$_2$**, does not affect their observable properties in quite the same way, but the introduction of -SO$_3$H functionalities by PSM has unarguably created two stable and highly efficient proton conductors, **53-S** and **88B-S**.

Considering the high proton conductivity of these PSM materials, we have further explored the prospect of fabricating these MOF-based proton conductors as fillers in an organic polymer, resulting in polymer-MOF mixed matrix membranes (MMMs).

3.3.9. PXRD analysis of the membranes

The PXRD patterns of the organic polymer, OPBI [poly(4,4′-diphenylether-5,5′-bibenzimidazole)], post-synthetically modified MOFs, **53-S** and **88B-S**, and their corresponding 5% and 7.5% composite MMMs are shown in Figure 3.9 (a and b). OPBI is amorphous in nature and exhibits a broad signal in the 2θ range of 15° – 35°.[55] On the contrary, the mixed matrix membranes prepared with **88B**-**S** (**5%** and **7.5%**) and **53-S** (**5%** and **7.5%**) show a certain order of crystallinity. Several new intense peaks can be observed in the PXRD patterns of **53-S@OPBI** and **88B-S@OPBI** membranes (Figures 3.9a and

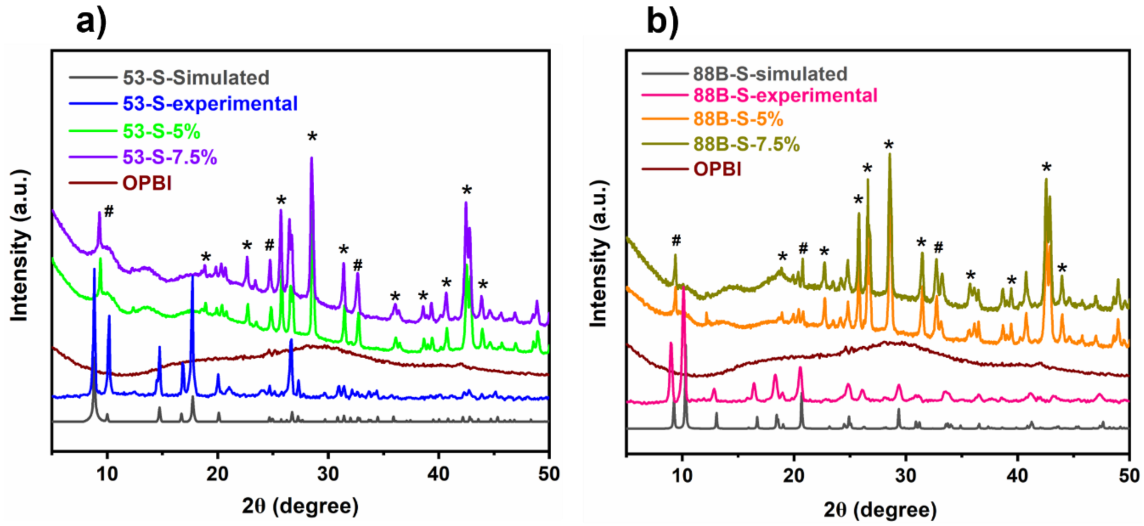

Figure 3.9. (a) PXRD patterns of OPBI, **53-S**, MMMs (**53-S-5%** and **53-S-7.5%**) compared with the simulated PXRD pattern of MIL-53; (b) PXRD patterns of OPBI**, 88B-S**, MMMs (**88B-S-5%** and **88B-S-7.5%**) compared with the simulated PXRD pattern of **MIL-88B**.

3.9b), particularly in the 2θ range of 20º - 45º. These new peaks indicate the generation of crystalline ordering in the MMMs, probably originating from strong interfacial H-bonding interactions between the OPBI polymer matrix and the MOF nanofillers. The presence of the functionalities like primary amines, secondary amines and –SO_3H groups in the MOF gives ample scope of H-bonding with the OPBI polymer. An increase in the intensity of these new peaks while increasing the MOF loading from 5% to 7.5% for both **53-S@OPBI** and **88B-S@OPBI** membranes, further proves the role of MOF nanofillers in modifying the structural arrangement inside the MMMs. Because of the very low loading of MOFs (5% and 7.5%) in the MMMs, their PXRD peaks were found to have been masked by those of the polymer.

The parent MOFs as such were further analysed after treatment with formic acid, using PXRD, FT-IR, FESEM and DLS techniques, and their structural integrity was found to be well maintained during the treatment; detailed discussion has been provided in appendix 3 (Section A3.8).

3.3.10. FT-IR spectral analysis of the membranes

FT-IR spectral analysis of the MOF loaded OPBI membranes further supports the inference drawn from PXRD studies. For both **88B-S** and **53-S** loaded MMMs, the peaks corresponding to the aromatic C-H stretching (3060 cm^{-1}) and aliphatic C-H stretching (2921 cm^{-1}) become more prominent (Figures A3.21 and A3.22, Appendix 3) as compared

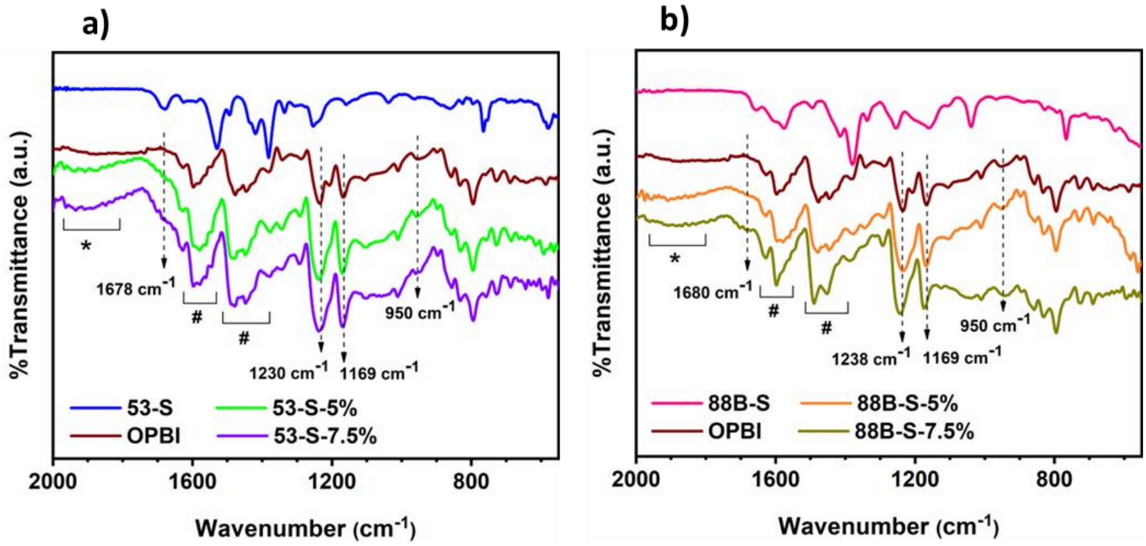

Figure 3.10. (a) ATR-FTIR spectra of **53-S**, OPBI and MMMs (**53-S-5%** and **53-S-7.5%**); (b) ATR-FTIR spectra of **88B-S**, OPBI and MMMs (**88B-S-5%** and **88B-S-7.5%**).

to those of OPBI. The non-hydrogen bonded 'N-H' groups of OPBI (3413 cm^{-1}) show decreased peak intensity in the MOF loaded composite membranes. For **88B-S-7.5%** and **53-S-7.5%** membranes, the 'N-H' peak vanishes entirely indicating the formation of strong interactions between polymer and MOF functionalities through the involvement of H-bonding between the free 'N-H' groups of **OPBI** and the dangling '$-SO_3H$' and amine functionalities of the MOF nanofillers. Here we also found an increase in the intensity of O-H stretching band in going from OPBI to MMMs (Figures A3.21 and A3.22, Appendix 3) which indicates an increase in the number of water molecules present in the membrane matrix and their participation in H-bonding. Due to such interactions present in the MMMs, few positional shifting of peaks along with appearance of new peaks can be observed (Figure 3.10a and 3.10b). For example, a new peak at ~1680 cm^{-1} and around 1800 cm^{-1} (marked with *) can be observed for both **88B-S** and **53-S** loaded membranes and the intensity of these peaks increased from 5% to 7.5% loaded membranes. An increase in intensity of the peaks and spectral broadening can be observed at around 950 cm^{-1}, 1169 cm^{-1} and 1230-1238 cm^{-1} in the IR spectra of both the **53-S** and **88B-S** based MMMs. Especially, the peaks of OPBI, situated in the range of 1440-1480 cm^{-1} (in plane benzimidazole ring deformation) and in the range of 1580-1620 cm^{-1} (C=C/C=N stretching)[56-58] are found to be markedly changed in case of both **53-S** and **88B-S** based MMMs (marked #; Figure 3.10a and 3.10b). Thus, from the analysis of FT-IR spectra, it can be confirmed that there is significant interaction between the MOFs (nanofillers) and the polymer giving rise to the new crystalline planes which are also observed in the PXRD plots of fabricated MMMs.

3.3.11. FESEM, AFM and HR-TEM image analysis of the membranes

The surface and cross-sectional morphology of the filler loaded MMMs have been analyzed using FESEM imaging technique and are found to have entirely different morphology compared to pristine OPBI membrane. Unlike OPBI, the **53-S-7.5%** membrane exhibits sponge like layered morphology with homogeneous dispersion of **53-S** MOF nanofillers all over the membrane cross-section (Figure 3.11b). For **88B-S-7.5%** membrane, dense fibrillar network type morphology with impregnation of MOF nanofillers into the porous cross-sectional region is observed (Figure 3.11c). The altered morphology is a direct consequence of the interactions present between the OPBI polymer and the **53-S** / **88B-S** MOFs. This kind of morphology contributes significantly towards the reinforcement of a

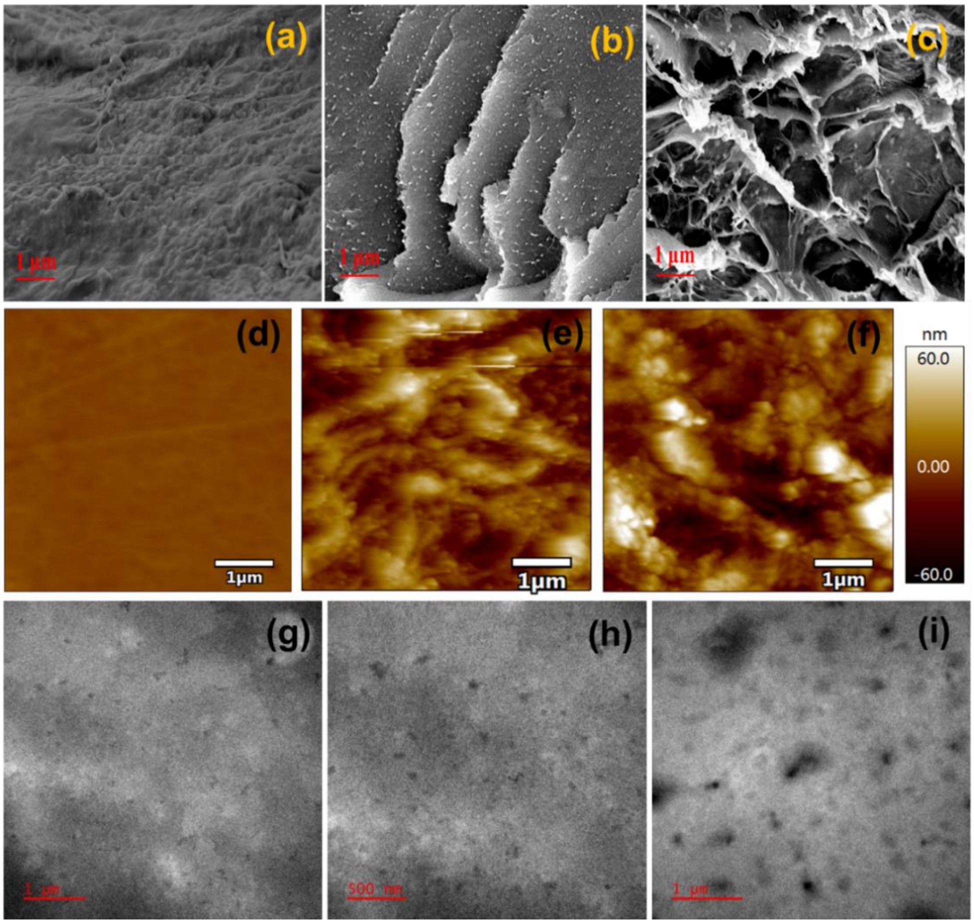

Figure 3.11. (a) Cross-sectional FESEM morphology of pristine OPBI, (b) **53-S-7.5%**, and (c) **88B-S-7.5%** MMMs. (d) AFM surface topology of OPBI (e) **53-S-7.5%,** and (f) **88B-S-7.5%** membranes. (g, h) TEM images of **53-S-7.5%,** (i) TEM images of **88B-S-7.5%** membrane.

membrane's thermal, mechanical, and tensile properties.[16] The surface morphology of **53-S-7.5%** and **88B-S-7.5%** membranes were also analyzed by FESEM (see Appendix 3, Figure A3.23) where the dispersion of MOF nanofillers over the membrane surface can be observed. The 2D surface topology of the MMMs was further investigated by atomic force microscopy (AFM) imaging. Here as well, the uniform dispersion of MOF fillers all over the membrane surface is observed along with the generation of bright and dark areas on the membrane's surface (Figure 3.11d- 3.11f) which represents the hydrophilic and hydrophobic regions,respectively owing to the presence of hydrophilic MOFs in the MMMs.[59,60] Unlike OPBI, the surface roughness is also found to have been increased in the MOF loaded MMMs (Figure A3.24, Table A3.6, Appendix 3) – an important factor for reinforcement of the mechanical properties in the MMMs.[61]

From transmission electron microscopy (TEM) images as well, we can observe the uniform distribution of MOF nanofillers in the dense polymeric network of **53-S-7.5%** and **88B-7.5%** (Figure 3.11g- 3.11i). The observed morphology is the result of strong H-bonding that are generated by the interactions of the functionalities present on the MOF framework (primary amines, secondary amines and hydrophilic –SO_3H groups) and the imidazole groups of OPBI polymer. Such interactions lead to the generation of new crystalline ordering as observed from the PXRD patterns of the MMMs.[62]

3.3.12. TGA of the membranes

The thermogravimetric (TG) traces for OPBI, **88B-S@OPBI and 53-S@OPBI** membranes are given in the Figure 3.12a and the magnified portion in the temperature range 400 ºC - 700 ºC is shown in the Figure A3.25a (Appendix 3). The first step of weight loss occurs at 200 ºC due to the loss of H-bonded water molecules in all the cases. The degree of weight loss at 200 ºC in case of the **53-S@OPBI** and **88B-S@OPBI** membranes is much more compared to OPBI may be because of higher water content in the membranes because of the presence of MOF nanofillers with hydrophilic –SO_3H functionalities. The next step of weight loss is observed around 350 ºC – 400 ºC for MMMs which corresponds to the decomposition of organic moieties present in the MOFs. Degradation of the polymeric backbone occurred beyond 550 ºC. [50,55]

The TG traces for PA doped OPBI, **88B-S-7.5%** and **53-S-7.5%** membranes are shown in Figure 3.12b and Figure A3.25b, appendix 3 [magnified TGA plot (100 ºC - 400

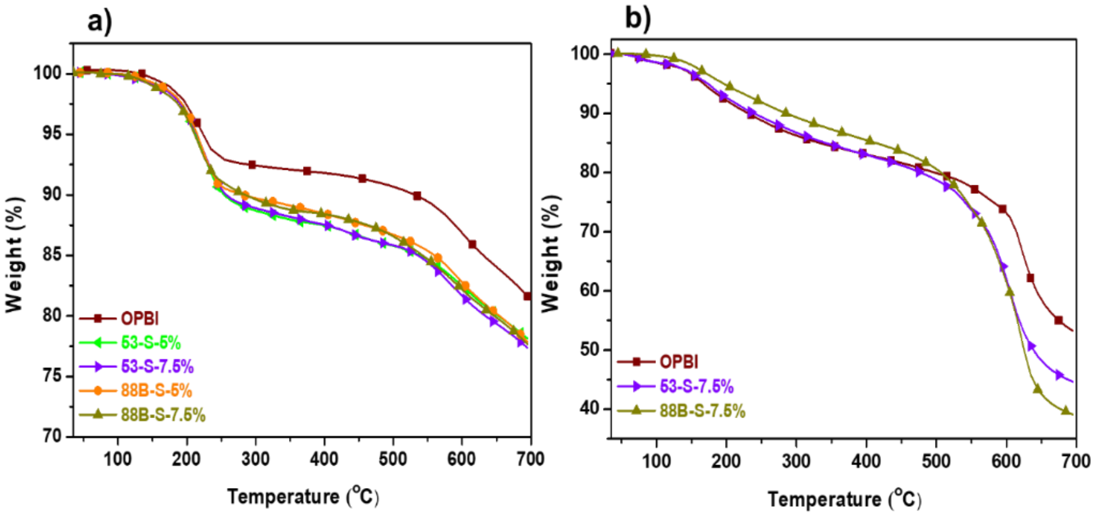

Figure 3.12. TGA plots of (a) OPBI, **53-S** and **88B-S** MMMs, and (b) PA doped OPBI, **53-S-7.5%** and **88B-S-7.5%** membranes.

°C)]. The first weight loss step for all the PA doped membranes is observed between 100 – 200 °C due to the evaporation of absorbed moisture in them.[55,63] This is followed by a constant and gradual weight loss up to 550 °C possibly due to the gradual evaporation of PA or its self-condensation.[16] Beyond 550 °C, all the membranes show a huge weight loss corresponding to the degradation of the polymer backbone. The total amount of weight% lost at 700 °C is highest for **88B-S-7.5%** followed by **53-S-7.5%** and then pristine OPBI membrane which correlates with the amount of PA doping in these membranes – pristine OPBI < **53-S-7.5%** < **88B-S-7.5%**. Here it is interesting to note that though **88B-S-7.5%** had the highest PA loading, the amount of its weight lost in the temperature range of 100 – 400 °C (Figure A3.25b, Appendix 3) was also the least. Similar observations are found for **53-S-7.5%** which also showed slightly less weight loss compared to OPBI in the above-mentioned temperature range. This indicates that the MMMs not only have higher PA loading level but also a higher PA retention capacity than pristine OPBI over a wide range of temperature. The reason behind the exceptional PA loading and its retention even at high temperatures is probably due to the generation of strong H-bonding interactions involving the PA molecules, the –SO_3H groups, primary and secondary amines of the MOFs along with the imidazole –N= and –NH functionalities of the OPBI as shown in Scheme A3.1 (Appendix 3).

3.3.13. Water uptake (WU), ion exchange capacity (IEC), swelling ratio (SWR) and PA loading level of the membranes

The WU, ion exchange capacity (IEC), PA doping level, SWR in water and in PA for all the MMMs and pristine OPBI membrane are given in the Table 3.1 and appendix 3, Table A3.7; and the detailed experimental procedures of all these measurements are provided in section 3.2.3.1. The WU capacity for all the MMMs is found to be significantly superior to that of OPBI. Moreover, with an increase in the MOF filler loading level in the membranes from 5% to 7.5%, there is a gradual increase in their WU capacity (Table 3.1). **88B-S-7.5%** shows slightly higher WU (18.09 wt.%) than **53-S-7.5%** (16.86 wt%), which may be due to the presence of higher number of hydrophilic −SO_3H functionality in the former. The ion exchange capacity (IEC) of all the MOF@OPBI composites were found to be superior compared to OPBI, and the IEC of the MMMs increases with increasing MOF loading (Table A3.7, Appendix 3). The SWR of the **53-S@OPBI** and **88B-S@OPBI** MMMs follow a decreasing trend with increasing MOF loading in the membranes. The swelling ratios for **88B-S-7.5**% and **53-S-7.5%** in water are 2.38 and 1.89 wt%, respectively, and in PA are 2.23 and 1.66 wt%, respectively, which are much lower than the SWR of pristine OPBI membrane (in water 4.27 wt% and in PA 6.07 wt%). The lower swelling in case of MMM samples may be because of the strong H-bonding interactions already present in the composite polymer matrix which probably does not allow the PA molecules to break these

Table 3.1. Water uptake (WU), swelling ratio (SWR) in water and in PA, PA doping level of all the MMMs, pristine OPBI and **88B-7.5%** membranes [a]

Sample name	*Water uptake (wt%)*	*Swelling ratio in water (%)*	*Swelling ratio in PA (%)*	*PA loading (no. of mol/PBI r.u.)*
OPBI	11.48 (1.59)	4.27 (1.18)	6.07 (1.31)	15.88 (2.47)
53-S-5%	14.07 (0.87)	2.09 (0.61)	1.84 (0.37)	23.74 (1.33)
53-S-7.5%	16.86 (0.79)	1.89 (0.47)	1.66 (0.25)	25.24 (1.09)
88B-S-5%	15.27 (1.03)	2.77 (0.81)	2.32 (0.54)	26.75 (1.76)
88B-S-7.5%	18.09 (1.12)	2.38 (0.59)	2.23 (0.47)	27.71 (1.44)
88B-7.5%	-	-	2.11 (1.14)	20.65 (1.37)

[a] The numbers in the bracket are standard deviations obtained from the experiments.

interactions and penetrate inside the bulk of the membrane to cause swelling. The PA doping level for OPBI is 15.88 mol/repeat unit which increases with increasing amount of MOF loading in the membranes (Table 3.1). For **53-S@OPBI** and **88B-S@OPBI** doped membranes, the highest degree of PA loading is achieved for **53-S-7.5%** (25.24 mol/repeat unit) and **88B-S-7.5%** (27.71 mol/repeat unit), respectively. Such an increase with respect to that of pristine OPBI can be a cumulative effect of several contributing factors: (a) with increased loading of **53-S** and **88B-S** MOFs in the OPBI polymer network, more functional groups become available for H-bonding with the PA molecules as depicted in Scheme A3.1 (Appendix 3), (b) due to the presence of the strong interactions between the MOF nanofillers and OPBI polymer backbone, a regular pattern and ordering are created in the composite as also observed in PXRD analysis. The spaces, thus formed between the polymer chains due to these interactions, might take up a significant amount of PA.[64] Here it is noteworthy that the absorbed PA molecules exert a plasticizing effect on the MMMs which affect the original crystalline ordering in the polymer matrix. It is caused due to partial breakage of the pre-existing H-bonds along with generation of new H-bonds involving the $-SO_3H$ and N-H groups of the composite and the newly absorbed PA molecules.[65] And finally porous fibrillar morphology (as observed from the FESEM images of the membrane cross-section) might also have contributed towards higher uptake of PA than pristine OPBI. As a test to validate this argument, we have even studied the PA doping level of a MMM named 88B-7.5% which was prepared using unmodified **Fe-MIL-88B-NH$_2$** as nanofillers. And as expected, due to the absence of $-SO_3H$ functionality on the MOF nanofillers, it resulted in a much lower PA loading [20.65 mol/repeat unit (r.u.)] in 88B-7.5% as compared to **88B-S-7.5%**. This observation signifies the important role of $-SO_3H$ group containing side arms in the post-synthetically modified MIL-MOFs in increasing the PA loading of their respective MMMs.

3.3.14. Proton conductivity studies of the membranes

Proton conductivity studies were carried out for all the PA loaded MMMs and pristine OPBI using electrochemical impedance spectroscopy employing a four-electrode setup; the detailed experimental procedure is given in section 3.2.3.3. The impedance measurements were carried out in the temperature range of 30 ºC – 160 ºC under anhydrous conditions. The proton conductivity values for all the membranes were calculated from their corresponding Nyquist plots after fitting the experimental data with the appropriate equivalent circuit (for details, see section A3.10, Figure A3.26, Appendix 3).

All the PA doped MMMs are found to have superior proton conductivity than PA doped OPBI membrane. OPBI itself has a conductivity of 0.065 S cm^{-1} at 160 °C while **53-S-5%** and **53-S-7.5%** membranes display conductivity of 0.207 S cm^{-1} and 0.253 S cm^{-1}, respectively at 160 ºC (Figure 3.13a; Tables A3.8 and A3.10, Appendix 3). , Proton conductivity values of 0.244 S cm^{-1} and 0.304 S cm^{-1} are obtained at 160 ºC for **88B-S-5%** and **88B-S-7.5%** membranes (Figure 3.13a; Tables A3.9-A3.10, Appendix 3). The conductivity of **88B-S-7.5%** is the highest among all the MMMs and a significant ~5-fold increase compared to OPBI. The considerable increase in the proton conductivity of the MMMs than its parent OPBI is a result of the higher water uptake capacity and improved PA loading and retention capacity of the MMMs. Similarly, the slightly higher PA loading in the **88B-S-7.5%** membrane than the **53-S-7.5%** membrane might have been the primary reason behind the observed higher proton conductivity of the former. We have even studied the proton conducting properties of PA doped 88B-7.5% membrane (prepared using unmodified **Fe-MIL-88B-NH$_2$** as nanofillers) to understand the effect of the absence of $-SO_3H$ functionalities in the membrane matrix. And as expected, the proton conductivity for 88B-7.5% membrane (0.151 Scm^{-1} at 160 ºC) is found to be significantly lower than the proton conductivity of **88B-S-7.5%** membrane (0.304 S cm^{-1}) under identical experimental conditions. In fact, it is lower than all the **53-S** and **88B-S** MMMs. Thus, it can be inferred

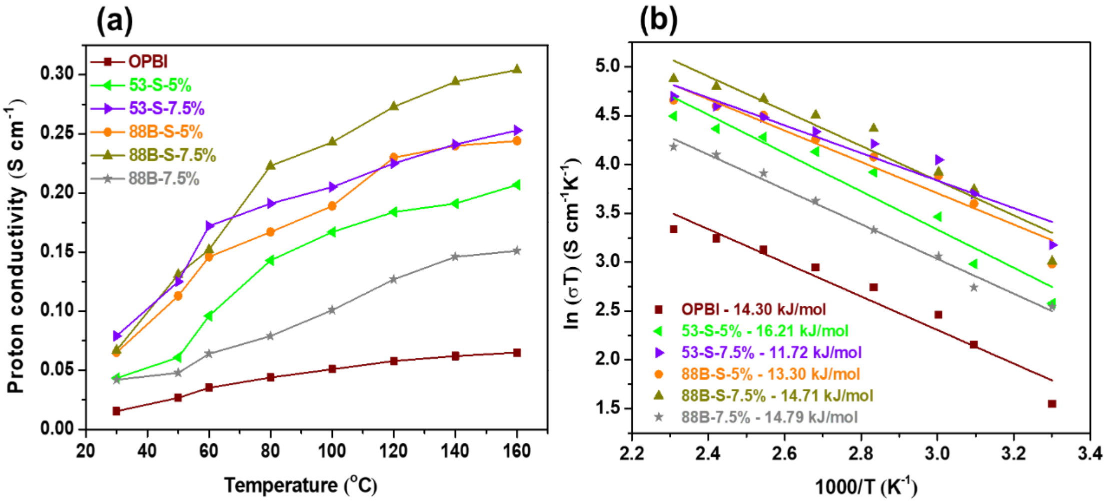

Figure 3.13. (a) Proton conductivity values of OPBI, **53-S** and **88B-S** loaded MMMs along with **88B-7.5%** membrane. (b) Arrhenius activation energy plot of OPBI and the MMMs.

that the presence of larger amount of hydrophilic $-SO_3H$ functionalities in the **88B-S** MOF over **53-S** has improved proton conductivity for **88B-S@OPBI** MMMs. Higher number of '$-SO_3H$' functionalities help in creating efficient hydrophilic ion channels which enables higher PA loading and thereby superior proton conduction. **88B-S-7.5%** and **53-S-7.5%** membranes were studied for isothermal proton conductivity measurement at 160 ^oC for 36 h. Section A3.11, Figure A3.27 (Appendix 3) summarizes the observations obtained from isothermal proton conductivity studies and shows that the MMMs can act as efficient and stable proton conductors for a prolonged period. The activation energy (E_a) of proton conduction for all the membranes was calculated from the Arrhenius plots (Figure 3.13b). The E_a values for all the samples ranges from ~11 – 16 kJ/mol (0.11 – 0.15 eV/atom) which signifies that proton conduction associated with the membranes occurs predominantly through Grotthuss mechanism. The PA molecules hydrogen bonded with the OPBI polymer and the functional groups on the MOF nanofillers, facilitate the proton hopping through the matrix and therefore, the MMMs display efficient proton conduction.[66] The Arrhenius plots also show slight deviations from linearity especially in the lower temperature suggesting that the proton conduction might have been partly contributed via vehicular mechanism performed by the PA molecules through diffusion of proton among the MOF particles present in the polymer matrix, in addition to prevalent Grotthuss mechanism.[55,67]

So, in our present work we have been successful in preparing new sets of composite membranes which have almost 4-5 times enhanced proton conductivity than that of pristine OPBI, and these MMMs can function as efficient proton exchange membranes (PEMs) for a prolonged period of time. But for a PEM to be useful for practical purposes, it needs to be robust and durable as well. For that we have done a detailed study of the thermomechanical properties of the MMMs, and their PA leaching analysis as described in the following sections.

3.3.15. Thermomechanical properties of the membranes

3.3.15.1. Storage modulus (E')

Temperature responsive storage modulus (E′) plots for all the MMMs and pristine OPBI membrane were obtained using dynamic mechanical analyzer (DMA). The stability of all the composite membranes was found to be superior to that of OPBI (Figure 3.14a). The corresponding storage moduli values at 100 ^oC and 400 ^oC for all the membranes are tabulated in Table A3.11 (Appendix 3). The storage modulus of the MMMs were found to increase proportionally with increasing loading (wt%) of MOF fillers in them. In fact, the storage modulus of **88B-S-7.5%** and **53-S-7.5%** are much higher than that of OPBI at both 100 ºC and 400 ºC. Such an increase in the stability of the MMMs is a cumulative result of (i) homogeneous dispersion of the MOF nanofillers throughout the polymer matrix as evident from FESEM, AFM and TEM analysis, (ii) largely altered cross-sectional morphology (Figure 3.11) and (iii) generation of certain crystalline ordering in the composite matrix. In other words, the homogeneous dispersion of MOF nanofillers in the OPBI network of the MMMs generated strong and uniform MOF-polymer interactions which helped in creating reinforcement effect in the composite. Here it is noteworthy to mention that the **88B-S7.5%** membrane exhibits slightly higher storage modulus than that of the **53S-7.5%** membrane. Between **88B-S-5%** and **53S-5%** membranes, the **53S-5%** membrane has slightly higher storage modulus than that of **88B-S-5%**, above 275 °C. The high storage modulus values of the fabricated MMMs makes them superior candidates for high temperature PEMs. The glass transition temperature (T_g) obtained from the DMA Tan δ plot is given in Figure A3.28, Section A3.16 (Appendix 3). The oxidative stability of the fabricated mixed matrix membranes has been measured by treating the membranes with Fenton’s reagent at elevated temperature for a prolonged 100 h. The detailed experimental procedure and results obtained from the oxidative stability analysis are given in the appendix 3 (Figure A3.29, Section A3.17). The oxidative stability data clearly demonstrate the higher chemical stability of the composite membrane compared to that of pristine OPBI.

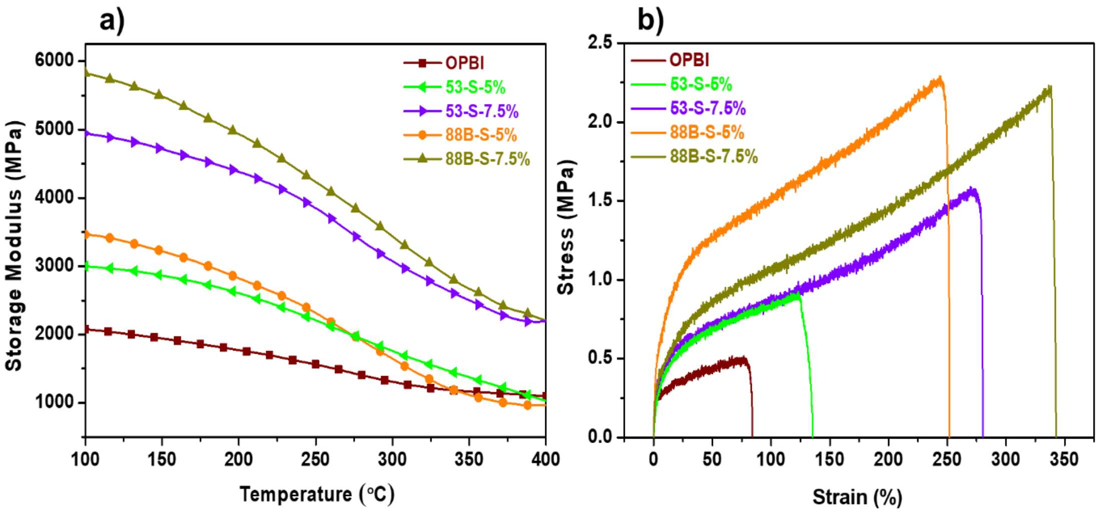

Figure 3.14. (a) Storage modulus data of OPBI and composite MMMs. (b) Stress−strain profile of PA loaded OPBI, MMMs.

3.3.15.2. Tensile stress-strain profile

The tensile stress-strain profiles for all the PA doped MMMs along with PA doped OPBI are given in the Figure 3.14b and also the tensile stress (MPa) and elongation at break (%) values of all the membranes obtained from these plots are tabulated in the Table A3.12. Here as well, all the MMMs show better stress-strain profile than OPBI due to the same factors responsible for their superior storage modulus, as discussed in the preceding section. With increasing MOF loading from 5% to 7.5%, the tensile stress values of the composites are found to be slightly decreased with noteworthy increment in the elongation at break value. The reason behind such observation can be attributed to the partially affected acid-base interactions between the imidazole N-H of OPBI and the dangling hydrophilic $-SO_3H$ groups of MOF after the introduction of PA molecules in the membrane. This phenomenon is well-known as the plasticizing effect of PA molecules on the PA doped membranes.[65,68] Tensile properties of **88B-S@OPBI** membranes are also found to be better than **53-S@OPBI** membranes.

3.3.16. PA leaching analysis of the PA doped membranes

In order to check the PA retention efficiency of the PEMs, acid leaching analysis was performed with the PA doped MMMs and the obtained results are provided in the Figure 3.15a. OPBI membrane as such is not good at holding PA in its matrix and loses around 43.9% of PA in the first hour of leaching experiment which increases to 65% and 70.7% after the 2nd and 3rd hour, respectively. On the contrary, the MMMs are found to be very efficient in retaining the PA under similar experimental conditions. Moreover, the PA retention capacity of the membranes are also found to be increased with increasing MOF content in the MMMs. **53-S-5%** and **88B-S-5%** membranes show a weight loss of 30.63% and 23.89%, respectively after 3 h of exposure to the water vapor, while **53-S-7.5%** and **88B-S-7.5%** membranes showed a 22.3% and 18.34% loss of their initial weight after 3 h of leaching experiment. Here as well, we find that the **88B-S** MOF loaded MMMs are better than **53-S** loaded MMMs with respect to retention of PA. The higher retention capacity of PA in the membranes is directly linked to the amount of H-bonding the PA molecules have with the rest of the polymer, and sulfonic acid groups, primary and secondary amines of MOF. The PA leaching in 88B-7.5% MMM is 40.35% of its initial weight after 3 h of leaching test which is much higher compared to **88B-S-7.5%** MMM owing to the absence of $-SO_3H$ groups in the former.

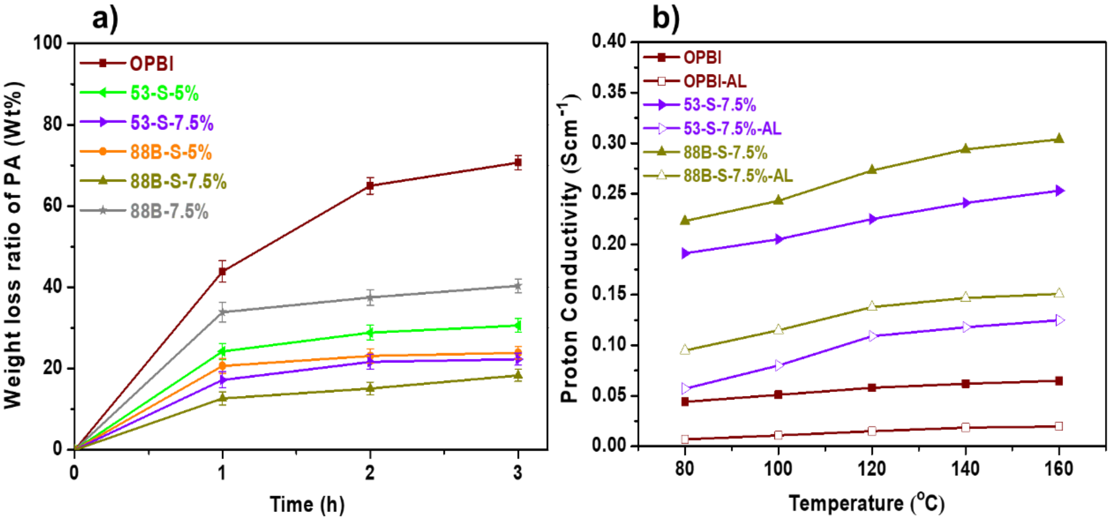

Figure 3.15. (a) PA leaching study of OPBI, MMMs of **53-S** and **88B-S** along with **88B-7.5%** membrane for 3 h. (b) Proton conductivity of post PA leached OPBI, **53-S** and **88B-S** MMMs in comparison with fresh samples proton conductivity. AL in the figure signifies after leaching data.

The superior PA retention ability of the MOF loaded membranes are also confirmed by post PA leaching proton conductivity studies. After performing the PA leaching experiments, the surface of the membranes was wiped out to remove any moisture or PA on it. Then the conductivity of the membranes was measured from 80 ºC to 160 ºC under anhydrous condition and compared with the conductivity results obtained with freshly PA doped membranes (Figure 3.15b). The PA leached **88B-S-7.5%-AL** and **53-S-7.5%-AL** (AL stands for after leaching) membranes have a proton conductivity value of 0.151 S cm^{-1} and 0.125 S cm^{-1}, respectively, at 160 ºC, which is significantly high compared to the proton conductivity of OPBI-AL (0.0198 S cm^{-1}). These experimental findings convey the importance of using MOFs as nanofillers in the MMMs which helps in modulating various chemical and physical properties of the membrane, thereby improving its all-round performance as a PEM. The use of post synthetic modification on the **MIL-53** and **MIL-88B** MOFs further helps to enrich the MOF surface with acidic −SO_3H groups which, in turn, helps in building extensive H-bonded networks in the MMMs. This helps in increasing the proton conduction in the MMMs further.

Comparison of the current results with previous literature reports

We have made an effort to provide a brief literature survey by comparing the results obtained in this work with previous reported works in this field. We have compared the proton conductivity values of the synthesized flexible MOFs (**53-S** and **88B-S**) in the present work with the other flexible MOF based proton conductors in the relevant literature (see Appendix 3: Section A3.18, Table A3.13), which highlights the role of post synthetic modification in creating better MOF-based proton conductors. The prepared MMMs (**88B-S-7.5%** and **53-S-7.5%**) in this work are also found to function as efficient PEMs and are among the best with respect to various other MOF-based MMMs reported in the literature (see Appendix 3: Section A3.18, Table A3.14).

3.4 CONCLUSIONS

The present work endeavors to explore the role of post-synthetic modification (PSM) to introduce new functionalities in two flexible MIL MOFs – **Fe-MIL-53-NH$_2$** and **Fe-MIL-88B-NH$_2$**. We could successfully modify the primary amine (-NH$_2$) functionalities present on the framework of both the MOFs and replace them with -NH(CH$_2$CH$_2$CH$_2$SO$_3$H). Due to the slightly larger pore volume and higher framework flexibility of MIL-88B than MIL-53 in general, it helped in obtaining higher functionalization of the **Fe-MIL-88B-NH$_2$** framework and overall better proton conductivity. For both the MOFs, PSM increased the amount of H-bonded network within the framework; for **Fe-MIL-53-NH$_2$**, it further helped to increase its water-uptake capacity. The MOFs thus formed after PSM - **53-S** and **88B-S**, are characterized with much more efficient and stable proton conducting properties than their parent MOFs. Since MOFs as such are difficult to be directly used for practical application, we have even prepared mixed matrix membranes (MMMs) of **53-S** and **88B-S** MOFs by blending them with an organic polymer OPBI. The prepared MMMs perform as efficient proton conductors under anhydrous conditions when doped with phosphoric acid (PA). These MMMs not only function as efficient proton exchange membranes but are also very stable and durable, having good thermo-mechanical and tensile properties in addition to having good PA retention capacity. All the MMMs studied in this work, **53-S (-5%** and **-7.5%)** and **88B-S (-5%** and **-7.5%)** came about as much improved proton conductors than the pristine OPBI membrane without any filler loading. The reason for such an outcome is the extensive network of interactions generated between the MOF nanofillers and the polymer. This highlights the importance of post synthetic modification on the MIL-53 and MIL-88B MOFs in improving the performance of the MMMs further. This work showcases the synthesis of post synthetically modified super proton conducting flexible MOFs and their role as nanofillers in MMMs in order to modulate various chemical and physical properties of the membrane and thereby improving its all-round performance as a PEM.

Appendix 1: Instrumental details and sample preparation.

Appendix 3: Results and discussions on data obtained for the characterization of MOFs and membranes; a brief literature survey.

3.5 REFERENCES

1. Sun, X.; Liu, S.; Zhang, S.; Dang, T.; Tian, H.; Lu, Y.; Liu, S. High Proton Conductivity Achieved by the Self-Assembly of POM Based Acid−Base Adduct in SBA-15 over a Wide Range from −40 to 85 °C. *ACS Appl. Energy Mater.* **2020**, *3*, 1242–1248.
2. Colomban, P. Proton conductors and their applications: A tentative historical overview of the early researches. *Solid State Ionics* **2019**, *334*, 125–144.
3. Ye, Y.; Gong, L.; Xiang, S.; Zhang, Z.; Chen, B. Metal–Organic Frameworks as a Versatile Platform for Proton Conductors. *Adv. Mater.* **2020**, *32*, 1907090.
4. Otake K.; Kitagawa, H. Control of Proton-Conductive Behavior with Nanoenvironment within Metal–Organic Materials. *Small* **2021**, *17*, 2006189.
5. Ramaswamy, P.; Wong N. E.; Shimizu, G. K. H. MOFs as proton conductors – challenges and opportunities. *Chem. Soc. Rev.* **2014**, *43*, 5913–5932.
6. Biradha, K.; Goswami, A.; Moi, R.; Saha, S. Metal-Organic Frameworks as Proton Conductors: Strategies for Improved Proton Conductivity. *Dalton Trans.* **2021**, *50*, 10655–10673.
7. Li, A-L.; Gao, Q.; Xu, J.; Bu, X-H. Proton-conductive metal-organic frameworks: Recent advances and Perspectives. *Coord. Chem. Rev.* **2017**, *344*, 54–82.
8. Liu, R.; Wang, D-Y.; Shi, J-R.; Li, G. Proton conductive metal sulfonate frameworks. *Chem. Rev.* **2021**, *431*, 213747.
9. Lim, D-W.; Kitagawa, H. Rational strategies for proton-conductive metal–organic frameworks. *Chem. Soc. Rev.*, **2021**, *50*, 6349–6368.
10. Chen, X.; Li, G. Proton conductive Zr-based MOFs. *Inorg. Chem. Front.* **2020**, *7*, 3765–3784.
11. Liu, S-S.; Liu, Q-Q.; Huang, S-Z.; Zhang, C.; Dong, X-Y.; Zang, S-Q. Sulfonic and phosphonic porous solids as proton conductors. *Coord. Chem. Rev.* **2022**, *451*, 214241.
12. Huang, S-Z.; Liu, S-S.; Zhang, H-j.; Han, Z.; Zhao, G.; Dong, X-Y.; Zang, S-Q. Dual-Functional Proton-Conducting and pH-Sensing Polymer Membrane Benefiting from a Eu-MOF. *ACS Appl. Mater. Interfaces* **2020**, *12*, 28720−28726.
13. Escorihuela, J.; Narducci, R.; Compañ, V.; Costantino, F. Proton Conductivity of Composite Polyelectrolyte Membranes with Metal-Organic Frameworks for Fuel Cell Applications. *Adv. Mater. Interfaces* **2019**, *6*, 1801146.
14. Liu, Y-R.; Chen, Y-Y.; Zhuang, Q.; Li, G. Recent advances in MOFs-based proton exchange membranes. *Coordination Chemistry Reviews,* **2022**, *471*, 214740.
15. Feng, L.; Hou, H. B.; Zhou, H. UiO-66 Derivatives and Their Composite Membranes for Effective Proton Conduction. *Dalton Trans.* **2020**, *49*, 17130–17139.
16. Mukhopadhyay, S.; Das, A.; Jana, T.; Das, S. K. Fabricating a MOF Material with Polybenzimidazole into an Efficient Proton Exchange Membrane. *ACS Appl. Energy Mater.* **2020**, *3*, 7964–7977.
17. Koo, W-T.; Jang, J-S.; Kim, I-D. Metal-Organic Frameworks for Chemiresistive Sensors. *Chem* **2019**, *5*, 1938−1963.
18. Lustig, W. P.; Mukherjee, S.; Rudd, N. D.; Desai, A. V.; Li, J.; Ghosh, S. K. Metal–organic frameworks: functional luminescent and photonic materials for sensing applications. *Chem. Soc. Rev.* **2017**, *46*, 3242−3285.
19. Dhakshinamoorthy, A.; Li, Z.; Garcia, H. Catalysis and photocatalysis by metal organic frameworks. *Chem. Soc. Rev.* **2018**, *47*, 8134—8172.
20. Mukhopadhyay, S.; Basu, O.; Nasani, R.; Das, S. K. Evolution of metal organic frameworks as electrocatalysts for water oxidation. *Chem. Commun.* **2020**, *56*, 11735−11748.
21. Li, H-Y.; Zhao, S-N.; Zang, S-Q.; Li, J. Functional metal–organic frameworks as effective sensors of gases and volatile compounds. *Chem. Soc. Rev.* **2020**, *49*, 6364−6401.

22. Yang, S.; Li, X.; Zeng, G.; Cheng, M.; Huang, D.; Liu, Y.; Zhou, C.; Xiong, W.; Yang, Y.; Wang, W.; Zhang, G. Materials Institute Lavoisier (MIL) based materials for photocatalytic Applications. *Coord. Chem. Rev.* **2021**, *438,* 213874.
23. Ponomareva, V. G.; Kovalenko, K. A.; Chupakhin, A. P.; Dybtsev, D. N.; Shutova, E. S.; Fedin, V. P. Imparting High Proton Conductivity to a Metal−Organic Framework Material by Controlled Acid Impregnation. *J. Am. Chem. Soc.* **2012**, *134*, 15640−15643.
24. Zhang, W.; Lu, Y.; Zhang, S.; Dang, T.; Tian, H.; Zhong, Z.; Liu, S. Proton conductors with wide operating temperature domains achieved by applying a dual-modification strategy to MIL-101. *Dalton Trans*. **2021**, *50*, 18053–18060.
25. Ru, C.; Gu, Y.; Na, H.; Li, H.; Zhao, C. Preparation of a Cross-linked Sulfonated Poly(arylene ether ketone) PEM with Enhanced Proton Conductivity and Methanol Resistance by Introducing Ionic Liquid Impregnated MOF. *ACS Appl. Mater. Interfaces* **2019**, *11*, 31899–31908.
26. Zheng, X.; Zhao, X.; Huang, J.; Yang, H.; Wang, Q.; Liu, Y.; Gong, P.; Tian, L.; Xiao, H.; Liu, Z. Proton conductivity study on three CS/IL@fle-MOF membranes. *Appl Organomet Chem.* **2020**, *34*, e5981.
27. Liu, J.; Zou, X,; Liu, C.; Cai, K.; Zhao, N.; Zheng, W.; Zhu. G. Ionothermal synthesis and proton-conductive properties of NH_2-MIL-53 MOF nanomaterials. *CrystEngComm*, **2016**, *18*, 525–528.
28. Ponomareva, V. G.; Aliev, S. B.; Shutova, E. S.; Pishchur, D. P.; Dybtsev D. N.; and Fedin, V. P. Materials with high proton conductivity above 200 ºC based on a nanoporous metal–organic framework and non-aqueous ionic media. *RSC Adv*. **2017**, *7*, 403–407.
29. Shigematsu, A.; Yamada, T.; Kitagawa, H. Wide Control of Proton Conductivity in Porous Coordination Polymers. *J. Am. Chem. Soc*. **2011**, *133*, 2034–2036.
30. Qiu, M.; Wu, H.; Cao, L.; Shi, B.; He, X.; Geng, H.; Mao, X.; Yang, P.; Jiang, Z. Metal-organic nanogel with sulfonated 3D continuous channels as proton conductor. *ACS Appl. Mater. Interfaces* **2020**, *12*, 19788–19796.
31. Li, Z-H.; Zeng, H.; Zeng, G.; Ru, C.; Li, G.; Yan, W.; Shi, Z.; Feng, S. Multivariate Synergistic Flexible Metal-Organic Frameworks with Superproton Conductivity for Direct Methanol Fuel Cells. *Angew. Chem. Int. Ed.* **2021**, *60*, 26577–26581.
32. Wu, B.; Lin, X.; Ge, L.; Wu, L.; Xu, T. A novel route for preparing highly proton conductive membrane materials with metal-organic frameworks. *Chem. Commun.* **2013**, *49*, 143–145.
33. Liu, S-S.; Han, Z.; Yang, J-S.; Huang, S-Z.; Dong, X-Y.; Zang, S-Q. Sulfonic Groups Lined along Channels of Metal−Organic Frameworks (MOFs) for Super-Proton Conductor. *Inorg. Chem.* **2020**, *59*, 396–402.
34. Lim, D-W.; Sadakiyo, M.; Kitagawa, H. Proton transfer in hydrogen-bonded degenerate systems of water and ammonia in metal–organic frameworks. *Chem. Sci.* **2019**, *10*, 16–33.
35. Lim, D-W.; Kitagawa, H. Proton Transport in Metal−Organic Frameworks. *Chem. Rev.* **2020**, *120*, 8416−8467.
36. Bauer, S.; Serre, C.; Devic, T.; Horcajada, P.; Marrot, J.; Férey, G.; Stock, N. High-Throughput Assisted Rationalization of the Formation of Metal Organic Frameworks in the Iron(III) Aminoterephthalate Solvothermal System. *Inorg. Chem.* **2008**, *47*, 7568-7576.
37. Loiseau, T.; Serre, C.; Huguenard, C.; Fink, G.; Taulelle, F.; Henry, M.; Bataille, T.; Férey, G. A Rationale for the Large Breathing of the Porous Aluminum Terephthalate (MIL-53) Upon Hydration. *Chem. Eur. J.* **2004**, *10*, 1373−1382.
38. Millange, F.; Serre, C.; Guillou, N.; Férey, G.; Walton, R. I. Structural Effects of Solvents on the Breathing of Metal– Organic Frameworks: An In Situ Diffraction Study. *Angew. Chem. Int. Ed.* **2008**, *47*, 4100 –4105.
39. Llewellyn, P. L.; Horcajada, P.; Maurin, G.; Devic, T.; Rosenbach, N.; Bourrelly, S.; Serre, C.; Vincent, D.; Loera-Serna, S.; Filinchuk, Y.; Férey, G. Complex Adsorption of Short Linear Alkanes in the Flexible Metal-Organic-Framework MIL-53(Fe). *J. Am. Chem. Soc.* **2009**, *131*, 13002 –13008.
40. Millange, F.; Guillou, N.; Walton, R. I.; Grenéche, J-M.; Margiolaki, I.; Férey, G. Effect of the nature of the metal on the breathing steps in MOFs with dynamic frameworks. *Chem. Commun.* **2008**, 4732–4734.
41. Ma, M.; Bétard, A.; Weber, I.; Al-Hokbany, N. S.; Fischer, R. A.; Metzler-Nolte, N. Iron-Based Metal−Organic Frameworks MIL-88B and NH_2-MIL-88B: High Quality Microwave Synthesis and Solvent-Induced Lattice "Breathing". *Cryst. Growth Des*. **2013**, *13*, 2286−2291.
42. Aljammal, N.; Jabbour, C.; Chaemchuen, S.; Juzsakova T.; Verpoort, F. Flexibility in Metal–Organic Frameworks: A Basic Understanding. *Catalysts* **2019**, *9*, 512.

43. Pham, H.; Ramos, K.; Sua, A.; Acuna, J.; Slowinska, K.; Nguyen, T.; Bui, A.; Weber, M. D. R.; Tian. F. Tuning Crystal Structures of Iron-Based Metal−Organic Frameworks for Drug Delivery Applications. *ACS Omega* **2020**, *5*, 3418−3427.
44. Pham, M-H.; Vuong, G-T.; Vu, A-T.; Do, T-O. Novel Route to Size-Controlled Fe-MIL-88B_NH_2 Metal_Organic Framework Nanocrystals. *Langmuir* **2011**, *27*, 15261–15267.
45. Scherb, C.; Koehn, R.; Bein, T. Sorption behavior of an oriented surface-grown MOF-film studied by in situ X-ray diffraction. *J. Mater. Chem.* **2010**, *20*, 3046–3051.
46. Cai, X.; Lin, J.; Pang, M. Facile Synthesis of Highly Uniform Fe-MIL-88B Particles. *Cryst. Growth Des.* **2016**, *16*, 3565−3568.
47. Horcajada, P.; Salles, F.; Wuttke, S.; Devic, T.; Heurtaux, D.; Maurin, G.; Vimont, A.; Daturi, M.; David, O.; Magnier, E.; Stock, N.; Filinchuk, Y.; Popov, D.; Riekel, C.; Férey, G.; Serre, C. How Linker's Modification Controls Swelling Properties of Highly Flexible Iron(III) Dicarboxylates MIL-88. *J. Am. Chem. Soc*. **2011**, *133*, 17839–17847.
48. Mukhopadhyay, S.; Debgupta, J.; Singh, C.; Sarkar, R.; Basu, O.; Das. S. K. Designing UiO-66-Based Superprotonic Conductor with the Highest Metal−Organic Framework Based Proton Conductivity. *ACS Appl. Mater. Interfaces* **2019**, *11*, 13423−13432.
49. Yuan, R.; Yue, C.; Qiu, J.; Liu F.; A.; Li. Highly efficient sunlight-driven reduction of Cr(VI) by TiO_2@NH_2-MIL-88B(Fe) heterostructures under neutral conditions. *Applied Catalysis B-Environmental* **2019**, *251*, 229-239.
50. Mukherjee, N.; Das, A.; Dhara, M.; Jana, T. Surface Initiated RAFT Polymerization to Synthesize N-Heterocyclic Block Copolymer Grafted Silica Nanofillers for Improving PEM Properties. *Polymer.* **2021**, *236*, 124315.
51. Bakangura, E.; Wu, L.; Ge, L.; Yang, Z.; Xu, T. Mixed Matrix Proton Exchange Membranes for Fuel Cells: State of the Art and Perspectives. *Prog. Polym. Sci.* **2016**, *57*, 103–152.
52. Liu, Q.; Li, Z.; Wang, D.; Li, Z.; Peng, X.; Liu, C.; Zheng, P. Metal Organic Frameworks Modified Proton Exchange Membranes for Fuel Cells. *Front. Chem.* **2020**, *8*, 694.
53. Taylor, J. M.; Dekura, S.; Ikeda, R.; Kitagawa, H. Defect Control to Enhance Proton Conductivity in a Metal−Organic Framework. *Chem. Mater.* **2015**, *27*, 2286−2289.
54. Yang, F.; Xu, G.; Dou, Y.; Wang, B.; Zhang, H.; Wu, H.; Zhou, W.; Li, J-R. Chen, B. A flexible metal–organic framework with a high density of sulfonic acid sites for proton conduction. *Nature Energy* **2017**, *2*, 877–883.
55. Singha, S.; Jana, T. Structure and Properties of Polybenzimidazole/Silica Nanocomposite Electrolyte Membrane: Influence of Organic/Inorganic Interface. *ACS Appl. Mater. Interfaces* **2014**, *6*, 21286–21296.
56. Sannigrahi, A.; Ghosh, S.; Maity, S.; Jana, T. Polybenzimidazole gel membrane for the use in fuel cell. *Polymer,* **2011,** *52,* 4319-4330.
57. Das, A.; Sana, B.; Bhattacharyya, R.; Ghosh, P. C.; Jana, T. Cross-Linked Alkaline Anion Exchange Membrane from N-Spirocyclic Quaternary Ammonium and Polybenzimidazole. *ACS Appl. Polym. Mater.* **2022**, *4*, 1523-1534.
58. Maity, S.; Jana, T. Soluble Polybenzimidazoles for PEM: Synthesized from Efficient, Inexpensive, Readily Accessible Alternative Tetraamine Monomer. *Macromolecules* **2013**, *46*, 6814–6823.
59. Priyangga, A.; Mumtazah, Z.; Junoh, H.; Jaafar, J.; Atmaja, L. Morphology and Topography Studies of Composite Membranes Developed from Chitosan/ Phthaloyl Chitosan Consisting Multi-Walled Carbon Nanotube/Montmorillonite as Filler. *J. Membr. Sci. Res.* **2021**, *7*, 295–304.
60. Muthumeenal, A.; Neelakandan, S.; Kanagaraj, P.; Nagendran, A. Synthesis and Properties of Novel Proton Exchange Membranes Based on Sulfonated Polyethersulfone and N-Phthaloyl Chitosan Blends for DMFC Applications. *Renew. Energy* **2016**, *86*, 922–929.
61. Dai, X.; Cao, Y.; Shi, X.; Wang, X. The PLA/ZIF-8 Nanocomposite Membranes: The Diameter and Surface Roughness Adjustment by ZIF-8 Nanoparticles, High Wettability, Improved Mechanical Property, and Efficient Oil/Water Separation. *Adv. Mater. Interfaces* **2016**, 1600725.
62. Kutcherlapati, S. R.; Koyilapu, R.; Jana, T. Poly(N-Vinyl Imidazole) Grafted Silica Nanofillers: Synthesis by RAFT Polymerization and Nanocomposites with Polybenzimidazole. *J. Polym. Sci. Part A Polym. Chem.* **2018**, *56*, 365–375.
63. Singha, S.; Jana, T. Influence of Interfacial Interactions on the Properties of Polybenzimidazole/Clay Nanocomposite Electrolyte Membrane. *Polymer.* **2016**, *98*, 20–31.
64. Lobato, J.; Cañizares, P.; Rodrigo, M. A.; Úbeda, D.; Pinar, F. J. A Novel Titanium PBI-Based Composite Membrane for High Temperature PEMFCs. *J. Membr. Sci.* **2011**, *369*, 105–111.

65. Jiang, J.; Zhu, X.; Qian, H.; Xu, J.; Yue, Z.; Zou, Z.; Yang, H. Cross-Linked Sulfonated Poly(Ether Ether Ketone) Electrolytes Bearing Pendent Imidazole Groups for High Temperature Proton Exchange Membrane Fuel Cells. *Sustain. Energy Fuels* **2019**, *3*, 2426–2434.
66. Vilčiauskas, L.; Tuckerman, M. E.; Bester, G.; Paddison, S. J.; Kreuer, K. D. The Mechanism of Proton Conduction in Phosphoric Acid. *Nat. Chem.* **2012**, *4*, 461–466.
67. Escorihuela, J.; Sahuquillo, Ó.; García-Bernabé, A.; Giménez, E.; Compañ, V. Phosphoric Acid Doped Polybenzimidazole (PBI)/Zeolitic Imidazolate Framework Composite Membranes with Significantly Enhanced Proton Conductivity under Low Humidity Conditions. *Nanomaterials* **2018**, *8*, 775.
68. Dang, J.; Zhao, L.; Zhang, J.; Liu, J.; Wang, J. Imidazole Microcapsules toward Enhanced Phosphoric Acid Loading of Polymer Electrolyte Membrane for Anhydrous Proton Conduction. *J. Membr. Sci.* **2018**, *545*, 88–98.

CHAPTER 4

Tuning the Electrochemical and Catalytic ORR Performance of C_{60} by its Encapsulation in ZIF-8: A Solid-State Analogue of Dilute Fullerene Solution

OVERVIEW:

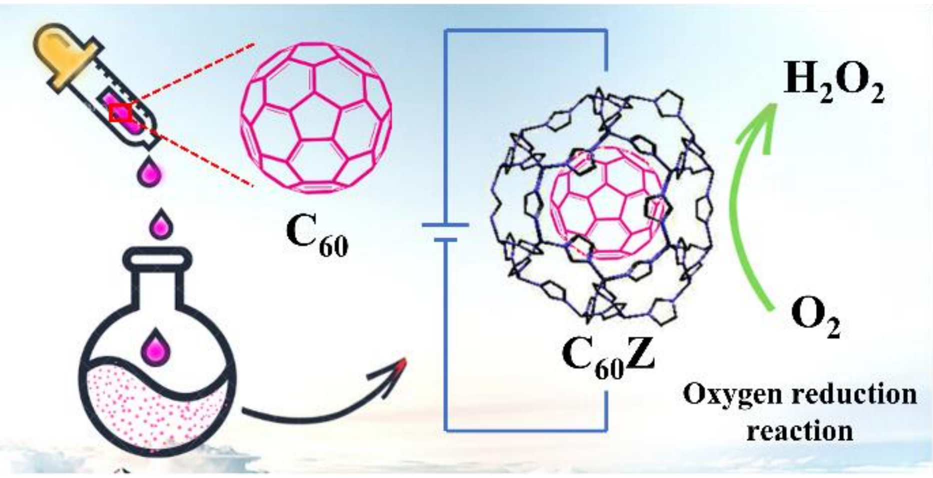

Metal–organic frameworks (MOFs) with intrinsic electrochemical activity have received significant attention in the last two decades, mainly because of the high density of physically separated active sites. Yet, the potential of chemical tunability, spatial confinement and scope of heterogenization in the electrochemically inactive MOFs have been less explored. Here, we have shown that fullerene C_{60}, well-known for its rich reductive electrochemistry, when encapsulated inside zeolitic imidazolate framework-8 (ZIF-8) to prepare a heterogeneous composite (**C_{60}Z**), can act as a catalyst for the oxygen reduction reaction (ORR) at a lower overpotential with better selectivity than bare C_{60} *per se*. Spectroscopic and electrochemical characterization methods prove significant interactions between the ZIF-8 host and the C_{60} guest, which results in the modification of the electro- chemical behavior of C_{60} inside ZIF-8 and thereby causes an enhanced electrochemical ORR performance of the guest. The mono-confinement of C_{60} inside ZIF-8 also results in spatial separation of C_{60} molecules, which is highly effective for preserving its dilute solution-like behavior in solid-state inside the framework matrix. Furthermore, we have explored the scope of device processability of this solid-state analogue of dilute C_{60} solution *i.e.*, **C_{60}Z**, by its fabrication into a polymer membrane (**C_{60}Z–PVA** thin film) which could retain the physical properties of the **C_{60}Z**.

4.1. INTRODUCTION

Metal-organic frameworks (MOFs) have emerged as a class of materials with widely varying scope for applications ─ from gas storage and separation to molecular sensing, optics, and catalysis.[1-7] The most critical characteristics which render the material viable for such applications are its large surface area, porosity, and scope for chemical tunability.[8] MOFs can serve as hosts to a variety of guests, giving rise to unique supramolecular systems of potential applications.

Ever since the discovery of fullerene C_{60} in 1985, a huge wave of research followed.[9] This hollow spherical allotrope of carbon has a perfectly symmetric structure, highly delocalized π- electron density, and the ability to accept electrons in its low lying LUMOs, which has drawn significant attention.[9-15] The ground state of the molecule is a closed shell with h_u HOMO and triply degenerate t_{1u} LUMO.[16] So, theoretically, the molecule should accept at least 6 electrons under applied cathodic potential, which was also experimentally verified by extensive research.[17-22] Practically, $\mathbf{C}_{60}$ can be electrochemically reduced in a reversible stepwise manner (with uniform step heights) up to $\mathbf{C}_{60}^{6-}$ in a highly dilute solution of $\mathbf{C}_{60}$ in a non-polar solvent under an inert atmosphere.

The property of fullerene to function as an electron sink has made it of significant interest to material scientists, especially in the field of optoelectronic devices,[23-30] and catalysis.[31-38] Many of these applications in ORR catalysis are based on the ability of fullerene C_{60} to form stable donor-acceptor systems, for example, heteroatom doped-fullerene, C_{60}-CNT system, supramolecular hybrids with 2D-nanostructures, *etc*.[31-38] The reason behind the impressive catalytic activity of these metal-free systems has been attributed to the intermolecular donor-acceptor charge transfer in the catalyst.[32]

In our present work, we have designed a MOF−C_{60} based host-guest composite, where fullerene C_{60} (guest) is encapsulated in the cages of ZIF-8 MOF (host) using solution-state *in situ* synthetic strategy (Scheme 4.1). The selection of ZIF-8 as a host for the encapsulation of C_{60}, was crucial, considering the host-guest size match; according to which, only one C_{60} molecule (geometric diameter ~7.1 Å and Van Der Waals diameter ~10.3 Å)[15] could be confined in one cavity of ZIF-8 (cavity diameter ~11.6 Å) and there is no scope of its leaching out since the window aperture (diameter ~3.4 Å) of the cavity is much smaller.[39] The situation can be compared to a '*ship in a bottle*' approach.[40-42] Spatial separation and mono-confinement of C_{60} in the cages of ZIF-8 helps the $\mathbf{C_{60}Z}$ composite to retain most of the molecular properties of C_{60}. Additionally, C_{60} displays unique electrochemical properties in the $\mathbf{C_{60}Z}$ composite due to the modified microenvironment and electronic charge transfer. The electron-donating nature of ZIF-8 and the electron-accepting property of fullerene C_{60} are the two crucial complementary factors facilitating the charge transfer process for **C_{60}Z**.[42] The charge transfer plays a vital role in enhancing electrocatalytic ORR activity of the **C_{60}Z**, compared to non-encapsulated C_{60}. The ORR is one of the most important and widely studied reactions in life processes such as biological respiration and energy-converting systems, e.g., fuel cells and metal-air batteries.[43] In an aqueous solution, ORR occurs mainly by two pathways: (i) 4e-4H$^+$ proton-coupled electron transfer (PCET) to form H_2O, and (ii) 2e-2H$^+$ PCET to form H_2O_2. Here, we have shown that the **C_{60}Z** having a low loading of active species (one C_{60} per 10 cages of ZIF-8), acts as a better heterogeneous electrocatalyst for ORR than C_{60} *per se* in terms of (1) higher catalytic current density; (2) lower overpotential requirement and (3) better selectivity towards H_2O_2 product generation over a wide potential window. All of these imply functional tunning to better catalytic activity by modification of the microenvironment of C_{60} inside MOF.

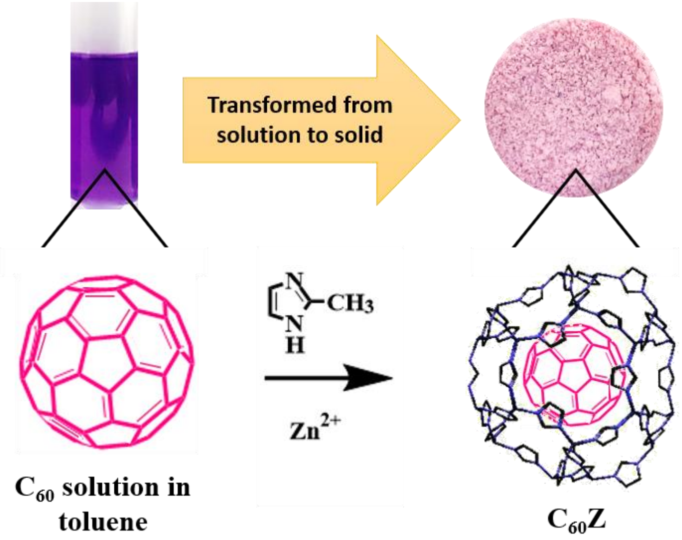

Scheme 4.1. Schematic representation of the formation of **C_{60}Z** by *in situ* encapsulation of C_{60} inside ZIF-8.

There have been few reports of fullerene-MOF assemblies, which discuss their fundamental structural properties,[44.45] and potential applications in gas storage, gas separation,[46-48] catalysis, electrochemical energy storage, among others.[49-51] Earlier, Yang and co-workers prepared a composite using C_{60} and ZIF-8 MOF to be used as a precursor for the synthesis of C_{60}@N-MPC through carbonization, for application in lithium-ion batteries; where the C_{60} molecules served the role of pore expander.[49] However, the prominent presence of crystalline planes similar to that of solid C_{60} in the powder X-ray diffraction (PXRD) pattern of the precursor indicates the presence of aggregated fullerenes.

Popov, Užarević and their co-workers recently reported a series of composites where C_{60} was loaded in ZIF-8 in a high percentage (up to 100% occupancy of total available cages).[50]

A detailed study of the electronic and electrochemical properties of the title material **C_{60}Z** reveals that, while on the one hand, it shows notable similarities with a dilute solution of C_{60} (due to preservation of its molecularity in solid-state), on the other hand, it shows a significant difference in its electrochemical behaviour owing to the modified microenvironment. The synthesis of **C_{60}Z** composite and the optimization of C_{60} loading in it are discussed in detail in the following section and in appendix 4. The synthesized **C_{60}Z** composite has been characterized by various techniques and its properties compared with the non- encapsulated solid/aggregated C_{60}, C_{60} in dilute solution and ZIF-8.

4.2. EXPERIMENTAL SECTION

4.2.1. Materials

All the chemicals were used as received without any further purification. Zinc nitrate hexahydrate {$Zn(NO_3)_2.6H_2O$} was purchased from Finar chemicals. 2-methylimidazole (2-mIm) and fullerene C_{60} (99.5% purity) were purchased from Sigma Aldrich. Polyvinyl alcohol (PVA) was obtained from Merck. Methanol, acetonitrile, and toluene were purchased from Finar chemicals.

4.2.2. Synthesis

4.2.2.1. Synthesis of ZIF-8

0.450 g (2.5 mmol) of $Zn(NO_3)_2.6H_2O$ was dissolved in 12 mL of methanol and in a separate round bottom flask (100 mL), 1 g (12.2 mmol) of 2-methyl imidazole (2-mIm) was dissolved with 12 mL of methanol. The methanolic solution of $Zn(NO_3)_2$ was slowly added into the flask, under stirring. The reaction mixture was left undisturbed for 12 hours and the product ZIF-8 was obtained as a white precipitate. It was collected by centrifugation and was washed repeatedly with methanol (6 times over a course of 2 days) and dried in a hot air oven at 70 °C for 24 hours.

4.2.2.2. Synthesis of C_{60}Z-n (n = A, B, C, D and E): C_{60} loading variations

The precursor solutions were prepared by mixing the reagents in the specified proportion listed in table 4.1. The methanolic solution of 2-methyl imidazole (2-mIm) was taken in a round bottom flask (100 mL) and kept under stirring. Initially, one-fourth of the $Zn(NO_3)_2.6H_2O$ solution was added dropwise into the methanolic solution of 2-methyl imidazole until turbidity appeared. Then, both the fullerene C_{60} solution and the $Zn(NO_3)_2$ solution were added dropwise simultaneously into the flask, under vigorous stirring. The reaction mixture was left undisturbed for 12 hours and the product **C_{60}Z-n** (n = A, B, C, D and E) was obtained as precipitate. The product was collected by centrifugation and was washed repeatedly with methanol (6 times over a course of 2 days). Following this, the product was kept under stirring in toluene for 1 day, during which the solvent was changed thrice (or till a colourless supernatant was achieved), to get rid of any surface adsorbed fullerene. Then, the product **C_{60}Z-n** (n = A, B, C, D and E) was collected and washed twice with methanol, to remove toluene from the pores of the composite. The product was obtained as a light purple coloured powder, after being dried at 70 °C for 24 hours.

Table 4.1. Reagent amounts for **C_{60}Z-n** (n = A, B, C, D and E)

Name of Sample	C_{60} (mg) in toluene (mL)	$ZnNO_3.6H_2O$ (g) in methanol (mL)	2-mIm (g) in methanol (mL)
C_{60}Z-A	2mg/ 4ml	0.450 g/ 10mL	1g/ 10mL
C_{60}Z-B	5 mg/ 5ml	0.450 g/ 10mL	1g/ 10mL
C_{60}Z-C or C_{60}Z	10 mg/ 10ml	0.450 g/ 10mL	1g/ 10mL
C_{60}Z-D	15 mg/ 15ml	0.450 g/ 10mL	1g/ 10mL
C_{60}Z-E	20 mg/ 20ml	0.450 g/ 10mL	1g/ 10mL

0.450 g $ZnNO_3.6H_2O$ - 2.5 mmol; 1 g 2-mIm - 12.2 mmol; 10 mg C_{60} - 0.014 mmol.

The loading of C_{60} in these composites (**C_{60}Z-A**, **C_{60}Z-B**, **C_{60}Z-C**, **C_{60}Z-D** and **C_{60}Z-E)** was calculated by elemental analysis.

4.2.2.3. Synthesis of C_{60}Z – 17% and C_{60}Z – 33% by mechanochemical technique

Synthesis of C_{60}Z – 17%: Zinc oxide (ZnO, 40 mg), 2-methyl imidazole (80 mg) and C_{60} (10 mg) were placed into a stainless-steel jar with two stainless steel balls (7 mm). The mixture was ground for 10 min at 30 Hz, followed by addition of 45 µL ethanol and 6 mg of NH_4Cl, and subsequent milling for 45 min. The product was collected by centrifugation and was washed repeatedly with ethanol and toluene (3 times each) over a course of 2 days. The product was dried at 70 °C for 24 hours.

Synthesis of C_{60}Z – 33%: The synthesis was performed using similar method as that of **C_{60}Z – 17%**. The amount of C_{60} used was 20 mg.

Both materials were structurally characterized and the loading of C_{60} in them was calculated from CHN elemental analysis.

4.2.2.4. Synthesis of (C_{60}+ZIF-8) physical mixture

(C_{60}+ZIF-8) was prepared by treating pre-synthesized ZIF-8 with a saturated solution of C_{60} in toluene for 12 hours. The product was then washed with toluene to get rid of excess C_{60} from the MOF surface. This way it was ensured that the C_{60} present is only surface adsorbed. The synthetic procedure also ensures that none of the C_{60} molecules get encapsulated in the ZIF-8 pores, but only get adsorbed on the surface.

4.2.2.5. Fabrication of C_{60}Z into C_{60}Z-PVA composite membrane

Synthesis of PVA membrane: A 1 wt% homogeneous solution of commercially available PVA was prepared in milli-Q water and poured onto a glass Petri dish. The solvent was evaporated slowly at 70 °C. The formed membrane was then peeled out and dried in vacuum at 100 °C to remove the trace of solvent molecules.

Synthesis of C_{60}Z-PVA composite membrane:

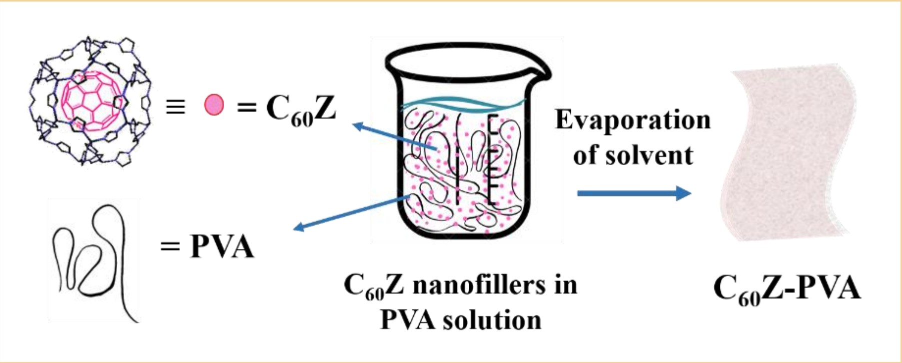

Scheme 4.2. A schematic representation of the fabrication of **C_{60}Z** into the membrane (**C_{60}Z-PVA**).

This homogenous nanocomposite membrane was prepared by solution casting method. 20 mg of the **C_{60}Z** composite was dispersed in 10 mL of milli-Q water by sonicating it for 30 minutes. Another solution of 200 mg of PVA in 10 mL of milli-Q water was prepared separately. These two separately prepared mixtures were then added together such that the final PVA concentration in solution was 1 wt% and the amount of **C_{60}Z** was 10 wt% (with respect to polymer weight). This polymer-nanocomposite blend was stirred vigorously at room temperature for 24 h to obtain a uniform dispersion. It was then poured onto a glass Petri dish and the solvent was evaporated slowly at 70 °C. The formed membrane was then peeled out and dried in vacuum at 100 °C to remove the trace of solvent molecules.

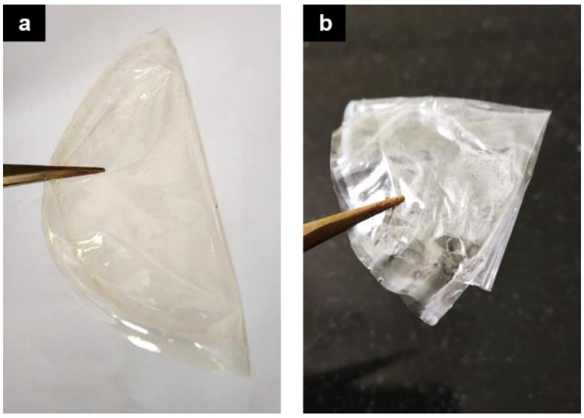

Figure 4.1. Photographs of (a) **C_{60}Z-PVA** membrane and (b) PVA membrane.

4.2.3. Methods

The instrumental details of all the experiments are provided in appendix 1.

4.2.3.1. Methodology for non-aqueous electrochemical measurements

The electrochemical measurements in non-aqueous medium were carried out in a conventional three-electrode configuration with carbon paper or modified carbon paper as working electrode and two platinum wires of suitable surface area as the counter electrode and pseudo-reference electrode, respectively. Electrochemical analysis on C_{60} was carried out in homogeneous mode employing typically 6×10^{-4} M solution of C_{60} in 0.1 M solution of tetrabutylammonium perchlorate (TBAP, supporting electrolyte) in 1:2 dry acetonitrile/toluene solvent mixture. For heterogeneous electrochemical analysis of **C_{60}Z**, 4 mg of the sample was mixed with 1 mg of acetylene carbon black and 1 mL of 3:2 ethanol/water mixture. 10 µL of 5 wt% nafion (aq.) was added to it as binder. The mixture was sonicated till a homogeneous suspension was obtained. 40 µL of this homogeneous ink was then drop-casted on a carbon paper electrode and dried at 70 ^{o}C under IR lamp to obtain our **C_{60}Z** modified working electrode. 0.1 M solution of TBAP in 1:2 dry acetonitrile/toluene mixture was used as electrolyte. All the experiments were carried out under N_2 atmosphere, and the electrolyte was purged with N_2 for at least 30 mins prior to each experiment. Electrochemical responses were recorded in -0.1 V/s scan rate, unless specified otherwise. All the potential values reported for non-aqueous electrochemical analysis, are with respect to ferrocene-ferrocenium (Fc^+/Fc) couple (Figure A4.9, Appendix 4).

4.2.3.2. Methodology for electrochemical study of ORR catalysis

The electrochemical measurements for investigating oxygen reduction reaction (ORR), were carried out in a gas tight cell with three-electrode setup. Ag/AgCl was used as the reference electrode, glassy carbon as the working electrode, and Pt as the counter electrode. All the measurements for C_{60}, **C_{60}Z**, and ZIF-8, were done in heterogeneous mode. For all the electrochemical analysis (except for RRDE experiments), the coating sample was prepared using 4 mg of the sample, mixed with 1 mg of acetylene carbon black, 1 mL of 3:2 ethanol/water mixture and 10 μL of 5 wt% nafion (aq.) as binder. Sample preparation for RRDE measurements required the addition of 80 μL of 5 wt% nafion (aq.) as binder. The mixture was sonicated till a homogeneous suspension was obtained. 10 μL of this homogeneous ink was then drop-casted on glassy carbon electrode/ glassy carbon ring-disk electrode and dried at 70 °C under IR lamp to obtain our catalyst modified working electrode. 0.1 M KOH was used as electrolyte. For obtaining a Ar saturated/O_2 saturated system, the electrolyte was purged with Ar/O_2 for at least 30 mins prior to each experiment.

4.3. RESULTS AND DISCUSSIONS

4.3.1. Powder X-ray diffraction (PXRD) analysis

The PXRD pattern of **C_{60}Z**, including the position of the peaks and their relative intensities, matched well with the simulated PXRD pattern of ZIF-8, indicating that there has been no noticeable change in the crystal parameters of ZIF-8 framework of **C_{60}Z**, due to the encapsulation of C_{60} (Figure 4.2a; Figure A4.1, Appendix 4).

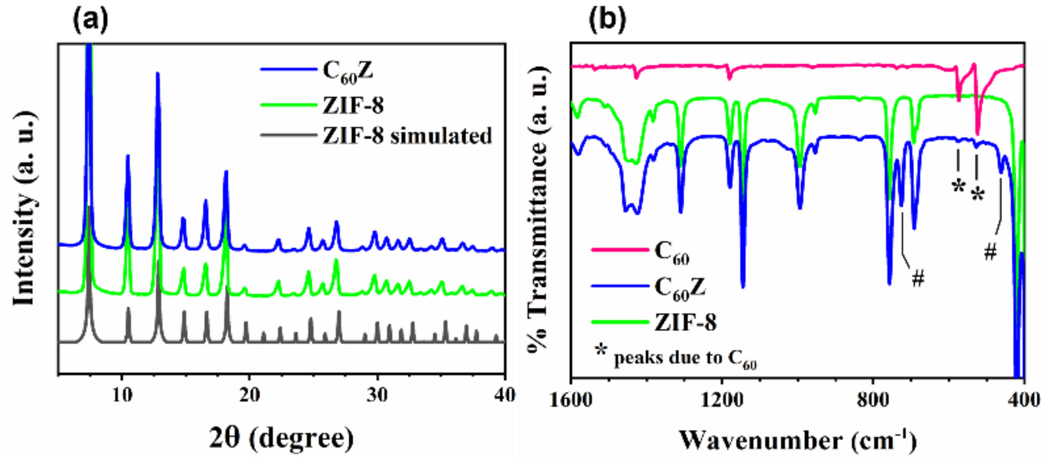

Figure 4.2. (a) PXRD patterns of simulated ZIF-8, synthesized ZIF-8 and **$C_{60}Z$**. (b) FT-IR spectra of C_{60}, ZIF-8 and **$C_{60}Z$** (400-1600 cm^{-1}). * marked peaks refer to those originating from C_{60}. # marked peaks refer to those originating from the interactions of C_{60} and **$C_{60}Z$**.

4.3.2. Fourier transformed-infrared (FT-IR) spectral analysis

The FT-IR spectrum of ZIF-8 shows two weak peaks at 3132 cm^{-1} and 2928 cm^{-1} for ‘C–H’ aromatic and aliphatic stretching, respectively (Figure A4.2, Appendix 4). A medium peak at 1586 cm^{-1} is due to ‘C=N’ stretching. The several peaks in the region of 1460 - 1300 cm^{-1} are a result of 2-methyl imidazole ring stretching. The two peaks at 1146 cm^{-1} and 995 cm^{-1} are due to C–N aromatic stretching and bending, respectively. The two peaks at 760 cm^{-1} and 695 cm^{-1} were owing to C–H bending and out-of-plane bending of 2-methyl imidazole ring. The strong peak at 425 cm^{-1} is because of Zn–N stretching which indicates the successful formation of the ZIF-8 framework. The FT-IR spectrum of fullerene C_{60} is rather simple with only four peaks at 527 cm^{-1}, 575 cm^{-1}, 1184 cm^{-1} and 1428 cm^{-1}, due to its highly symmetric structure. The FT-IR spectrum of **$C_{60}Z$** displays all the prominent features of ZIF-8 (Figure 4.2b). Because of the low concentration of C_{60}, two of its peaks (1184 cm^{-1} and 1428 cm^{-1}) are completely masked by the features of ZIF-8 while the other two (527 cm^{-1} and 575 cm^{-1}; marked with *****) appear at the same position as in non-encapsulated C_{60} (Figure 4.2b). Moreover, the newly generated peaks (725 cm^{-1} and 461 cm^{-1}; marked with #) observed in the **$C_{60}Z$** spectrum, indicate interactions between C_{60} (guest) and ZIF-8 (host).

4.3.3. Raman spectral analysis

The Raman spectrum of **$C_{60}Z$** displays characteristic features for both C_{60} and ZIF-8 (Figure 4.3). The position and intensity of the peaks corresponding to ZIF-8 are similar to those of pristine ZIF-8, which indicates the preservation of the ZIF-8 framework in **C_{60}Z**.[52] But, it is interesting to note that the position of the peaks of **C_{60}Z**, that is corresponding to C_{60} are shifted to lower frequencies compared to solid C_{60}. For solid C_{60} *per se*, the three most intense peaks corresponding to $H_g(1)$, Ag(1) and the pentagonal pinch mode (PPM) Ag(2), are observed at 271 cm^{-1}, 493 cm^{-1} and 1465 cm^{-1}, respectively. In **C_{60}Z**, all these peaks are red-shifted to 261 cm^{-1}, 484 cm^{-1}, and 1458 cm^{-1}, respectively. The red-shift can be reasoned in two ways: (1) weakening of the C-C bonds of C_{60} in **C_{60}Z**.[53] This can happen if the fullerene molecule either donates its π-electron density or accepts electron in its π^* orbitals. Since the Zn metal nodes of ZIF-8 have filled d-orbitals (d^{10}), there is no scope of π-electron donation from C_{60} to it. But the ZIF-8 framework can donate electron density to the π^* orbitals of C_{60} molecules. (2) Mono-confinement of C_{60} in nanocages (~1.1 nm) of ZIF-8 can be considered as the extreme limit of reduced size for a C_{60} nanocrystal because, in general, the Raman frequency decreases with the reduction in the size of nanocrystals.[54] The observed shift in peak positions can be a cumulative effect of both the factors resulting from the encapsulation of C_{60} molecules in ZIF-8.

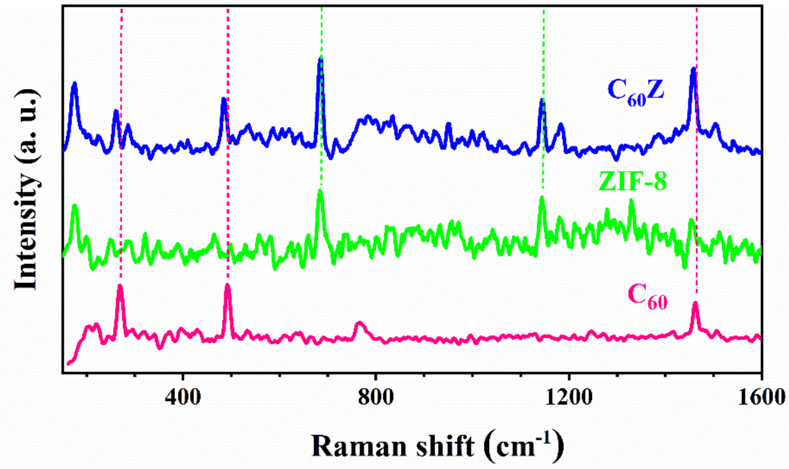

Figure 4.3. Raman Spectra of C_{60}, ZIF-8 and **C_{60}Z**.

4.3.4. N_2 sorption isotherm and BET surface area analysis

The N_2 sorption isotherms of **C_{60}Z** and ZIF-8 (Figure A4.4, Appendix 4) are Type-I isotherm, a characteristic of the microporous material. Brunauer–Emmett–Teller (BET) surface area of **C_{60}Z** (1090.83 m^2/g) has been calculated to be lower than pristine ZIF-8 (1373.72 m^2/g). The lowering of surface area by ~280 m^2/g results from C_{60} molecules occupying a fraction of the total pores in ZIF-8. According to the CHN elemental analysis, there is one C_{60} molecule per ten nanocages of ZIF-8 in **C_{60}Z** composite (section A4.2,

Appendix 4). This accounts for 10% occupancy of the cages, relative to the maximum theoretical number of cages available. From the TGA analysis, C_{60} was estimated to be about 1.24% (w/w) of **C_{60}Z** (section A4.5, Appendix 4).

4.3.5. FESEM and HR-TEM image analysis

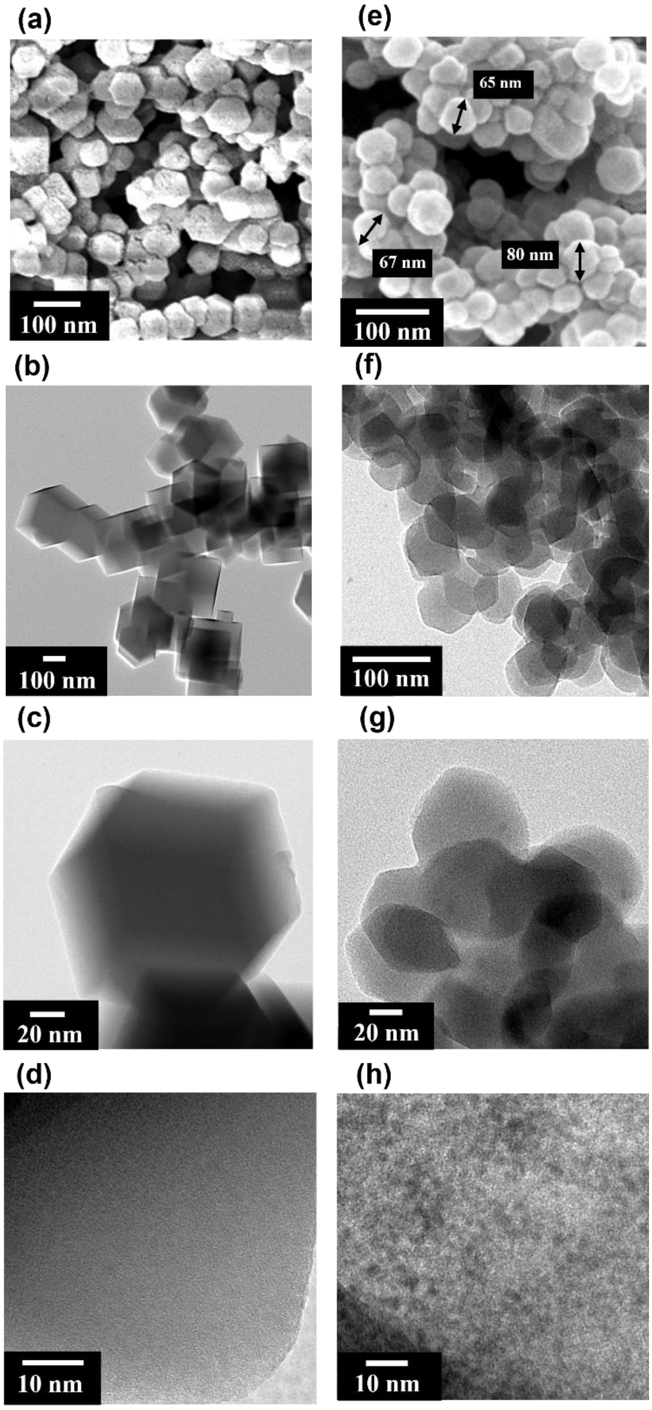

Figure 4.4. FESEM (a), TEM (b, c) and HR-TEM (d) images of ZIF-8 nanocrystals. FESEM (e), TEM (f, g) and HR-TEM (h) images of **C_{60}Z** nanocrystals.

From FESEM and HR-TEM images of the ZIF-8 (Figure 4.4a, 4.4b, 4.4c) and the **C_{60}Z** (Figure 4.4d, 4.4e, 4.4f), both are found to have rhombohedral morphology. A comparison of the HR-TEM images (Figure 4.4d and 4.4h) shows the presence of C_{60} in **C_{60}Z** in the form of small dark spots.

4.3.6. Electronic absorbance spectral analysis

To explore the photophysical properties of the composite **C_{60}Z,** the Kubelka-Munk converted solid-state DR (diffused reflectance) electronic spectrum of **C_{60}Z** was compared with that of solid C_{60} *per se* and diluted *n*-hexane (liquid) solution of C_{60} (Figure 4.5). As can be observed, the features of **C_{60}Z** are significantly different from those of solid C_{60}, but bear an uncanny resemblance with C_{60} in solution,[55] that is, the encapsulated C_{60} molecules inside the MOF matrix behave very similar to a dilute (liquid) solution of C_{60}. The position of the peaks at 256 nm and 328 nm falling in the strong band region (200 nm – 350 nm), were identical in both C_{60} (in dilute liquid solution) and **C_{60}Z** (in solid state). Since the HOMO-LUMO transitions in fullerene C_{60} is parity forbidden, the electronic spectrum displays very weak band intensity in the region of 450 nm – 650 nm. A magnified view of this region provided in the inset of Figure 4.5, shows that the corresponding absorption spectra for C_{60} in solution and **C_{60}Z**, has one to one matching with one another. In pure solid phase, C_{60} molecules stay in a closed packed structure which has a characteristic feature in its electronic spectrum.[56] On the other hand, in the case of homogeneous liquid

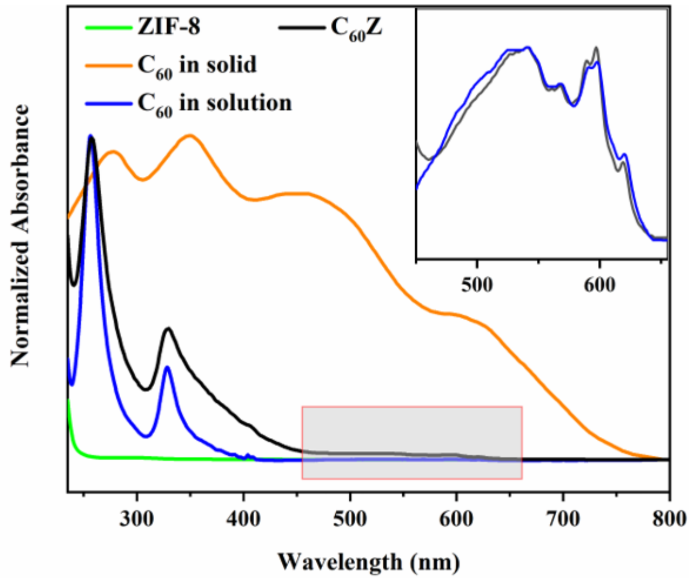

Figure 4.5. Electronic absorbance spectra of C_{60} in n-hexane solution and K-M converted UV/Vis-DRS spectra of solid C_{60}, ZIF-8 and **C_{60}Z**; inset: magnified view of the highlighted region in C_{60} solution and **C_{60}Z** spectra.

solution state, depending on the nature of the solvent and the concentration of C_{60} in it, the molecules can stay as discrete entity or can form agglomerated phases constituting of loosely packed molecules of C_{60}. With varying extent of such assembly, the absorption spectrum of the solution changes dramatically.[57] This implies that the UV-visible spectral feature of a C_{60} molecule in true sense can only be achieved by employing a highly diluted solution of C_{60}.

The similarity between the electronic spectrum of **C_{60}Z** and C_{60} in diluted solution, is a direct consequence of the mono-confinement and low loading of C_{60} molecules (*vide supra*) inside ZIF-8, resulting in effective spatial separation and minimum scope of interaction among the encapsulated C_{60} molecules.Furthermore, photoluminescence (PL) measurements have been carried out on the **C_{60}Z** (solid), ZIF-8 (solid), and C_{60} (dilute liquid solution).

4.3.7. Photoluminescence (PL) spectral analysis

The PL spectrum of C_{60} was recorded in toluene at room temperature with excitation wavelength λ_{exc} at 450 nm. The PL spectrum of C_{60} (Figure 4.6; inset) displays a weak and broad emission feature stretching from 650 nm to 780 nm. This emission band corresponds to the $S_1(^1T_{1g}, {}^1T_{2g}, {}^1G_g) \rightarrow S_0(^1A_g)$ transition of the C_{60} molecule.[58] But since the first excited state S_1 of the molecule is degenerate and has mixed character of $^1T_{1g}$, $^1T_{2g}$ and ^1G_g,

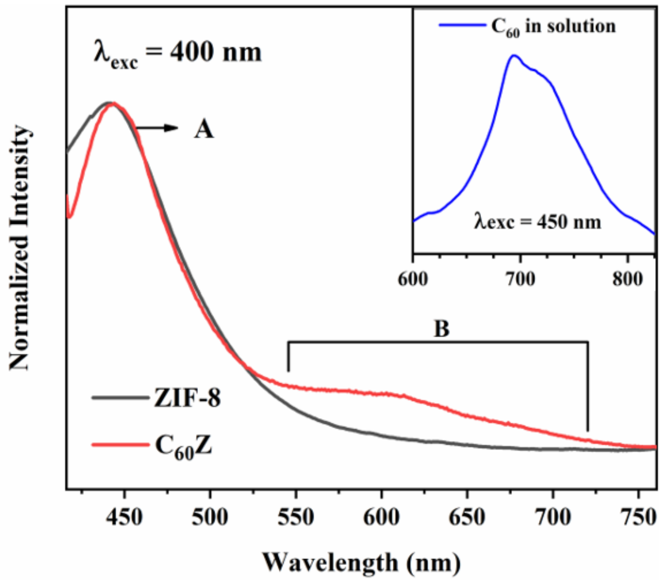

Figure 4.6. Fluorescence emission spectra of ZIF-8 and **C_{60}Z** (λ_{exc} = 400 nm); inset: emission spectra of C_{60} in toluene solution (λ_{exc} = 450 nm).

the transition $S_0 \rightarrow S_1$ or *vice versa*, is parity forbidden. Due to this, the absorption at longer wavelength (450-650 nm) is very weak (*vide supra*) and so is the fluorescence emission (quantum yield ~ 8.5×10^{-4}). The PL emission profile of ZIF-8 was recorded in solid state with excitation wavelength λ_{exc} at 400 nm. The PL spectrum for ZIF-8 (Figure 4.6) displays one strong peak centered around 445 nm, which can be attributed to the coordinated 2-methyl imidazolate of ZIF-8. The PL spectrum of **C_{60}Z** displays a strong peak around 445 nm (peak A; Figure 4.6) originating from the inherent luminescence of the ZIF-8 and a broad band stretching from 540 nm to 730 nm (band B; Figure 4.6) owing to encapsulated C_{60}.[59,60] Interestingly, the emission band of encapsulated C_{60} has undergone a blue shift by ~90 nm compared to that of C_{60} *per se* in solution, which can be an outcome of the electronic interaction between the guest (C_{60}) and the host (ZIF-8), as evident from XP spectral analysis. The charge transfer from ZIF-8 to the π^* orbitals of encapsulated C_{60} molecules can increase the energy of the LUMO and cause a blue shift.[61,62]

4.3.8. X-ray photoelectron spectral analysis

The interaction between the electron-rich surface of ZIF-8, and the encapsulated C_{60} molecule is further confirmed by X-ray photoelectron spectroscopy (XPS). For XPS, the samples were coated with a thin layer of gold to improve their electrical conductivity following earlier reports.[43,63] The surface survey of both ZIF-8 and **C_{60}Z** displays signals of Au (4f and 4d), C1s, N1s, O1s, and Zn2p core levels (Figure A4.7 and A4.8, Appendix 4). The presence of an oxygen signal is possibly a result of exposure of the samples to air, which might have resulted in reactions between the uncoordinated Zn nodes and water, CO_2 from air.[63,64] The deconvoluted C1s XPS (Figure 4.7) for ZIF-8 displays three peaks, centered around 284.8 eV, 285.8 eV and 288.5 eV, which are assigned to three types of carbon: C=C, C-N and C(O)O, respectively. The deconvoluted XPS of C1s for **C_{60}Z** (Figure 4.7a) consists of four types of carbon; out of which three peaks, centered around 285.2 eV, 286.7 eV and 288.2 eV are assigned to C=C, C-N and C(O)O. The fourth peak around 283.6 eV (marked with *) originates from the carbon atoms of encapsulated C_{60} molecules.[32] This lower-side binding energy peak provides a strong argument supporting the probable electronic charge transfer from ZIF-8 to C_{60}. Additionally, the N1s XPS of ZIF-8, has one peak around 399.4 eV (Figure 4.7b), while for **C_{60}Z**, there is an additional peak at higher binding energy, 402.3 eV (marked with *, Figure 4.7a). Such a situation can arise because of the electron density shift from the 2-methyl imidazole of ZIF-8 to the

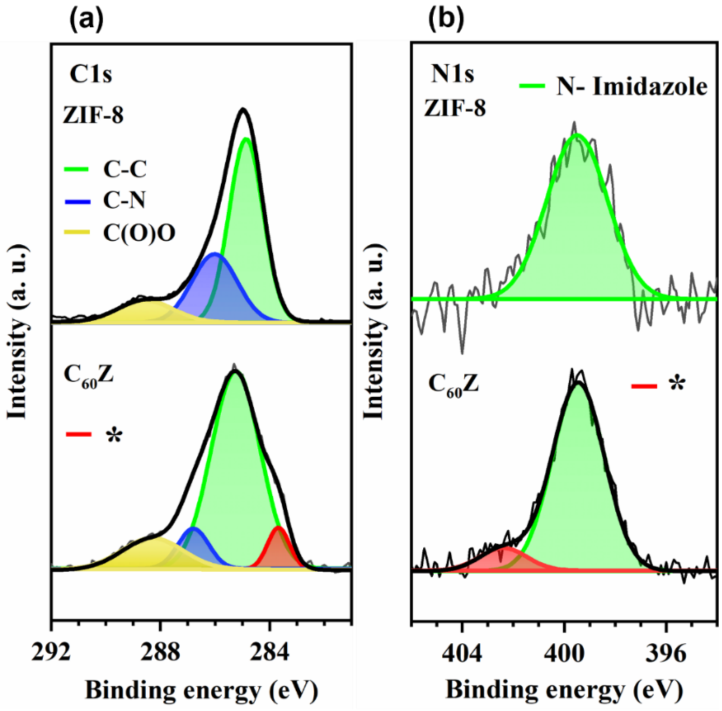

Figure 4.7. X-ray photoelectron spectra of (a) C1s of ZIF-8 and **C_{60}Z**. The red coloured area under the curve marked with * refers to C-atoms of C_{60} having lower binding energy. (b) N1s of ZIF-8 and **C_{60}Z.** The red coloured area under the curve marked with * refers to N-atoms of the ZIF-8 framework in **C_{60}Z** having higher binding energy.

encapsulated C_{60}. Additionally, the positional shift of the XP peak of ‘C-N’ carbon of **C_{60}Z** (Figure 4.7a) towards higher binding energy by ~0.9 eV than ZIF-8, is another convincing proof of this charge transfer. As the electron density drifts from the N atom of 2-methyl imidazolate ligand of ZIF-8 to the guest C_{60}, electronic redistribution occurs in the ligand, and the adjacent C-atoms (i.e., the ‘C-N’ carbon atoms) acquire partial positivity, which helps in the stabilization of the complete host-guest system. Complementarily, the C-atoms in C_{60}, accepting electrons from the ZIF-8 framework, appear in the lower binding energy region. ZIF-8 is well-known for electron- donating capacity,[42] while fullerene C_{60} can function as an efficient electron sink;[65,66] this paves the way for the charge transfer mechanism to operate in the **C_{60}Z** composite.

4.3.9. Electrochemical analysis

4.3.9.1. Electrochemical analysis of C_{60}Z in non-aqueous media

The successful encapsulation of C_{60} molecules in the ZIF-8 cavity prompted us to compare the electrochemical response of **C_{60}Z** with that of C_{60} *per se*. The electrochemical measurements have been carried out in conventional three-electrode configuration with 0.1

M solution of tetrabutylammonium perchlorate (TBAP, supporting electrolyte) in 1:2 dry acetonitrile-toluene solvent mixture under nitrogen atmosphere. For all the non-aqueous electrochemical experiments, the potential values are reported with respect to the ferrocenium- ferrocene (Fc^+/Fc) couple. A detailed description of the relevant electrochemical methodology is provided in the appendix 4 (section 4.2.3).

The cyclic voltammogram of ZIF-8 shows no response in the potential window of our interest. The cyclic voltammogram of dilute solution of C_{60} as such (Figure 4.8) presents stepwise four one-electron-redox-couples (reversible), corresponding to C_{60}/C_{60}^{-}, C_{60}^{-}/C_{60}^{2-}, C_{60}^{2-}/C_{60}^{3-} and C_{60}^{3-}/C_{60}^{4-} with $E_{1/2}$ (vs. Fc^+/Fc) values at -0.65 V (A1'/C1'), -1.11 V (A2'/C2'), -1.61 V (A3'/C3') and -2.07 V (A4'/C4') respectively. All the successive reduction potentials were evenly spaced at ~0.45 V. This unique feature of evenly spaced reduction potentials is a property of molecules having delocalized LUMOs.[65] The highly delocalised π-electron density of C_{60} gives rise to the uniformly spaced reduction potentials. In the case of **C_{60}Z**, the cyclic voltammogram (Figure 4.8) displays two broad cathodic and anodic peaks, within the operational potential window. Considering the broad nature of these peaks, cyclic voltammogram with low scan rate (10 mV s^{-1}) and differential-pulse voltammogram (DPV) (for experimental details please see Section A4.8, Appendix 4) have

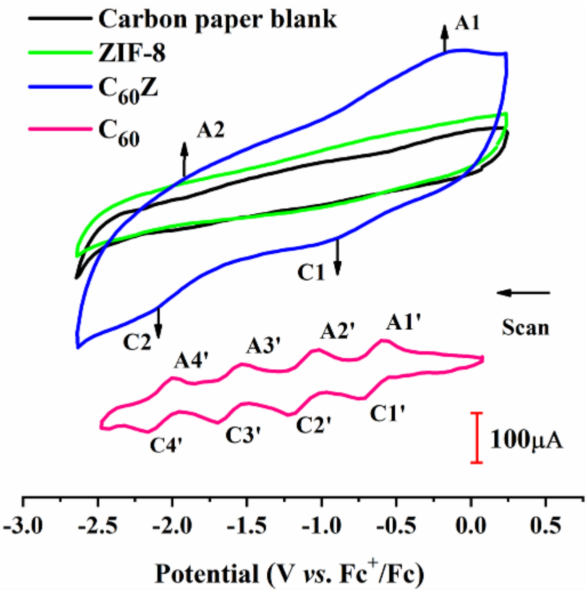

Figure 4.8. Cyclic voltammograms of blank carbon paper (as the working electrode), ZIF-8, **C_{60}Z** (both are insoluble in the 1:2 acetonitrile/toluene solvent mixture; so, these were coated separately from ethanol/water mixture on the carbon cloth working electrode by drop-casting) modified carbon paper and C_{60} (dissolved in 1:2 acetonitrile/toluene mixture, at a concentration of 6×10^{-4} M). All the electrochemical measurements were performed in a 1:2 acetonitrile/toluene solvent mixture taking 0.1 M tetrabutylammonium perchlorate (TBAP) as the supporting electrolyte, under a nitrogen atmosphere at 100 mV s^{-1} scan rate.

been recorded (Figure A4.10, Appendix 4), which help us in attributing the position of these peaks. The cathodic peaks are centered around -0.90 V (C1) and -2.10 V (C2) while the anodic peaks are at -0.17 V(A1) and -1.9 V (A2), relative to Fc^+/Fc. On comparing the voltammograms for **C_{60}Z** (solid-state) and C_{60} in solution, each of these peaks is attributed to 2-electron processes, such that, C1, C2, A2 and A1 correspond to $C_{60} \rightarrow C_{60}^{2-}$ (reductive response), $C_{60}^{2-} \rightarrow C_{60}^{4-}$ (reductive response), $C_{60}^{4-} \rightarrow C_{60}^{2-}$ (oxidative response) and $C_{60}^{2-} \rightarrow C_{60}$ (oxidative response), respectively. This observation is striking and notably different from the cyclic voltammetric features of **C_{60}** in liquid solution. Considering the delocalized LUMOs of the C_{60} molecule *per se*, the cyclic voltammetric feature of **C_{60}Z** was unanticipated before. However, the electronic charge transfer between the host ZIF-8 and the guest fullerene C_{60} (*vide supra*), can result in such a prominent change in the electrochemical behaviour of the composite. The redox peaks in the **C_{60}Z** voltammogram are unevenly spaced or, to be specific, are placed in pairs i.e., the first and second *one-electron-reduction* of the encapsulated fullerene C_{60} corresponding to the transfer of first and second electrons require similar reduction potential (i.e., $C_{60} \rightarrow C_{60}^{1-} \rightarrow C_{60}^{2-}$) in case of the composite. Similarly, the transfer of the third and fourth (i.e., $C_{60}^{2-} \rightarrow C_{60}^{3-} \rightarrow C_{60}^{4-}$), also occur at potential close to each other. There can be two underlying reasons for such a behaviour: (i) the π-electron density on C_{60} inside ZIF-8 is no longer fully delocalised and (ii) the response might be a result of the C_{60} molecule undergoing Jahn-Teller distortion inside ZIF-8 cavity. Both these factors may have cumulatively contributed to the observed electrochemical response. The C_{60} molecule is confined within the cavity of ZIF-8 and is under a completely different microenvironment than it is in the liquid solution. The close proximity of the C_{60} molecule with the inner surface of the ZIF-8 cavity (~ 1 Å) leaves enough scope for interaction between the inner surface of the MOF and the encapsulated C_{60} molecule. There is a high probability of π-π interaction between the 2-methyl imidazole rings of the framework and the encapsulated **C**$_{60}$ molecule. From the XPS data, we get a clear indication of charge transfer happening between the host and guest (Figure 4.7). In liquid solution, the C_{60} molecules are in an isotropic environment but, while in ZIF-8, the surrounding framework is crystalline and rigid, and the electronic environment is non-symmetrical.

This means that the interactions between the guest and host are localized and can be anisotropic in nature. Altogether, the Zn^{2+} ions and the 2-methyl imidazolate ligand of the ZIF-8 framework can possibly localize the π-electron density of C_{60}. And, this is what restricts the absolute delocalization of electron density all over the C_{60} molecule, thereby resulting in unevenly spaced redox responses.

Now, neutral fullerene C_{60} is a centrosymmetric molecule (I_h symmetry) with a closed-shell ground state electronic configuration. But, when the molecule is reduced to C_{60}^{-}, it will tend to undergo Jahn-Teller distortion to lower the symmetry and lift the degeneracy of the triply degenerate LUMOs. This distortion would result in splitting of the t_{1u} orbitals (LUMOs), which means that the first two electrons corresponding to the reduction of C_{60} and C_{60}^{-} respectively, should occupy orbital(s) of the same energy. The addition of a third electron in this case corresponding to the reduction of C_{60}^{2-}, requires higher energy as can be seen from the voltammograms (Figure 4.8). The spacing between C1 and C2 is larger than that of C2’ and C3’. This would generate a spin doublet ground state for C_{60}^{3-}.[65] Next, the fourth incoming electron occupies an orbital of the same energy as the third. Examples of Jahn-Teller distortions in C_{60} anions have been documented before but, in crystals, where the anion was trapped along with some cationic species in the form of solid. [65] A comparable situation can arise when C_{60} participates in site-specific anisotropic host-guest interactions with the ZIF-8 inner surface while being confined within its pores. Of note, in solution, due to the averaged out non-perturbing environment where the molecule is free to undergo all its allowed modes of molecular vibrations, the Jahn-Teller distortion in the molecular anion can be dynamic. This might cause the anions to behave as though in I_h symmetry in liquid solution. X-ray crystallographic data revealed that, a discrete C_{60}^{-} ion is axially compressed (oblate) while, C_{60}^{2-} is axially elongated (prolate).[67,68] In the case of $[Ni(Cp^*)_2][C_{60}]$.PhCN crystal, because of the interactions between C—H of the permethylated cyclopentadienyl ligand and the hexagonal faces of fullerene C_{60}, the fullerene C_{60} possessed orientational ordering, resulting in observable Jahn-Teller distortion in the anion.[68] In our case, a similar situation might be responsible for the observed electrochemical response of **C_{60}Z**.

Thus, it can be inferred that the electrochemical behaviour of the confined C_{60} molecule in ZIF-8 is different from dilute non- aqueous (liquid) solution of the same. Due to the modification in the immediate micro-environment of C_{60} inside the ZIF-8 cavity, C_{60} and its electrochemically generated anions interact with the ZIF-8 surface. Owing to all these factors put together, the successive one-electron reduction potentials of fullerene C_{60} inside ZIF-8 becomes different than that of a dilute liquid solution of fullerene C_{60}. The encapsulated C_{60} in the composite can undergo stepwise two $2e^-$ reductions within a similar potential range, unlike the free C_{60}.

Furthermore, consecutive cycles of cyclic voltammograms of **C60Z** were recorded and compared with C_{60} itself (homogeneous liquid solution) and the composite **C60Z** to understand their relative electrochemical stabilities. C_{60} was found to be unstable as within only 10 cycles of consecutive cyclic voltammetric analysis; the reproducibility of the nature of cyclic voltammograms decreased rapidly (Figure 4.9a). In a homogeneous solution, fulleride ion is a highly reactive species with labile π-electron density. Thus, it can readily bind with other C_{60} molecules, or any other suitable nearby substrate and thereby undergo chemical transformation. On the other hand, no notable change was observed in the electrochemical behaviour of the confined C_{60} inside ZIF-8 during the 200 cycles of cyclic voltammetry (Figure 4.9b). This suggests that the nano-confinement through tailoring of molecular C_{60} into the cavity of ZIF-8 enhances the electrochemical stability of the confined C_{60} and also the fulleride ions inside **C60Z**, generated under the application of cathodic potential. The scope of interaction between the guest C_{60} and the host ZIF-8 plays a crucial role in this notable enhancement of stability. This enhancement of the electrochemical stability of C_{60} inside **C60Z** is a significant achievement and can be crucial for its probable application in device fabrication.

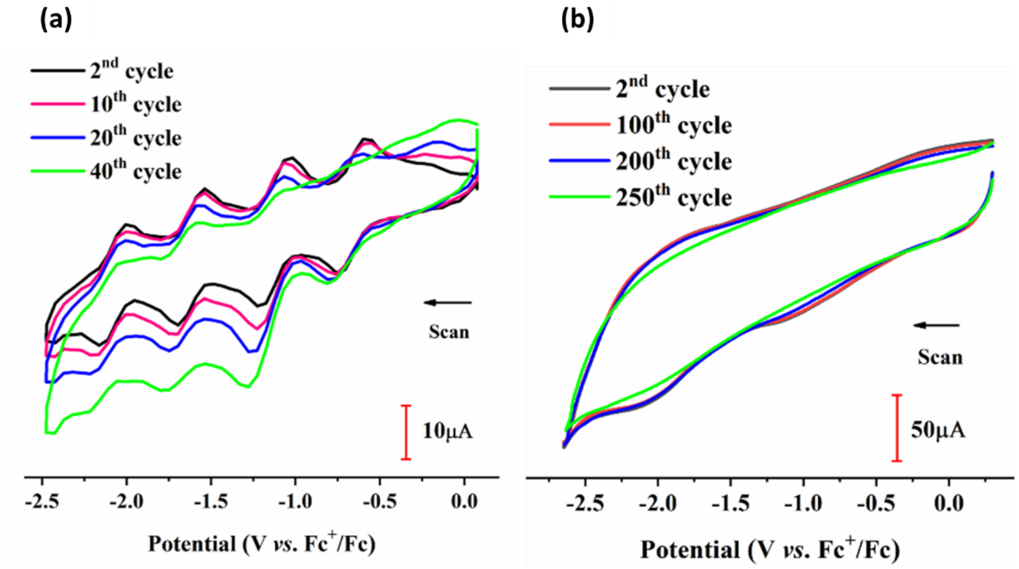

Figure 4.9. (a) Cyclic voltammograms of C_{60} (6×10^{-4} M solution in a 1:2 dry acetonitrile/toluene mixture) at 2nd, 10th, 20th and 40th cycle. (b) Cyclic voltammograms of **C60Z** at 2nd, 100th, 200th and 250th cycles. All the electrochemical measurements were performed in a 1:2 acetonitrile/toluene solvent mixture taking 0.1 M tetrabutylammonium perchlorate (TBAP) as the supporting electrolyte, under a nitrogen atmosphere at 100 mV s^{-1} scan rate.

4.3.9.2. Electrochemical analysis of oxygen reduction reaction (ORR) catalysis

C_{60} is well-known for its capacity to perform electrocatalytic ORR,[36] and several attempts are being made for its heterogenization and to improve it as a catalyst.[31-38] However, the spatial separation and electronic redistribution due to modification in the immediate microenvironment as the result of encapsulation in a rigid yet porous molecular framework is of huge potential in terms of systematically modifying the electrochemical properties of C_{60}. Thus, electrocatalytic oxygen reduction reaction (ORR) performed by **C_{60}Z** was studied as a model electrochemical reaction and compared with that of C_{60} (non-encapsulated) and ZIF-8. All the electrochemical measurements were performed in a gas-tight cell with a three-electrode setup; Ag/AgCl was used as the reference, glassy carbon as the working, and Pt as the counter electrode. A detailed description of the relevant electrochemical methodology is provided in section 4.2.3. The electrochemical activity of **C_{60}Z** towards ORR was evaluated by electrochemical measurements in Ar- and O_2-saturated 0.1 M KOH solution (Figure A4.11, Appendix 4). No obvious reduction peak is present in the Ar-saturated solution, but there is a huge current increment in the O_2-saturated solution, suggesting a distinct electrocatalytic activity toward ORR for **C_{60}Z**. Comparing the activity of **C_{60}Z** with that of C_{60} (Figure 4.10), it is found that the synthesized **C_{60}Z** composite has demonstrated a considerably higher catalytic current density of 2.6 mA cm^{-2}, than C_{60} (1.4 mA cm^{-2}) at 0.3 V (vs. RHE). Of note, the loading of C_{60} inside **C_{60}Z** is much lower compared to that of solid C_{60} fabricated on a glassy carbon electrode. Despite such a low density of C_{60} in **C_{60}Z**, the observed high catalytic current

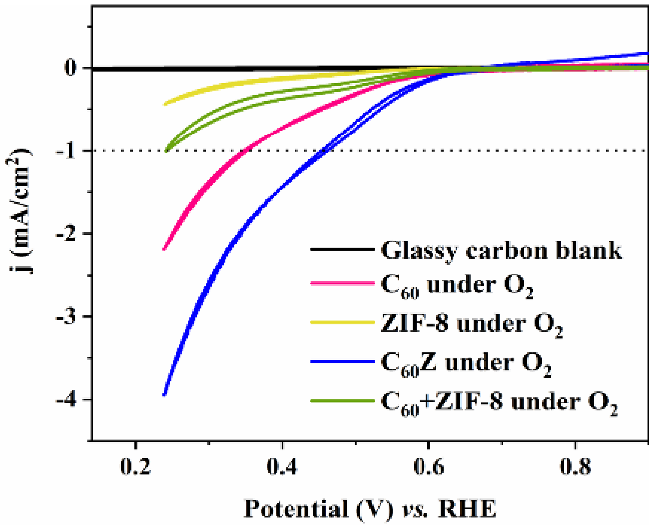

Figure 4.10. Cyclic voltammograms of blank glassy carbon (as working electrode), C_{60}, ZIF-8, **C_{60}Z** and (C_{60}+ZIF-8) at 100 mV s^{-1} scan rate, in O_2 saturated 0.1 M KOH.

density emphasizes a better electrocatalytic ORR performance of **C_{60}Z**. This is possibly a consequence of (a) host-guest supramolecular interactions (b) better accessibility and therefore a better mass transport of (OH^-, O_2) and (H_2O_2, H_2O) to and from the catalytically active C_{60} entrapped in the porous framework, compared to densely packed solid C_{60} loaded on a conventional flat solid surface. Unlike a flat surface, where the catalysis can be greatly hindered by the mass transport limitations, the low loading of C_{60} (10% occupancy of available cages) inside ZIF-8 combined with the highly porous structure of the MOF may enable participation of most of the entrapped C_{60} to ORR catalysis and thereby contribute significantly to the observed high catalytic current density.

Moreover, the onset potential (defined here as the potential required to achieve a catalytic current density of 1 mA cm^{-2})[69] for **C_{60}Z** is less than that of free C_{60} by ~100 mV. This improvement in the inherent electrocatalytic ORR activity of the encapsulated C_{60} can be considered to be an effect of the electron enrichment of the C_{60} inside the MOF; similar effects have been observed to play a pivotal role in carbon nanomaterial-based ORR electrocatalysts.[31,32] The increased catalytic current and lower onset potential requirement for electrocatalytic ORR performed by **C_{60}Z** establishes the significance of designing suitable host-guest composite using porous frameworks (e.g., MOFs).

The selectivity of the **C_{60}Z** composite towards the electrocatalytic generation of H_2O_2 through ORR has evaluated using the rotating ring-disk electrode technique (rotation rate of 1600 rpm). The percentage of H_2O_2 generated from the ORR could be quantified from the ring and disk current as obtained from Figure 4.11a. The product selectivity of the catalyst **C_{60}Z** has been determined at different applied potentials and compared with that of C_{60}. The **C_{60}Z** composite displays a much higher selectivity towards H_2O_2 production than C_{60} itself over a wide range of potential (Figure 4.11b). Thus, the composite **C_{60}Z**, as prepared from the encapsulation of C_{60}, turned out to be a better ORR catalyst than C_{60} itself, both in terms of electrocatalytic activity and product selectivity. Furthermore, negligible loss in catalytic current during 4 hours of chronoamperometric measurement at 0.45 V (vs RHE) (Figure A4.12, Appendix 4) shows **C_{60}Z** to be stable towards electrocatalytic ORR.

In order to compare the effect of C_{60} loading variation on the catalytic activity of the composite, two samples were prepared having approximately double and triple the

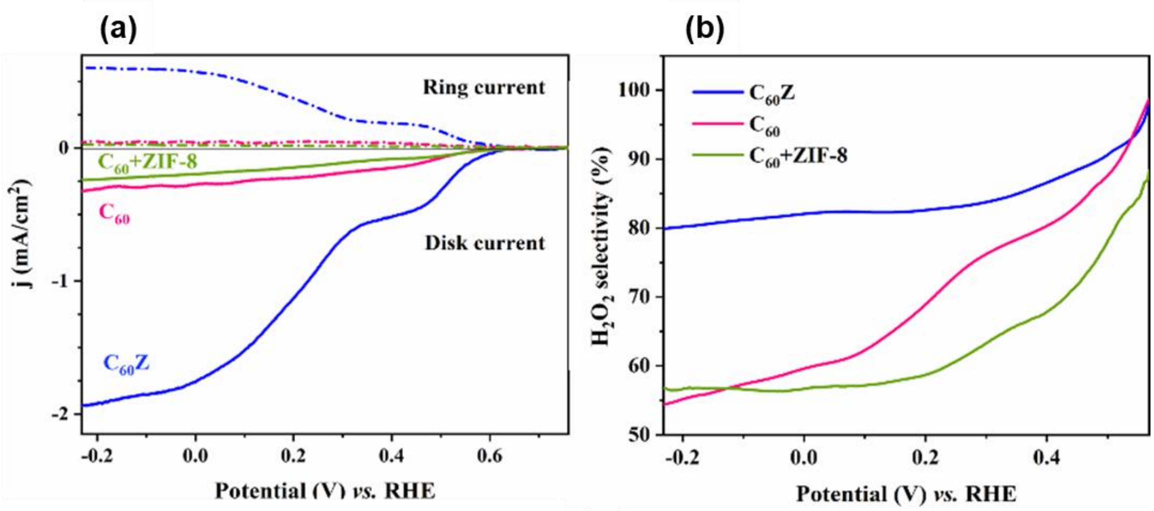

Figure 4.11. (a) Polarization curves of C_{60}, **C_{60}Z** and (C_{60} + ZIF-8) for the oxygen reduction reaction (ORR) and H_2O_2 generation using a rotating ring-disk electrode (RRDE) at 1600 rpm, and 10 mV s^{-1} scan rate, in O_2 saturated 0.1 M KOH; (b) H_2O_2 product selectivity of C_{60}, **C_{60}Z** and (C_{60} + ZIF-8) as obtained from the RRDE method.

amount of C_{60} loading as compared to **C_{60}Z**. The detailed characterization and electrochemical studies of these composites are provided in appendix 4 (section A4.9). These composites named as **C_{60}Z – 17%** and **C_{60}Z – 33%**, contains 1 C_{60} per 6 ZIF-8 and 1 C60 per 3 ZIF-8 cages, respectively, which account for approximately 17% and 33% occupancy, respectively of the maximum theoretical number of cages available. With the use of **C_{60}Z – 17%** sample, the ORR catalytic current (Figure A4.15, Appendix 4) enhances, as can be expected due to an increase in the number of catalytically active centers. A higher loading of active species in the composite means higher density of active catalysts near the electrode surface which eventually may lead to increase in catalytic current density. Although, the enhancement (11% increase in current density) is not exactly proportional to the extent of increase in the density of active sites. The H_2O_2 product selectivity (Figure A4.16, Appendix 4) is similar to that of **C_{60}Z**. With increasing the loading further with **C_{60}Z – 33%** composite, the cataytic current did not show any improvement. This might happen because the diffusion of reactants/ products to and from all the catalytically active centers might get hindered with higher loading of guests in the pores of ZIF-8. This implies that maintaining an optimum loading of guest in matrix is beneficial for acheiving better electrocatalytic activity.

To negate the possibility of any surface-bound C_{60} playing the key role in the enhanced electrocatalytic activity and better product selectivity of **C_{60}Z**, a physical mixture (C_{60}+ZIF-8) was prepared using pre-synthesized ZIF-8, as part of controlled experiments (section A4.10, Appendix 4). For the sake of comparability, the content of C_{60} in the physical mixture was maintained almost same as the loading amount of C_{60} in **C_{60}Z**. Characterization of the material using PXRD (Figure A4.17), FT-IR (Figure A4.18) and UV (Figure A4.19), confirmed that the properties of (C_{60}+ZIF-8) are different from that of **C_{60}Z**. The electrochemical ORR activity of (C_{60}+ZIF-8) physical mixture is comparable to that of C_{60} but considerably different than **C_{60}Z** (Figure 4.10). The catalytic current density as well as product selectivity are considerably improved for **C_{60}Z**, even though both the compounds have almost equal amount of C_{60} content. This further proves that (a) the **C_{60}Z** composite is not a case of MOF surface-bound C_{60} but the C_{60} molecules are encapsulated within the cavities of the ZIF-8; (b) the electronic charge transfer, due to the encapsulation process for **C_{60}Z**, plays a major role behind the observed improved performance of **C_{60}Z** compared to C_{60} as such and (C_{60}+ZIF-8) physical mixture in terms of ORR onset potential requirement and selectivity towards H_2O_2 production.

4.3.10. Fabrication of C_{60}Z into a membrane

C_{60} molecule as such is known to have extremely low solubility in most of the common solvents, which makes it difficult to obtain C_{60} in a processable form. It further tends to form aggregates over time in the solution, thereby altering its electronic properties. So, getting this molecule into a processable form is as important as getting that form to retain the dilute solution-like properties of fullerene C_{60}. Solid **C_{60}Z** demonstrates the electronic properties analogous to that of a dilute solution of fullerene. But, for such solid crystalline material to be usable in devices, it is always preferable to process it into films. The processability of **C_{60}Z** has been attempted by incorporating **C_{60}Z** into a polymer-supported membrane as nano-fillers, following a reported protocol[70] (Scheme 4.2) using polyvinyl alcohol (PVA) (detailed synthesis provided in section 4.2.2). The synthesized composite membrane **C_{60}Z-PVA** was characterized using PXRD, FT-IR and FESEM (section A4.11, Appendix 4), and its features are compared with those of **C_{60}Z** and PVA. The PXRD pattern (Figure A4.20) and FT-IR spectrum (Figure A4.21) of **C_{60}Z-PVA** matched predominantly with those of PVA, and the characteristic peaks due to **C_{60}Z** are similarly positioned as in unmodified **C_{60}Z**. The FESEM images of the cross-section of the **C_{60}Z-PVA** membrane (Figure A4.22, Appendix 4) shows the dispersed **C_{60}Z** nanofillers across the membrane. An EDX mapping of the **C_{60}Z-PVA** membrane clearly shows the uniform dispersion of

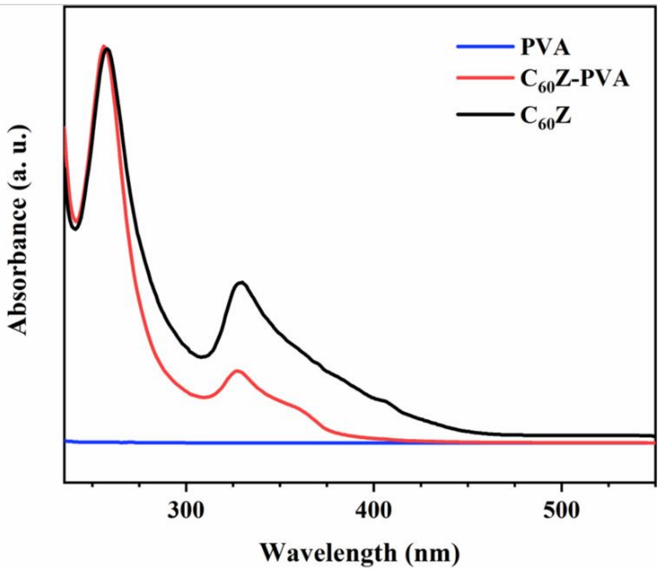

Figure 4.12. UV-Visible absorption spectra of **C_{60}Z**, PVA and **C_{60}Z-PVA**.

C_{60}Z nanofillers in the membrane (Figure A4.22, Appendix 4). PVA does not have any noticeable absorption in the UV-visible region (Figure 4.12), the **C_{60}Z-PVA** membrane however, shows strong absorption due to the presence of **C_{60}Z** composite as nanofillers. The positions of the absorption peaks match quite well with those of **C_{60}Z** (Figure 4.12). Thus, it can be inferred that the electronic properties of this solid-state analogue (**C_{60}Z**) of dilute liquid fullerene solution, are well retained in its processed form **C_{60}Z-PVA**. Although a detailed study of real-field application is out of the scope of this work, such an approach to prepare composite membranes with different polymers and **C_{60}Z** can prove to be of huge potential for various electrochemical and photophysical applications.

Thus, the present study offers the scope of development of functional materials using simple molecules (e.g., fullerene) and MOFs (*e.g.* ZIF-8), by exploiting their unique supramolecular interactions. And for such examples, the selection of MOF plays a key role in the modified functional behaviour of the material. In our case, three-fold benefits of using ZIF-8 MOF as host are found: (a) facile mass transport through porous MOF framework; (b) mono-confinement of C_{60} in a single cavity and thereby homogeneous distribution along with high dilution (1 in each 10 cages) of C_{60} molecules and (c) high mechanical stability of the guest C_{60} in **C_{60}Z** (since there is no scope of its leaching out). In addition, this particular approach has also helped us to overcome one major drawback of fullerene – its tendency to form aggregates over time, which poses serious challenges towards using fullerene C_{60} for practical applications.[71-74] But in our case, the composite

C_{60}Z has one C_{60} molecule per ten cages of ZIF-8. It gives rise to an excellent dispersion of fullerene C_{60} inside ZIF-8 MOF, where C_{60} molecules practically have no scope of interaction amongst themselves.

Thus, the major findings of this work can be summarized as (1) confinement-induced modification of electrochemical behavior and enhanced electrochemical stability of C_{60} in **C_{60}Z**; (2) improved catalytic activity of **C_{60}Z** in terms of lower overpotential requirement and higher catalytic current compared to free C_{60} towards ORR; (3) inheritance of similar photophysical property in **C_{60}Z** composite and its processed form **C_{60}Z-PVA**, which is comparable to that of fullerene in dilute solution. This approach of fabricating molecular level non-aggregated fullerene in solid, porous MOF matrix and thereby in a polymer-supported thin film, opens up a wide range of scope of using fullerene in a solid matrix as a solid-dilute-solution of fullerene for device making.

4.4 CONCLUSIONS

In this work, mono-confinement of C_{60} in every 1 out of 10 cavities/pores of ZIF-8 MOF is successfully performed such that the composite possesses homogeneously distributed, spatially separated, nano-sized, C_{60} molecules in a solid MOF matrix. This makes the composite possess similarities with a dilute solution of C_{60} prepared in liquid solution. The synthetic strategy depicts a pathway to inherit the properties of molecular C_{60} and counteracts the possibility of aggregation._The supramolecular interactions give rise to interesting outcomes, observable through the electrochemical and photoluminescence responses. The long-term electrochemical stability of the encapsulated molecular C_{60} and improved catalytic activity towards electrocatalytic ORR, show the huge scope of application for the fullerene-MOF composite. This work also highlights the usefulness of MOFs as host materials. The emergent and lesser-known electrochemistry and photophysics of this composite are not only important from the fundamental point of view, but also for device making. We have further demonstrated the processibility of the insoluble **C_{60}Z** composite by fabricating it as nanofillers into a polymer-supported thin film; which also retains the characteristics of the title composite.

Appendix 1: Instrumental details and sample preparation.

Appendix 4: Characterization of **C_{60}Z-n**; calculation of C_{60} loading level in **C_{60}Z-n**; calculation of band gap from Tauc plots; details of controlled experiment with higher C_{60}

loaded **C_{60}Z** composites, and a physical mixture (C_{60}+ZIF-8); characterization of **C_{60}Z-PVA** membrane.

4.5 REFERENCES

1. Morris, R. E.; Wheatley, P. S. Gas Storage in Nanoporous Materials. *Angew. Chem. Int. Ed.* **2008**, *47*, 4966−4981.
2. James, S. L. Metal-organic frameworks. *Chem. Soc. Rev.* **2003**, *32*, 276–288.
3. Kitagawa, S.; Kitaura R.; Noro, S.-i. Functional Porous Coordination Polymers. *Angew. Chem. Int. Ed.* **2004**, *43*, 2334–2375.
4. Evans O. R.; Lin, W. Crystal Engineering of NLO Materials Based on Metal−Organic Coordination Networks. *Acc. Chem. Res.* **2002**, *35*, 511–522.
5. Dincă, M.; Long, J. R. Hydrogen storage in microporous metal-organic frameworks with exposed metal sites. *Angew. Chem. Int. Ed.* **2008**, *47*, 6766–6779.
6. Mukhopadhyay, S.; Basu, O.; Nasani, R.; Das, S. K. Evolution of metal organic frameworks as electrocatalysts for water oxidation. *Chem. Commun.* **2020**, *56*, 11735–11748.
7. Gao, R.; Kodaimati, M. S.; Yan, D. Recent advances in persistent luminescence based on molecular hybrid materials. *Chem. Soc. Rev.* **2021**, *50*, 5564–5589.
8. Islamoglu, T.; Goswami, S.; Li, Z.; Howarth, A. J.; Farha, O. K.; Hupp, J. T. Postsynthetic Tuning of Metal-Organic Frameworks for Targeted Applications. *Acc. Chem. Res.* **2017**, *50*, 805−813.
9. Dubois, D.; Kadish, K. M.; Flanagan, S.; Wilson, L. J. Electrochemical detection of fulleronium and highly reduced fulleride (C_{60}^{5-}) ions in solution. *J. Am. Chem. Soc.* **1991**, *113*, 7773-7774.
10. Xie, Q.; Perez-Cordero, E.; Echegoyen, L. Electrochemical detection of C_{60}^{6-} and C_{70}^{6-}: Enhanced stability of fullerides in solution, *J. Am. Chem. Soc.* **1992**, *114*, 3977-3980.
11. Olah, G. A.; Bucsi, I.; Aniszfeld, R.; Prakash, G. K. S. Chemical reactivity and functionalization of C_{60} and C_{70} fullerenes, *Carbon* 1992, **30**, 1203-1211.
12. Olah, G. A.; Bucsi, I.; Lambert, C.; Aniszfeld, R.; Trivedi, N. J.; Sensharma, D. K.; Prakash, G. K. S. Polyarenefullerenes, $C_{60}(H\text{-}Ar)_n$, obtained by acid-catalyzed fullerenation of aromatics. *J. Am. Chem. Soc.* **1991**, *113*, 9387-9388.
13. Fagan, P. J.; Calabrese, J. C.; Malone, B. Metal complexes of buckminsterfullerene (C_{60}). *Acc. Chem. Res.* **1992**, *25*, 134-142.
14. Tzirakis M. D.; Orfanopoulos, M. Radical Reactions of Fullerenes: From Synthetic Organic Chemistry to Materials Science and Biology. *Chem. Rev.* **2013**, *113*, 5262−5321.
15. Balch, A. L.; Olmstead, M. M. Reactions of Transition Metal Complexes with Fullerenes (C_{60}, C_{70}, etc.) and Related Materials. *Chem. Rev.*, **1998**, *98*, 2123-2165.
16. Orlandi, G.; Negri, F. Electronic states and transitions in C_{60} and C_{70} fullerenes. *Photochem. Photobiol. Sci.* **2002**, *1*, 289–308.
17. Ohsawa, Y.; Saji, T. Electrochemical detection of C_{60}^{6-} at low temperature. *J. Chem. Soc., Chem. Commun.* **1992**, 781-782.
18. Xie, Q.; Pe´ rez-Cordero, E.; Echegoyen, L. Electrochemical detection of C_{60}^{6-} and C_{70}^{6-}: Enhanced stability of fullerides in solution. *J. Am. Chem. Soc.* **1992**, *114*, 3978-3980.
19. Winkler, K.; Costa, D. A.; Balch, A. L.; Fawcett, W. R.; The electroreduction of C_{60} films in solutions containing crown ether complexes of alkali metal cations. *J. Electroanal. Chem.* **1998**, *456*, 229-237.
20. Nakamura, E.; Isobe, H.; Functionalized Fullerenes in Water. The First 10 Years of Their Chemistry, Biology, and Nanoscience. *Acc. Chem. Res.* **2003**, *36*, 807-815.
21. Sherigara, B. S.; Kutner, W.; D'Souza, F. Electrocatalytic Properties and Sensor Applications of Fullerenes and Carbon Nanotubes. *Electroanalysis* **2003**, *15*, 753-772.
22. Jariwala, D.; Sangwan, V. K.; Lauhon, L. J.; Marks, T. J.; Hersam, M. C. Carbon nanomaterials for electronics, optoelectronics, photovoltaics, and sensing. *Chem. Soc. Rev*. **2013**, *42*, 2824-2860.
23. Ohkubo, K.; Kotani, H.; Shao, J. G.; Ou, Z. P.; Kadish, K. M.; Li, G. L.; Pandey, R. K.; Fujitsuka, M.; Ito, O.; Imahori, H.; Fukuzumi, S. Production of an Ultra-Long-Lived Charge-Separated State in a Zinc Chlorin–C_{60} Dyad by One-Step Photoinduced Electron Transfer. *Angew. Chem., Int. Ed.* **2004**, *43*, 853-856.
24. Bendikov, M.; Wudl, F. Tetrathiafulvalenes, Oligoacenenes, and Their Buckminsterfullerene Derivatives: The Brick and Mortar of Organic Electronics. *Chem. Rev.* **2004**, *104*, 4891-4946.

25. Guldi, D. M.; Luo, C. P.; Koktysh, D.; Kotov, N. A.; Da Ros, T.; Bosi, S.; Prato, M. Photoactive Nanowires in Fullerene−Ferrocene Dyad Polyelectrolyte Multilayers. *Nano Lett.* **2002**, *2*, 775-780.
26. Guenes, S.; Neugebauer, H.; Sariciftci, N. S. Conjugated Polymer-Based Organic Solar Cells. *Chem. Rev*. **2007**, *107*, 1324-1338.
27. Mihailetchi, V.; Van Duren, K. K.; Blom, P.; Hummelen, J. C.; Janssen, R.; Kroon, J.; Rispens, M.; Verhees, W.; Wienk, M. Charge Transport and Photocurrent Generation in Poly(3-hexylthiophene): Methanofullerene Bulk-Heterojunction Solar Cells. *Adv. Funct. Mater*. **2006**, *16*, 699-708.
28. Li, M.; Xu, P.; Yang, J.; Yang, S. Donor-π-acceptor double-cable polythiophenes bearing fullerene pendant with tunable donor/acceptor ratio: A facile postpolymerization. *J. Mater. Chem*. **2010**, *20*, 3953-3960.
29. Wang, S.; Xiao, S.; Li, Y.; Shi, X.; Du, C.; Fang, H.; Zhu, D. Synthesis and characterization of new C_{60}–PPV dyads containing carbazole moiety. *Polymer* **2002**, *43*, 2049-2054;
30. Collavini, S.; Delgado, J. L. Fullerenes: the stars of photovoltaics, *Sustainable Energy Fuels*. **2018**, *2*, 2480–2493.
31. Hasanzadeh, A.; Khataee, A.; Zarei, M.; Zhang, Y. Two-electron oxygen reduction on fullerene C_{60}-carbon nanotubes covalent hybrid as a metal-free electrocatalyst. *Scientific Reports* **2019**, *9*, 13780.
32. Gao, R.; Dai, Q.; Du, F.; Yan, D.; Dai, L. C_{60}-Adsorbed Single-Walled Carbon Nanotubes as Metal-Free, pH-Universal, and Multifunctional Catalysts for Oxygen Reduction, Oxygen Evolution, and Hydrogen Evolution. *J. Am. Chem. Soc*. **2019**, *141*, 11658−11666.
33. Wakahara, T.; Sathish, M.; Miyazawa, K.; Ito, O. Electrochemical Characterization of Catalytic Activities of C_{60} Nanowhiskers to Oxygen Reduction in Aqueous Solution. *Fuller. Nanotub. Carbon Nanostructures* **2014**, *23*, 509–512.
34. Gao, F.; Zhao, G-L.; Yang, S.; Spivey, J. J. Nitrogen-Doped Fullerene as a Potential Catalyst for Hydrogen Fuel Cells. *J. Am. Chem. Soc.* **2013**, *135*, 3315−3318.
35. Ahsan, Md A.; He, T.; Eid, K.; Abdullah, A. M.; Curry, M. L.; Du, A.; Santiago, A. R. P.; Echegoyen, L.; Noveron, J. C. Tuning the Intermolecular Electron Transfer of Low-Dimensional and Metal-Free BCN/C_{60} Electrocatalysts via Interfacial Defects for Efficient Hydrogen and Oxygen Electrochemistry. *J. Am. Chem. Soc.* **2021**, *143*, 1203−1215.
36. Chen, X.; Chang, J.; Ke, Q. Probing the activity of pure and N-doped fullerenes towards oxygen reduction reaction by density functional theory. *Carbon* **2018**, *126*, 53-57.
37. Vashchenko, A. V.; Kuzmin, A. V.; Shainyan, B. A. Single Si-doped fullerene as a catalyst in the oxygen reduction reaction: A quantum chemical insight. *Int J Quantum Chem*. **2021**, ***7***, e26565.
38. Girôn, R. M.; Marco-Martinez, J.; Bellani, S.; Insuasty, A.; Rojas, H. C.; Tullii, G.; Antognazza, M. R.; Filippone, S.; Martin, N. Synthesis of modified fullerenes for oxygen reduction reactions. *J. Mater. Chem. A* **2016**, *4*, 14284–14290.
39. Park, K. S.; Ni, Z.; Côté, A. P.; Choi, J. Y.; Huang, R.; Uribe-Romo, F. J.; Chae, H. K.; O'Keeffe, M.; Yaghi, O. M. Exceptional chemical and thermal stability of zeolitic imidazolate frameworks. *PNAS* **2006**, *27*, 10186 –10191.
40. Mukhopadhyay, S.; Basu, O.; Kar, A.; Das, S. K. Efficient Electrocatalytic Water Oxidation by Fe(salen)–MOF Composite: Effect of Modified Microenvironment. *Inorg. Chem*. **2020**, *59*, 472-483.
41. Manna, P.; Debgupta, J.; Bose, S.; Das, S. K. A Mononuclear Co(II) Coordination Complex Locked in a Confined Space and Acting as an Electrochemical Water-Oxidation Catalyst: A "Ship-in-a-Bottle" Approach. *Angew.Chem. Int.Ed.* **2016**, *55*, 2425 –2430.
42. Mukhopadhyay, S.; Debgupta, J.; Singh, C.; Kar, A.; Das, S. K. A Keggin Polyoxometalate Shows Water Oxidation Activity at Neutral pH: POM@ZIF-8, an Efficient and Robust Electrocatalyst, *Angew.Chem.Int. Ed.* **2018**, *57*,1918 –1923.
43. Kulkarni, A.; Siahrostami, S.; Patel, A.; Nørskov, J. K. Understanding Catalytic Activity Trends in the Oxygen Reduction Reaction. *Chem. Rev.* **2018**, *118*, 2302−2312.
44. Musser, A. J.; Neelakandan, P. P.; Richter, J. M.; Mori, H.; Friend, R. H.; Nitschke, J. R. Excitation Energy Delocalization and Transfer to Guests within $M^{II}_4L_6$ Cage Frameworks. *J. Am. Chem. Soc.* **2017**, *139*, 12050- 12059.
45. Feng, Y.; Wang, T.; Li, Y.; Li, J.; Wu, J.; Wu, B.; Jiang, L.; Wang, C. Steering Metallofullerene Electron Spin in Porous Metal–Organic Framework. *J. Am. Chem. Soc*. **2015**, *137*, 15055- 15060.
46. Gao, Y.; Wu, X.; Zeng, X. C. Designs of fullerene-based frameworks for hydrogen storage. *J. Mater. Chem. A* **2014**, *2*, 5910-5914.

47. Thornton, A. W.; Nairn, K. M.; Hill, J. M.; Hill, A. J.; Hill, M. R. Metal−Organic Frameworks Impregnated with Magnesium-Decorated Fullerenes for Methane and Hydrogen Storage. *J. Am. Chem. Soc*. **2009**, *131*, 10662- 10669.
48. Yuan, Y.; Cui, P.; Tian, Y.; Zou, X.; Zhou, Y.; Sun, F.; Zhu, G. Coupling fullerene into porous aromatic frameworks for gas selective sorption. *Chem. Sci*. **2016**, *7*, 3751-3756.
49. Guan, J.; Zhong, X.; Chen, X.; Zhu, X.; Li, P.; Wu, J.; Lu, Y.; Yu, Y.; Yang, S. Expanding pore sizes of ZIF-8-derived nitrogen-doped microporous carbon via C_{60} embedding: toward improved anode performance for the lithium-ion battery. *Nanoscale* **2018**, *10*, 2473-2480.
50. Martinez, V.; Karadeniz, B.; Biliškov, N.; Lončarić, I.; Muratović, S.; Žilić, D.; Avdoshenko, S. M.; Roslova, M.; Popov, A. A.; Užarević, K. Tunable Fulleretic Sodalite MOFs: Highly Efficient and Controllable Entrapment of C_{60} Fullerene via Mechanochemistry. *Chem. Mater.* **2020**, *32*, 10628−10640.
51. Wu, J.; Wang, S.; Lei, Z.; Guan, R.; Chen, M.; Du, P.; Lu, Y.; Cao, R.; Yang, S. Pomegranate-like C_{60}@cobalt/nitrogen-codoped porous carbon for high-performance oxygen reduction reaction and lithium-sulfur battery. *Nano Res.* **2020**, *14*, 2596–2605.
52. Tanaka, S.; Fujita, K.; Miyake, Y.; Miyamoto, M.; Hasegawa, Y.; Makino, T.; Van der Perre, S.; Remi, J. C. S.; Assche, T. V.; Baron, G. V.; Denayer, J. F. M. Adsorption and Diffusion Phenomena in Crystal Size Engineered ZIF-8 MOF. *J. Phys. Chem. C* **2015**, *119*, 28430−28439.
53. Chase, B.; Fagan, P. J. Substituted C_{60} molecules: a study in symmetry reduction. *J. Am. Chem. Soc.* **1992**, *114*, 2252-2256.
54. Yang, C. C.; Li, S. Size-dependent Raman red shifts of semiconductor nanocrystals. *J. Phys. Chem. B* **2008**, *112*, 14193–14197.
55. Saraswati, T. E.; Setiawan, U. H.; Ihsan, M. R.; Isnaeni, I.; Herbani, Y. The Study of the Optical Properties of C_{60} Fullerene in Different Organic Solvents, *Open Chem.* **2019**, *17*, 1198−1212.
56. Lee, J.; Cho, M.; Fortner, J. D.; Hughes, J. B.; Kim, J–H. Transformation of Aggregated C_{60} in the Aqueous Phase by UV Irradiation. *Environ. Sci. Technol.* **2009**, *43*, 4878–4883.
57. Mchedlov-Petrossyana, N. O.; Kamneva, N. N.; Al-Shuuchi, Y. T. M.; Marynin, A. I.; Shekhovtsov, S. V. The peculiar behavior of fullerene C_{60} in mixtures of 'good' and polar solvents: Colloidal particles in the toluene–methanol mixtures and some other systems. *Colloids and Surfaces A: Physicochem. Eng. Aspects* **2016**, *509*, 631–637.
58. Pavlovich, V. S.; Shpilevsky, E. M. Absorption and fluorescence spectra of C_{60} fullerene concentrated solutions in hexane and polystyrene at 77–300 K. *J. Appl. Spectrosc.* **2010**, *77*, 335-342.
59. Zhao, Y.; Fang Y.; Jiang, Y. Fluorescence study of fullerene in organic solvents at room temperature. *Spectrochim. Acta A* **2006**, *64*, 564–567.
60. Kim, D.; Lee, M. Observation of fluorescence emission from solutions of C_{60} and C_{70} fullerenes and measurement of their excited-state lifetimes. *J. Am. Chem. Soc.* **1992**, *114*, 4429−4430.
61. Biswal, B. P.; Shinde, D. B.; Pillai, V. K.; Banerjee, R. Stabilization of graphene quantum dots (GQDs) by encapsulation inside zeolitic imidazolate framework nanocrystals for photoluminescence tuning. *Nanoscale* **2013**, *5*, 10556–10561.
62. Gu, G.; Ding, W.; Cheng, G.; Zhang, S.; Du, Y.; Yang, S. Photoluminescence studies on C_{60} trapped in NiY zeolite. *Chem. Phys. Lett.* **1997**, *270*, 135-138.
63. Tian, F.; Cerro, A. M.; Mosier, A. M.; Wayment-Steele, H. K.; Shine, R. S.; Park, A.; Webster, E. R.; Johnson, L. E.; Johal, M. S.; Benz, L. Surface and Stability Characterization of a Nanoporous ZIF-8 Thin Film. *J. Phys. Chem. C* **2014**, *118*, 14449−14456.
64. Woll, C. The chemistry and physics of zinc oxide surfaces, *Prog. Surf. Sci.* **2007**, *82*, 55−120.
65. Reed, C. A.; Bolskar, R. D. Discrete Fulleride Anions and Fullerenium Cations. *Chem. Rev.* **2000**, *100*, 1075-1120.
66. Martín, N.; Sánchez, L.; Illescas, B.; Pérez, I. C_{60}-Based Electroactive Organofullerenes. *Chem. Rev.* **1998**, *98*, 2527-2548.
67. Wan, W. C.; Liu, X.; Sweeney, G. M.; Broderick, W. E. Structural Evidence for the Expected Jahn-Teller Distortion in Monoanionic C_{60}: Synthesis and X-ray Crystal Structure of Decamethylnickelocenium Buckminsterfulleride. *J. Am. Chem. Soc.* **1995**, *117*, 9580-9581.
68. Paul, P.; Xie, Z.; Bau, R.; Boyd, P. D. W.; Reed, C. A. Ordered Structure of a Distorted C_{60}^{2-} Fulleride Ion. *J. Am. Chem. Soc*. **1994**, *116*, 4145−4146.
69. Liberman, I.; Shimoni, R.; Ifraemov, R.; Rozenberg, I.; Singh, C.; Hod, I. Active-Site Modulation in an Fe-Porphyrin-Based Metal–Organic Framework through Ligand Axial Coordination: Accelerating Electrocatalysis and Charge-Transport Kinetics. *J. Am. Chem. Soc.* **2020**, *142*, 1933−1940.

70. Mukhopadhyay, S.; Das, A.; Jana, T.; Das, S. K. Fabricating a MOF Material with Polybenzimidazole into an Efficient Proton Exchange Membrane. *ACS Appl. Energy Mater.* **2020**, *3*, 7964- 7977.
71. Prylutskyy, Y. I.; Buchelnikov, A. S.; Voronin, D. P.; Kostjukov, V. V.; Ritter, U.; Parkinson, J. A.; Evstigneev, M. P. C_{60} fullerene aggregation in aqueous solution, *Phys. Chem. Chem. Phys*. **2013**, *15*, 9351-9360.
72. Dattani, R.; Gibson, K. F.; Few, S.; Borg, A. J.; DiMaggio, P. A.; Nelson, J.; Kazarian, S. G.; Cabral, J. T. Fullerene oxidation and clustering in solution induced by light. *J Colloid and Interfac Sci.* **2015**, *446*, 24-30.
73. Yang, X.; Niu, M.; Bi, P.; Chen, Z.; Liu, J.; Hao, X. Suppressing Thermally Induced Fullerene Aggregation in Organic Solar Cells by Employing Plastic Network. *J. Phys. Chem. C* **2018**, *122*, 9843−9851.
74. Maggini, M.; De Faveri, C.; Scorrano, G.; Prato, M.; Brusatin, G.; Guglielmi, M.; Meneghetti, M.; Signorini, R.; Bozio, R. Synthesis and Optical-Limiting Behavior of Hybrid Inorganic–Organic Materials from the Sol–Gel Processing of Organofullerenes. *Chem-Eur. J*. **1999**, *5*, 2501-2510.

CHAPTER 5

A 60-Electron-reduced {Mo_{132}} POM Acting as a Sink to Accommodate 60 More Electrons: a Stable Heterogeneous HER Electrocatalyst

OVERVIEW:

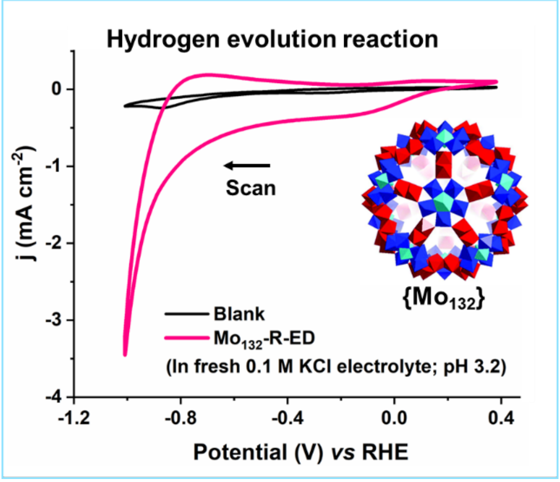

Developing an efficient and stable hydrogen evolution reaction (HER) catalyst is of utmost importance nowadays. Polyoxometalates (POMs) are well-known for their reversible redox activity, which make them high-potential materials for energy applications. In this work, we report an 120-electron-reduced heterogeneous electrocatalyst **Mo_{132}-R-ED**, synthesized by the electrochemical reduction of a highly water soluble, 60-electron-reduced giant POM, {Mo_{132}}. Using several characterization techniques and performing redox titration, it was confirmed that, **Mo_{132}-R-ED** contains parent 60-electron-reduced {Mo_{132}} clusters which are further reduced by ~ 60 more electrons. While parent water-soluble-{Mo_{132}} itself is not catalytically active towards HER, **Mo_{132}-R-ED** is found to be a stable and efficient electrocatalyst towards HER, having a hydrogen evolution turn over frequency of ~ 0.52 **s^{-1}** at 1 mA cm^{-2} current density.

5.1. INTRODUCTION

Polyoxometalates (POMs) are a unique class of inorganic compounds that are well-known for their highly reversible redox activity.[1,2] These metal oxide clusters can exist in a wide range of redox states and valences, which makes these materials of interest to materials chemists. For example, the green-colored Keggin POM $[Co^{II}W^{VI}{}_{12}O_{40}]^{6-}$ is known to exist in blue-colored $[Co^{II}W^{VI}{}_{10}W^{V}{}_{2}O_{40}]^{8-}$ form as well.[3] These excess electrons are known to hop between the tungsten metal ions in the POM. Moreover, the molecular orbitals formed by the involvement of oxygen atoms in the cluster, also help in delocalizing the electron density all over the structure, in turn stabilizing the system. This example showcases the ability of a POM to act as a stable and efficient molecular electron sink. Because of such features, POMs are being explored for various applications such as, supercapacitors, battery, electrocatalysis, and photocatalysts.[4-8]

The Keplarate $\{Mo_{132}\}$, a giant-POM, was first reported by Müller *et. al.* in 1998.[9] It has a spherical shape with a diameter of ~ 2.9 nm. It exists in I_h (icosahedral) symmetry, with more than 500 atoms constituting the structure, hence also known as '*inorganic super fullerene*'. The large size of the molecular anion and its unique structure sparked the interest of experimental as well as theoretical chemists.[10-14] $\{Mo_{132}\}$ has chemical formula $[(NH_4)_{42}\{Mo_{132}O_{372}(CH_3COO)_{30}(H_2O)_{72}\}\cdot ca.300\ H_2O\cdot ca.10\ CH_3COONH_4]$. The $\{Mo_{132}\}$ structure has two kinds of building blocks: pentagonal $\{(Mo^{VI})Mo^{VI}{}_5\}$ and dimeric $\{Mo^VMo^V\}$ (Figure 5.1). 12 of these pentagonal blocks and 30 of these dimers constitute the icosahedron. This means that $\{Mo_{132}\}$ has 72 Mo^{VI} and 60 Mo^V centers, that is, the relevant molecular cluster is reduced by 60 electrons.

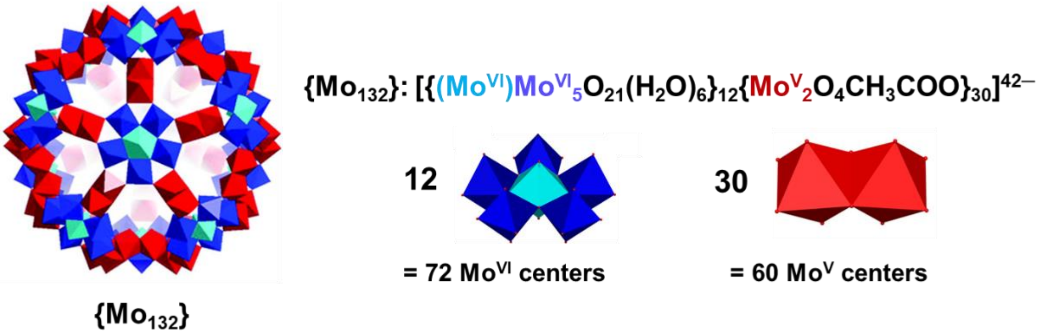

Figure 5.1. Polyhedral représentation of $\{Mo_{132}\}$ and its building blocks.

In this work, we have developed a $\{Mo_{132}\}$-based stable heterogeneous HER electrocatalyst. And interestingly, the electrocatalyst ***Mo₁₃₂-R-ED***, is synthesised by reducing the already 60-electron-reduced-$\{Mo_{132}\}$ molecular cluster by 60 more electrons, electrochemically. The reduction of the $\{Mo_{132}\}$ molecules led to the bridging together of these balls to form large assemblies, insoluble in water. Thus, the resulting electrocatalyst ***Mo₁₃₂-R-ED*** contains 120 electrons per $\{Mo_{132}\}$ cluster. The further reduction of the 60-electron-reduced$\{Mo_{132}\}$ molecules by 60 more electrons is unprecedented, and has never been reported before, to the best of our knowledge.

5.2. EXPERIMENTAL SECTION

5.2.1. Materials

All the chemicals were used as received without any further purification. Ammonium heptamolybdate tetrahydrate ($(NH_4)_6Mo_7O_{24}\cdot4H_2O$), ammonium acetate ($CH_3COONH_4$), hydrazine sulphate ($N_2H_4\cdot H_2SO_4$) and glacial acetic acid (CH_3COOH) were purchased from SRL chemicals. Potassium permanganate ($KMnO_4$) and oxalic acid $(COOH)_2$ were purchased from FINAR chemicals. Double distilled water was used for synthesis.

5.2.2. Synthesis

5.2.2.1. Synthesis of {Mo_{132}} [$(NH_4)_{42}\{Mo^{VI}_{72}Mo^{V}_{60}O_{372}(CH_3COO)_{30}(H_2O)_{72}\}\cdot$ca. 300 $H_2O\cdot$ca. 10 CH_3COONH_4].

The synthesis of {Mo_{132}} was adapted from an earlier report, which yielded octahedral microcrystals.[9] 5.6g (4.5mmol) of $(NH_4)_6Mo_7O_{24}\cdot4H_2O$ and 12.5g (162.2mmol) of CH_3COONH_4 were dissolved in 250 ml of water. To it, 0.8g of $N_2H_4\cdot H_2SO_4$ (6.1mmol) was added while stirring. At this point the solution turned pale green, which then turned to blue, and then deep blue with time. After 10 minutes 83 ml of 50% glacial acetic acid was added to the reaction mixture and stirred for another 20 minutes. This reaction mixture was then kept in rest at 22 °C for four days. Dark brown crystals of {Mo_{132}} were filtered, washed with ethanol and diethyl ether, and then dried in air.

5.2.2.2. Synthesis of Mo_{132}-R-ED

For the synthesis of **Mo_{132}-R-ED**, a 3-electrode electrochemical cell was employed. Pt mesh electrode with fret separation, was used as the counter electrode while Ag/AgCl was used as the reference. Glassy carbon or carbon paper were used as the working electrode, as and when required. A homogeneous solution of ~10 mg of {Mo_{132}} in 10 mL of 0.1 M aqueous solution of KCl (pH 3.2) was kept in the electrochemical cell. This solution was then treated with reduction potential by cycling the voltametric scans from 0.38 V to -1.12 V (versus RHE) at a scan rate of 0.05 V s^{-1}. The product **Mo_{132}-R-ED** was deposited on the electrodes as a dark brown product.

To get the product in bulk, ~30 mg of {Mo_{132}} in 30 mL of 0.1 M aqueous solution of KCl (pH 3.2) was taken, and Pt wire was used as the working electrode.

5.2.3. Methods

Mo_{132}-R-ED was characterised by FESEM, EDX, CHN, ICP-OES, FT-IR, Raman, electronic absorption and X-ray photoelectron spectroscopy.

The instrumental details of all the experiments are provided in appendix 1.

5.2.3.1. Redox titration

The compounds {Mo_{132}} and **Mo_{132}-R-ED** were titrated with oxidant $KMnO_4$ to determine the number of Mo^V centers in the respective samples.

{Mo_{132}}: For the titration, 50 mg of {Mo_{132}} was dissolved in 10 mL of water, taken in a conical flask. To it, 1 drop of concentrated sulfuric acid was added and the mixture was immediately titrated against freshly prepared 0.01 M aqueous $KMnO_4$ solution. During the titration the color of the solution changed from brown to blue. The titrant was slowly added till the color of the solution changed from blue to colorless. The volume of titrant was noted and the number of Mo^V ions in the sample was calculated.

Mo_{132}-R-ED: For the titration, 50 mg of finely ground **Mo_{132}-R-ED** and 10 mL of water were taken in a conical flask, and the mixture was sonicated till a uniform dispersion was achieved. To it, 1 drop of concentrated sulfuric acid was added and the mixture was immediately titrated against freshly prepared 0.01 M aqueous $KMnO_4$ solution. During the titration, the color of the solution changed from brown to blue. The titrant was slowly added till all the solid in the flask dissolved and the color of the solution changed from blue to colorless. The volume of titrant was noted and the number of Mo^V ions in the sample was calculated.

The freshly prepared 0.01 M aqueous $KMnO_4$ solution was standardized against 0.01 M aqueous oxalic acid solution.

5.2.3.2. Electrochemical measurements for catalytic HER

The electrochemical measurements for investigating hydrogen evolution reaction (HER) were conducted using a Zahner Zanium electrochemical workstation operated with Thales software. For all the experiments, 3-electrode electrochemical cell was employed. Pt wire was used as the counter electrode, Ag/AgCl was used as the reference, and glassy carbon was used as the working electrode. 0.1 M aqueous solution of KCl (pH 3.2) was used as the supporting electrolyte and the electrochemical responses were recorded at 0.05 V s^{-1} scan rate, unless specified otherwise.

5.2.3.3. Quantitative Hydrogen evolution experiment

To determine the amount of evolved hydrogen (H_2) gas over time, bulk electrolysis was carried out for deposited **Mo_{132}-R-ED** using a two-electrode setup, at a constant current density of −1 mA cm^{-2} for a period of 3 h. A known amount of electrocatalyst was coated on a carbon paper working electrode of area 2 cm^2, and a large area platinum flag was used as the counter electrode. 0.1 M KCl (pH 3.2) was used as the electrolyte. This experiment was conducted in a home-built electrochemical cell with a graduated column for collection of H_2 gas, by downward displacement of electrolyte solution from the column (Figure 5.2). The design of the cell ensures that the H_2 and O_2 gas evolved at the working electrode and counter electrode, respectively, does not mix.

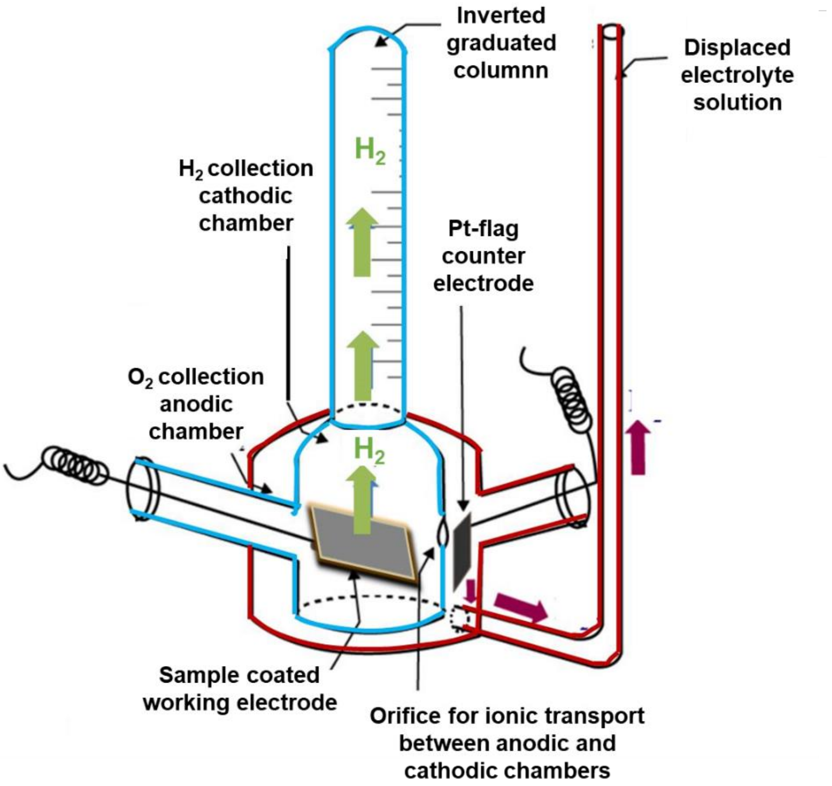

Figure 5.2. Schematic of the home-made quantitative gas determination set up used to calculate Faradaic efficiency of **Mo_{132}-R-ED.**

5.3. RESULTS AND DISCUSSIONS

5.3.1. Electrochemical synthesis of Mo_{132}-R-ED

The water insoluble compound **Mo_{132}-R-ED**, was synthesized by the electrochemical reduction of a homogenous solution {Mo_{132}}. Figure 5.3 shows the continuous increase in cathodic current density with subsequent cycling of the potential from 0.38 V to -1.12 V (versus RHE). This electrochemical response gives the indication of the formation and deposition of an electroactive material (**Mo_{132}-R-ED**) on the surface of the electrode. A comparison of the FESEM images of a carbon paper (working electrode) and after the electrochemical synthetic procedure, clearly shows the deposition of **Mo_{132}-R-ED** on the surface of the electrode (Figure 5.4). An energy dispersive X-ray elemental (EDX) mapping of the deposited material (Figure 5.5) shows the presence of Mo, O, C, and N, the constituent elements of {Mo_{132}}. Figure 5.6 shows the stepwise deposition of **Mo_{132}-R-ED** on the electrode surface with subsequent cycling of reduction potentials. As can be

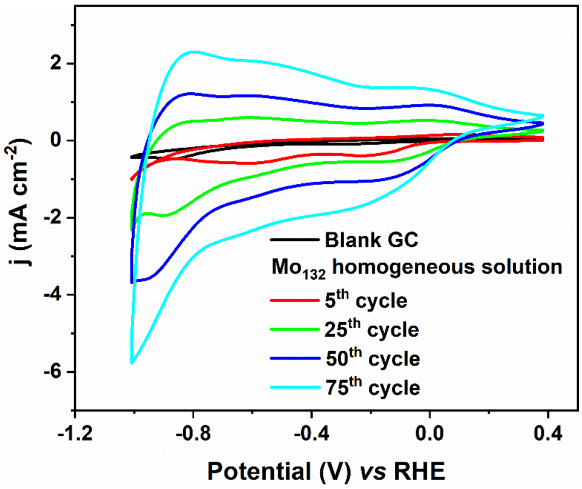

Figure 5.3. Cyclic voltammograms during the synthesis of **Mo_{132}-R-ED**.

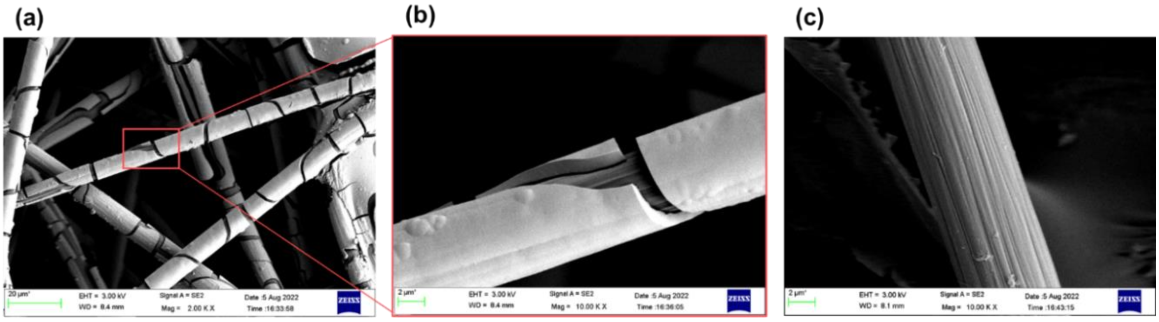

Figure 5.4. a) Deposition of **Mo_{132}-R-ED** on the surface of carbon paper electrode; b) Magnified view of the **Mo_{132}-R-ED** deposited carbon tube; c) Magnified view of carbon tube without deposition.

seen from the images, the deposition starts in the form of small spherical balls, of the initial size order of ~10 nm. These balls then grow in size with subsequent potential cycling, and eventually cover the entire electrode surface.

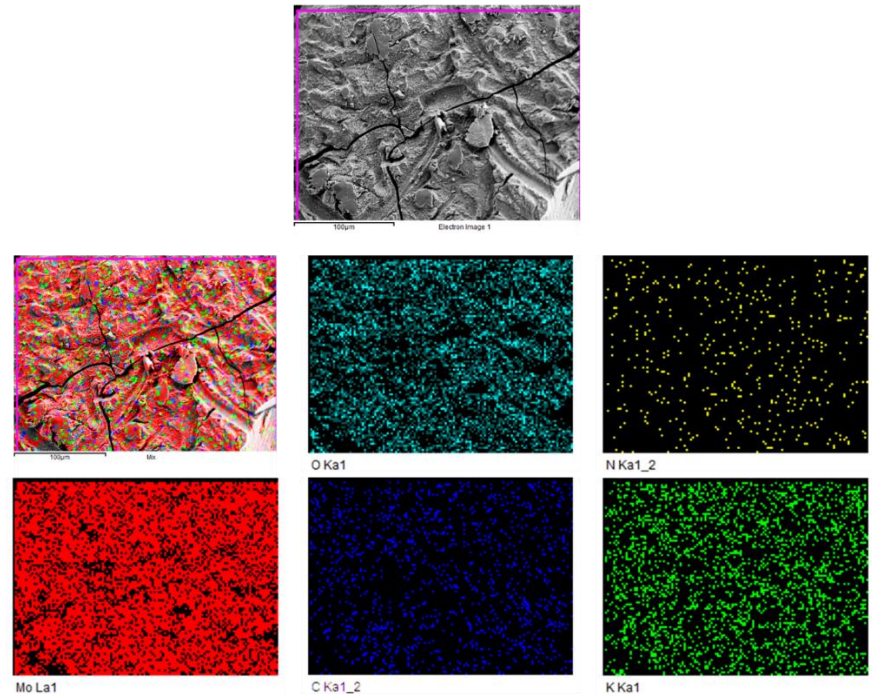

Figure 5.5. EDX elemental mapping of the surface of **Mo_{132}-R-ED**.

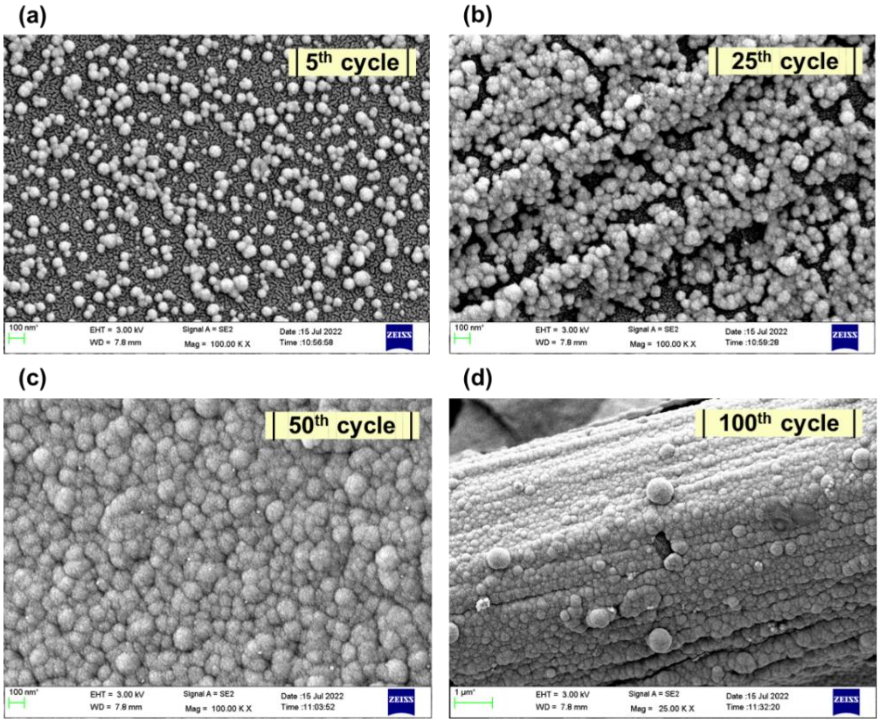

Figure 5.6. FESEM images of **Mo_{132}-R-ED** on carbon paper electrode, showing the stepwise generation of deposition. Images taken after 5th (a), 25th (b), 50th (c), and 100th (d) cycle of cyclic voltammetry during synthesis.

5.3.2. Fourier transformed-infrared (FT-IR) spectral analysis

The FT-IR spectrum for {Mo_{132}} matches well with the reported literatures [ν(OH---H) 3400 cm^{-1}; ν(NH in NH_4^+) 3200 cm^{-1}; δ(H_2O) 1620 cm^{-1}; ν_{as}(COO^- coordinated) 1540 cm^{-1}; δ(NH_4^+) 1411 cm^{-1}; 1270, δ_{ip}(C-CH_3, rocking), 1041 cm^{-1}; ν(Mo=O) 964 cm^{-1}; ν(O-Mo-O/Mo-O-Mo) 934, 843 cm^{-1}; ν(Mo-$O_{\mu2}$-Mo/ Mo-$O_{\mu3}$-Mo) 775, 704, 665, 627 cm^{-1}].[15,16] A comparison of the FT-IR spectra for {Mo_{132}} and **Mo_{132}-R-ED** (Figure 5.7 a and b) shows that the {Mo_{132}} molecules are stable during the course of synthesis of **Mo_{132}-R-ED**. In addition to it, there are some red-shifts in the peak positions for **Mo_{132}-R-ED** in the fingerprint region (Figure 5.7 b) with respect to those of {Mo_{132}}[964→954; 843→802; 775→741, 665→648, 627→612], which probably occurs due to the reduction of the molecule as well as due to possible new bond formation between the {Mo_{132}} molecules (during self-assembly or aggregation) to generate **Mo_{132}-R-ED**.[16,17] An analysis of the spectra also reveals that, there has been a loss in the number of ammonium counterions, in **Mo_{132}-R-ED**. The CHN elemental analysis (Table A5.1, Appendix 5) also confirms the lowering in ammonium content in the compound. Now, from EDX elemental mapping (Figure 5.5), it was found that **Mo_{132}-R-ED** also contains a considerable amount of potassium in the structure. Since potassium chloride was used as the electrolyte during the synthesis of **Mo_{132}-R-ED**, it is highly possible that the smaller potassium ions replace some of the ammonium ions and thus balance the overall negative charge on the molecules.

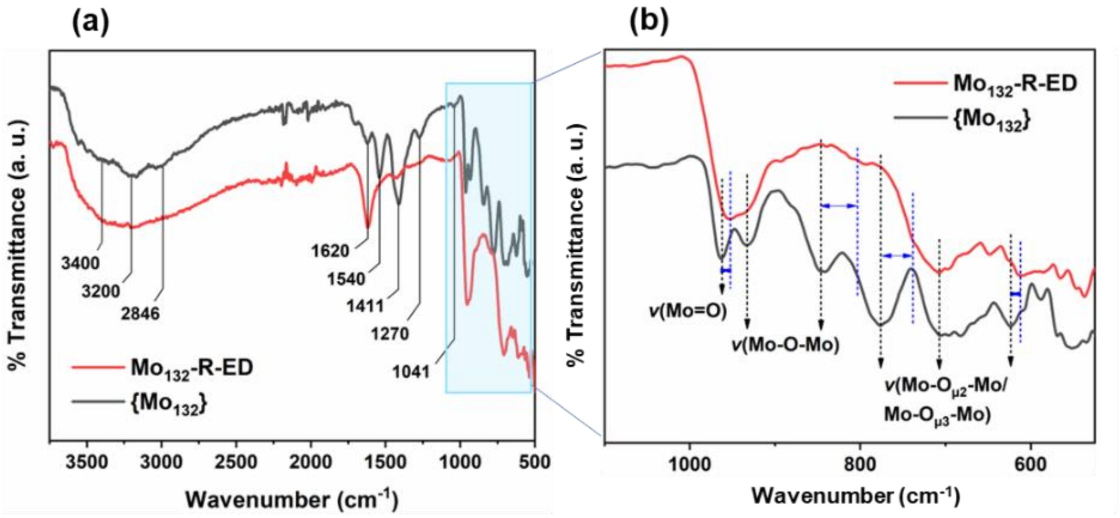

Figure 5.7. a) FT-IR spectra of {Mo_{132}} and **Mo_{132}-R-ED**; b) magnified view of the FT-IR fingerprint region (black lines denote the peak positions for {Mo_{132}}, and blue lines denote the shifted peak positions for **Mo_{132}-R-ED**).

5.3.3. Raman spectral analysis

The Raman spectrum for $\{Mo_{132}\}$ shows two distinct bands at ~370 cm^{-1} (H_g) and ~875 cm^{-1} (A_g), originating from the secondary Mo moieties and symmetric stretching of Mo-O-Mo, respectively (Figure 5.8).[16,18] The Raman spectrum for **Mo_{132}-R-ED** feature the characteristic peaks corresponding to pristine $\{Mo_{132}\}$, Interestingly, for the peak corresponding to symmetric stretching of Mo-O-Mo in **Mo_{132}-R-ED**, a blue shift is observed, which probably occurred due to an increase in rigidity of the Mo-O-Mo bonds.[15] Similar observations were found for a case of reduction of $[Co^{II}W_{12}O_{40}]^{6-}$ anion by two electrons to $[Co^{II}W_{12}O_{40}]^{8-}$.[3] As it was expected in this case, the excess electrons were found to be residing on the tungsten atoms, but, along with that, there was also an accumulation of negative charge density on the bridging oxygen atoms. As a result of this, the displacement parameters of the bridging oxygen atoms got significantly lowered and thus made the bonds rigid. A similar mechanism of charge delocalization can be expected to be taking place in our case as well, since W and Mo are from the same group. The possible accumulation of negative charge density on the bridging oxygen atoms of Mo-O-Mo bonds might have increased the rigidity of the bonds, hence showing the blue shift in Raman spectrum.

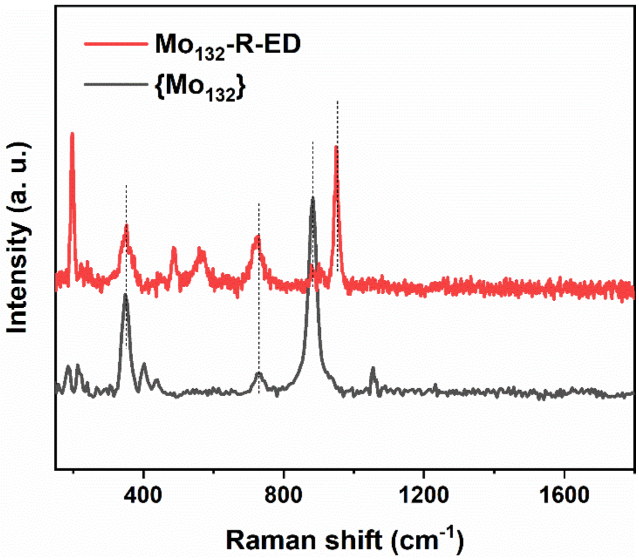

Figure 5.8. Raman spectra of $\{Mo_{132}\}$ and **Mo_{132}-R-ED**.

5.3.4. Electronic absorption spectral analysis

The electronic absorption spectra of $\{Mo_{132}\}$ and **Mo_{132}-R-ED**, measured in diffuse reflectance mode, reveals that there is a significant difference between their electronic energy levels (Figure 5.9). This result can be expected to be a consequence of electrochemical reduction of the $\{Mo_{132}\}$ molecules present in **Mo_{132}-R-ED**.

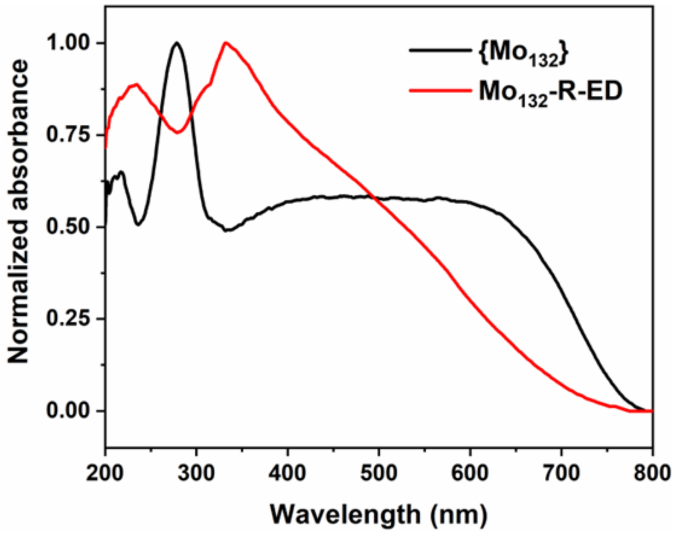

Figure 5.9. Electronic absorbance spectra of $\{Mo_{132}\}$ and **Mo_{132}-R-ED**, measured in diffuse reflectance mode.

5.3.5. Determination of the number of Mo^V centers in Mo_{132}-R-ED

5.3.5.1. X-Ray photoelectron spectral analysis

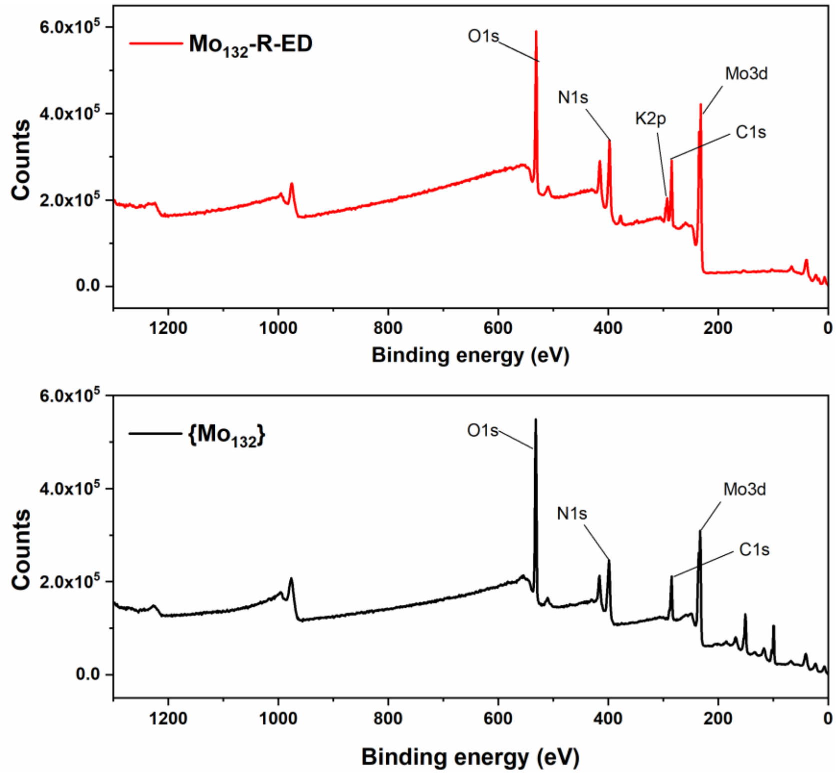

Figure 5.10. XP survey spectra for $\{Mo_{132}\}$ and **Mo_{132}-R-ED**.

To better understand the result of electrochemical reduction of {Mo_{132}}, X-ray photoelectron spectroscopy (XPS) was used (survey spectra provided in Figure 5.10). The XP spectrum for Mo_{3d} {Mo_{132}} (Figure 5.11 a) shows its characteristic doublet ($3d_{5/2}$ and $3d_{3/2}$) originating from spin-orbit coupling. The experimental curve was deconvoluted using Lorentzian–Gaussian functions into two pairs of doublets corresponding to Mo^{V} and Mo^{VI}. For both {Mo_{132}} and **Mo_{132}-R-ED**, the peaks at 232.6 eV and 235.6 eV were assigned to Mo^{V}, while the peaks at 233.6 eV and 236.7 eV were assigned to Mo^{VI} (Figure 5.11).[19,20] For {Mo_{132}}, the ratio between the peak areas for Mo^{V} and Mo^{VI} is approximately 1:1.2, which matches well with the number of Mo^{V} and Mo^{VI} centers in {Mo_{132}}, that is 60 and 72, respectively. However, for **Mo_{132}-R-ED**, the amount of Mo^{V} centers is considerably higher than Mo^{VI} (Figure 5.11 b).

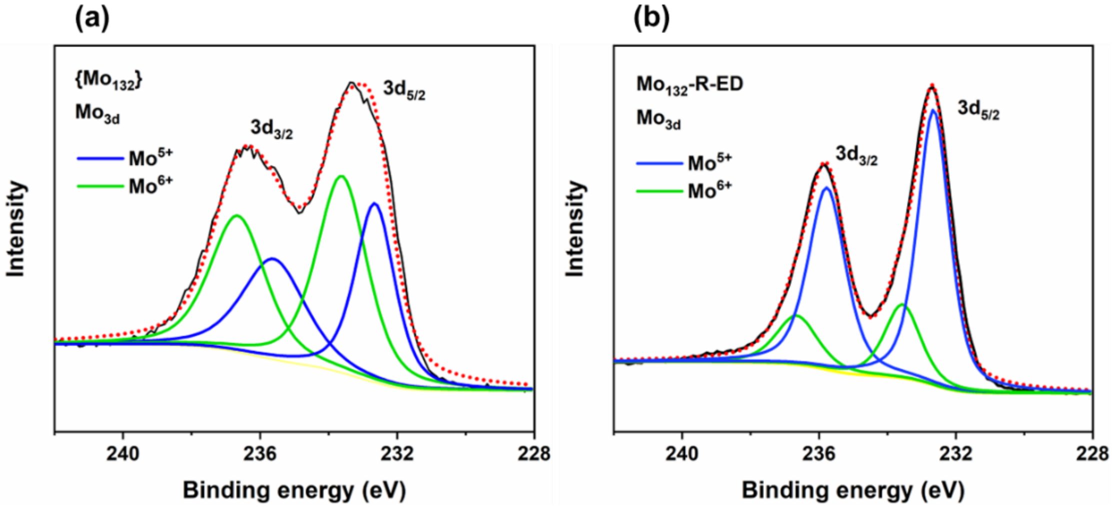

Figure 5.11. a) XP spectra of a) {Mo_{132}}, and b) **Mo_{132}-R-ED**.

5.3.5.2. Redox titration

To quantify the number of Mo^{V} in **Mo_{132}-R-ED** accurately, redox titration was done, following a previous report (detailed methodology provided in section 5.2.3.1).[21] In brief, a specific amount of **Mo_{132}-R-ED** was taken, and with the help of redox titration, the total number of Mo^{V} ions in the sample amount could be calculated. Now, from ICP-OES analysis, the total number of Mo ions present in the sample was determined (Table A5.2, Appendix 5). Combining these two techniques, the total number of Mo^{V} ions present per {Mo_{132}} cluster in **Mo_{132}-R-ED**, was calculated. To check the accuracy of this method, we conducted the same experiment for pristine {Mo_{132}}, and the number of Mo^{V} ions per cluster was estimated to be ~ 60.1, which matches very well with the theoretical value of

60. In case of **Mo_{132}-R-ED**, it was found that, for each cluster of $\{Mo_{132}\}$, there is approximately 120 Mo^{V} centers. This means that the $\{Mo_{132}\}$ clusters in **Mo_{132}-R-ED**, have been reduced by ~ 60 more electrons. The further reduction of the partially reduced $\{Mo_{132}\}$ molecules by these many electrons is unprecedented, and has never been reported before, to the best of our knowledge.

5.3.5.3. Theoretical background

The further reduction of $\{Mo_{132}\}$ clusters by specifically 60 electrons, is crucial here. To reason out this observation, we looked into the molecular and electronic structure of $\{Mo_{132}\}$, studied using first-principles density functional theory (DFT), and previously reported by Bo and coworkers.[14] From this study it was found that, the LUMO of $\{Mo_{132}\}$ has a significant contribution from the *d*-orbitals of Mo centers, which combine in anti-bonding to the *p*-orbitals of the bridging oxygens (Figure 5.12). The information, which is noteworthy here, is that the Mo-centers contributing to the LUMO, are the ones in octahedral geometry, structurally situated at the vertices of the $\{(Mo)\mathbf{Mo_5}\}$ pentagon (polyhedral représentation of $\{Mo_{132}\}$ and its building blocks are provided in figure 5.1); while the central Mo in pentagonal bipyramidal geometry, has zero contribution to the LUMO. This means that, in the $\{Mo_{132}\}$ cluster, there are only 60 out of 72 Mo^{VI} centers, which are available in LUMO. This might explain why the number of electrons by which the $\{Mo_{132}\}$ cluster got reduced, is 60; that is, these 60 $Mo^{VI} \rightarrow Mo^{V}$. During the electrochemical synthesis of **Mo_{132}-R-ED**, the $\{Mo_{132}\}$ molecules (present in solution) coming in contact with the cathode electrode surface get reduced, and probably when more

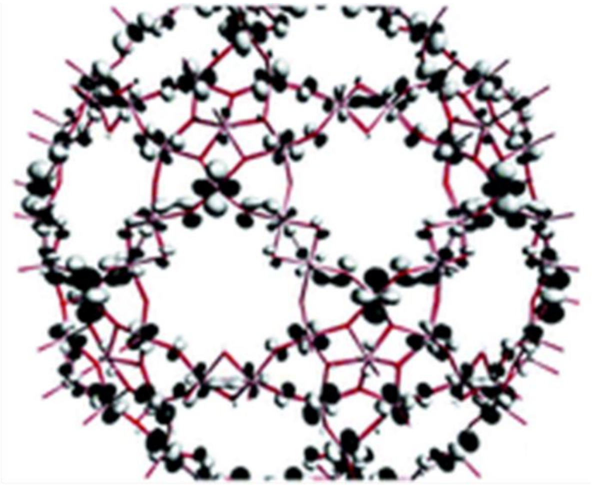

Figure 5.12 Plot of the lowest unoccupied molecular orbital (LUMO) of Mo_{132}.[14]

of these highly reduced $\{Mo_{132}\}$ clusters come in contact with each other, they aggregate *via* potassium ion (K^+) to form the water insoluble assemblies of 120-electron reduced $\{Mo_{132}\}$ clusters. The aggregation of this super-reduced $\{Mo_{132}\}$ clusters through hydronium ($\{H_3O\}^+$) ions, cannot be completely ruled out, since we are dealing with electrochemical reduction at considerably low pH of 3.2.

5.3.6. Electrochemical analysis of hydrogen evolution reaction (HER) catalysis

Here, it is interesting to find that the highly reduced **Mo_{132}-R-ED** species is catalytically active towards hydrogen evolution reaction (HER). Now, there are several reports of preparing Mo-based electrocatalysts such as molybdenum carbides (Mo_2C) and transition metal doped Mo_2C, for HER, by annealing $\{Mo_{132}\}$ hence, using $\{Mo_{132}\}$ as a precursor.[22-24] But it is for the first time that an HER electrocatalyst has been developed with $\{Mo_{132}\}$ clusters in it (a true catalyst, not a pre-catalyst!). From the cyclic voltammograms recorded in dry THF, with sequential addition of water (Figure 5.13a), and with sequential addition of 0.1 M acetic acid (Figure 5.13b), it was found that the electrocatalyst **Mo_{132}-R-ED**, functions through proton assisted water reduction to generate hydrogen. **Mo_{132}-R-ED** gave an appreciable current density of ~3 mA cm^{-2} at −1.1 V (*vs* RHE) and was found to be stable for more than 500 catalytic cycles, with a negligible 90 µA cm^{-2} loss of catalytic current density (Figure 5.14a).

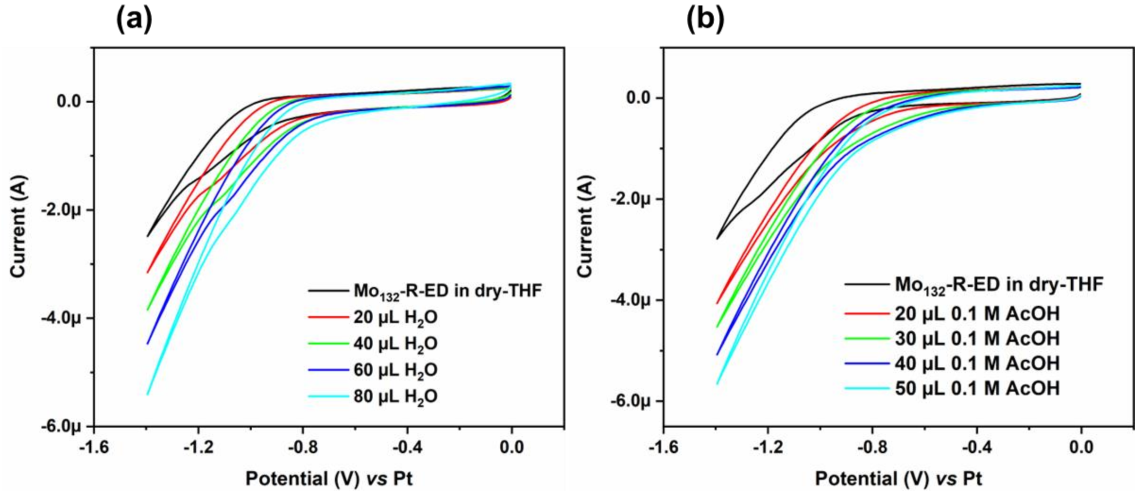

Figure 5.13. Cyclic voltammograms of **Mo_{132}-R-ED** recorded in 0.1 M TBAP, dry THF at 50 mV s^{-1} scan rate, with sequential addition of H_2O (a), and of 0.1 M acetic acid (b).

The electrocatalyst also gave a stable current density of ~0.75 mA cm^{-2} for more than 10 hours of constant potential electrolysis (CPE) at −0.81 V (*vs* RHE) (Figure 5.14b). FESEM imaging and energy dispersive X-ray (EDX) elemental mapping analysis of the electrode before and after the measurement (Figures 5.15 and 5.16), show negligible change in the morphology and composition of the electrocatalyst, respectively.

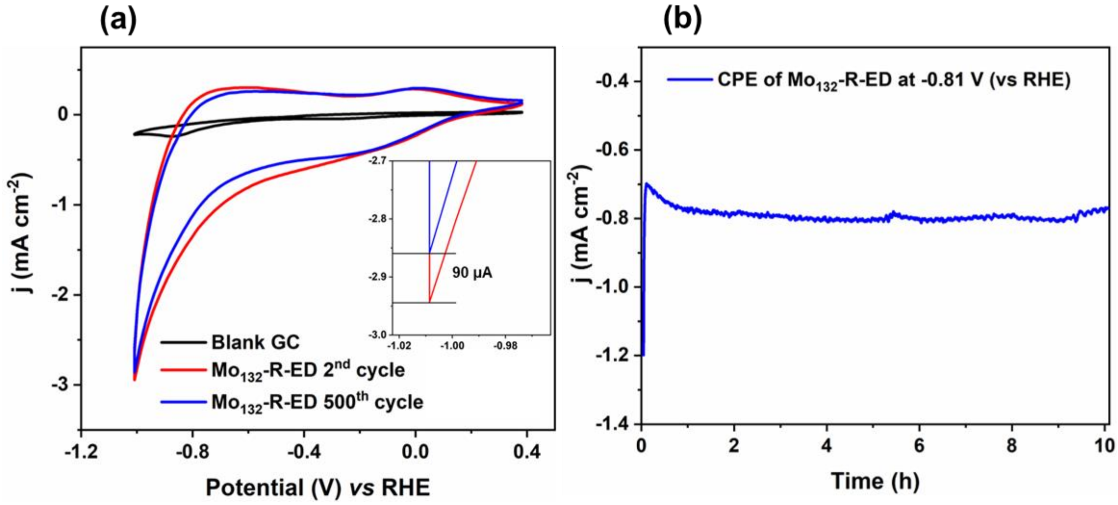

Figure 5.14. a) Cyclic voltammograms of **Mo_{132}-R-ED** and blank glassy carbon electrode. b) Comparison of the 2nd and 500th cycle of cyclic voltammogram for **Mo_{132}-R-ED**. c) Constant potential electrolysis (CPE) response of **Mo_{132}-R-ED** at −0.81 V (vs RHE) for 10 hours. All the experiments were conducted in 0.1 M KCl (pH 3.2), and the voltammograms were recorded at 50 mv s^{-1} scan rate.

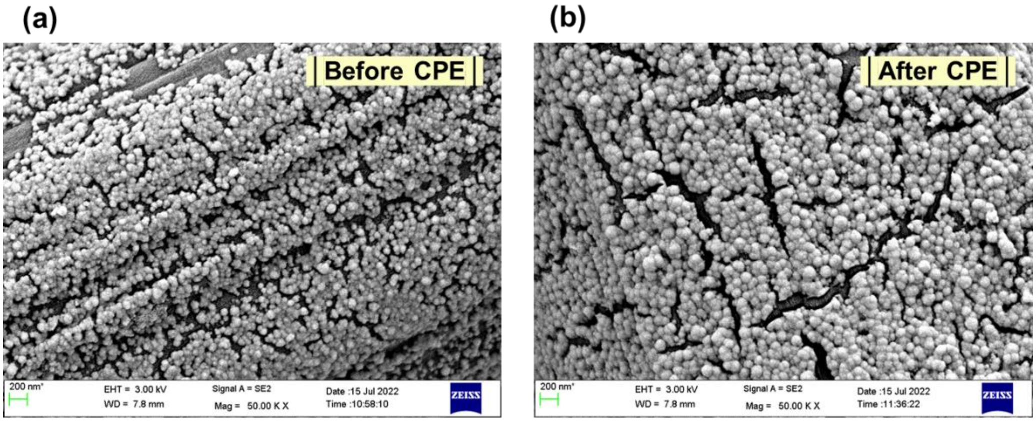

Figure 5.15. FESEM images of **Mo_{132}-R-ED** on carbon paper electrode, a) before, and b) after constant potential electrolysis.

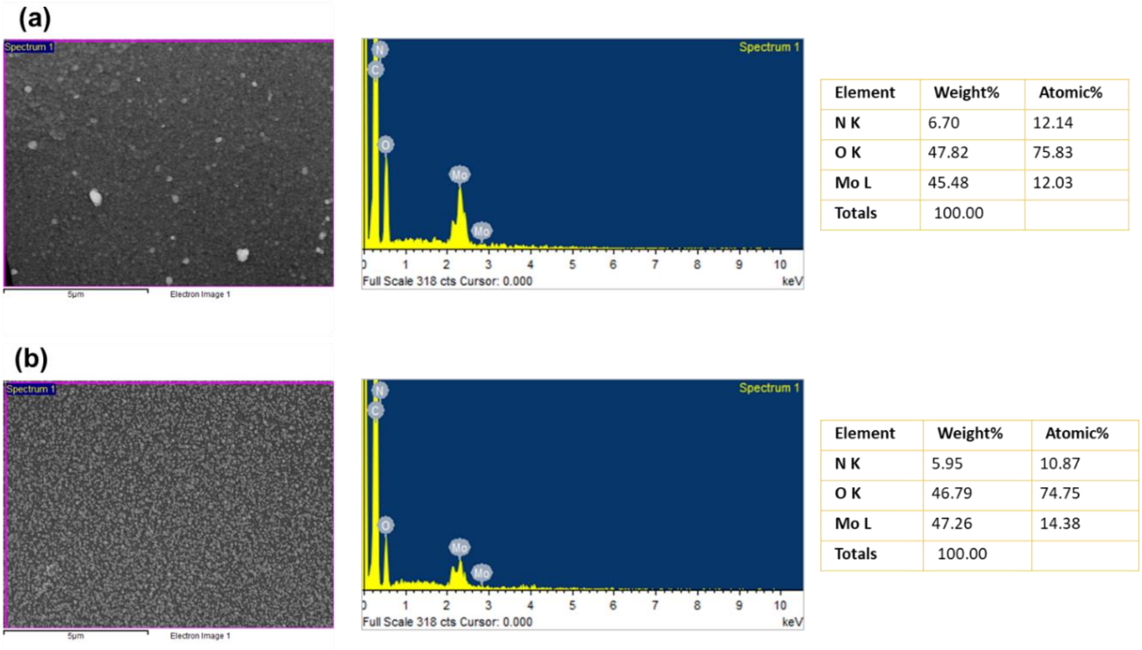

Element	Weight%	Atomic%
N K	6.70	12.14
O K	47.82	75.83
Mo L	45.48	12.03
Totals	100.00	

Element	Weight%	Atomic%
N K	5.95	10.87
O K	46.79	74.75
Mo L	47.26	14.38
Totals	100.00	

Figure 5.16. EDX elemental mapping of **Mo_{132}-R-ED** on carbon paper electrode, a) before, and b) after constant potential electrolysis.

To understand the kinetic aspect of the electrocatalysis, iR (cell resistance)-corrected Tafel plot (Figure 5.17 a) was derived from a linear scan voltammogram recorded at a slow scan rate of 2 mv s^{-1}. **Mo_{132}-R-ED** was found to have an overpotential of 880 mV at a current density of 1 mA cm^{-2}, and a Tafel slope of ~ 90 mV/decade. The cyclic voltammograms recorded at various scan rates show the increasing current density with increasing scan rates (Figure 5.18a). From figure 5.17 b, we find a linear dependence of the peak current (i_p) on the square root of scan rate, which shows that the catalytic process taking place at the electrode surface is diffusion controlled.

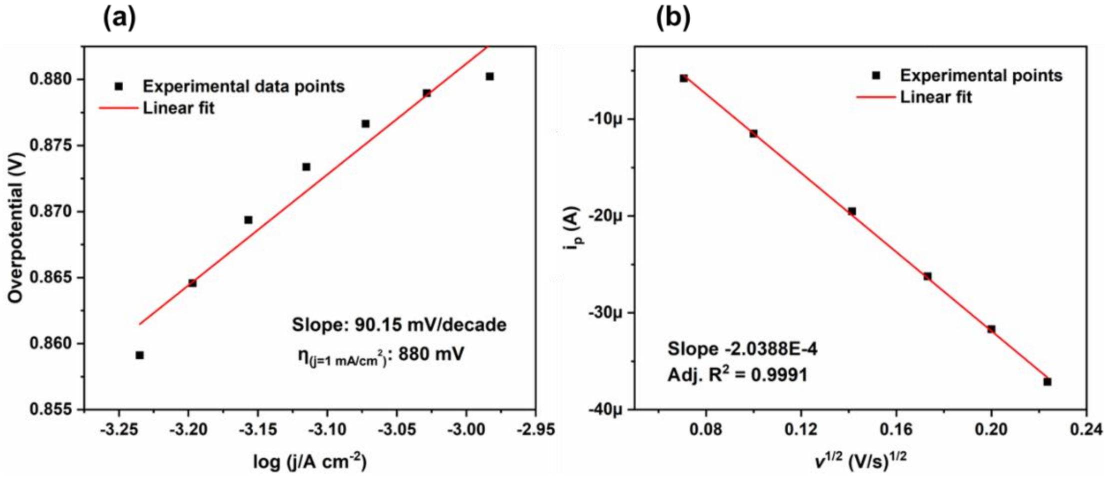

Figure 5.17. a) Tafel plot for **Mo_{132}-R-ED**, constructed from LSV at a slow scan rate of 2 mv s^{-1}, recorded in 0.1 M KCl (pH 3.2); b) Peak current (i_p) as a function of square root of scan rate.

Calculation of Faradaic Efficiency

The Faradaic efficiency of the electrocatalyst, as estimated from the volume of hydrogen generated at the electrode during bulk electrolysis, was found to be ~ 87.8 % which shows that **Mo_{132}-R-ED** is an efficient electrocatalyst, since there are no major side reactions occurring alongside HER. Detailed methodology of the Faradaic efficiency measurement experiment is provided in section 5.2.3.3.

The amount of H_2 evolved during the above-mentioned bulk electrolysis experiment, at a constant current density of -1 mA cm^{-2} for a period of 3 h, is 1.1 mL.
Thus, the number of moles of H_2 evolved = (1.1/22400) mol = 4.91×10^{-5} mol.

$$H_2 \text{ (ideal)} = \frac{\text{Q (total charge)}}{\text{n (no. of electrons required for the chemical change)} \times \text{1 Farad}}$$

Here, H_2(ideal) for 3 h = $(1 \text{ x } 10^{-3} \times 3 \times 3600) / (2 \times 96500)$ mol = 5.595×10^{-5} mol.

Thus, Faradaic efficiency = 87.8 %

Calculation of Turnover Frequency (TOF) for H_2 evolution

The turnover frequency (TOF), defined here as the number of H_2 molecules generated by per active center of **Mo_{132}-R-ED** per second, for a current density of 1 mA cm^{-2}, was calculated to be ~ 0.52 **s^{-1}** (calculation given below). It shows that **Mo_{132}-R-ED** is an active and efficient electrocatalyst towards HER.

$$\text{TOF} = \frac{\text{Current density at given over potential}}{\text{n (no. of electrons involved in the reaction)} \times \text{1 Farad} \times \text{no. of active centers}}$$

For HER, n = 2; the number of active centers on the electrode surface, was determined from the slope of the plot between peak current (i_p) and scan rate (Figure 5.18b), as derived from figure 5.18a.

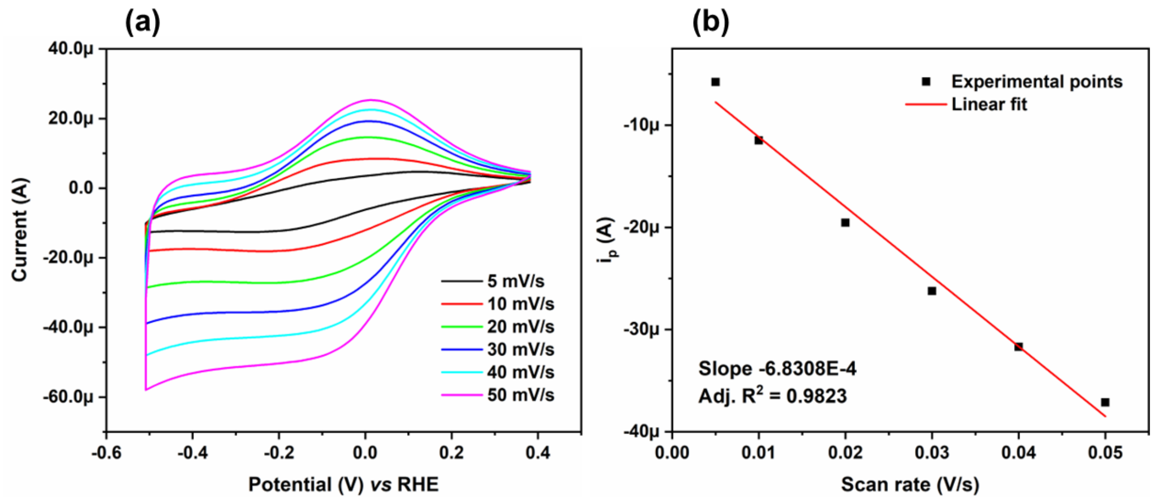

Figure 5.18. (a) Cyclic voltammograms of **Mo_{132}-R-ED** recorded in 0.1 M KCl (pH 3.2) at different scan rates; (b) Peak current (i_p) as a function of scan rate, as derived from figure A5.10.

Now, slope of peak current (i_p) vs scan rate = $n^2F^2A\Gamma_0 / 4RT$

slope = 6.8308×10^{-4} F

n = no. of electrons involved in the redox step (1)

F = Farad

A = geometric area of the electrode surface (0.0706 cm^2)

R = Ideal gas constant

T = temperature during experiment (298 K)

Γ_0 = Surface density of active centers

Hence, surface density of active centers (Γ_0) = 1.0026×10^{-8} moles

Thus, the TOF of **Mo_{132}-R-ED** electrocatalyst at a current density of −1 mA cm^{-2} = 0.517 s^{-1}.

5.4 CONCLUSIONS

The present work reports a stable and efficient heterogeneous hydrogen evolution reaction (HER) electrocatalyst **Mo_{132}-R-ED**, synthesised by the electrochemical reduction of giant {Mo_{132}} icosahedral cluster (which is already 60-electron reduced cluster), to be able to further reduce it electrochemically by another 60 electrons, while retaining the cluster intact, is a feat. The {Mo_{132}} clusters in **Mo_{132}-R-ED** are thus essentially 120 electron-reduced. From previous reports on the molecular and electronic structure of

$\{Mo_{132}\}$, it could be inferred that the addition of excess electrons to the cluster, probably results in occupation of metal centered LUMOs. Though, a contribution of bridging oxygen atoms in delocalizing the electron density, is also indicated by Raman spectroscopy. This work in overall, shows the versatile chemistry of POMs and the potential of these materials for energy conversion application.

Appendix 1: Instrumental details and sample preparation.

Appendix 5: CHN and ICP-OES elemental analysis.

5.5 REFERENCES

1. Gumerova, N. I.; Rompel, A. Synthesis, structures and applications of electron-rich polyoxometalates. *Nature Reviews Chemistry* 2018, *2*, 0112.
2. Gao, Y.; Choudhari, M.; Such, G. K.; Ritchie, C. Polyoxometalates as chemically and structurally versatile components in self-assembled materials. *Chem. Sci.* **2022**, *13*, 2510−2527.
3. Casan-Pastor, N.; Gomez-Romero, P.; Jameson, G. B.; Baker, L. C. Crystal structures of. alpha-$[Co^{II}W_{12}O_{40}]^{6-}$ and its heteropoly blue 2e reduction product, alpha-$[Co^{II}W_{12}O_{40}]^{8-}$. Structural, electronic, and chemical consequences of electron delocalization in a multiatom mixed-valence system. *J. Am. Chem. Soc.* **1991**, *113*, 5658–5663.
4. Horn, M. R.; Singh, A.; Alomari, S.; Goberna-Ferrón, S.; Benages-Vilau, R.; Chodankar, N.; Motta, N.; Ostrikov, K.; MacLeod, J.; Sonar, P.; *et. al.* Polyoxometalates (POMs): from electroactive clusters to energy materials. *Energy Environ. Sci.* **2021**, *14*, 1652−1700.
5. Zhang, Y.; Liu, J.; Li, S.-L.; Su, Z.-M.; Lan, Y.-Q. Polyoxometalate-based materials for sustainable and clean energy conversion and storage. *EnergyChem* **2019**, *1*, 100021.
6. Rausch, B.; Symes, M. D.; Chisholm, G.; Cronin, L. Decoupled catalytic hydrogen evolution from a molecular metal oxide redox mediator in water splitting. *Science* **2014**, *345*, 1326−1330.
7. Ji, Y.; Huang, L.; Hu, J.; Streb, C.; Song, Y.-F. Polyoxometalate-functionalized nanocarbon materials for energy conversion, energy storage and sensor systems. *Energy Environ. Sci.* **2015**, *8*, 776–789.
8. Zhang, L.; Chen. Z. Polyoxometalates: Tailoring metal oxides in molecular dimension toward energy applications. *Int J Energy Res.* **2020**, *44*, 3316–3346.
9. Müller, A.; Krickemeyer, E.; Bögge, H.; Schmidtmann, M.; Peters, F. Organizational Forms of Matter: An Inorganic Super Fullerene and Keplerate Based on Molybdenum Oxide. *Angew. Chem. Int. Ed.* **1998**, *37*, 3359–3363.
10. Müller, A.; Polarz, S.; Das, S. K.; Krickemeyer, E.; Bögge, H.; Schmidtmann, M.; Hauptfleisch, B. “Open and Shut” for Guests in Molybdenum – Oxide-Based Giant Spheres, Baskets, and Rings Containing the Pentagon as a Common Structural Element. *Angew. Chem. Int. Ed.* **1999**, *38*, 3241–3245.
11. Kistler, M. L.; Bhatt, A.; Liu, G.; Casa, D.; Liu, T. A Complete Macroion−“Blackberry” Assembly−Macroion Transition with Continuously Adjustable Assembly Sizes in $\{Mo_{132}\}$ Water/Acetone Systems. *J. Am. Chem. Soc.* **2007**, *129*, 6453–6460.
12. Mitra, T.; Miro, P.; Tomsa, A. R.; Merca, A.; Bögge, H.; Ávalos, J. B.; Poblet, J. M.; Bo, C.; Müller, A. Gated and Differently Functionalized (New) Porous Capsules Direct Encapsulates' Structures: Higher and Lower Density Water. *Chem.–Eur. J.* **2009**, *15*, 1844−1852.
13. García-Rates, M.; Miró, P.; Poblet, J. M.; Bo, C.; Ávalos, J. B. Dynamics of Encapsulated Water inside Mo_{132} Cavities. *J. Phys. Chem. B* **2011**, *115*, 5980–5992.
14. Bo, C.; Miró, P. On the electronic structure of giant polyoxometalates: Mo_{132} vs. $W_{72}Mo_{60}$. *Dalton Trans.* **2012**, *41*, 9984-9988.
15. Grzhegorzhevskii, K.; Haouas, M.; Lion, M.; Vashurin, A.; Denikaev, A.; Marfin, Y.; Kim, G.; Falaise, C.; Cadot, E. Gigantic supramolecular assemblies built from dynamic hierarchical organization between inorganic nanospheres and porphyrins. *Chem. Commun.* **2023**, *59*, 86–89.
16. Abdelrahman, A. A.; Salem, H. M.; Mohammed, H. A.; Rabie, A. M. Facial synthesis of mesoporous $\{Mo_{132}\}$/BiOCl for the efficient oxidative desulfurization of fuel. *Inorg. Chem. Commun.* **2022**, *141*, 109568.

17. Rezvani, M. A.; Khandan, S. Synthesis and characterization of a new nanocomposite ($FeW_{11}V$@CTAB-MMT) as an efficient heterogeneous catalyst for oxidative desulfurization of gasoline. *Appl. Organometal. Chem.* **2018**, *32*, e4524.
18. Rezaeifard, A.; Haddad, R.; Jafarpour, M.; Hakimi, M. Catalytic Epoxidation Activity of Keplerate Polyoxomolybdate Nanoball toward Aqueous Suspension of Olefins under Mild Aerobic Conditions. *J. Am. Chem. Soc*. **2013**, *135*, 10036–10039.
19. Shi, Z.; Y. Zhou, Z.; Zhang, L.; Yang, D.; Mu, C.; Ren, H.; Shehzad, F. K.; Li, J. Fabrication and optical nonlinearities of composite films derived from the water-soluble Keplerate-type polyoxometalate and chloroform-soluble porphyrin. *Dalton Trans*. **2015**, *44*, 4102–4107.
20. Wagner, C. D.; Riggs, W. M.; Davis, L. E.; Moulder, J. F.; Muilenberg, G. E. *Handbook of X-ray Photoelectron Spectroscopy*, Perkin-Elmer, Minnesota, **1979**, ch. 2, pp. 104–105.
21. Müller, A.; Shah, S. Q. N.; Bögge, H.; Schmidtmann, M.; Kögerler, P.; Hauptfleisch, B.; Leiding, S.; Wittler, K. Thirty electrons “Trapped” in a spherical matrix: A Molybdenum oxide-based nanostructured Keplerate reduced by 36 electrons. *Angew. Chem. Int. Ed*. **2000**, *39*, 1614–1616.
22. Sun, B.; Wang, S.; Li, X.; Zhang, W.; Li, J.; Pan, Q.; Liu, F.; Su, Z. Giant polyoxomolybdate clusters - derived bimetallic Ni/Mo_2C catalyst for electrochemical hydrogen evolution. *Int. J. Hydrog. Energy* **2023**, *48*, 9353–9361.
23. Zhou, Z.; Yuan, Z.; Li, S.; Li, H.; Chen, J.; Wang, Y.; Huang, Q.; Wang, C.; Karahan, H. E.; Henkelman, G.; Liao, X.; Wei, L.; Chen, Y. Big to Small: Ultrafine Mo_2C Particles Derived from Giant Polyoxomolybdate Clusters for Hydrogen Evolution Reaction. *Small* **2019**, 15, e1900358.
24. Ge, R.; Huo, J.; Sun, M.; Zhu, M.; Li, Y.; Chou, S.; Li, W. Surface and Interface Engineering: Molybdenum Carbide–Based Nanomaterials for Electrochemical Energy Conversion. *Small* **2021**, *17*, 1903380.

CHAPTER 6

Concluding Remarks and Future Scope

6.1. CONCLUSION

The works described in this thesis entitled '*Designing of Functional Materials for Proton Conduction and Electrocatalysis*', endeavours to design and develop efficient metal-organic framework (MOF) based proton conductors, and electrocatalysts for oxygen reduction reaction (ORR) and hydrogen evolution reaction (HER). Here, it is worth mentioning that the works discussed in this thesis, focus on developing materials of application by modifying and improving the properties of already known parent materials, such as MOF-808 (**chapter 2**), MIL-MOFs (**chapter 3**), fullerene C_{60} (**chapter 4**) and $\{Mo_{132}\}$ (**chapter 5**). Now, there already exists a huge library of MOFs and other molecules, which can be of potential for developing novel materials of application; and this thesis work shows one possible way of achieving that.

Chapter 2 describes the design and synthesis of a series of sister MOFs (**MOF-808 A – D**), with controlled concentration of missing linker defects in them (defect density increases from **MOF-808 A → MOF-808 D**). The introduction of defects in the structure resulted in modified intrinsic properties such as, porosity, water sorptivity and acidity. The MOF with the optimum defect concentration **MOF-808 C**, has the highest water uptake capacity and acidity in the series. These properties are key in designing proton conductors functioning by Grotthuss mechanism. **MOF-808 C** shows a conductivity of 2.6×10^{-1} Scm^{-1}, which is the highest reported proton conductivity to date, for a pure MOF based proton conductor without any extensive modification. This work highlights the potential of structural tunability in MOFs to develop efficient proton conductors. We have extended this work further in a new direction, by assembling these title MOF-based proton conductors (**MOF-808 A – D**) with Pt disc electrode to demonstrate electrocatalytic HER. And interestingly, even though MOF-808 is not catalytically active towards HER, the catalytic current for **MOF-808 C** modified Pt electrode (**Pt- MOF-808 C**), was much higher than bare Pt electrode. This is probably a result of lowering in local pH around the Pt catalyst, along with efficient proton management around the active centers by the proton conducting MOF, during electrocatalysis.

As MOF chemists, one always strives to synthesize high quality single crystals, which is very important to obtain crucial structural information. But this work shows that, structural defects are not always detrimental. Systematic design strategies involving defect engineering can broaden the scope further to develop new functional materials from MOFs.

In the next work described in **chapter 3**, '*flexible MOF*'-based proton conductors were developed, while using post-synthetic modification (PSM) as a tool to modify the properties of the MOFs, **Fe-MIL-53-NH$_2$** and **Fe-MIL-88B-NH$_2$**. The choice of Fe(III) metal ion for these MOFs is crucial for the possible use of these MOFs for real applications, since Fe is non-toxic in nature. Using PSM, the primary amine (-NH$_2$) functionalities present on the framework of both the MOFs were successfully modified to -NH(CH$_2$CH$_2$CH$_2$SO$_3$H). The modified MOFs **53-S** and **88B-S**, have much improved proton conductivity than their respective parent MOFs **Fe-MIL-53-NH$_2$** and **Fe-MIL-88B-NH$_2$**. For both the MOFs, the introduction of sulphonic acid pendant groups by PSM, increases the amount of H-bonded network within the framework; for **53-S**, it further helps to increase its water-uptake capacity. Additionally, due to the higher flexibility of the MIL-88B framework, **88B-S** retains its proton conductivity over a wider range of relative humidity than **53-S**, which has lower framework flexibility. This comparison highlights the role of framework flexibility in designing better MOF-based proton conductors.

Now, since MOFs as such are difficult to be directly used for practical application, flexible membranes are required to be made from them. We have thus investigated, in this work, their applicability by fabricating these functionalized MOFs with organic polymers, resulting in polymer-MOF mixed matrix membranes (MMMs). Here, **53-S** and **88B-S** nanocrystals were used as fillers in OPBI polymer matrix. All the MMMs studied in this work, **53-S (-5%** and **-7.5%)** and **88B-S (-5%** and **-7.5%)** came about as much improved proton conductors than the pristine OPBI membrane without any filler loading. These MMMs not only function as efficient proton exchange membranes but are also much more stable and durable than the pristine OPBI membrane. The reason for such an outcome is the extensive network of interactions generated between the MOF nanofillers and the polymer. This highlights the importance of post synthetic modification on the MIL-53 and MIL-88B MOFs in improving the overall performance of the MMMs further.

The next part of this thesis work deals with developing electrocatalysts for energy conversion applications. **Chapter 4** describes the preparation of a host-guest heterogeneous composite (**C$_{60}$Z**), by *in situ* encapsulation of fullerene C$_{60}$ inside zeolitic imidazolate framework-8 (ZIF-8) MOF. **C$_{60}$Z** can act as an electrocatalyst for the oxygen reduction reaction (ORR) at a lower overpotential with better product selectivity for H$_2$O$_2$, than bare C$_{60}$ *per se*. The selection of ZIF-8 as a host for the encapsulation of C$_{60}$, was crucial, considering the host-guest size match; according to which, only one C$_{60}$ molecule could be confined in one cavity of ZIF-8, and there is no scope of its leaching out, since the window aperture of the cavity is much smaller. The situation can be compared to a '*ship in a bottle*' approach. Spatial separation and mono-confinement of C_{60} in the cages of ZIF-8 helps the **C_{60}Z** composite to retain most of the molecular properties of C_{60}. Here, it is noteworthy that, this particular approach has also helped us to overcome one major drawback of fullerene – its tendency to form aggregates over time, which poses serious challenges towards using fullerene C_{60} for practical applications. The composite **C_{60}Z** has 1 C_{60} molecule per 10 cages of ZIF-8, which means that the encapsulated C_{60} molecules practically have no scope of interaction amongst themselves. This strategy is highly effective in preserving the dilute solution-like behavior of C_{60} in solid-state; and therefore, **C_{60}Z** has been described as a '*solid-state analogue of dilute C_{60} solution*'.

Spectroscopic and electrochemical characterization methods prove significant interactions between the ZIF-8 host and the C_{60} guest, which results in the modification of the electro-chemical behavior of C_{60} inside ZIF-8, thereby improving the electrocatalytic ORR performance of the guest.

Chapter 5 depicts the development of a stable and efficient polyoxometalate (POM)-based heterogeneous hydrogen evolution reaction (HER) electrocatalyst **Mo_{132}-R-ED**. It has been synthesized by the electrochemical reduction of a highly water soluble, 60-electron-reduced giant POM, $\{Mo_{132}\}$. The reduction of the $\{Mo_{132}\}$ molecules led to the bridging together of these balls to form large assemblies, insoluble in water, which is **Mo_{132}-R-ED**. Using several characterization techniques and performing redox titration, it has been confirmed that, **Mo_{132}-R-ED** contains parent 60-electron-reduced $\{Mo_{132}\}$ clusters which are further reduced by ~ 60 more electrons. Such an observation is unprecedented and has never been reported before, to the best of our knowledge. From previous reports on the molecular and electronic structure of $\{Mo_{132}\}$, it can be inferred that the addition of excess electrons to the cluster, probably results in occupation of metal centered LUMOs. Though, a contribution of bridging oxygen atoms in delocalizing the electron density, is also indicated by Raman spectroscopy. In this work, it is interesting to find that, while parent water-soluble-$\{Mo_{132}\}$ itself is not catalytically active towards HER, **Mo_{132}-R-ED** is found to be a stable and efficient electrocatalyst towards HER, having a hydrogen evolution turn over frequency of ~ 0.52 $\mathbf{s^{-1}}$ at 1 mA cm^{-2} current density.

This work in overall, shows the versatile chemistry of POMs and the potential of these materials for energy conversion application.

6.2. FUTURE SCOPE OF WORK

In **chapter 2** we have seen that the assembly of **MOF-808 C** proton conducting MOF with Pt electrocatalyst (**Pt-MOF-808 C**), resulted in higher catalytic current density for HER, than bare Pt electrocatalyst. The MOF possibly helped in proton management, along with lowering the local pH around the catalytic center. Using the same strategy, more of such assemblies can be developed where a molecular HER catalyst is encapsulated/loaded in an efficient proton conducting MOF, to obtain improved heterogeneous catalyst.

In **chapter 3**, we have used MOF nanocrystals as nano-fillers in a OPBI polymer matrix to prepare MOF@polymer mixed matrix proton exchange membranes (PEMs). The incorporation of MOF nanofillers improved the overall performance of the PEM, as compared to pristine OPBI polymer membrane without any filler loading. Thus, similar MOF@polymer PEMs can be developed with other combinations of MOF and polymer. Particular emphasis should be given to functionalization of the MOF, since interaction between the polymer strands and the MOF nanocryatals is key to improving the proton conductivity and durability of the MMM. Once a PEM is developed, it can be tested in fuel cells to understand the real-life field application of these membranes.

Chapter 4 gives a strategy to retain the molecular properties of fullerene C_{60} in solid state by encapsulating the molecule inside the cages of ZIF-8 MOF. Similarly, for other molecules or molecular catalysts which need to be heterogenized without losing its inherent properties, encapsulation in MOF cages can be a useful strategy.

In **chapter 5**, we have discussed about, highly water-soluble giant-POM $\{Mo_{132}\}$. This molecule has an overall negative charge of 42, which is counter-balanced by ammonium cations. This, along with the large number of oxygen atoms present at the POM's surface, which can participate in extensive H-bonding with other water molecules, and the presence of additional water molecules in the structure, layering the inner surface of the $\{Mo_{132}\}$ sphere, make it an excellent candidate to be studied as a proton conductor. To study this material under humidity, the requirement is to make it insoluble in water. While **chapter 5** discusses one such strategy, there is a scope of finding other methods as well.

APPENDIX 1

Instrumental Details of Physical Characterizations

CHNS elemental analysis of the samples was done using EuroVector elemental analyser (EA3000).

Dynamic light scattering (DLS) particle size measurements of MOF samples dispersed in ethanol, were performed using a Zetasizer Nano S90 (Malvern Instruments, Germany) instrument operating at 4mW He-Ne laser with 633 nm wavelength.

Dynamic vapour sorption (DVS) analysis of all the samples was performed on a TA Q5000 SA instrument, at a temperature of 25 ^{o}C and under N_2 atmosphere. All the samples were activated at 120 °C for 12 hours, prior to the measurement.

Electrochemical impedance spectroscopy for the MOF pellet samples was conducted using a Zahner Zanium electrochemical workstation operated with Thales software. The membrane samples were studied using Auto lab Impedance analyser (PGSTAT302N) instrument.

Electronic absorption spectra of the samples were recorded using a Shimadzu-2600 spectrophotometer. The solid samples were directly deposited on a barium sulphate ($BaSO_4$) bed in the sample holder and the absorption spectra were recorded in diffuse reflectance mode. The reflectance spectra were converted to absorption spectra using the Kubelka-Munk function.

Quartz cuvettes of 1 cm path length were used for recording the absorbance spectrum of C_{60} in solution in chapter 4. The sample was prepared by ultrasonically dissolving C_{60} in n-hexane to attain a concentration of 4×10^{-5} M.

Field emission Scanning Electron Microscope (FE-SEM) imaging was carried out on a Carl Zeiss model Ultra 55 microscope. All samples were gold coated before imaging in FESEM.

The imaging of the cross-section morphology of the membranes in chapter 3, was done by breaking the membranes in liquid nitrogen.

EDX spectra and maps were recorded using Oxford Instruments X-MaxN SDD (50 mm^2) system and INCA analysis software.

Fourier transformed - infrared (FT-IR) spectra of the samples were recorded on an iD7 ATR Thermo Fisher Scientific-Nicolet iS5 instrument. The sample was directly put on the sample holder without any modification.

Inductively coupled plasma - optical emission spectrometry (ICP-OES) was used to estimate the amount of Zr present in the MOFs. An ICP-OES Varian 720-ES instrument was used. All samples were activated at 140 ^{o}C for 12 hours prior to the experiments.

I**nherent viscosity (I.V.)** of the poly (4,4'-diphenyl-5,5'-bibenzimidazole) (OPBI) polymer was measured at 30 °C in water bath with the help of Cannon (model F725) Ubbelohde capillary dilution viscometer and the I.V. values were calculated from the flow time data.

Mechanical properties of **OPBI** and MOF loaded MMMs were studied by using a dynamic mechanical analyser (DMA model Q-800). The rectangular shaped membranes' dimensions were approximately 30 mm × 7 mm × 0.02 mm (L × W × T). These were then clamped on the films tension clamp of the pre-calibrated instrument. The samples were annealed at 400 °C for 15 minutes and then scanned from 100 °C to 400 °C with a heating rate of 4 °C/min. The storage modulus (E') and tan δ values were measured at a constant linear frequency of 10 Hz with constant preloaded force of 0.01N.

N_2 gas sorption analysis of the samples was carried out on the Quantachrome Autosorb IQ2 instrument. All the samples were activated at 140 ℃ under vacuum for 18 hours, prior to N_2 sorption analysis. The temperature was maintained at 77 K during the experiment by a liquid nitrogen bath.

^{1}H nuclear magnetic resonance (NMR) spectra were recorded on a Bruker spectrometer (500 MHz). All samples were activated at 140 ^{o}C for 12 hours prior to the experiments.

Photoluminescence (PL) measurements were carried out on a FlouroLog-3 (Horiba Jobin Yvon) spectrometer. Quartz cuvettes of 1 cm path length were used for recording the emission profile of C_{60} in solution. The sample was prepared by ultrasonically dissolving C_{60} in toluene to attain a concentration of 1.8×10^{-3} M.

The PL of solid samples were measured by holding the sample in between two quartz plates.

Powder X-ray diffraction (PXRD) patterns were recorded on D8 Advance Bruker diffractometer. The diffraction patterns were analyzed using Bruker DIFFRAC plus EVA software.

Raman spectral analysis of the samples were carried out on a WITec model Alpha 300 R Raman microscope using 785 nm laser as the excitation source. The laser intensity was maintained constant for all the samples.

Tensile strength measurements (stress-strain profile) of all the PA doped **OPBI** membranes and MMMs were obtained from universal testing machine (UTM, INSTRON-5965) with 5 (kN) load cell. Dumbbell shaped specimens were prepared from membranes following ASTM standard D638 (Type IV specimen). Tensile properties of all the samples were measured at room temperature with a crosshead speed of 10 mm/min. 50 mm × 10 mm × 0.12 mm (L × W × T) sized PA doped films were used for this experiment.

Thermogravimetric analysis (TGA) of the samples were carried out on a PerkinElmer Simulteneous Thermal Analyzer STA 6000, under air, at a heating rate of 5 ^{o}C min^{-1}. All the samples were activated at 120 °C for 12 hours, prior to the measurement.
TGA of undoped **OPBI, 53-S** and **88B-S (-5%** and **-7.5%)** MMMs and their PA doped membranes were carried out at a heating rate of 10°C min^{-1} under nitrogen gas flow.

Titration of the membranes for determination of phosphoric acid (PA) doping levels, and ion exchange capacity (IEC), was performed using an Autotitrator (Model Metrohm702).

Transmission electron microscopy (TEM) imaging of the samples were carried out on a JEOL (JEM Model No. F200) TEM machine at an accelerating voltage of 200 kV. The dry powder samples were directly placed on the copper (200 mesh) grids.
The membrane samples were prepared by placing a drop of formic acid dispersed **53-S-7.5%** and **88B-S-7.5%** MMMs solution on carbon coated copper grids.

X-ray photoelectron spectra of the samples were recorded on an ESCALAB 250 X-ray photoelectron spectrometer using an Al-Kα radiation source. The MOF samples were analysed as such without any further modification. Due to the insulating nature of the

MOFs, charge neutralizing ion gun was used. All measured spectra were calibrated relative to the C 1s peak at 284.6 eV

APPENDIX 2

Supporting Data for Chapter 2

TABLE OF CONTENTS

Section A2.1. PXRD pattern of MOF-808-S

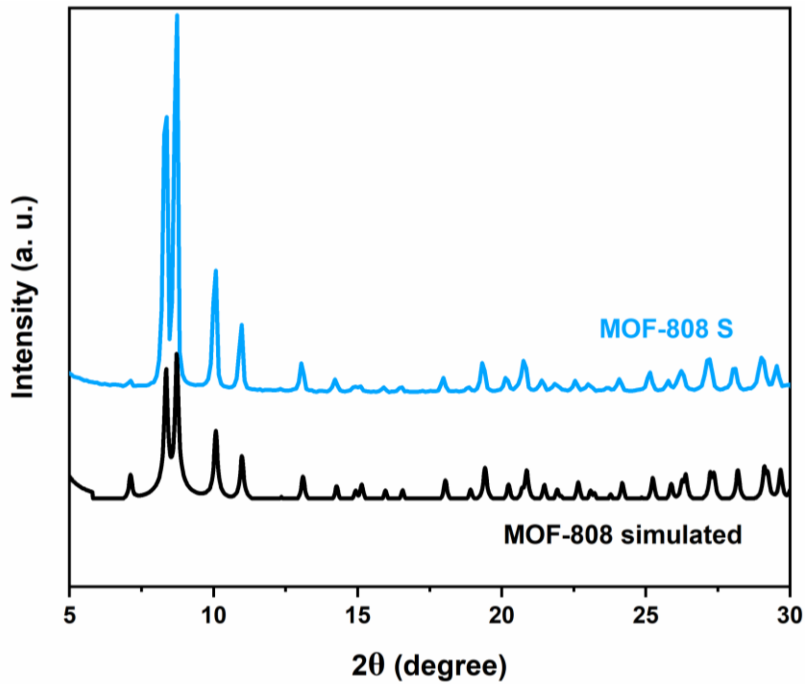

Figure A2.1. PXRD patterns of simulated MOF-808 and **MOF-808 S**.

Section A2.2. Fourier transformed - infrared (FT-IR) spectral analysis

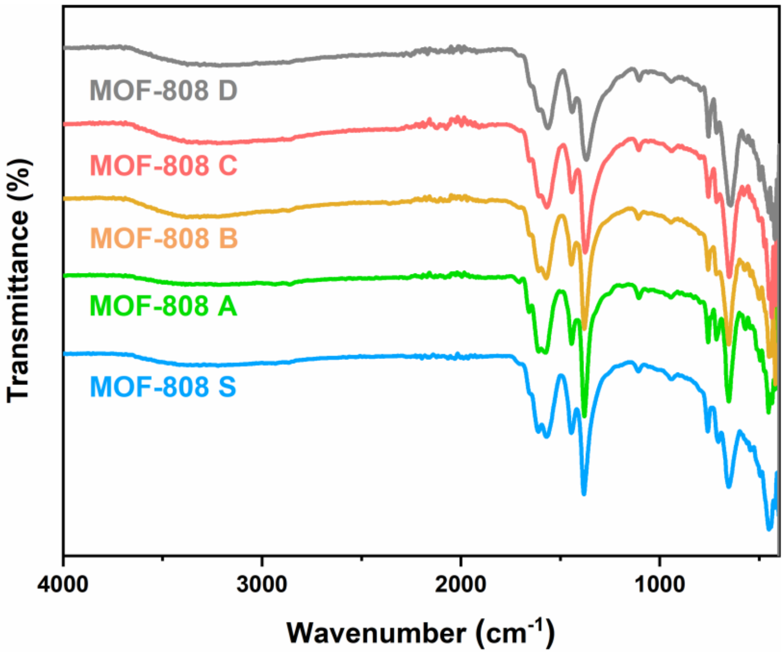

Figure A2.2. FTIR spectra of **MOF-808 S** and **MOF-808 A – D**.

Section A2.3. Calculation of linker defect sites from TGA

The reported formula of pristine MOF-808 is $Zr_6O_4(OH)_4[(C_6H_3)(COO)_3]_2(HCOO)_6$.[1] Molecular weight = 1363.7 g/mol.

During TGA, by heating the MOF till ~ 400 ^{o}C a plateau is obtained which represents the empty, solvent and modulator free, dehydroxylated MOF.[2] The structural formula then becomes $Zr_6O_9[(C_6H_3)(COO)_3]_2$. Molecular weight = 1105.3 g/mol; this plateau should ideally be found at 149.5% on the TGA trace (with respect to residual mass of $6(ZrO_2)$ at 600 ^{o}C).

At ~ 600 ^{o}C the MOF framework degrades completely to leave behind zirconium oxide $6(ZrO_2)$. Molecular weight = 739.3 g/mol; normalized to 100% on TGA trace.

Thus, the framework disintegration and organic linker loss occur in the temperature range of ~ (400 ^{o}C – 600 ^{o}C) during TGA measurement.

The theoretical weight loss for a perfect crystal structure would be = $\{(1105.3 - 739.3)/1105.3\} \times 100 = 33.11\%$ [This weight loss% is equivalent to the loss of 2 BTC linkers per secondary building unit (SBU)]

For the respective MOFs, an estimation of the weight loss% from 400 °C to 600 °C (from Figure 2.5a, chapter 2), then gives the number of missing linkers per node.

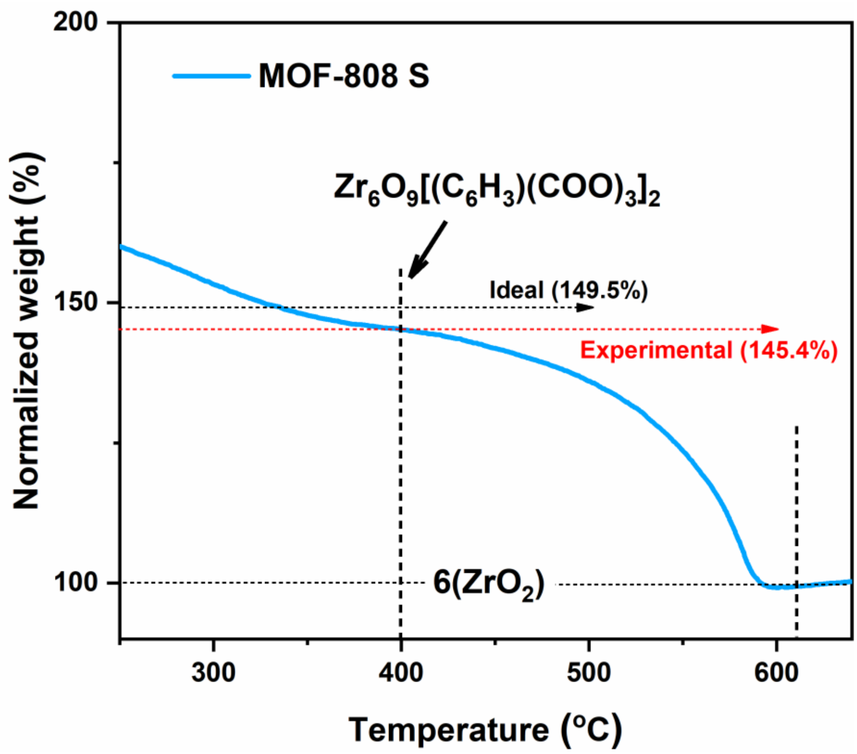

Figure A2.3. TG trace for **MOF-808-S**.

Table A2.1. Estimation of missing linkers per SBU from TGA.

Sample name	Number of missing linkers per SBU	Average number of linkers per SBU
MOF-808 S	0.123	1.87
MOF-808 A	0.055	1.94
MOF-808 B	0.29	1.71
MOF-808 C	0.475	1.52
MOF-808-D	0.253	1.74

Section A2.4. Quantification of defects from ICP-OES and ^{1}H-NMR

ICP-OES

For ICP-OES analysis, approximately 2 mg of the MOFs were digested in 5 mL of conc. HNO_3 acid (stock solution). Out of the 5 mL stock solution, 1 mL was taken and diluted to 10 mL (test solution), which was then analyzed to estimate Zr.

Table A2.2. Number of Zr per SBU of synthesized MOF-808.

Sample	**MOF-808 S**	**MOF-808 A**	**MOF-808 B**	**MOF-808 C**	**MOF-808 D**
Number of Zr per formula of MOF-808	5.8	5.6	5.7	5.6	4.9

^{1}H-NMR

To estimate the content of BTC in each of the MOFs, first, a calibration plot was prepared for known concentrations of H_3BTC, dissolved in 2M NaOH prepared in D_2O. Then, approximately 2 mg of the MOFs were digested in known volume of 2M NaOH in D_2O and the spectra were recorded. The concentration of BTC in each of these samples was then determined by correlating the peak integration from these spectra with the calibration plot. Tetramethylammonium chloride was taken as the internal standard (δ = 3 ppm) for all the experiments. Peaks observed at ~ 8.22 ppm and ~ 8.27 ppm are attributed to BTC and formate, respectively. Peak at ~ 2.1 ppm is probably due to the presence of dimethyl amine, a decomposition product of DMF. The other product of this hydrolysis is formate, which is formed in a 1:1 ratio with dimethylamine.

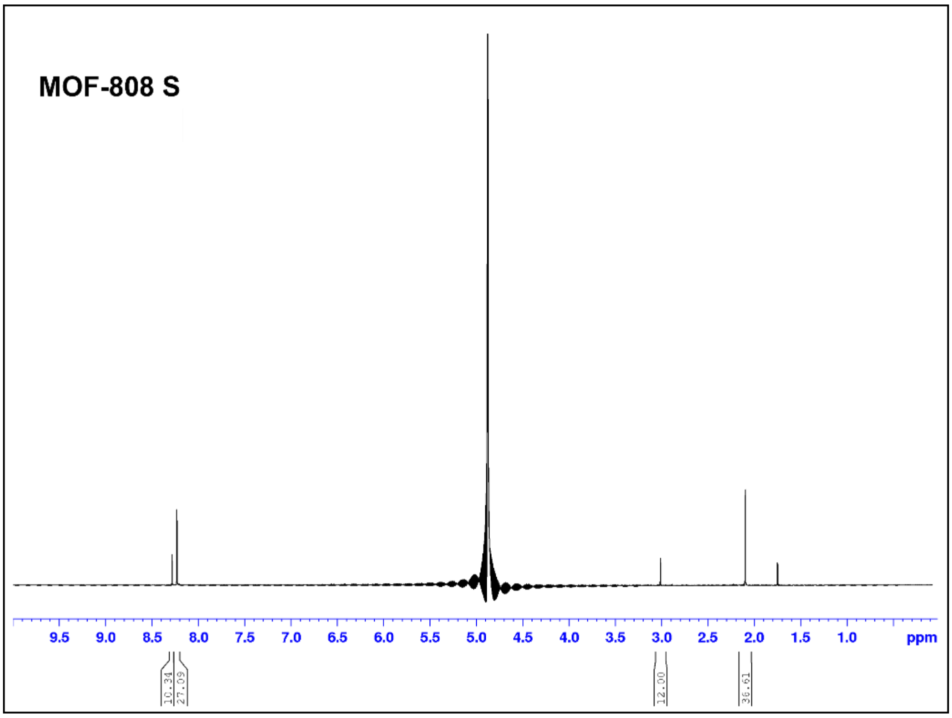

Figure A2.4. ^{1}H-NMR spectrum of **MOF-808 S** digested in 2 M NaOH solution prepared in D_2O.

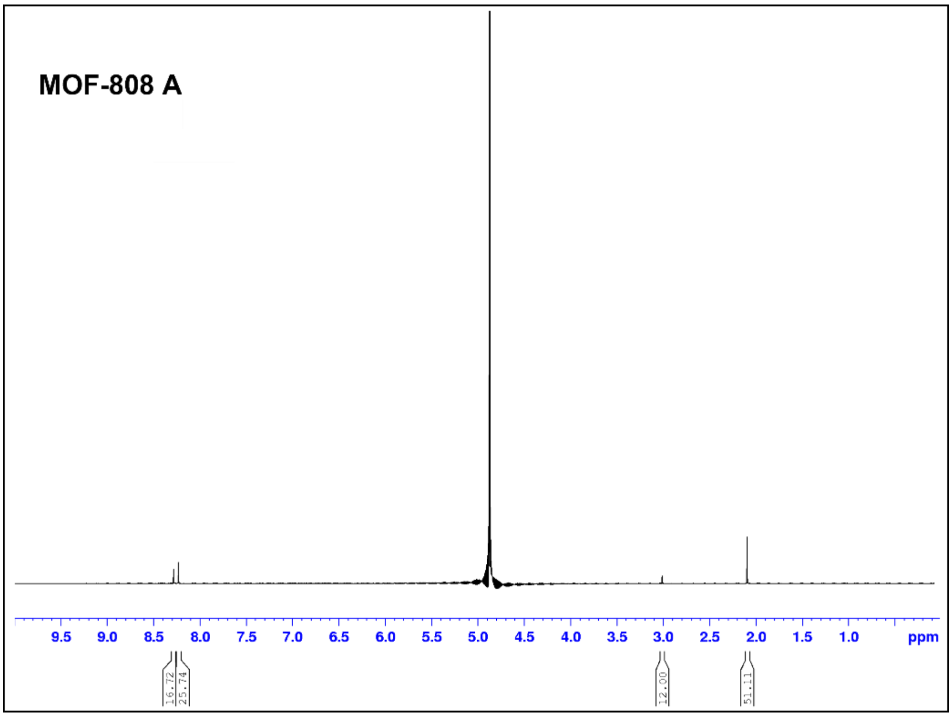

Figure A2.5. ^{1}H-NMR spectrum of **MOF-808 A** digested in 2 M NaOH solution prepared in D_2O.

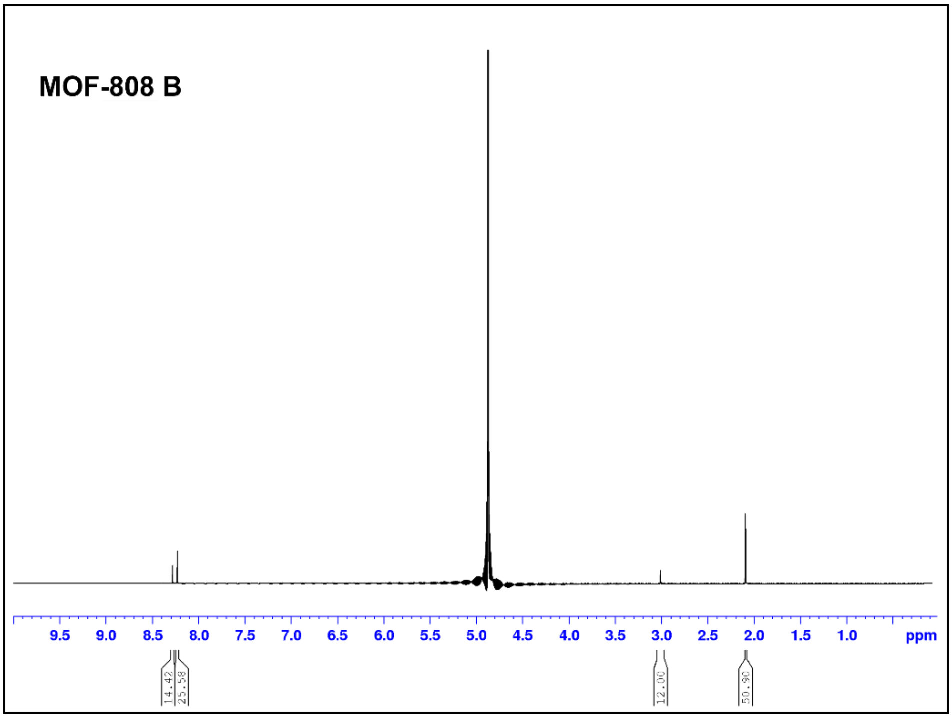

Figure A2.6. ^{1}H-NMR spectrum of **MOF-808 B** digested in 2 M NaOH solution prepared in D_2O.

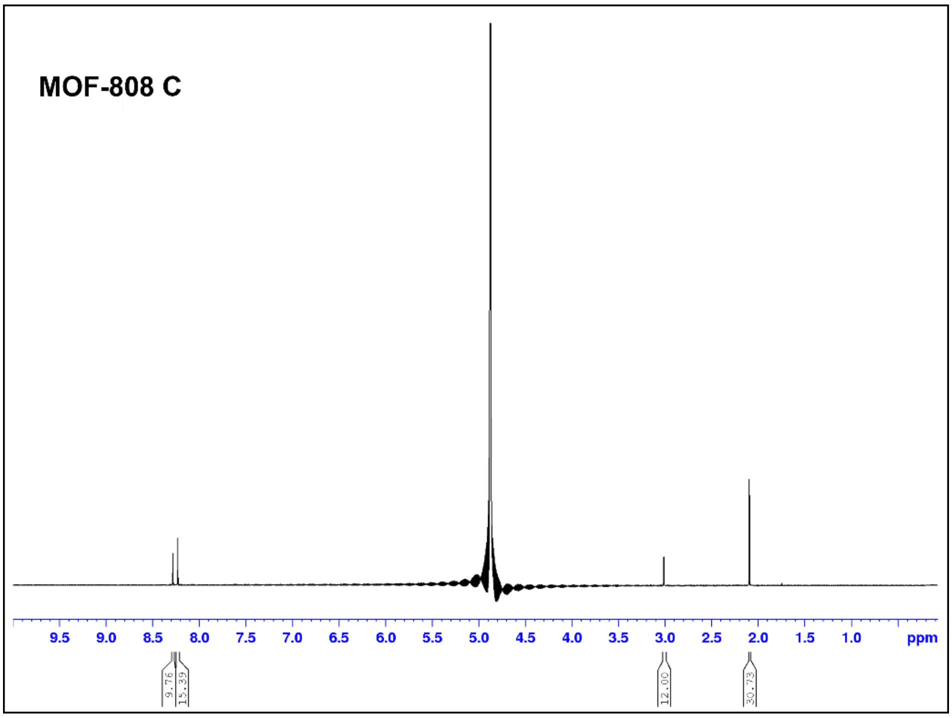

Figure A2.7. ^{1}H-NMR spectrum of **MOF-808 C** digested in 2 M NaOH solution prepared in D_2O.

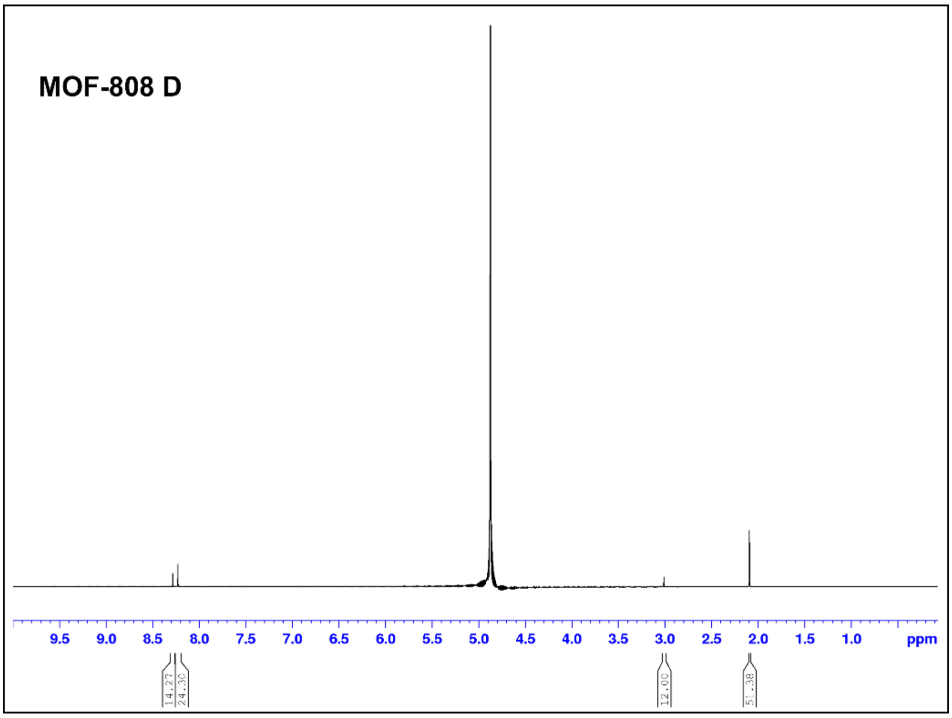

Figure A2.8. ^{1}H-NMR spectrum of **MOF-808 D** digested in 2 M NaOH solution prepared in D_2O.

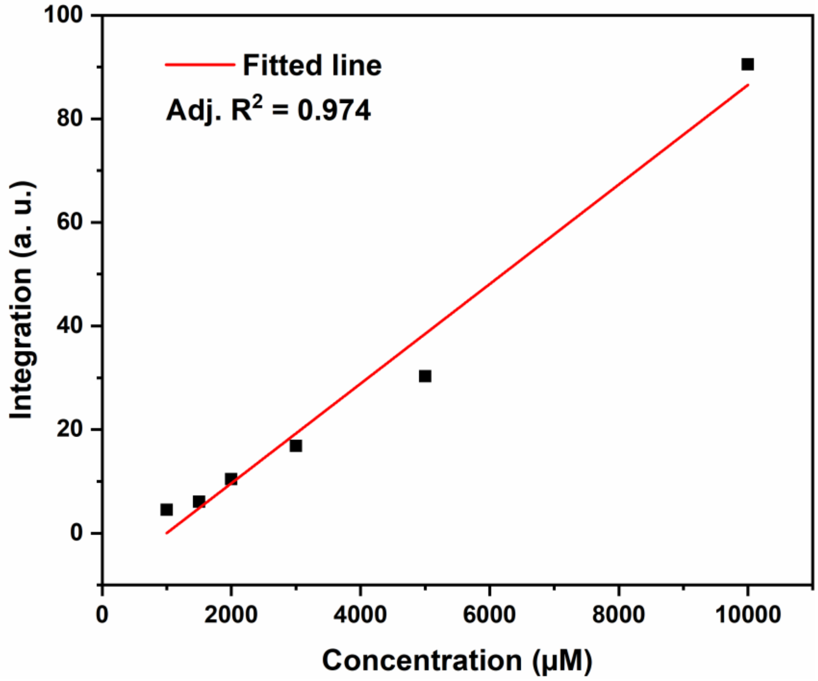

Figure A2.9. Calibration plot for known concentrations of BTC dissolved in 2M NaOH (in D_2O).

Table A2.3. Number of BTC per SBU of synthesized MOF-808.

Sample	MOF-808 S	MOF-808 A	MOF-808 B	MOF-808 C	MOF-808 D
Number of BTC per formula of MOF-808	1.81	1.84	1.67	1.33	1.60

The number of BTC linkers per formula of MOF-808 estimated from ^{1}H-NMR data (Table A2.3) matches quite well with the data obtained from TGA (Table A2.1) From the ^{1}H-NMR data, the formate concentration in the MOFs were also estimated. Now, since one of the decomposition products of DMF is formate, which is indistinguishable from the formate originally grafted in the MOFs, the formate integral was corrected by subtracting the contribution of formate derived from hydrolysis of DMF, in order to obtain the value associated with the cluster-bound formate.

Table A2.4. Number of formate per SBU of synthesized MOF-808.

Sample	MOF-808 S	MOF-808 A	MOF-808 B	MOF-808 C	MOF-808 D
Number of formate per formula of MOF-808	1.101	1.82	1.30	1.23	1.26

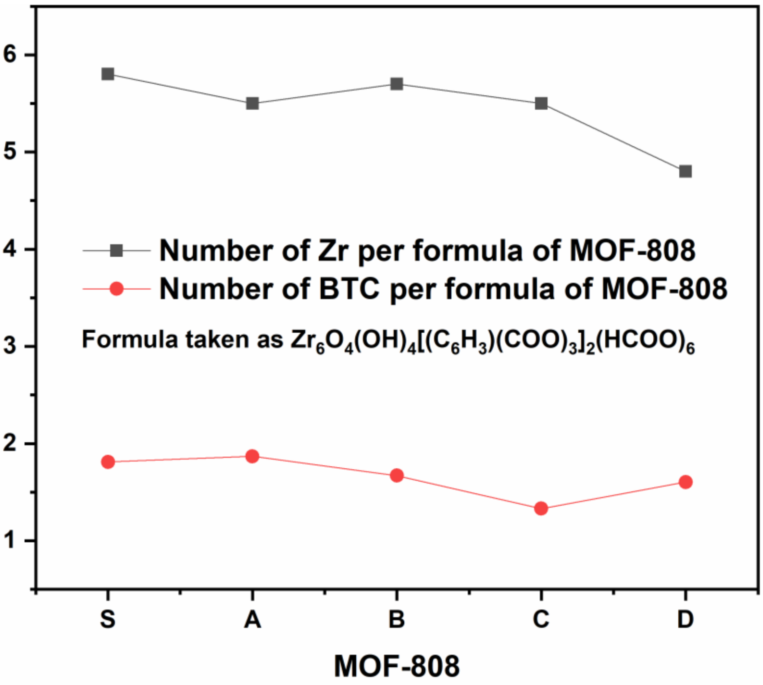

Figure A2.10. Comparison of the numbers of Zr and BTC per SBU of synthesized MOF-808, as determined from ICP-OES and ^{1}H-NMR.

Section A2.5. N_2 sorption analysis for MOF-808 S

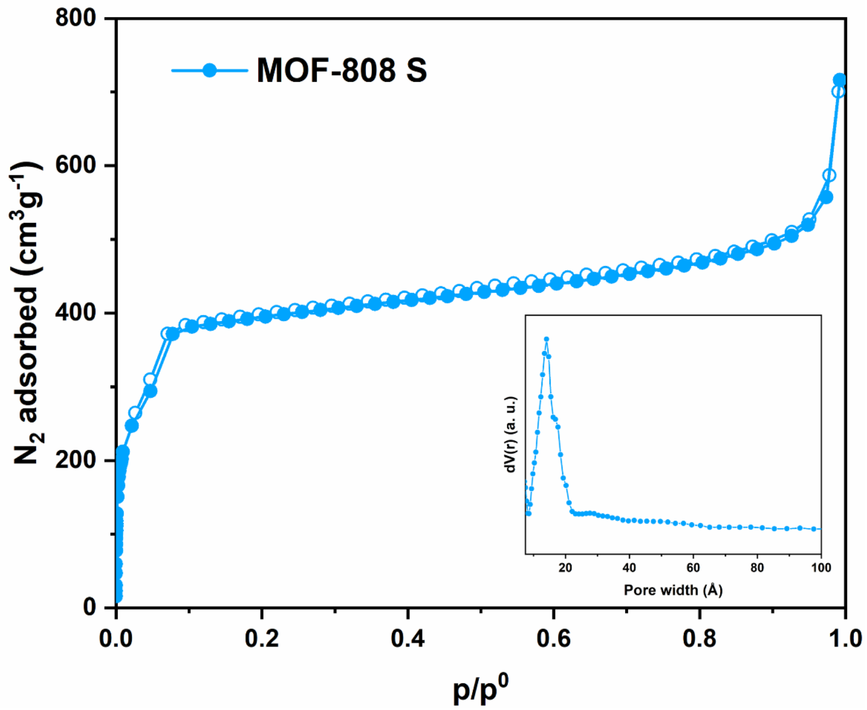

Figure A2.11. N_2 sorption isotherm and pore size distribution (inset) of **MOF-808 S**. Filled spheres denote adsorption, and hollow spheres denote desorption experimental data points.

Section A2.6. X-ray photoelectron spectra

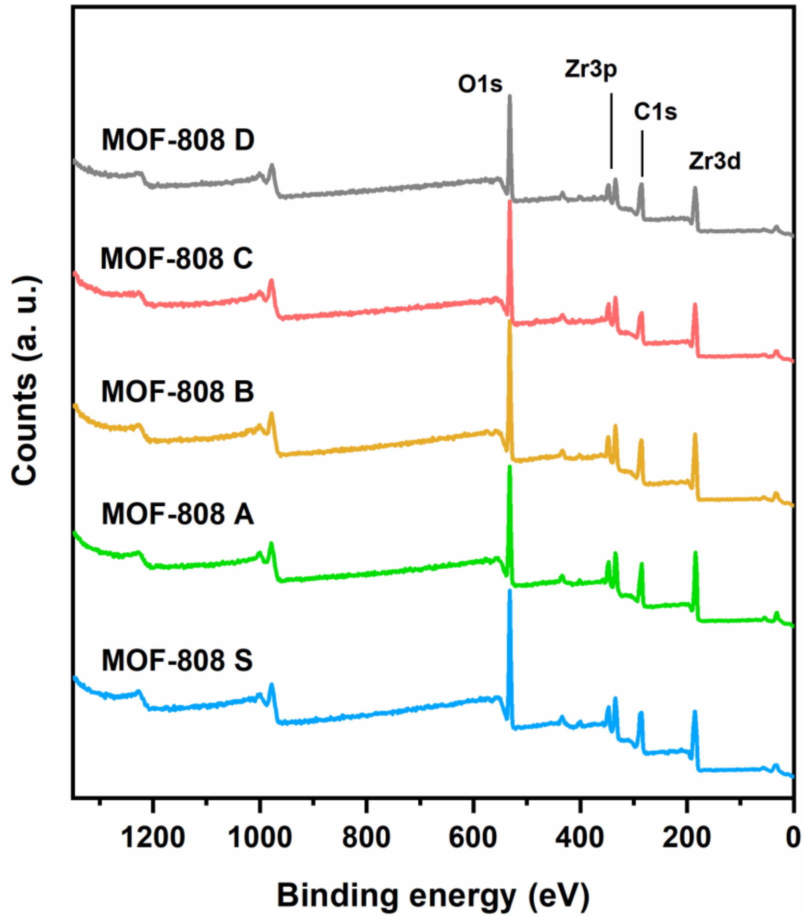

Figure A2.12. XPS survey scans of **MOF-808 S** and **MOF-808 A – D.**

Section A2.7. Dynamic vapour sorption (DVS) analysis

Dynamic vapour sorption (DVS) analysis of all the samples were performed at a temperature of 25 °C and under N_2 atmosphere. All the samples were activated at 120 °C for 12 hours, prior to the measurement.

Here, it is noteworthy that the defective **MOF-808 A** – **C** show significantly higher water sorptivity and its retention than **MOF-808 S** (Figure A2.13). Importantly, it is **MOF-808 C** which has the highest water uptake capacity in moderate to high relative humidity. It is probably the result of the high concentration of open metal sites created by missing linker defects – occupied by acidic OH^-/H_2O, while still maintaining good porosity and crystallinity.

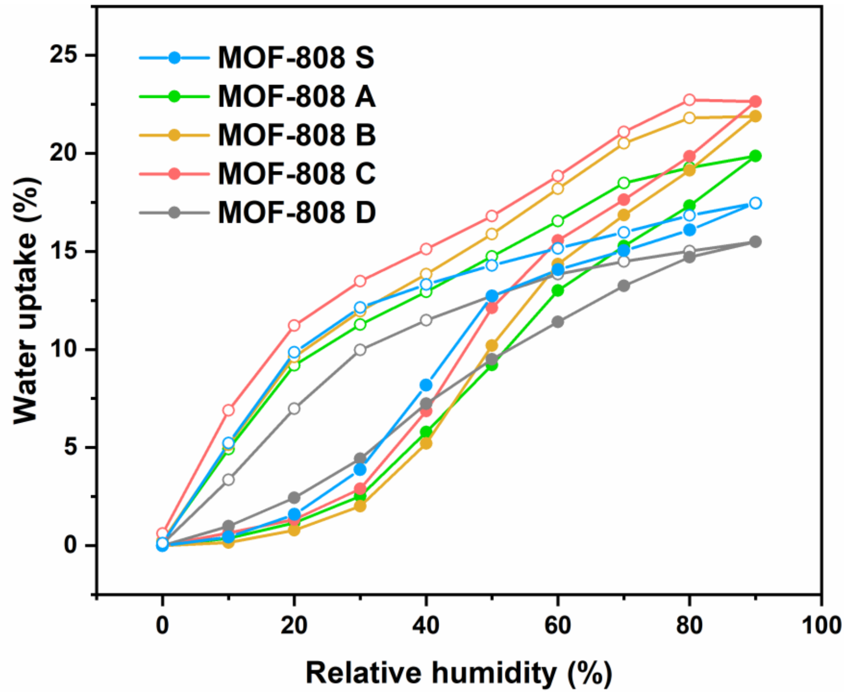

Figure A2.13. Dynamic vapour sorption isotherms for **MOF-808 A – D** and **MOF-808 S.**

Section A2.8. Experimental details of the acid-base titration

Methodology

The experimental method followed here was adapted from an earlier report by Klet *et. al*.[3] The MOF samples were powdered well with mortar and pestle prior to the experiment. Approximately 50 mg of the MOFs were added in 60 mL of 0.1M aqueous $NaNO_3$ solution and then kept under stirring overnight to equilibrate, covered with a parafilm. The pH of the solution was adjusted to 3 using 0.1 M aqueous HCl solution, then titrated with 40 µL injection volume of 0.1 M aqueous NaOH solution, up to pH 8. The injection rate was maintained at 0.02 mL min^{-1} and the solution was kept under vigorous stirring throughout the experiment. The pH of the solution was plotted against the volume of NaOH (0.1M aq.) used, to get the titration curves.

Acid-base titration curve for MOF-808 S

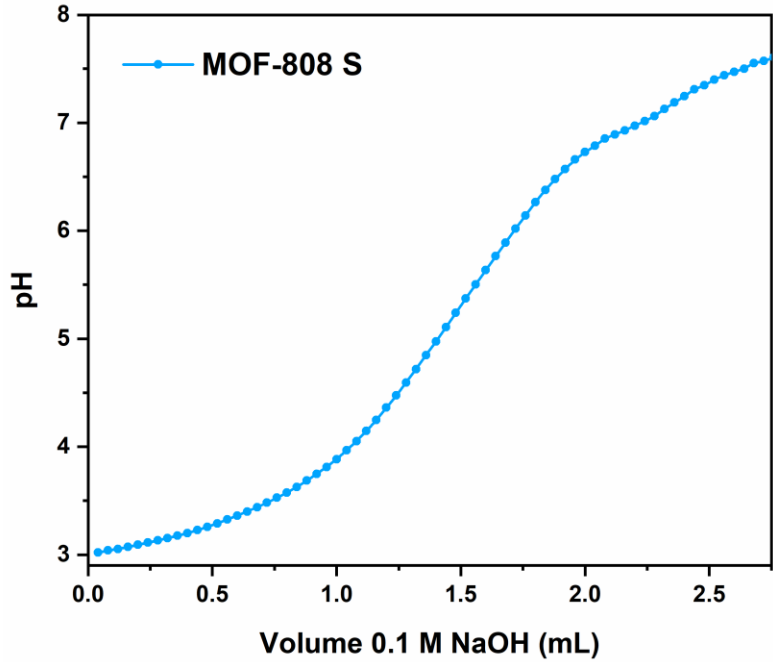

Figure A2.14. Acid-base titration curve for **MOF-808 S**.

Section A2.9. Electrochemical impedance spectroscopy

Impedance measurement under different temperature

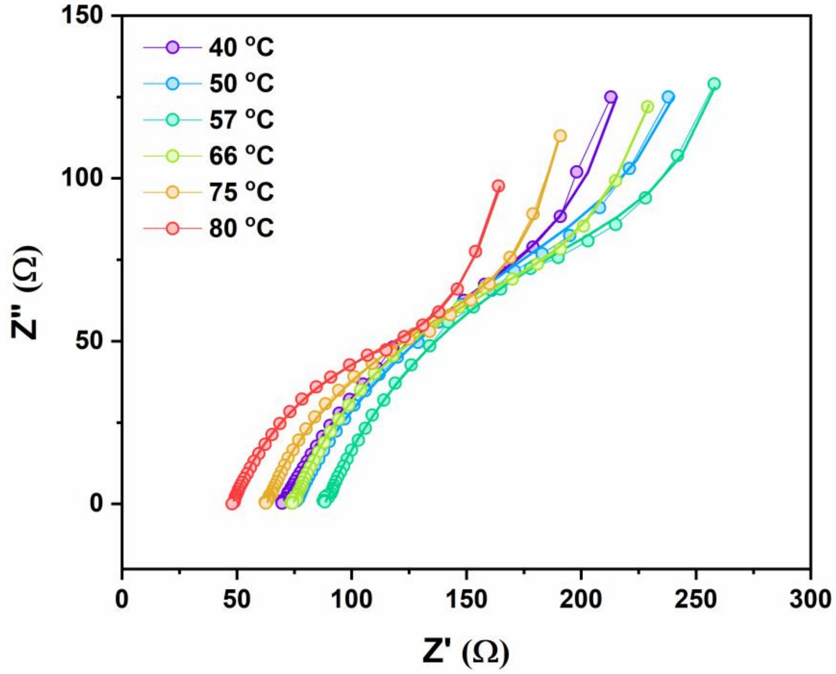

Figure A2.15. Nyquist plots of impedance measurements performed for **MOF-808 S** at a constant relative humidity of 98% and variable temperature. Spheres denote experimental data points; solid line denotes fitted curve.

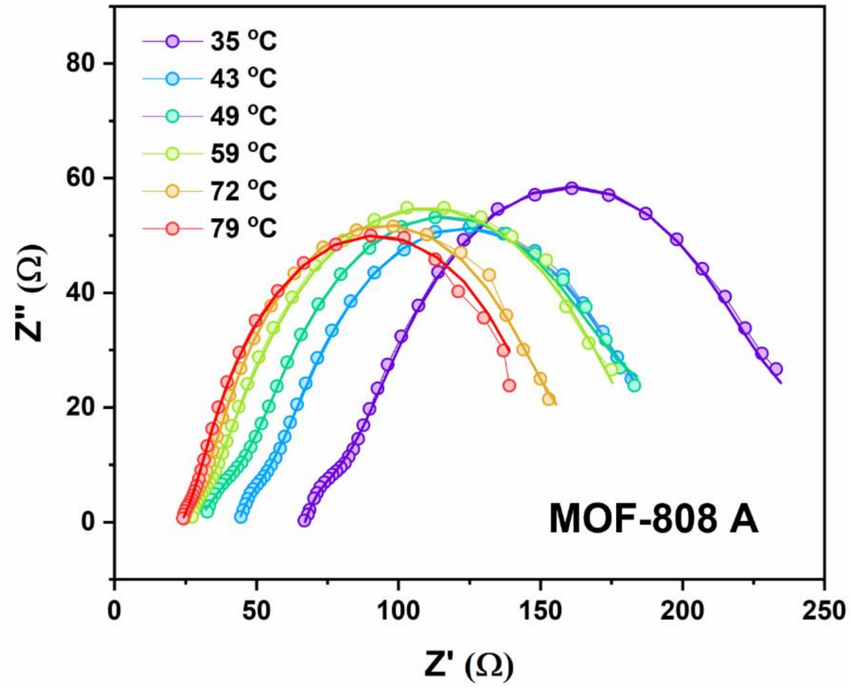

Figure A2.16. Nyquist plots of impedance measurements performed for **MOF-808 A** at a constant relative humidity of 98% and variable temperature. Spheres denote experimental data points; solid line denotes fitted curve.

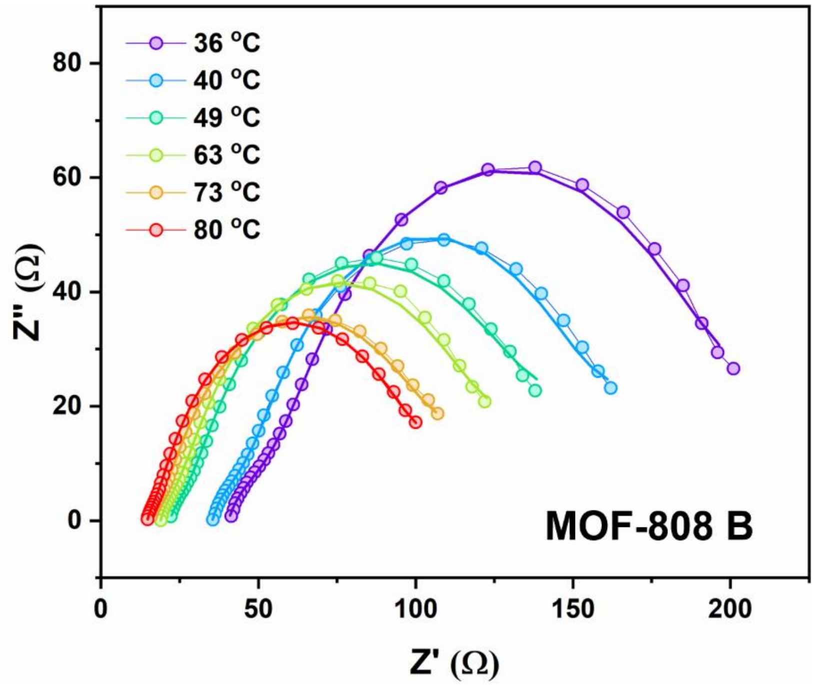

Figure A2.17. Nyquist plots of impedance measurements performed for **MOF-808 B** at a constant relative humidity of 98% and variable temperature. Spheres denote experimental data points; solid line denotes fitted curve.

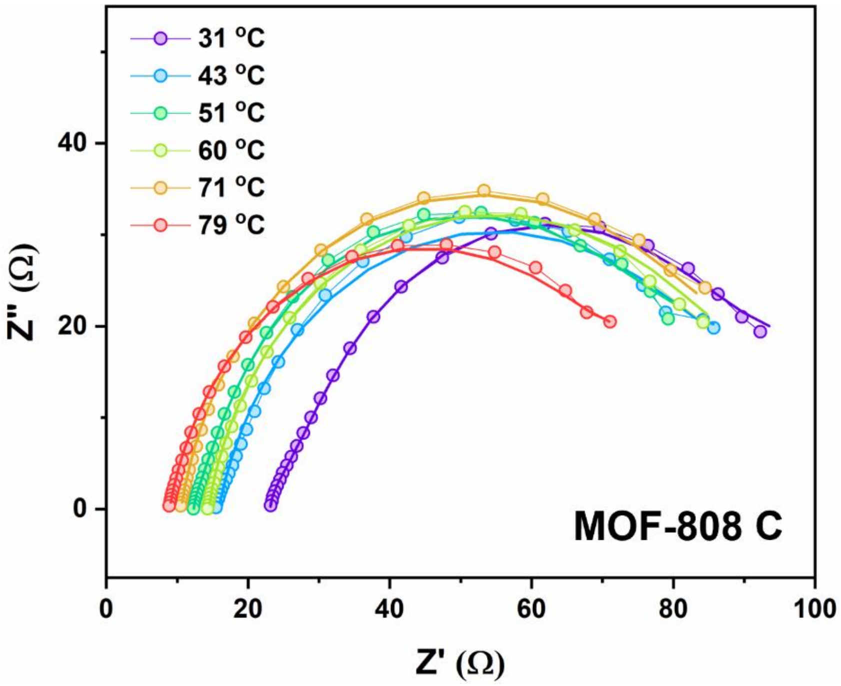

Figure A2.18. Nyquist plots of impedance measurements performed for **MOF-808 C** at a constant relative humidity of 98% and variable temperature. Spheres denote experimental data points; solid line denotes fitted curve.

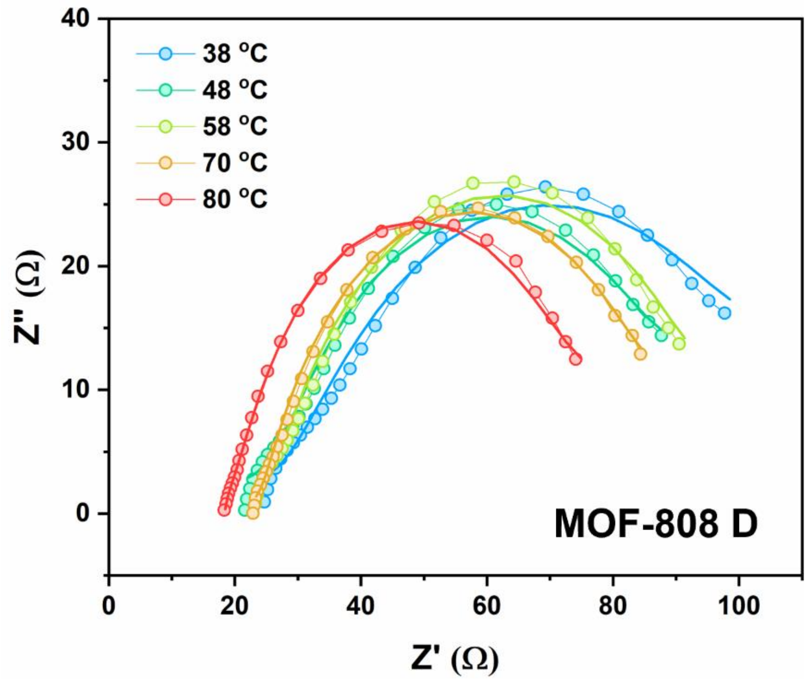

Figure A2.19. Nyquist plots of impedance measurements performed for **MOF-808 D** at a constant relative humidity of 98% and variable temperature. Spheres denote experimental data points; solid line denotes fitted curve.

Calculation of proton conductivity from Impedance spectra by fitting with an equivalent circuit

The proton conductivity of the MOFs was determined from the corresponding Nyquist plots after fitting them to the most suitable equivalent circuit using EC-Lab software.

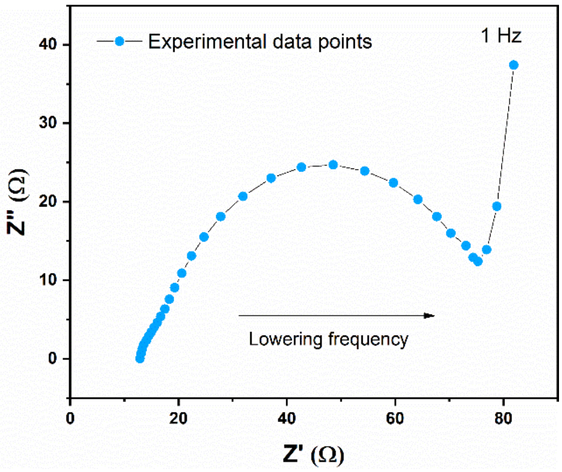

Figure A2.20. A representative Nyquist plot showing all the experimental datapoints over the entire frequency region.

In Figure A2.20, the Nyquist plot shows one small, perturbed semicircle in high frequency region, followed by a larger semicircle, and then a tail at low frequency region. This plot displays the general features obtained for **MOF-808 A – D** samples, and the simplest equivalent circuit which fitted these experimentally obtained data plots well, is given below. Since the conductivity of the samples is determined from the high frequency region of the Nyquist plot,[4,5a] the tail at the low frequency region has been omitted in all other plots for clarity.

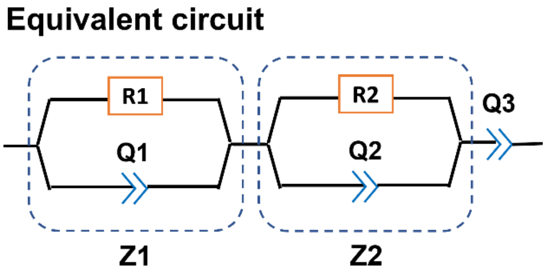

The equivalent circuit is composed of three parts – (1) the grain-interior impedance/bulk impedance (Z1); (2) the inter-grain impedance (Z2); (3) impedance at the electrode-solid electrolyte junction/interface given by the constant phase element (CPE) Q3, all connected in series.

Z1 and Z2 are both composed of a resistance (R) element and a constant phase element (Q) connected to each other in parallel mode. Here R1 accounts for the resistance faced during proton conduction through the bulk of the MOF nanocrystals (grain interior resistance); it is determined from the smaller semicircle at high frequency region of Nyquist plot. R2 accounts for the resistance faced during inter grain proton conduction, determined from the larger semicircle. Here Q1 and Q2 are constant phase elements (CPE) which account for the depressed semicircles observed in real experimental cases, due to the generation of non-ideal capacitance in bulk and interfaces. Similarly, to account for the non-ideal capacitance generated at the electrode/solid electrolyte interface, a CPE element Q3 is introduced.[5]

R1 depends on three factors. Those are a) intrinsic conductivity of the pelletized sample (**σ**); b) thickness of the pellet (**l**); c) area of cross-section of the pellet (**A**).

Calculation of proton conductivity from the R1 value

Resistivity (**ρ**) of a material = $(\mathbf{R} \times \mathbf{A})/\mathbf{l}$ ……. (1)

Thus, conductivity (**σ**) = $1/\ \boldsymbol{\rho} = \mathbf{l}/(\mathbf{R} \times \mathbf{A})$ ……. (2)

R = resistance of sample; **σ** = conductivity of the sample;

l = thickness of pellet

A = area of cross section of pellet

The conductivity for all the MOFs was calculated using similar data fitting and calculations.

Table A2.5. Proton conductivity of MOF-808 S in various temperatures.

Temperature (°C)	Conductivity (Scm^{-1})
40	0.00277
50	0.00257
57	0.0024
66	0.00265
75	0.0036
80	0.00601

Table A2.6. Proton conductivity of MOF-808 A in various temperatures.

Temperature (°C)	**Conductivity (Scm^{-1})**
35	0.00658
43	0.0079
49	0.01188
59	0.01579
72	0.02746
79	0.08075

Table A2.7. Proton conductivity of MOF-808 B in various temperatures.

Temperature (°C)	**Conductivity (Scm^{-1})**
36	0.00924
40	0.01081
49	0.01514
63	0.02129
73	0.03713
80	0.1477

Table A2.8. Proton conductivity of MOF-808 C in various temperatures.

Temperature (°C)	**Conductivity (Scm^{-1})**
31	0.01071
43	0.01449
51	0.02269
60	0.02647
71	0.0526
79	0.26074

Table A2.9. Proton conductivity of MOF-808 D in various temperatures.

Temperature (°C)	Conductivity (Scm^{-1})
38	0.00239
48	0.00276
58	0.00331
70	0.00509
80	0.01124

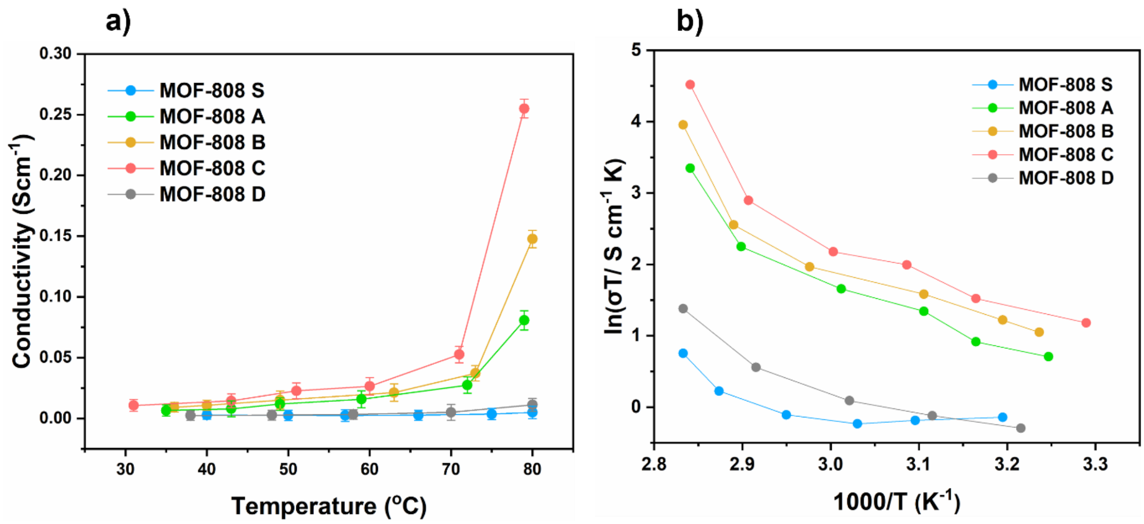

Figure A2.21. a) Comparison of proton conductivities for **MOF-808 A – D** and **MOF-808 S** at varying temperatures and 98% relative humidity (R.H.) along with standard deviation for 3 sets of measurements; b) Plot of ln(σT) versus 1000/T as derived from the mean values of figure A2.21a.

Figure A2.21 compares the observed proton conductivity for **MOF-808 A – D** and **MOF-808 S** along with the standard deviation for 3 sets of impedance measurement, to check the reproducibility of the data. From the figure it can be observed that the conductivity increases with increasing density of missing linker defects in the sister MOFs.

Determination of activation energy

Activation energies (E_a) for proton conductivity in **MOF-808 A – D** were calculated from the Arrhenius plot constructed between ln(σT) and 1000/T (Figure 6, chapter 2).

From Arrhenius equation, $\boldsymbol{\sigma T = \sigma_0 \times \exp(-E_a/RT)}$ ……. (3)

σ = proton conductivity of the sample

T = Temperature in Kelvin

E_a = Activation energy of proton conduction

R= Ideal gas constant

Arrhenius equation can be restructured as **$\ln(\sigma T) = \ln\sigma_0 - (Ea/RT)$** ……. (4)

Or, **$\ln(\sigma T) = \ln\sigma_0 + \{-E_a/(1000\times R)\ (1000/T)\}$** …….
(5)

From the plot between **$\ln(\sigma T)$** and **1000/T**, the slope of the straight line = **$-E_a/1000\times R$**

Impedance measurement under different relative humidity (R. H.)

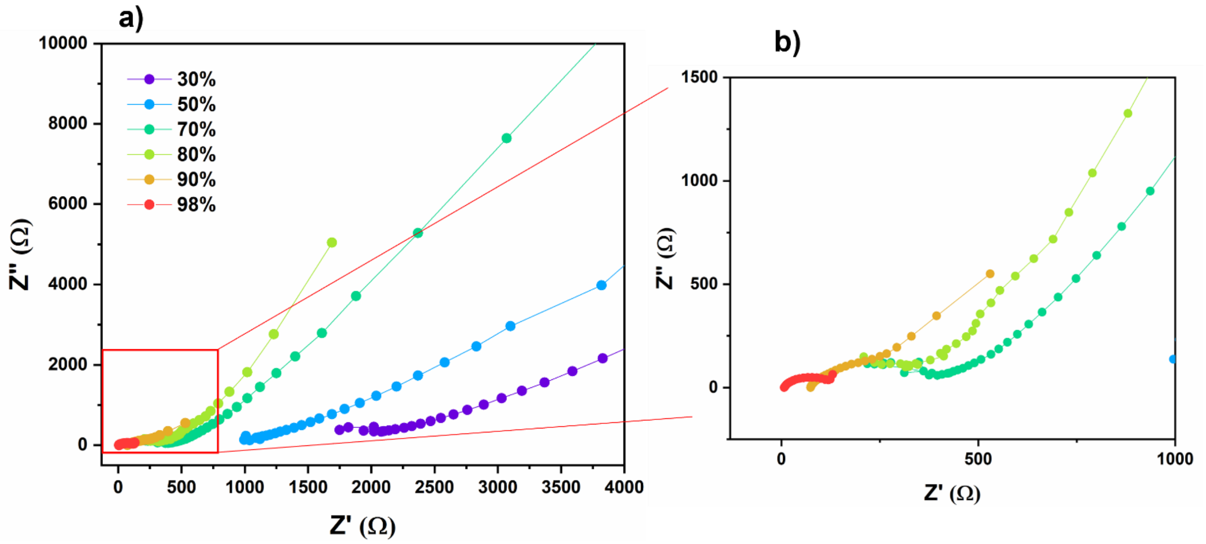

Figure A2.22. a) Nyquist plots of impedance measurements performed for **MOF-808 C** at a constant temperature of 60 ºC and variable humidity; b) an enlarged view of the Nyquist plots at higher humidity.

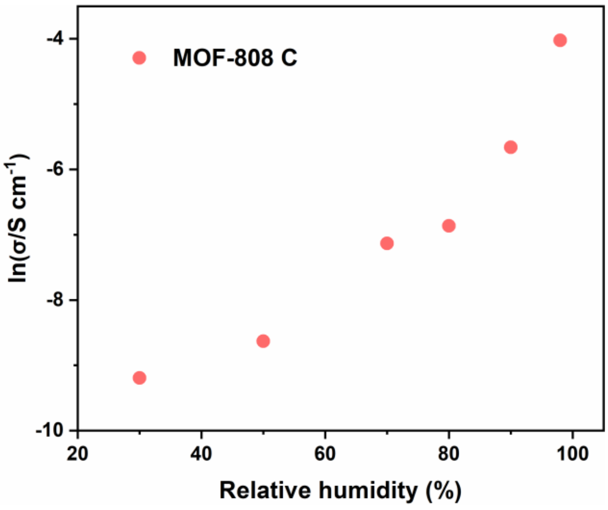

Figure A2.23. a) Plot of ln(conductivity) versus relative humidity for **MOF-808 C** as derived from figure A2.22.

Section A2.10. Controlled experiments on MOF-808 C

Capping of open metal sites by Benzoic acid (MOF-808 C-benz) and its effect on proton conductivity

There was no noticeable change in the PXRD pattern of **MOF-808 C-benz** from **MOF-808 C** (Figure A2.24). This means that the MOF-808 framework remains intact after the incorporation of benzoic acid into the structure. The FT-IR spectra of **MOF-808 C-benz** displays several new features as compared to **MOF-808 C** (Figure A2.25). For **MOF-808 C-benz** there is a change in relative intensity of the peaks originating from COO- stretch and a sharp increase in the peak intensity for aromatic C=C. This is accompanied by a lowering of O-H stretch band. There are also several new peaks (marked with *) generated at 1418 cm^{-1}, 1060 cm^{-1}, 1070 cm^{-1} and 1025 cm^{-1}, because of the incorporation of benzoic acid. The position of these peaks is consistent with earlier reports.[6]

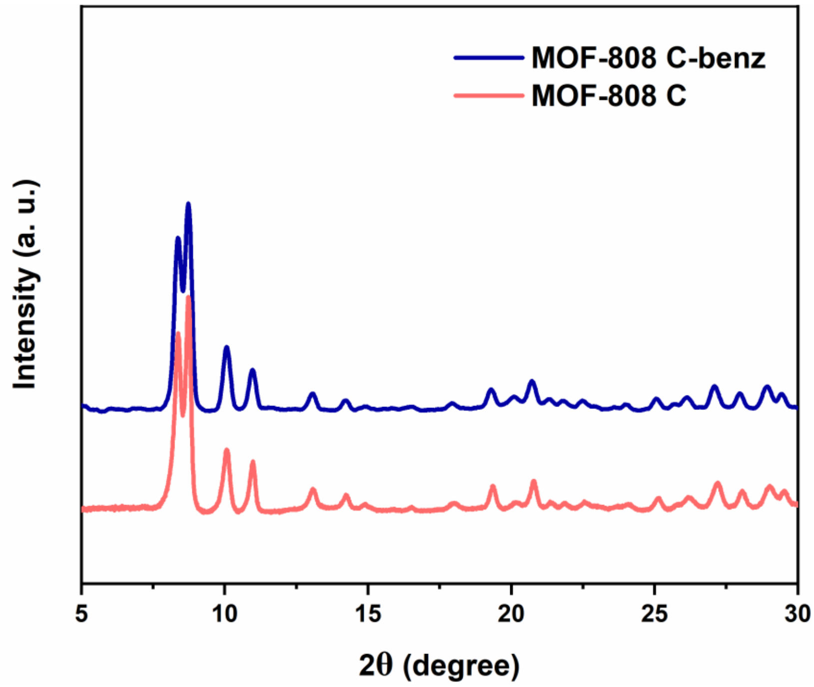

Figure A2.24. PXRD patterns of **MOF-808 C and MOF-808 C-benz**.

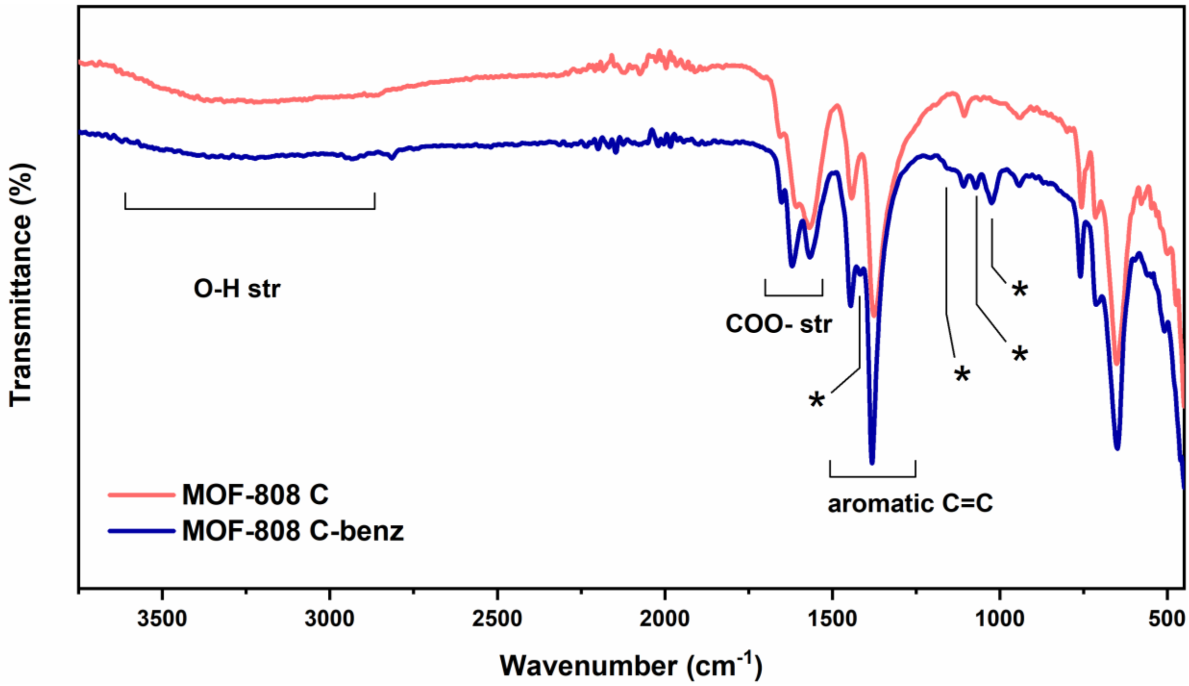

Figure A2.25. FTIR spectra of **MOF-808 C** and **MOF-808 C-benz**.

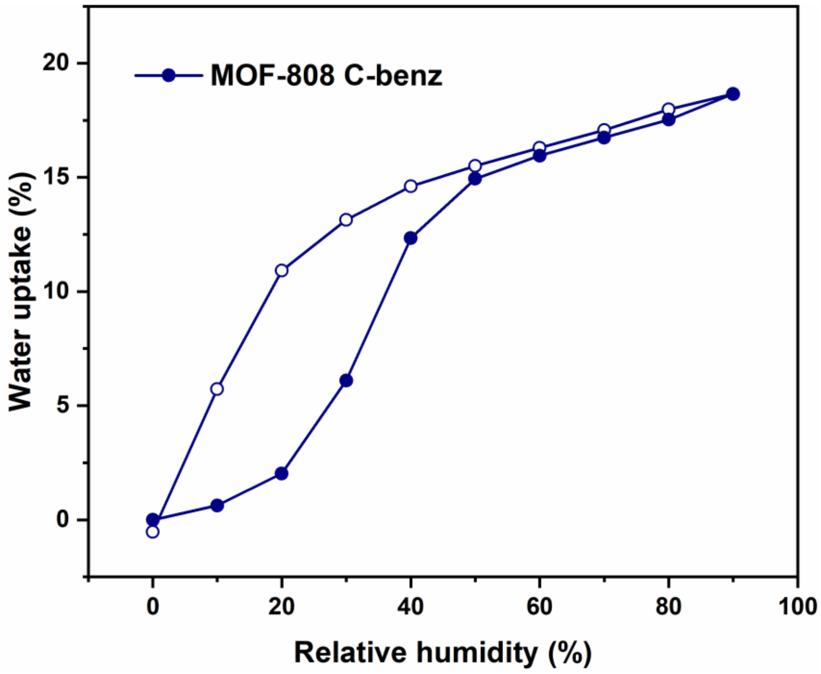

Figure A2.26. Water uptake capacity of **MOF-808 C-benz**.

MOF-808 C-benz: Impedance measurement under different temperatures

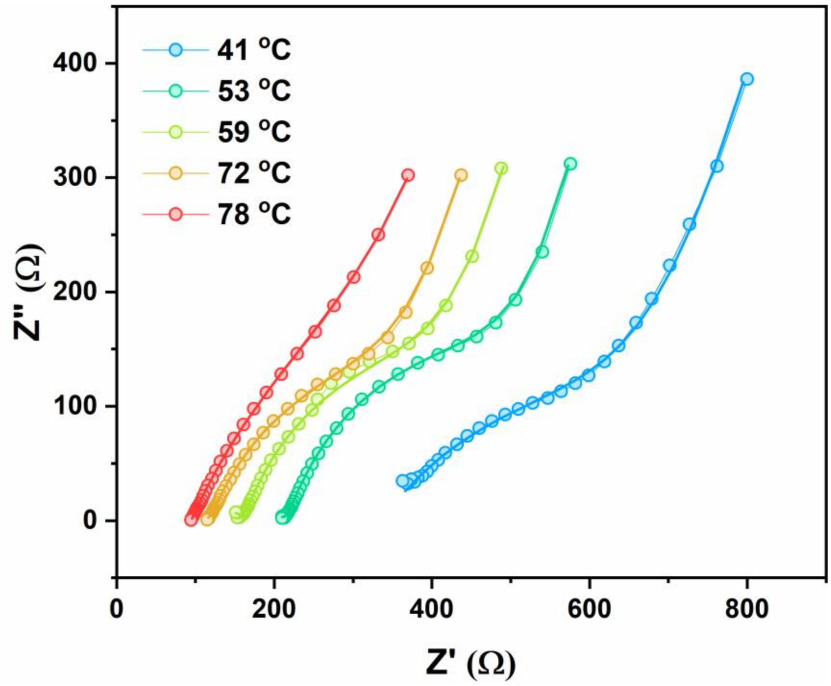

Figure A2.27. Nyquist plot for **MOF-808 C-benz** at a constant relative humidity of 98% and variable temperature. Spheres denote experimental data points; solid line denotes fitted curve.

Table A2.10. Proton conductivity of MOF-808 C-benz in various temperatures.

Temperature (°C)	**Conductivity (Scm^{-1})**
41	0.000391
53	0.000705
59	0.000903
71	0.00122
78	0.00146

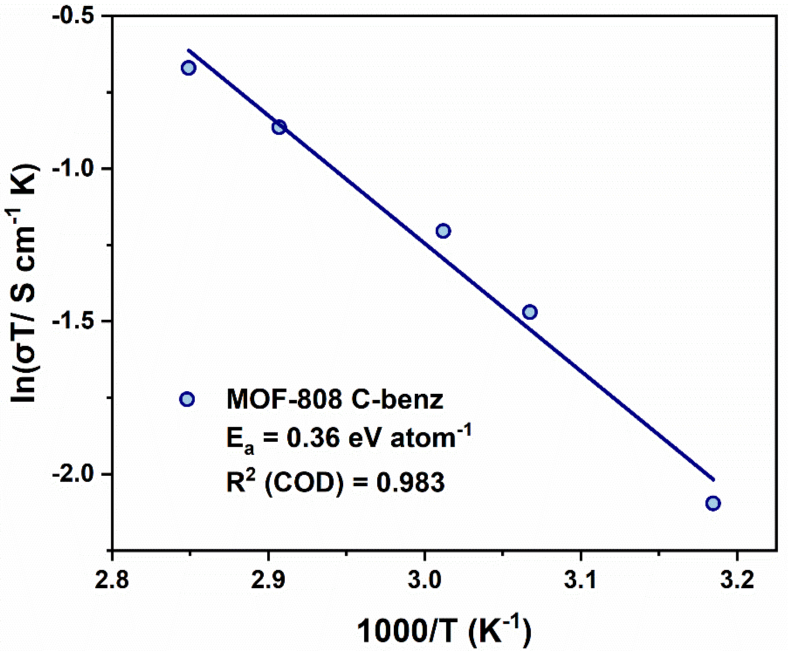

Figure A2.28. Arrhenius plot of proton conductivity for **MOF-808 C-benz** at 98% relative humidity (R.H.), along with the activation energy (E_a).

Exchange of acidic protons with Li^+ ions (MOF-808 C-Li) and its effect on proton conductivity

The PXRD pattern of **MOF-808 C-Li** is similar to that of **MOF-808 C** (Figure A2.29). This means that the MOF-808 framework remains intact after the exchange of the protons in the structure with lithium ions.

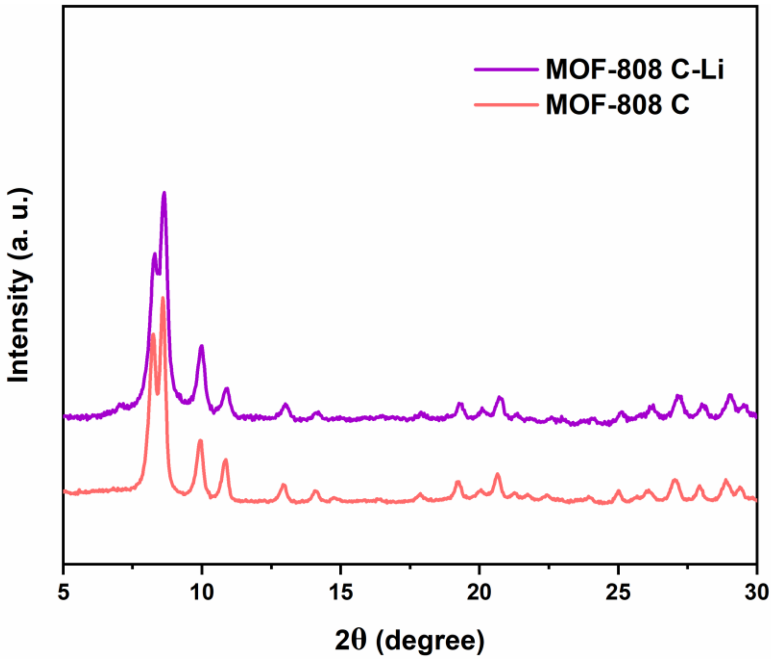

Figure A2.29. PXRD patterns of **MOF-808 C and MOF-808 C-Li**.

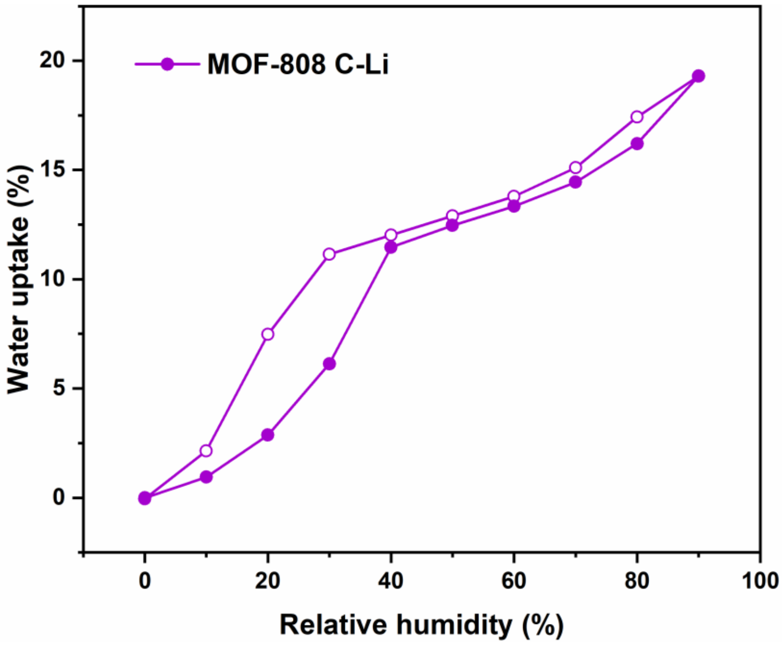

Figure A2.30. Water uptake capacity of **MOF-808 C-Li**.

MOF-808 C-Li: *Impedance measurement under different temperatures*

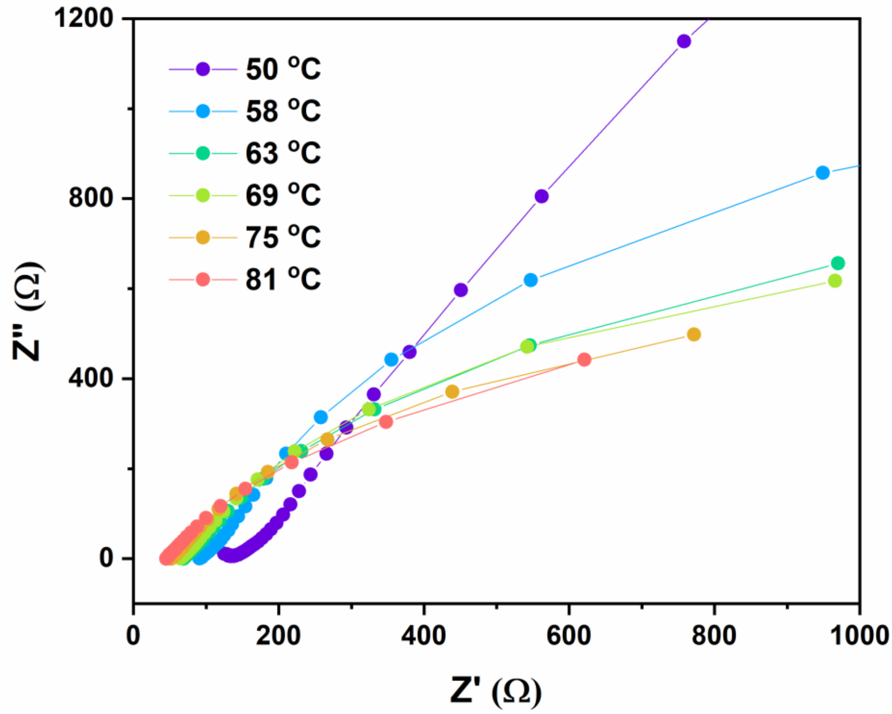

Figure A2.31. Nyquist plot for **MOF-808 C-Li** at a constant relative humidity of 98% and variable temperature. Spheres denote experimental data points; solid line denotes fitted curve.

Table A2.11. Proton conductivity of MOF-808 C-Li in various temperatures.

Temperature (°C)	Conductivity (Scm^{-1})
50	0.0008787
58	0.00121
63	0.00157
69	0.00169
75	0.00211
81	0.00244

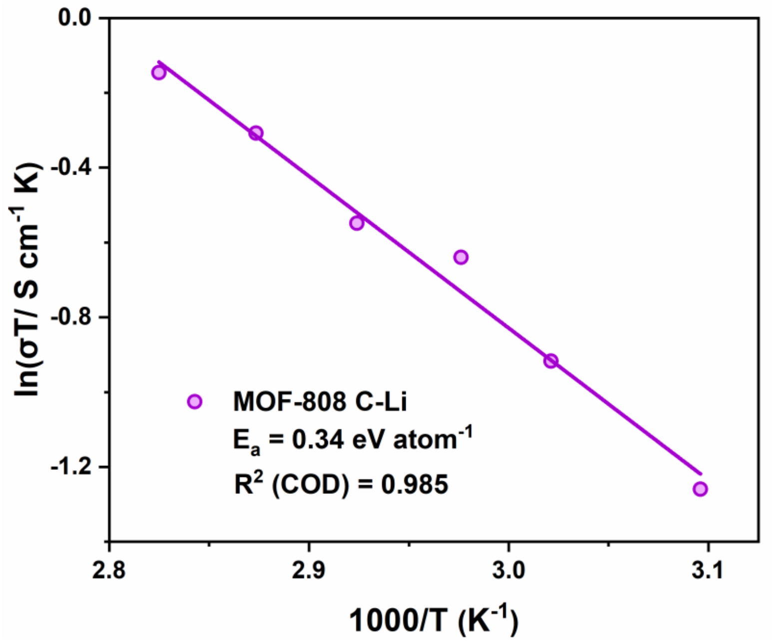

Figure A2.32. Arrhenius plot of proton conductivity for **MOF-808 C-Li** at 98% relative humidity (R.H.), along with the activation energy (E_a).

Section A2.11. Long term stability test under operational conditions

84 hours at 80 ºC durability test

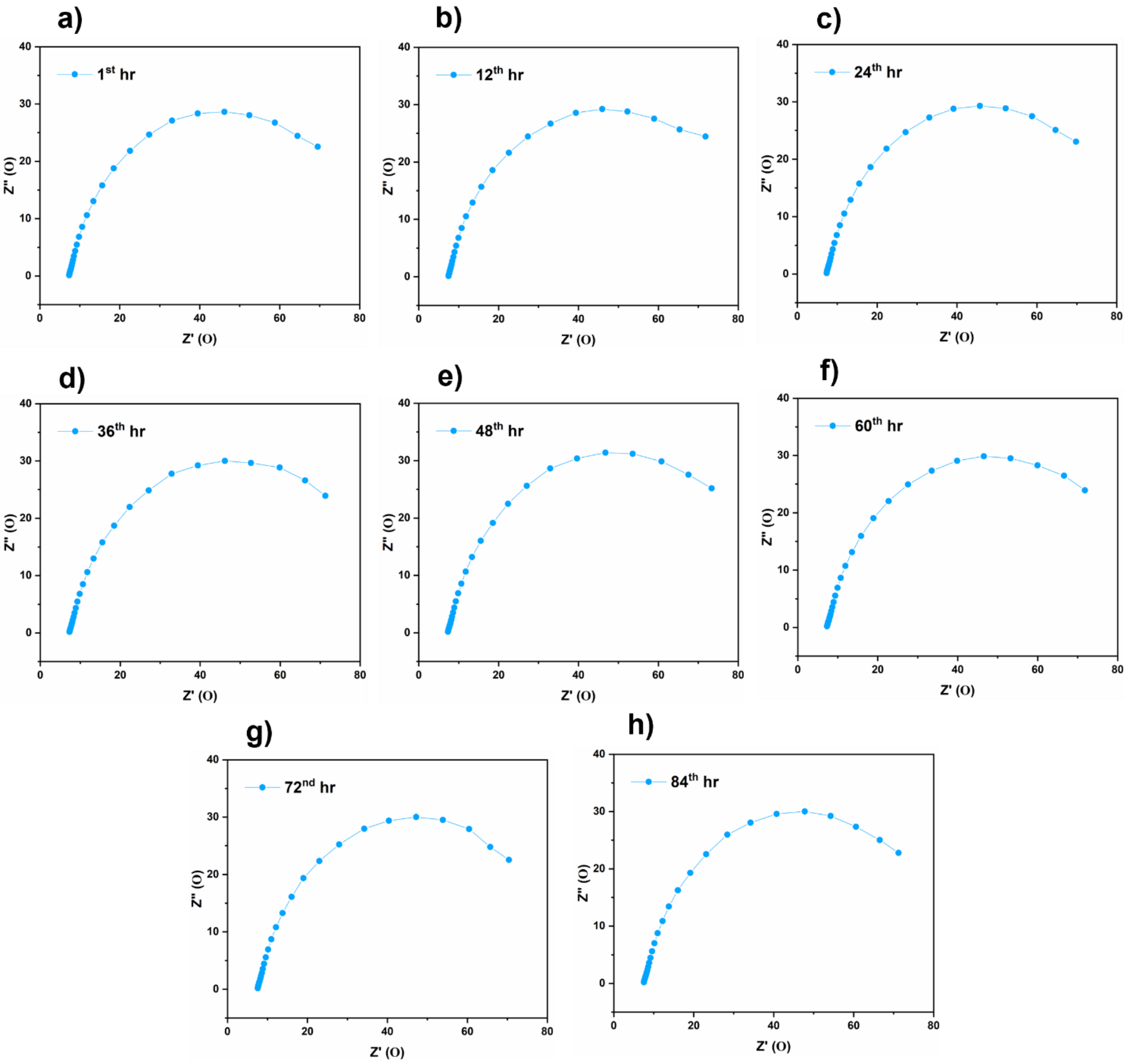

Figure A2.33. Nyquist plots for **MOF-808 C** at the constant temperature of 80 ºC and 98% relative humidity.

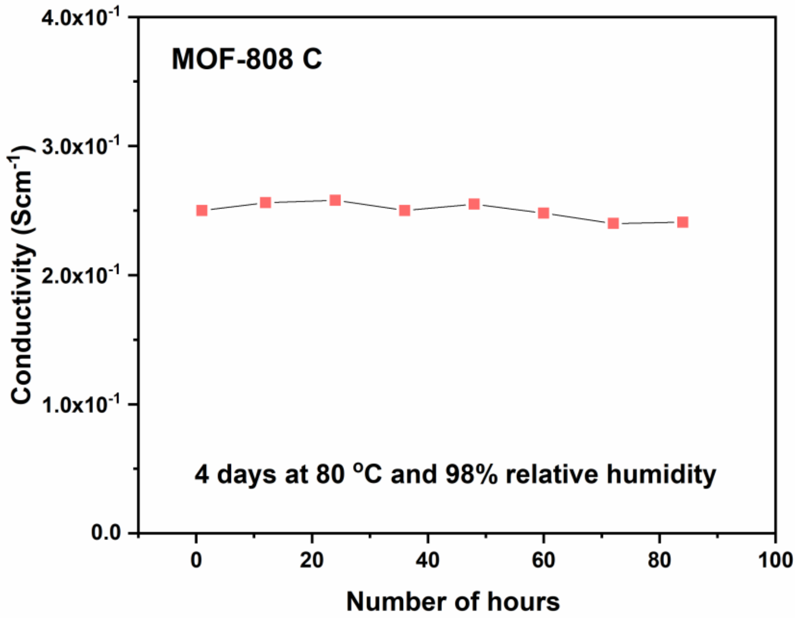

Figure A2.34. Proton conductivity of **MOF-808 C** at a constant temperature of 80 ºC and 98% relative humidity at different time intervals.

Consecutive heating-cooling cycles

To check the reusability of **MOF-808 C**, impedance measurements were done for three consecutive heating and cooling cycles, using a single pellet. The measurements were taken at two different temperatures – 40 ºC and 70 ºC, for each cycle, at 98% RH. Before any measurement at a given temperature, the sample pellet was kept for four hours to equilibrate. The Nyquist plots for both 40 ºC measurements (Figure A2.35) and 70 ºC (Figure A2.36) measurements were found to be highly reproducible, with very negligible loss in conductivity.

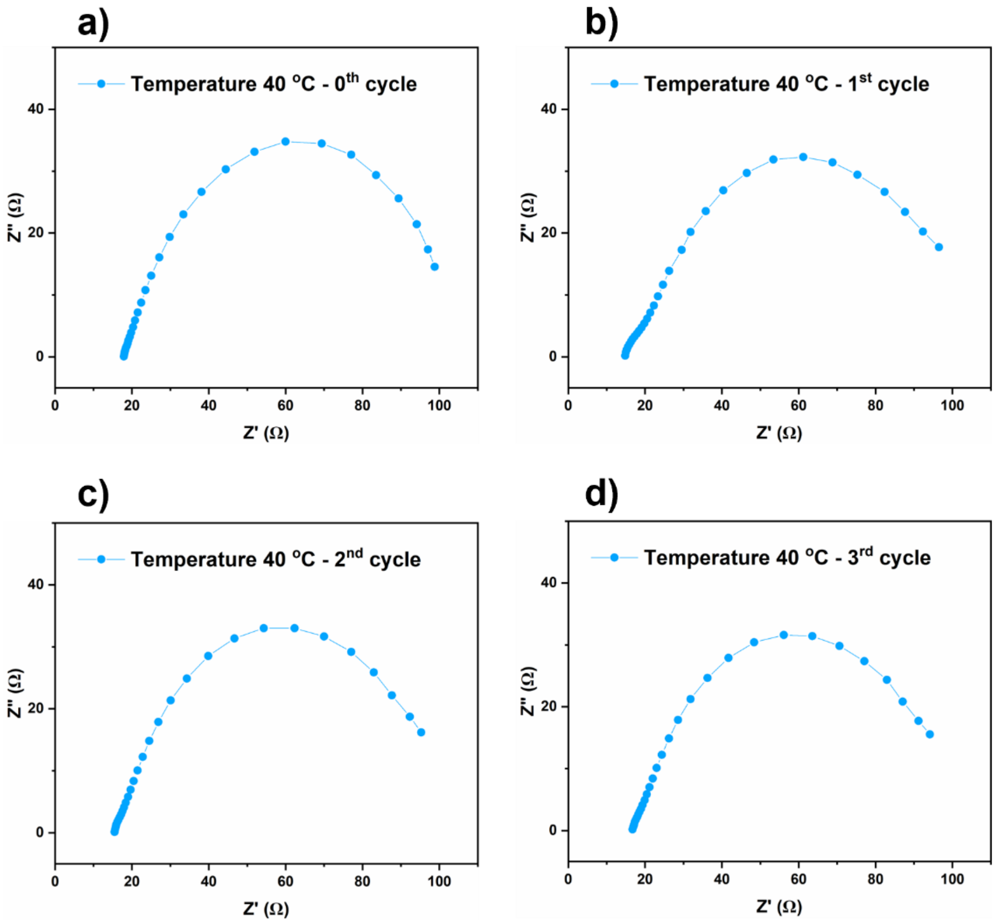

Figure A2.35. Nyquist plots for **MOF-808 C** at a constant temperature of 40 ºC and 98% relative humidity.

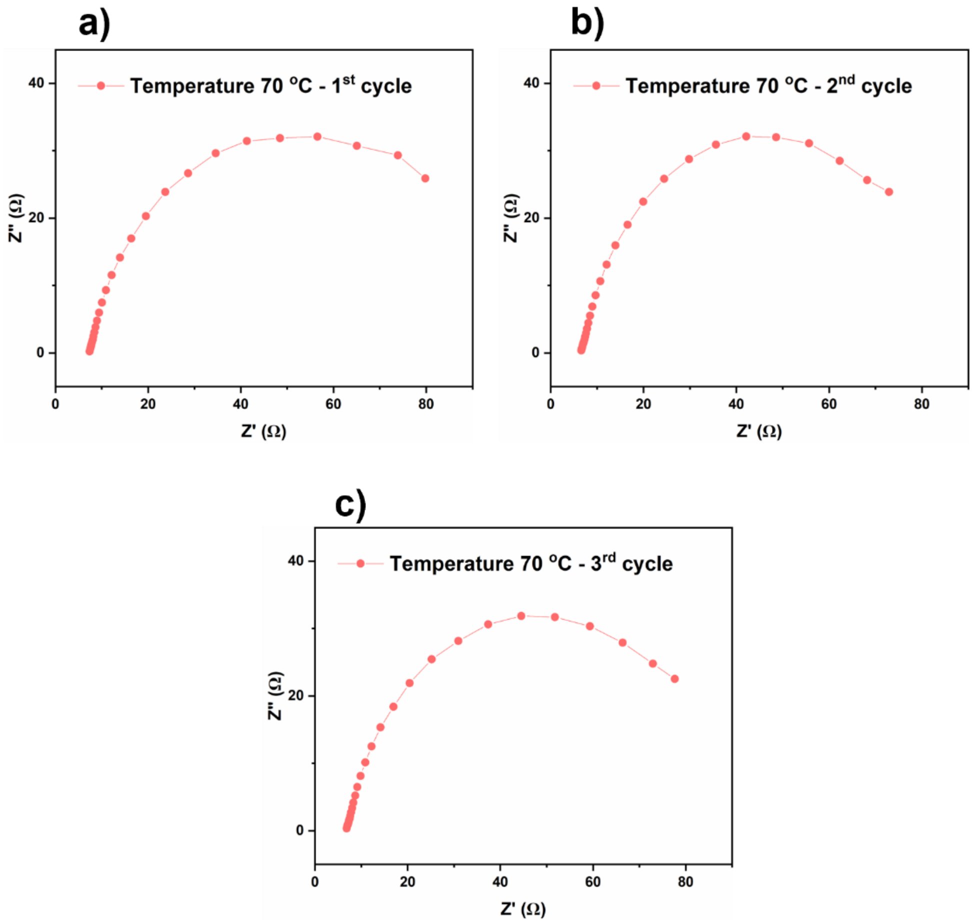

Figure A2.36. Nyquist plots for **MOF-808 C** at a constant temperature of 70 °C and 98% relative humidity.

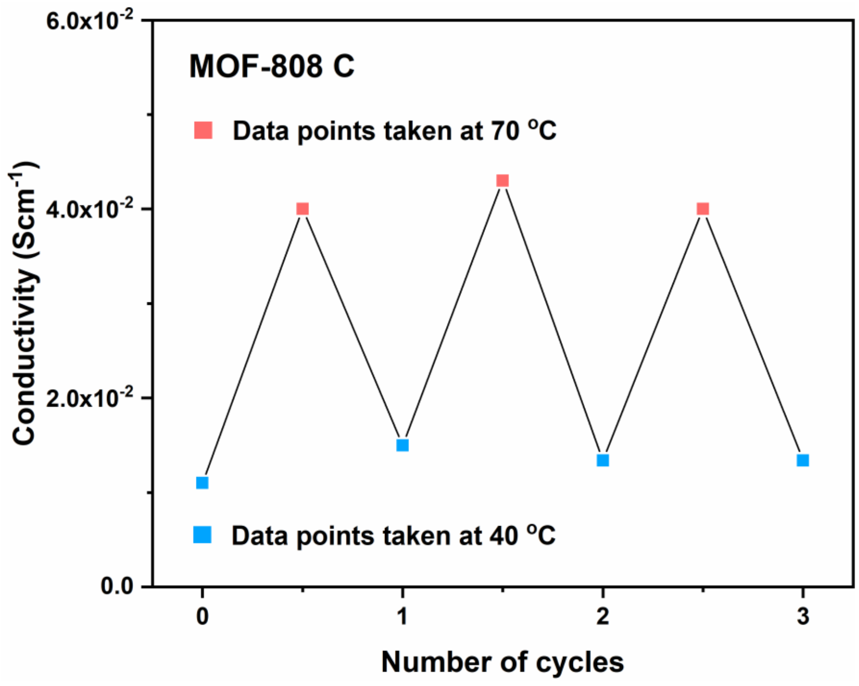

Figure A2.37. Proton conductivity of **MOF-808 C** at constant relative humidity of 98%, during consecutive heating-cooling cycles.

Material stability during proton conductivity measurements

Here, Figure A2.38 shows the horizontal view of a **MOF-808-C** pellet for representative purpose, prepared by grinding the as-synthesized sample to a fine powder and then keeping it under high hydraulic pressure, sandwiched between two carbon wafers. After the impedance measurements these pellets were then powdered and analysed using FESEM imaging, PXRD and FT-IR techniques.

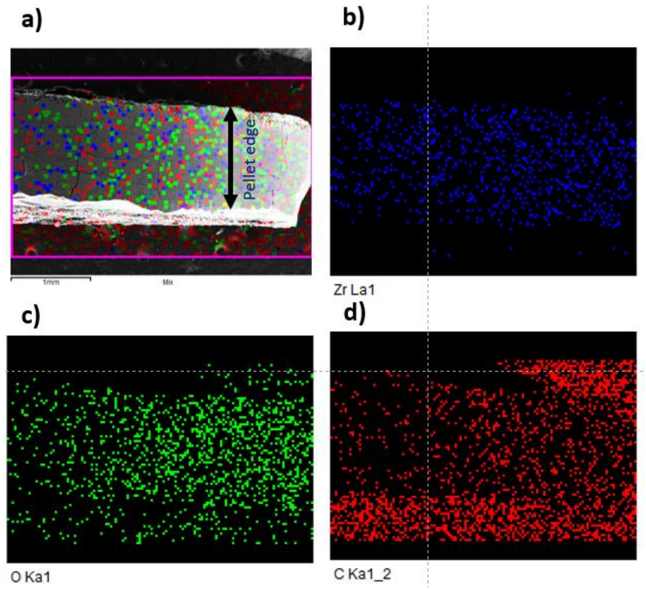

Figure A2.38. EDX analysis of a **MOF-808 C** pellet after proton conductivity measurements. a) elemental distribution of C, Zr and O on the selected area; b), c) and d) shows the elemental mapping of Zr, O and C, respectively.

In figure A2.38a, the FESEM image shows well-developed octahedral nanocrystals of **MOF-808 S**. The MOFs prepared in this work via the modified procedure yields smaller nanocrystals with more uniform size distribution. With decreasing modulator concentration in the reaction mixture from **MOF-808 A → D**, the size of the crystallites decreases further (Figure A2.39c, A2.39e, A2.39g and A2.39i). After pelletization under high pressure, the crystallites get clubbed together to form bigger particles where there is no distinguishable morphology (Figure A2.39d, A2.39f, A2.39h and A2.39j). Of note, comparison of the FESEM images for **MOF-808 C** after pelletization and after proton conductivity measurement (Figure A2.40) shows the similarity in the morphology. It indicates the fact that prolonged exposure of the pelletized MOF-808 sample to the 80 °C temperature and 98 % relative humidity did not change the morphology of the sample.

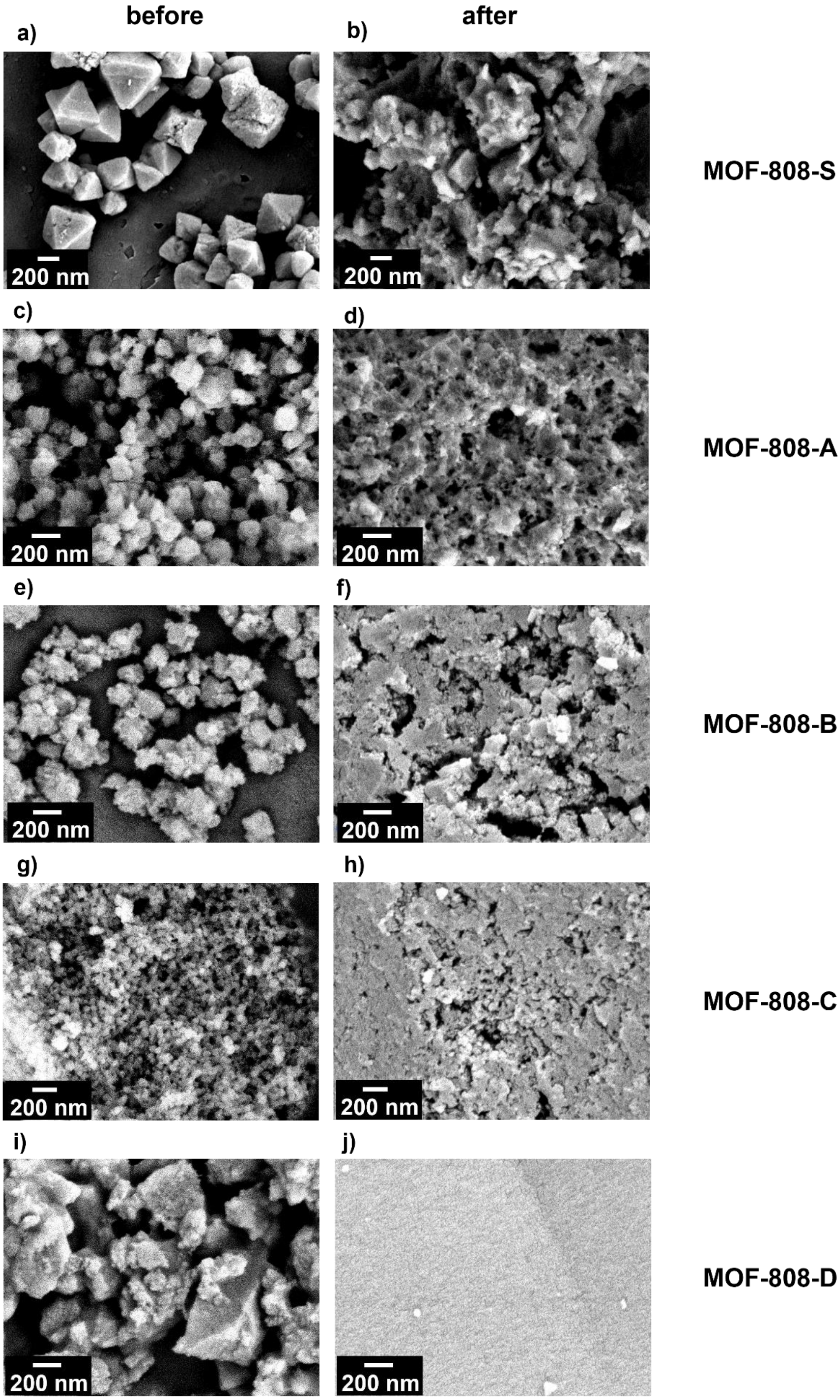

Figure A2.39. FESEM images of **MOF-808 S** and **MOF-808 A – D** before (a, c, e, g and i) and after (b, d, f, h and j) pelletization and proton conductivity measurement.

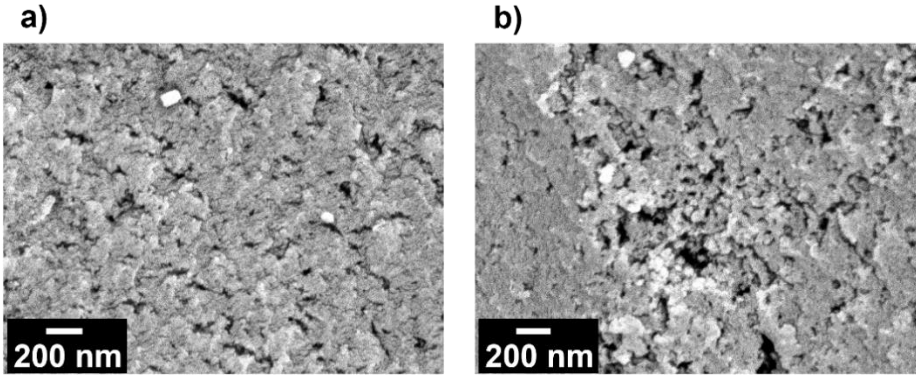

Figure A2.40. FESEM images of **MOF-808 C** after pelletization (a), after proton conductivity measurement (b).

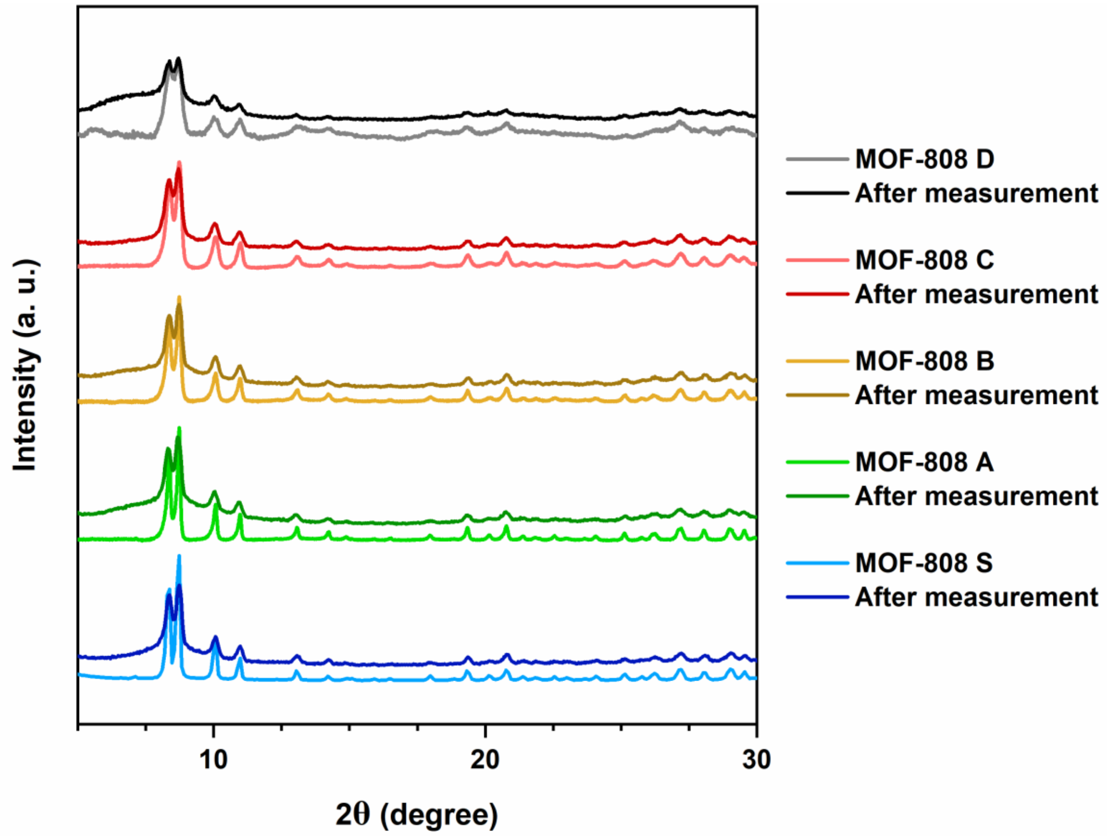

Figure A2.41. PXRD patterns of **MOF-808 S** and **MOF-808 A – D** before and after pelletization and proton conductivity measurement.

On comparing the PXRD patterns of **MOF-808 S** and **MOF-808 A – D** before and after pelletization and proton conductivity measurement, we find broadening of the peaks for the samples (Figure A2.41). This is probably caused due to the process of pellet making which includes grinding of the samples into fine powder, which is then subjected to high pressure to mould it into a pellet. As we know that particle size decreases during the process of the pelletization for **MOF-808 A - D** and **MOF -808 S**, it is expected to result into a broadening of the PXRD peaks. To confirm if the broadening is a result of the process of pelletization or due to some instability of the framework occurring during the procedure of impedance measurement, the PXRD pattern of **MOF-808 C** after measurement, was compared with that of another pellet before impedance measurement. And as can be seen from figure A2.42, the patterns for **MOF-808 C** after pelletization and after proton conductivity measurement match quite well, signifying that the sample is stable during the process of conductivity measurement.

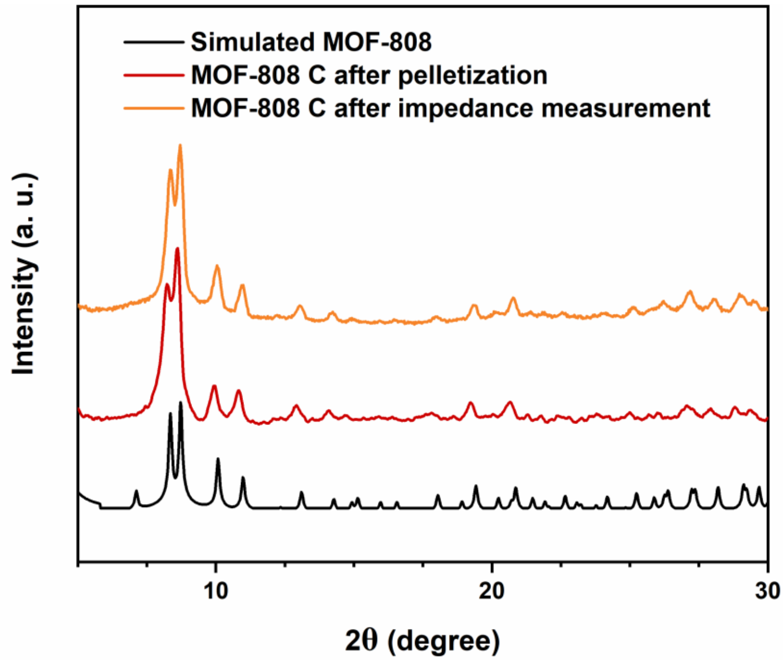

Figure A2.42. PXRD patterns of simulated MOF-808, **MOF-808 C** after pelletization and after proton conductivity measurement.

FT-IR analysis of the MOF samples before and after measurement was carried out in a similar way as that of PXRD. As can be seen from figure A2.43, the characteristic IR stretches of various functionality present in **MOF-808 A – D** and **MOF-808 S** were found to be similar before and after the process. However, the exposure of the samples to the humid condition at elevated temperature may have increased the water content in the sample. Furthermore, FT-IR spectra of **MOF-808 C** after pelletization and after proton conductivity measurement was also compared (figure A2.44). No notable difference could be observed before and after proton conductivity measurements. With the help of these experiments, we could conclude that the defective sister MOFs are stable towards proton conductivity measurements at mild conditions. The defect density in any of these MOFs are supposedly not so high that it led to a structural collapse at the experimental conditions (80 °C temperature and 98 % relative humidity).

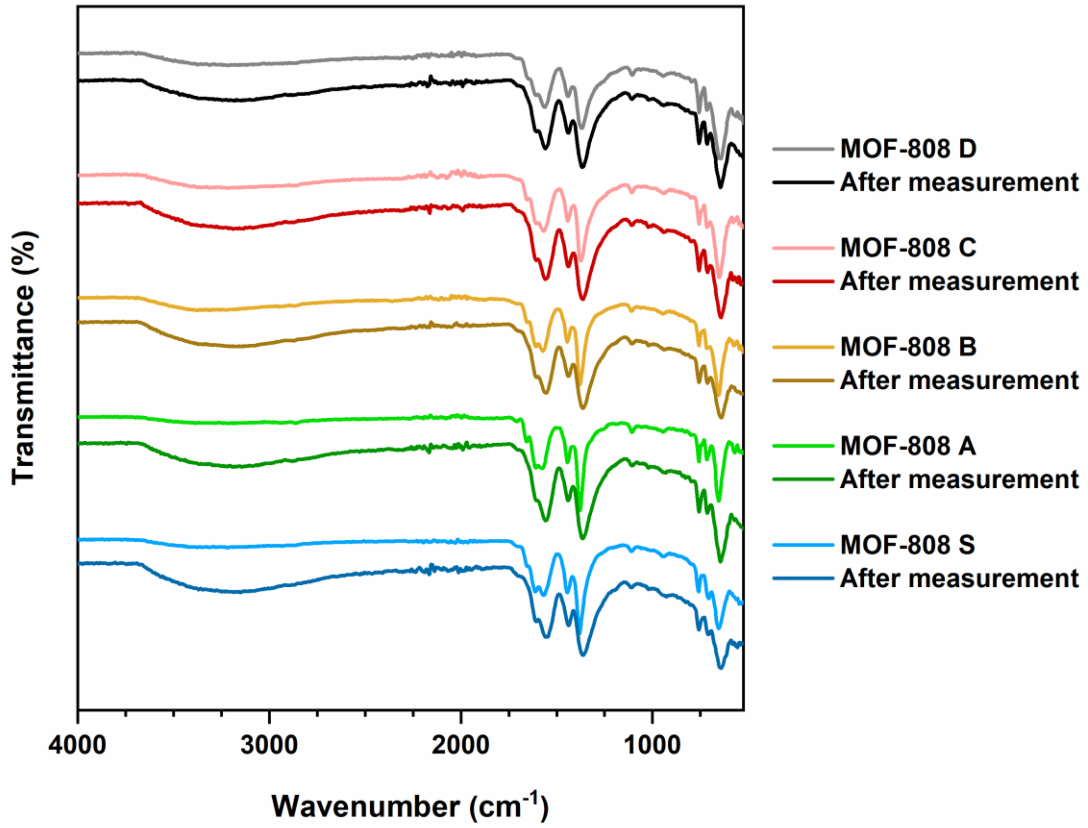

Figure A2.43. FTIR spectra of **MOF-808 S** and **MOF-808 A – D** before and after pelletization and proton conductivity measurement.

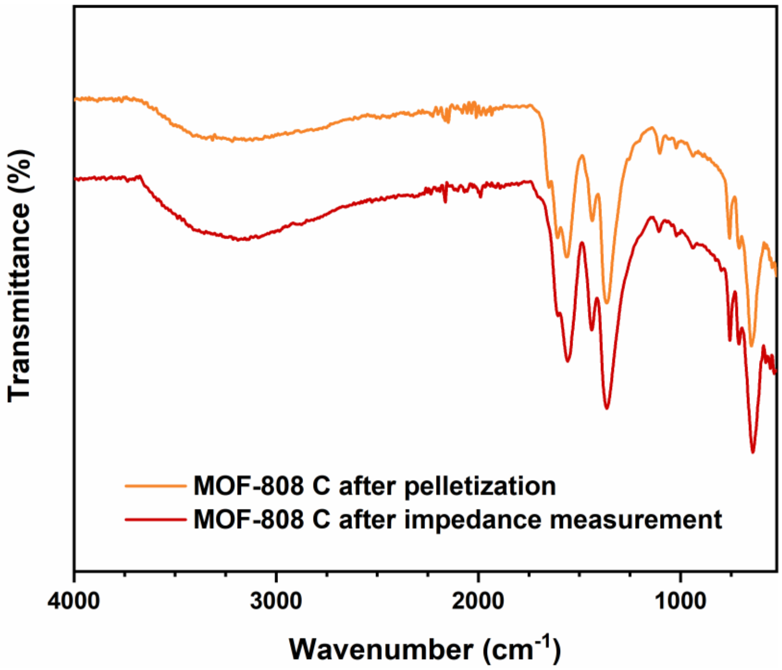

Figure A2.44. FT-IR spectra of **MOF-808 C** after pelletization and after proton conductivity measurement.

2-year stability test – Measurement of FT-IR, PXRD, and Proton Conductivity

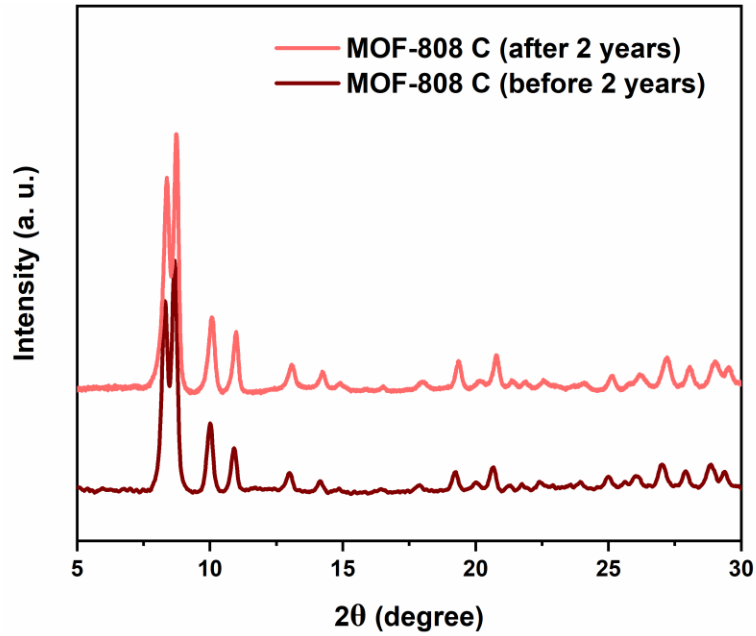

Figure A2.45. PXRD patterns of **MOF-808 C** before and after two years of storing in open-air condition at room temperature (25 ºC).

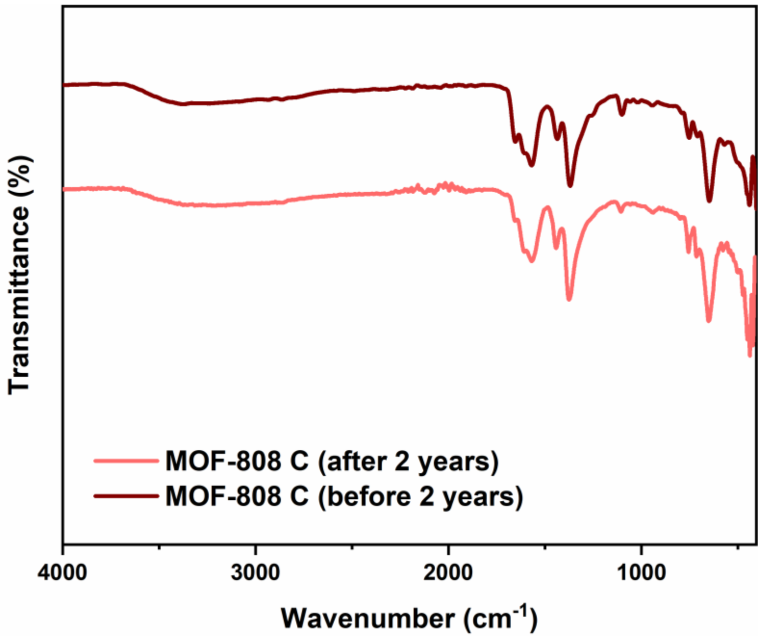

Figure A2.46. FTIR spectra of **MOF-808 C** before and after 2 years of storing in open-air condition at room temperature (25 ºC).

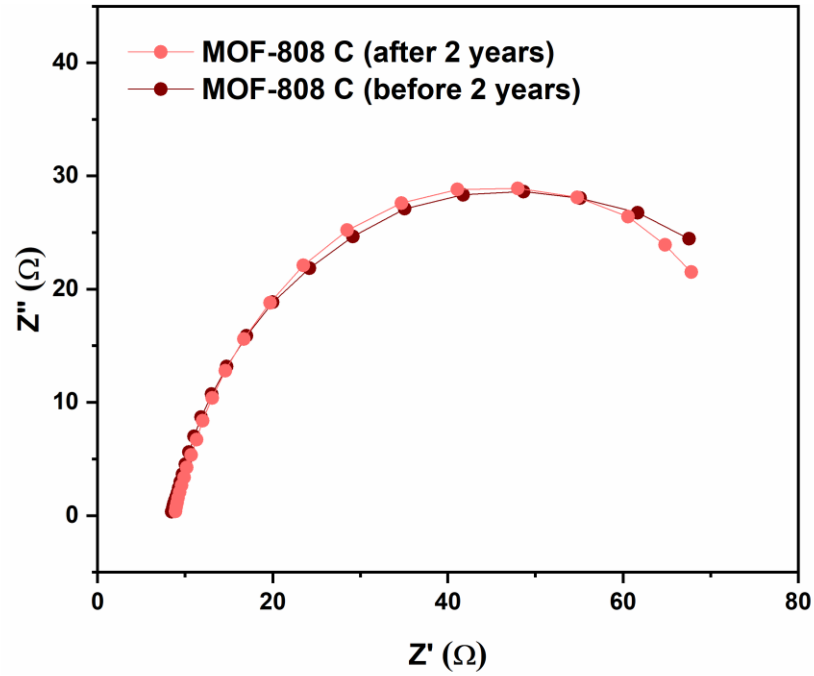

Figure A2.47. Nyquist plots of impedance measurements for **MOF-808 C** (at 80 °C, 98% RH) before and after 2 years of storing in open-air condition at room temperature (25 °C).

Table A2.12. Comparison of the porosity and proton conductivity for MOF-808 A – D with their corresponding ligand composition.

Sample	Number of BTC linkers per SBU (^{1}H-NMR)	Number of OH^- /H_2O per SBU	BET surface area (m^2g^{-1})	Proton conductivity at 80 °C, 98% R.H (Scm^{-1})
MOF-808 A	1.84	4.34048	1351.9	8.07×10^{-2}
MOF-808 B	1.67	5.02358	1494.5	1.47×10^{-1}
MOF-808 C	1.33	5.43438	1423.6	2.6×10^{-1}
MOF-808 D	1.60	5.13442	865.2	1.12×10^{-2}

Table A2.13. Proton conductivity values of MOF-808 A – D in comparison with other pure MOF based proton conductors having H_2O as pore guest and operating under humidity.

Sample	**Conductivity (Scm^{-1})**	**Conditions**	**Reference**
MOF-808 C	2.6×10^{-1}	80 °C, 98% RH	This work
PSM 1	1.64×10^{-1}	80 °C, 95% RH	4
IM-UiO-66-AS	1.54×10^{-1}	80 °C, 98% RH	7
MOF-808 B	1.47×10^{-1}	80 °C, 98% RH	This work
FCF 1	1.17×10^{-1}	100 °C, 98% RH	8
UiO-66(SO_3H)$_2$	8.4×10^{-2}	80 °C, 90% RH	9
MOF-808 A	8.07×10^{-2}	80 °C, 98% RH	This work
BUT-83	3.9×10^{-2}	80 °C, 97% RH	10
MIP-177-SO_4H-LT	2.6×10^{-2}	25 °C, 95% RH	11
KAUST-7′	2.0×10^{-2}	90 °C, 95% RH	12
CPM-103a	5.8×10^{-2}	22.5 °C, 98% RH	13
MOF-808 D	1.12×10^{-2}	80 °C, 98% RH	This work
CFA-17	2.1×10^{-3}	22 °C, 95% RH	14
[Cu_2(Htzehp)$_2$(4,4′-bipy)]·3H_2O	1.43×10^{-3}	80 °C, 95% RH	15

References

1. Furukawa, H.; Gándara, F.; Zhang, Y-B.; Jiang, J.; Queen, W. L.; Hudson, M. R.; Yaghi, O. M. Water Adsorption in Porous Metal−Organic Frameworks and Related Materials. *J. Am. Chem. Soc.* **2014**, *136*, 4369−4381.
2. Shearer, G. C.; Chavan, S.; Bordiga, S.; Svelle, S.; Olsbye, U.; Lillerud, K. P. Defect Engineering: Tuning the Porosity and Composition of the Metal−Organic Framework UiO-66 via Modulated Synthesis. *Chem. Mater.* **2016**, *28*, 3749−3761.
3. Klet, R. C.; Liu, Y.; Wang, T. C.; Hupp, J. T.; Farha, O. K. Evaluation of Brønsted acidity and proton topology in Zr- and Hf-based metal–organic frameworks using potentiometric acid–base titration. *J. Mater. Chem. A* **2016**, *4*, 1479–1485.
4. Mukhopadhyay, S.; Debgupta, J.; Singh, C.; Sarkar, R.; Basu, O.; Das, S. K. Designing UiO-66-Based Superprotonic Conductor with the Highest Metal−Organic Framework Based Proton Conductivity. *ACS Appl. Mater. Interfaces* **2019**, *11*, 13423−13432.
5. a) Taylor, J. M.; Dekura, S.; Ikeda, R.; Kitagawa, H. Defect Control to Enhance Proton Conductivity in a Metal−Organic Framework. *Chem. Mater.* **2015**, *27*, 2286−2289; b) Yang, F.; Xu, G.; Dou, Y.; Wang, B.; Zhang, H.; Wu, H.; Zhou, W.; Li, J-R. Chen, B. A flexible metal–organic framework with a high density of sulfonic acid sites for proton conduction. *Nature Energy* **2017**, *2*, 877–883; c) Randviir, E. P.; Banks, C. E. Electrochemical impedance spectroscopy: an overview of bioanalytical applications. *Anal. Methods* **2013**, *5*, 1098–1115.
6. Atzori, C.; Shearer, G. C.; Maschio, L.; Civalleri, B.; Bonino, F.; Lamberti, C.; Svelle, S.; Lillerud, K. P.; Bordiga, S. Effect of Benzoic Acid as a Modulator in the Structure of UiO-66: An Experimental and Computational Study. *J. Phys. Chem. C* **2017**, *121*, 9312–9324.
7. Li, X.-M.; Liu, J.; Zhao, C.; Zhou, J.-L.; Zhao, L.; Li, S.-L.; Lan, Y.-Q. Strategic hierarchical improvement of superprotonic conductivity in a stable metal–organic framework system. *J. Mater. Chem. A* **2019**, *7*, 25165-25171.
8. Qin, Y.; Gao, T.-l.; Xie, W.-P.; Li, Z.; Li, G. Ultrahigh Proton Conduction in Two Highly Stable Ferrocenyl Carboxylate Frameworks. *ACS Appl. Mater. Interfaces* **2019**, *11*, 31018–31027.
9. Phang, W. J.; Jo, H.; Lee, W. R.; Song, J. H.; Yoo, K.; Kim, B.; Hong, C. S. Superprotonic Conductivity of a UiO-66 Framework Functionalized with Sulfonic Acid Groups by Facile Postsynthetic Oxidation. *Angew. Chem., Int. Ed.* **2015**, *54*, 5142-5146.
10. Wu, H.; Yang, F.; Lv, X.-L.; Wang, B.; Zhang, Y.-Z.; Zhao, M.-J.; Li, J.-R. A stable porphyrinic metal–organic framework pore-functionalized by high-density carboxylic groups for proton conduction. *J. Mater. Chem. A* **2017**, *5*, 14525-14529.
11. Wahiduzzaman, M.; Wang, S.; Schnee, J.; Vimont, A.; Ortiz, V.; Yot, P. G.; Retoux, R.; Daturi, M. ; Lee, J. S.; Chang, J.-S.; Serre, C.; Maurin, G.; Devautour-Vinot, S. A High Proton Conductive Hydrogen-Sulfate Decorated Titanium Carboxylate Metal−Organic Framework. *ACS Sustainable Chem. Eng.* **2019**, *7*, 5776–5783.
12. Mileo, P. G. M.; Adil, K.; Davis, L.; Cadiau, A.; Belmabkhout, Y.; Aggarwal, H.; Maurin, G.; Eddaoudi, M.; Devautour-Vinot, S. Achieving Superprotonic Conduction with a 2D Fluorinated Metal–Organic Framework. *J. Am. Chem. Soc.* **2018**, *140*, 13156–13160.
13. Zhai, Q. G.; Mao, C.; Zhao, X.; Lin, Q.; Bu, F.; Chen, X.; Bu, X.; Feng, P. Cooperative Crystallization of Heterometallic Indium–Chromium Metal–Organic Polyhedra and Their Fast Proton Conductivity. *Angew. Chem., Int. Ed.* **2015**, *54*, 7886-7890.
14. Bunzen, H.; Javed, A.; Klawinski, D.; Lamp, A.; Grzywa, M.; Kalytta-Mewes, A.; Tiemann, M.; von Nidda, H.-A. K.; Wagner, T.; Volkmer, D. Anisotropic Water-Mediated Proton Conductivity in Large Iron(II) Metal–Organic Framework Single Crystals for Proton-Exchange Membrane Fuel Cells. *ACS Appl. Nano Mater.* **2019**, *2*, 291–298.
15. Li, R.; Wang, S.-H.; Chen, X.-X.; Lu, J.; Fu, Z.-H.; Li, Y.; Xu, G.; Zheng, F.-K.; Guo, G.-C.; Highly Anisotropic and Water Molecule-Dependent Proton Conductivity in a 2D Homochiral Copper(II) Metal–Organic Framework. *Chem. Mater.* **2017**, *29*, 2321–2331.

APPENDIX 3

Supporting Data for Chapter 3

TABLE OF CONTENTS

Section A3.1. Estimation of the number of NH_2-BDC molecules in Fe-MIL-53-NH_2 from TGA

The structural formula for **Fe-MIL-53-NH_2** is reported previously to contain hydrogen bonded NH_2-H_2BDC molecules in the channels of the MOF, in addition to the NH_2-BDC linkers in the framework.[1] But since the number of H-bonded NH_2-H_2BDC molecules in the framework can vary depending on the synthetic procedure, TGA was performed to determine the number of NH_2-BDC linkers and H-bonded NH_2-H_2BDC in the **Fe-MIL-53-NH2** MOF in our work. The TGA trace has been normalized to 100% with respect to the residual mass of $^1/_2(Fe_2O_3)$ at 500 °C.

During TGA, by heating the MOF till ~260 °C a plateau is obtained where the MOF can be considered as solvent-free. This step can be represented by the formula [Fe(OH)NH_2-BDC·xNH_2-H_2BDC]. On the TGA trace, this point comes at 371.7%.

At ~500 °C the MOF framework degrades completely to leave behind ferric oxide. Each formula unit of the MOF leaves $^1/_2(Fe_2O_3)$ as residue. Residual weight = ½ (MW of Fe_2O_3) = 79.845 g/mol; normalized to 100% on TGA trace.

Thus, the loss of mass occurring in the temperature range of ~ 270 °C − 500 °C is due to the loss of NH_2-BDC molecules present as the MOF linker as well as NH_2-H_2BDC acid molecules hydrogen bonded to the framework.

An estimation of the weight loss% from 270 °C to 500 °C (from Figure A3.1), then gives the number of NH_2-BDC and NH_2-H_2BDC molecules.

The structural formula for **Fe-MIL-53-NH2** in this work, as obtained from TGA is [Fe(OH)NH_2-BDC·0.25NH_2-H_2BDC].

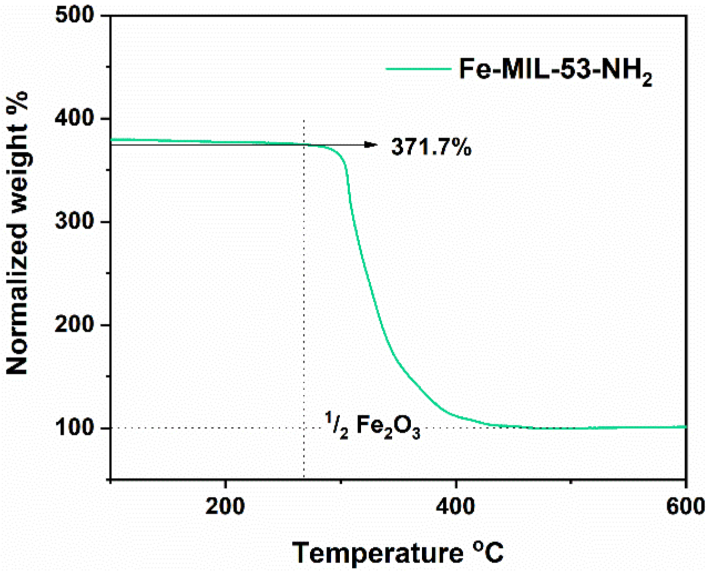

Figure A3.1. Thermogravimetric analysis of **Fe-MIL-53-NH2**.

Section A3.2. Estimation of the number of NH_2-BDC molecules in Fe-MIL-53-NH_2 from ICP-OES and ^{1}H-NMR

ICP-OES

For ICP-OES analysis, **Fe-MIL-53-NH_2** MOF sample was digested in aqua regia and the iron content present in the framework was estimated.

Sample	Iron (% by mass)
Fe-MIL-53-NH_2	17.65

^{1}H-NMR

To estimate the content of NH_2-BDC in **Fe-MIL-53-NH_2**, the MOF was digested in 1M NaOH in D_2O. 500 µL of this supernatant solution was added with 20 µL of 0.1 M H_3BTC solution in 1 M NaOH in D_2O, and the spectrum was recorded (Figure A3.2). Here the H_3BTC was taken as the internal standard ($\delta = 8.25$ ppm). The concentration of NH_2-BDC in the sample was then determined by correlating the peak integration for NH_2-BDC and BTC in the spectrum (Figure A3.2). For reference and to demarcate the peaks accurately, a separate solution of H_3BTC and NH_2-H_2BDC was prepared in 1 M NaOH in D_2O, and its ^{1}H-NMR spectrum was recorded (Figure A3.3). Peak observed at ~8.25 ppm is attributed to BTC; peaks observed at ~7.55 ppm, ~7.13 ppm and ~7.05 ppm are attributed to NH_2-BDC.

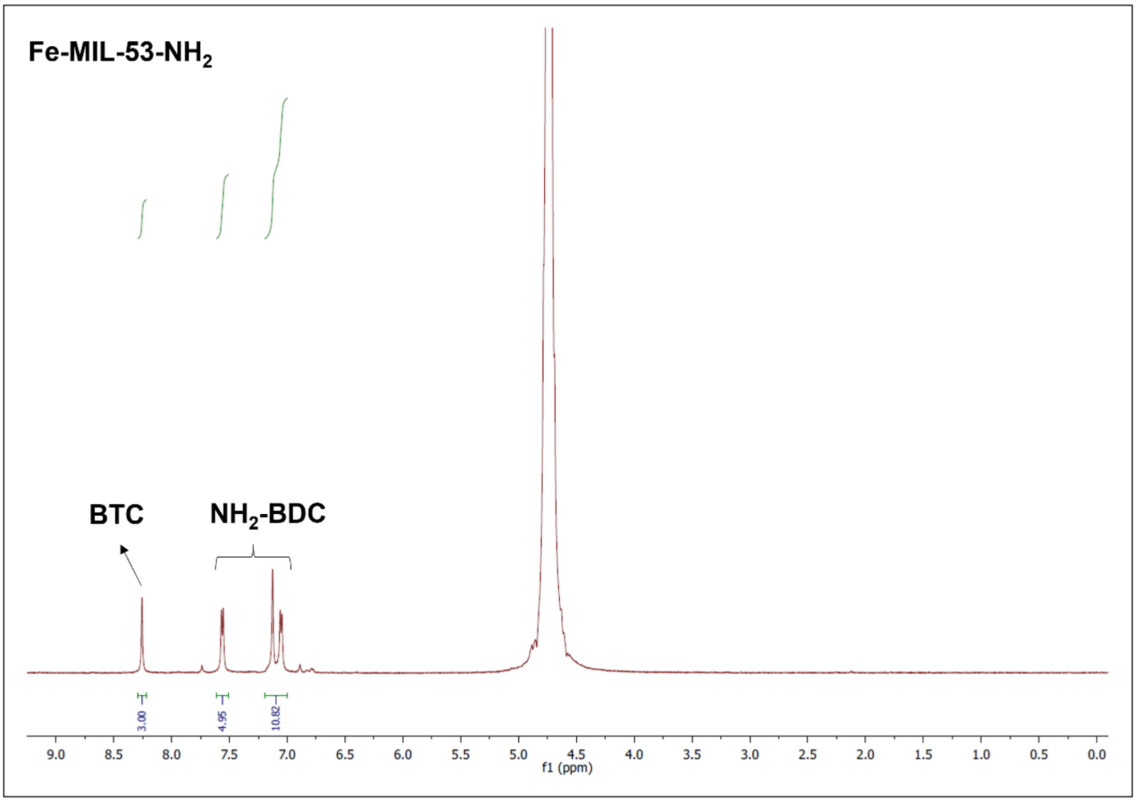

Figure A3.2. ^{1}H-NMR spectrum of **Fe-MIL-53-NH$_2$** in 1 M NaOH solution prepared in D_2O and using H_3BTC as internal standard.

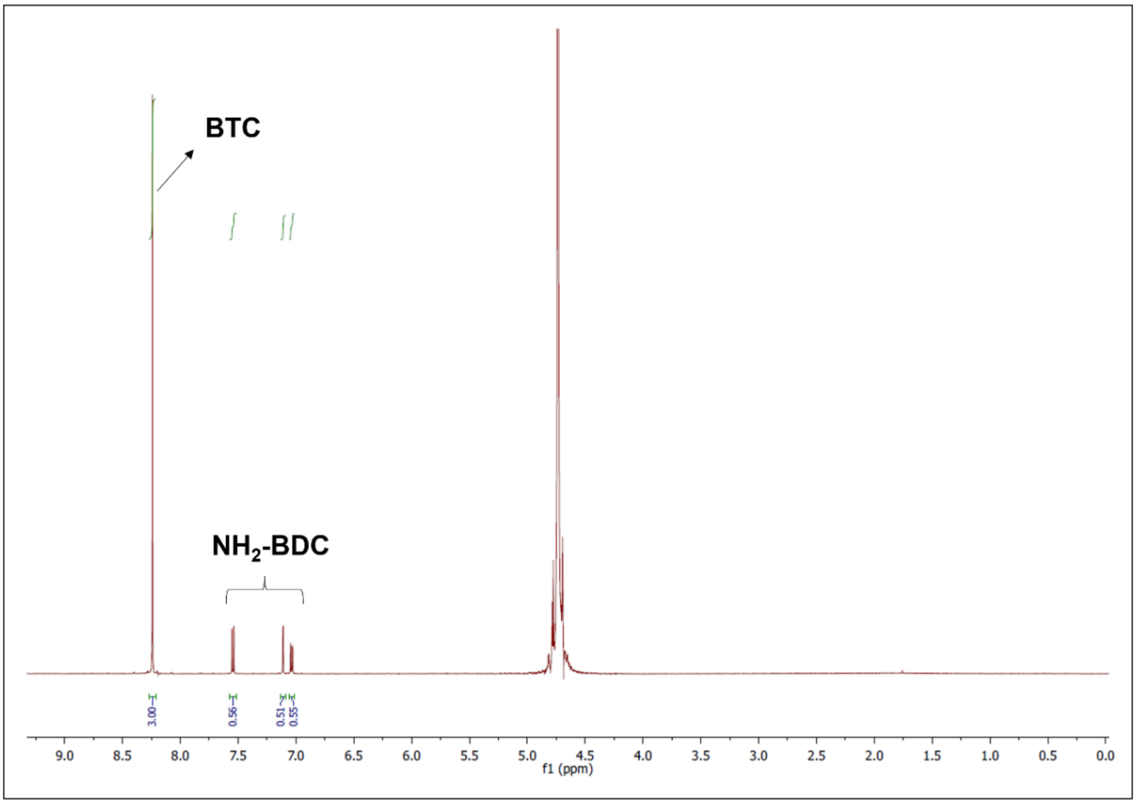

Figure A3.3. ^{1}H-NMR spectrum of H_3BTC and NH_2-H_2BDC in 1 M NaOH solution prepared in D_2O.

With the combination of ^{1}H-NMR and ICP-OES data, the estimated amount of NH_2-BDC in the sample was approximately 1.21 times the number of moles of iron present in the sample. Since for each Fe node in the MOF there should be 1 NH_2-BDC linker in the repeating unit, this means that the excess 0.21 fraction of NH_2-BDC molecules reside in the MOF as guests, H-bonded to the framework.

Thus, the structural formula for **Fe-MIL-53-NH_2** can be written as [Fe(OH)NH_2-BDC·0.21NH_2-H_2BDC]. This formula matches quite well with that obtained from TGA.

Section A3.3. Quantification of sulfonic acid loading from ICP-OES

To estimate the extent to which the -NH_2 groups of the MOFs are modified, ICP-OES was used. For this, the MOF samples were digested in aqua regia and the iron and sulfur content present in the framework was estimated.

Table A3.1. ICP-OES data for iron and sulfur.

Sample	Iron (% by mass)	Sulphur (% by mass)
53-S	16.36	2.46
88B-S	17.58	5.79

Fe-MIL-53-NH_2 has the structural formula [Fe(OH)NH_2-BDC·0.21NH_2-H_2BDC] (as determined from ^{1}H-NMR and ICP-OES) where for every mononuclear Fe node there is 1 NH_2-BDC in the framework and 0.21 NH_2-H_2BDC acid molecules in the channels of the framework, connected by H-bonds. This means for each Fe atom, there would be 1.21 NH_2-BDC in the MOF. During the post synthetic modification procedure, both NH_2-BDC linkers and NH_2-H_2BDC molecules might undergo modification.

Now, according to the ICP-OES analysis for every 100g of **53-S** MOF, there is 16.36 g of Fe ≡ 0.2929 moles of Fe, and 2.46 g of S ≡ 0.0767 moles of S.

Or, for 0.2929 moles of **53-S**, there is 0.0767 moles of S.

Or, 1 formula unit of **53-S** MOF has 0.2618 moles of S in it.

This means approximately 21.6% of the -NH_2 groups (NH_2-BDC/ NH_2-H_2BDC) in the **53-S** MOF are modified to -NH($CH_2CH_2CH_2SO_3H$).

Fe-MIL-88B-NH$_2$ has the chemical formula [$Fe_3O(OH_2)_3Cl(NH_2\text{-BDC})_3$] where for every trinuclear Fe node there are 3 NH_2-BDC linkers in the framework. Using similar calculations as detailed for **53-S**, the sultone modification in **88B-S** was estimated.

Approximately 57.3% of the -NH_2 groups (NH_2-BDC) in the **88B-S** MOF are modified to -$NH(CH_2CH_2CH_2SO_3H)$.

Section A3.4. FESEM images of parent MOFs

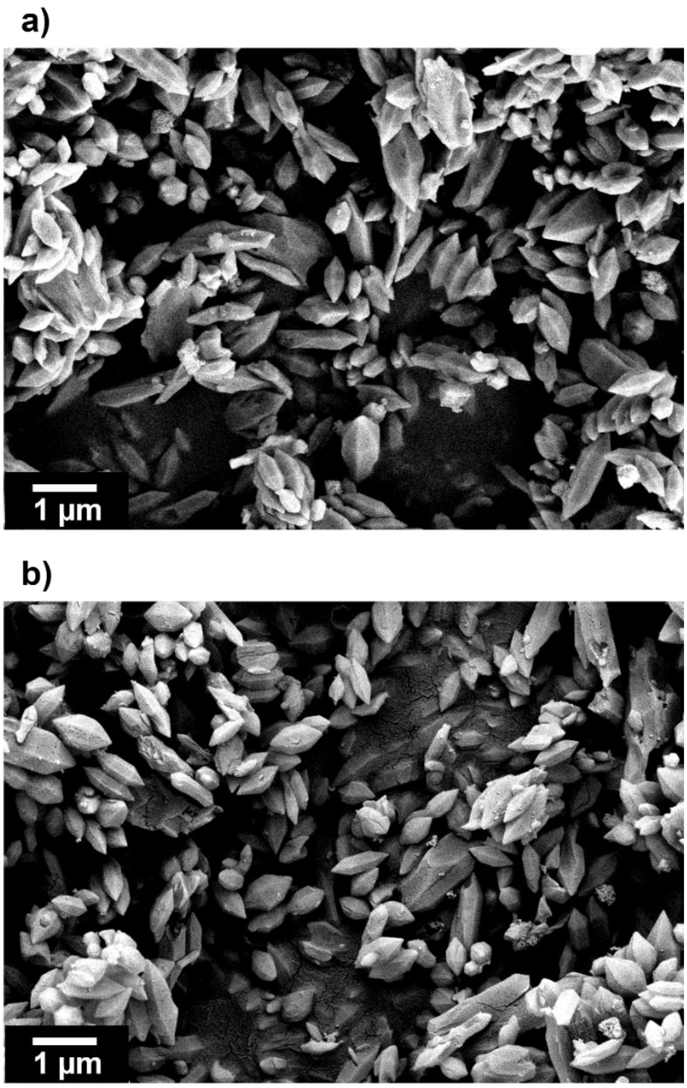

Figure A3.4. FESEM images of parent MOFs, **Fe-MIL-53-NH$_2$** and **Fe-MIL-88B-NH$_2$**.

Section A3.5. Thermogravimetric analysis (TGA)

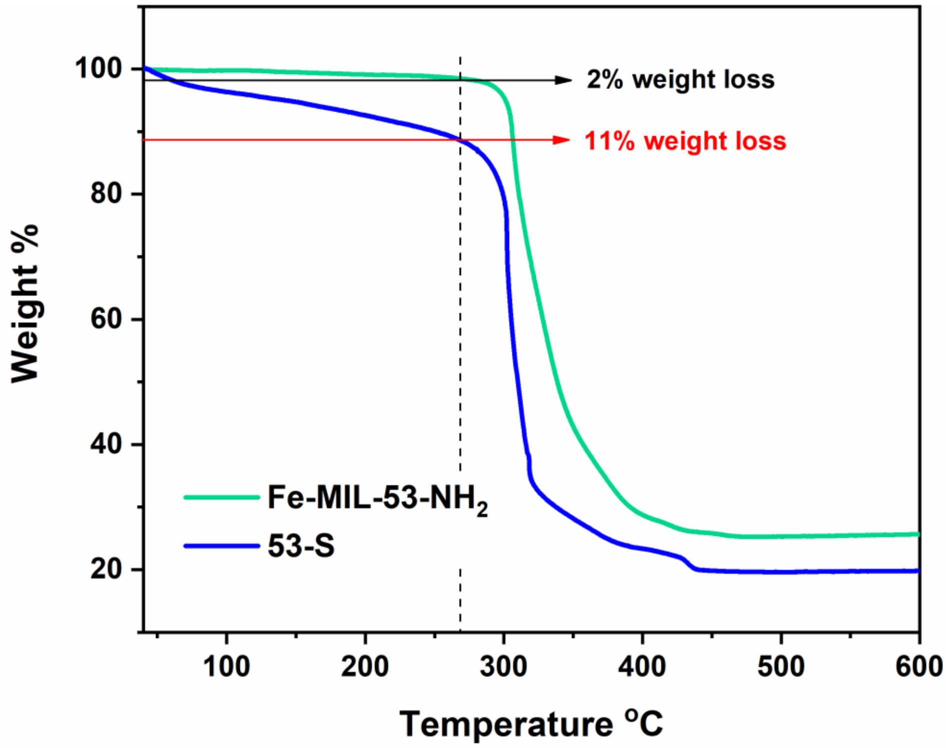

Figure A3.5. Thermogravimetric analysis of **53-S** and **Fe-MIL-53-NH$_2$**.

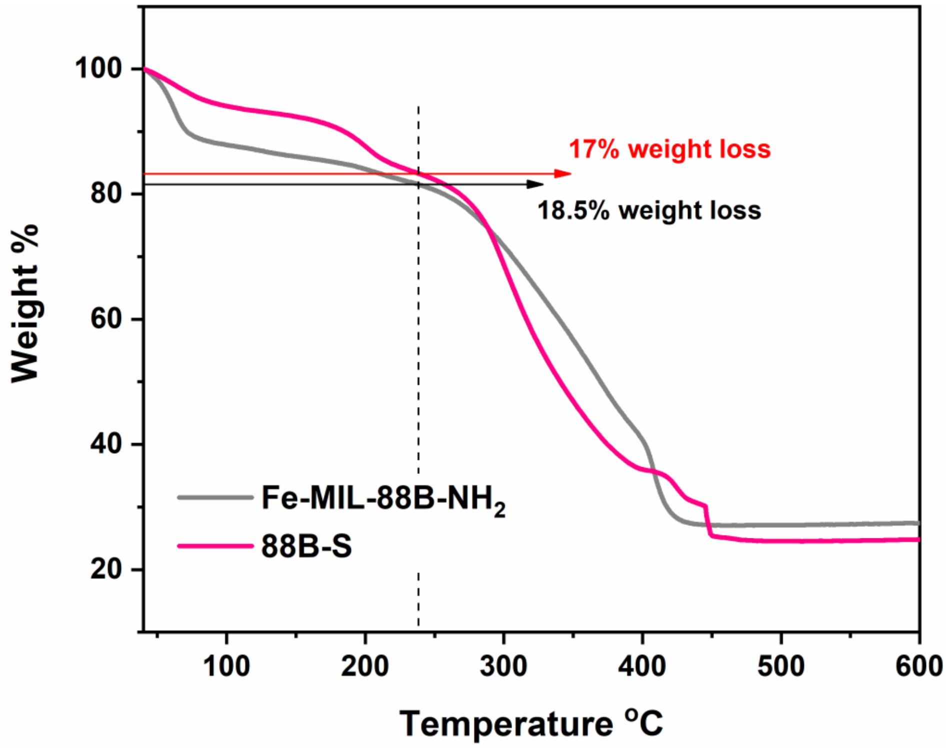

Figure A3.6. Thermogravimetric analysis of **88B-S** and **Fe-MIL-88B-NH$_2$**.

Section A3.6. Electrochemical impedance spectroscopy – MOF powder sample

Impedance measurement under different temperature

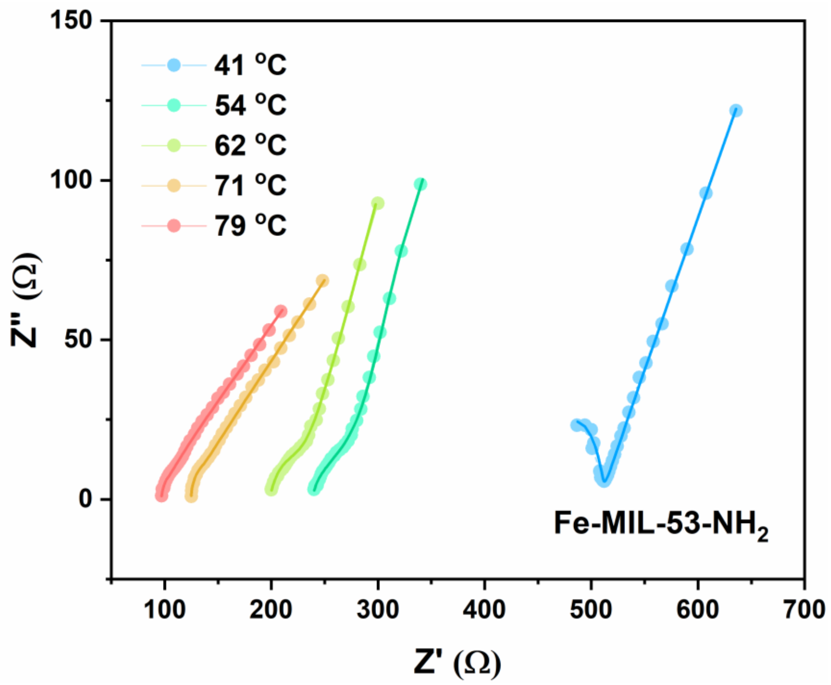

Figure A3.7. Nyquist plots of impedance measurements for **Fe-MIL-53-NH$_2$** at a constant relative humidity of 98% and variable temperature. Spheres denote experimental data points; solid line denotes fitted curve.

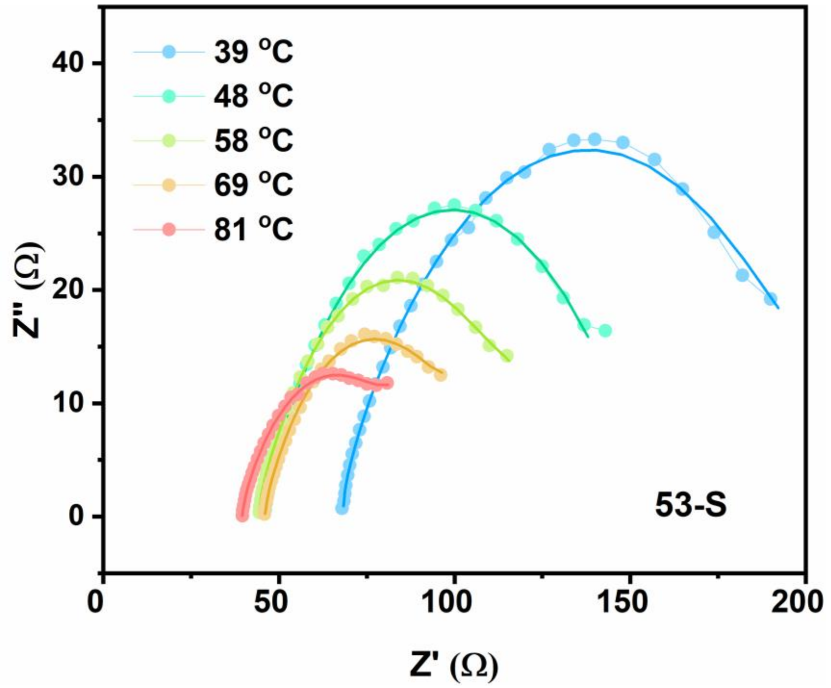

Figure A3.8. Nyquist plots of impedance measurements for **53-S** at a constant relative humidity of 98% and variable temperature. Spheres denote experimental data points; solid line denotes fitted curve.

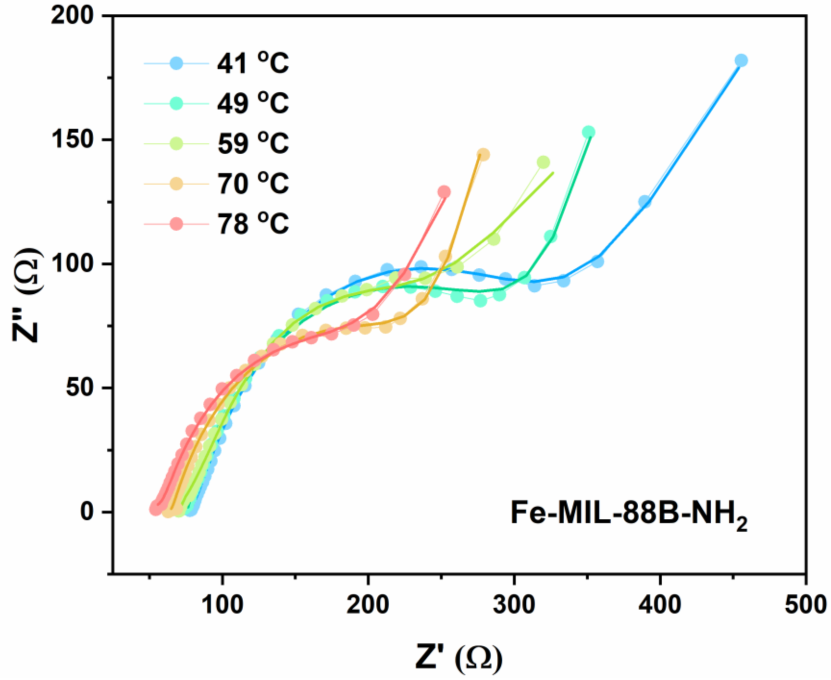

Figure A3.9. Nyquist plots of impedance measurements for **Fe-MIL-88B-NH$_2$** at a constant relative humidity of 98% and variable temperature. Spheres denote experimental data points; solid line denotes fitted curve.

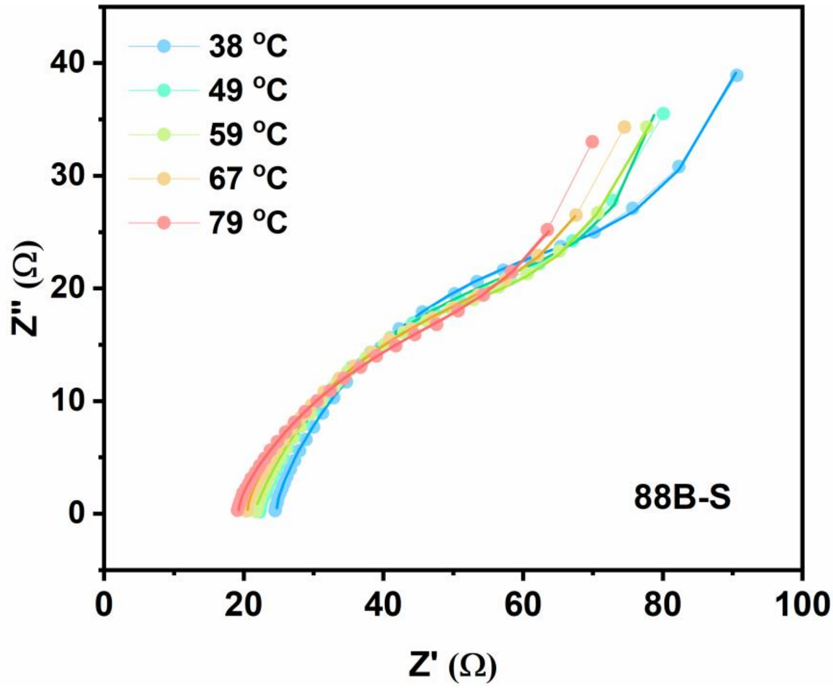

Figure A3.10. Nyquist plots of impedance measurements for **88B-S** at a constant relative humidity of 98% and variable temperature. Spheres denote experimental data points; solid line denotes fitted curve.

Calculation of proton conductivity from Impedance spectra by fitting with an equivalent circuit

The proton conductivity of the MOFs was determined from the corresponding Nyquist plots after fitting them to the most suitable equivalent circuit using EC-Lab software.

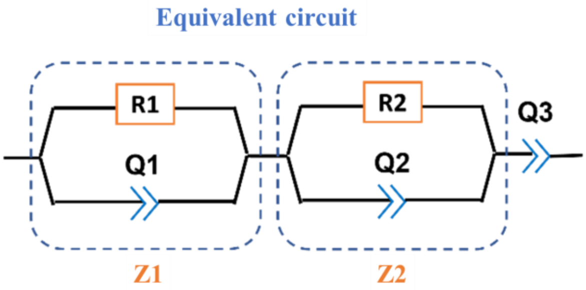

The equivalent circuit is composed of three parts – (1) the grain-interior impedance/bulk impedance (Z1); (2) the inter-grain impedance (Z2); (3) impedance at the electrode-solid electrolyte junction/interface given by the constant phase element (CPE) Q3, all connected in series.

Z1 and Z2 are both composed of a resistance (R) and a constant phase element (Q) connected to each other in parallel mode. Here R1 accounts for the bulk resistance/grain interior resistance of the MOF nanocrystals, while R2 represents the inter-gain resistance and charge transfer resistance existing between the electrodes and the pellet. Here Q1 and Q2 are constant phase elements (CPE) which account for the depressed semicircles observed in real experimental cases, due to the generation of non-ideal capacitance in bulk and interfaces. Similarly, to account for the non-ideal capacitance generated at the electrode/solid electrolyte interface, a CPE element Q3 is introduced.[2-4]

R1 depends on three factors. Those are: a) intrinsic conductivity of the pelletized sample (**σ**); b) thickness of the pellet (**l**); c) area of cross-section of the pellet (**A**).

Calculation of proton conductivity from the R1 value

Resistivity (**ρ**) of a material = $(\mathbf{R} \times \mathbf{A})/\mathbf{l}$ ……. (1)

Thus, conductivity (**σ**) = 1/ **ρ** = $\mathbf{l}/(\mathbf{R} \times \mathbf{A})$ ……. (2)

R = resistance of sample; **σ** = conductivity of the sample.

l = thickness of pellet

A = area of cross section of pellet

The conductivity values for all the MOFs were calculated using similar data fitting and calculations.

Table A3.2. Proton conductivity of **Fe-MIL-53-NH$_2$** in various temperatures.

Temperature (°C)	**Conductivity (Scm^{-1})**
79	0.00151
71	0.00124
62	0.000780
54	0.000655
41	0.000322

Table A3.3. Proton conductivity of **53-S** in various temperatures.

Temperature (°C)	**Conductivity (Scm^{-1})**
81	0.01298
69	0.00779
58	0.0059
48	0.00443
39	0.00309

Table A3.4. Proton conductivity of **Fe-MIL-88B-NH$_2$** in various temperatures.

Temperature (°C)	**Conductivity (Scm^{-1})**
78	0.00336
70	0.00287
59	0.00254
49	0.00243
41	0.00234

Table A3.5. Proton conductivity of **88B-S** in various temperatures.

Temperature (°C)	**Conductivity (Scm^{-1})**
79	0.01687
67	0.01326
59	0.01197
49	0.01092
38	0.00928

Determination of activation energy

Activation energies (E_a) for proton conductivity in **53-S** and **88B-S** were calculated from the Arrhenius plot constructed between ln(σT) and 1000/T (**Figure 4c**, chapter 3).

From Arrhenius equation, $\boldsymbol{\sigma T = \sigma_0 \times \exp(-E_a/RT)}$ ……. (3)

σ = proton conductivity of the sample

T = Temperature in Kelvin

$\mathbf{E_a}$ = Activation energy of proton conduction

R= Ideal gas constant

Arrhenius equation can be restructured as $\boldsymbol{\ln(\sigma T) = \ln\sigma_0 - (Ea/RT)}$ ……. (4)

Or, $\boldsymbol{\ln(\sigma T) = \ln\sigma_0 + \{-E_a/(1000\times R)\ (1000/T)\}}$ ……. (5)

From the plot between **ln(σT)** and **1000/T**, the slope of the straight line = $\boldsymbol{- E_a/1000\times R}$

Impedance measurement under different relative humidity (R. H.)

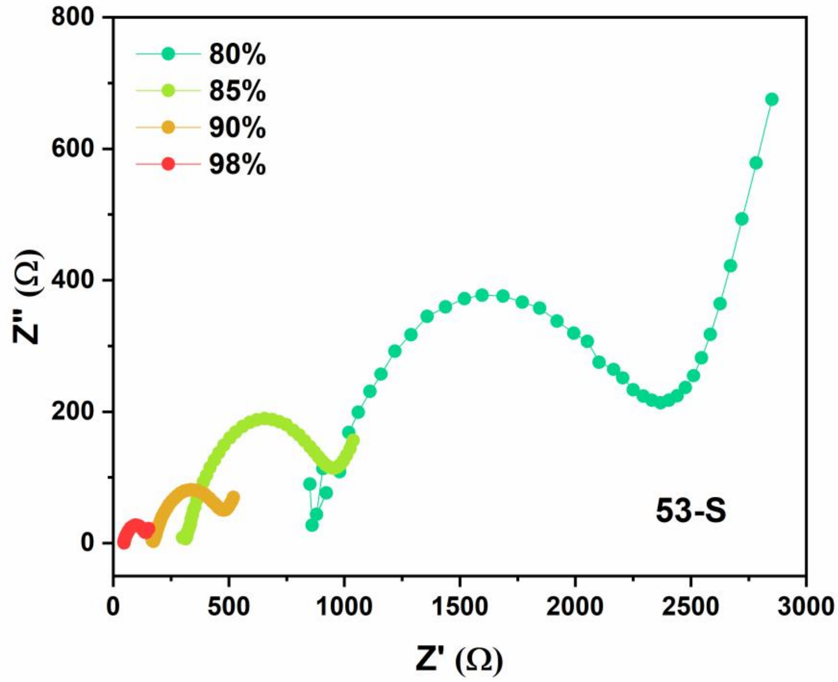

Figure A3.11. Nyquist plots of impedance measurements for **53-S** at a constant temperature of 45 °C and variable humidity.

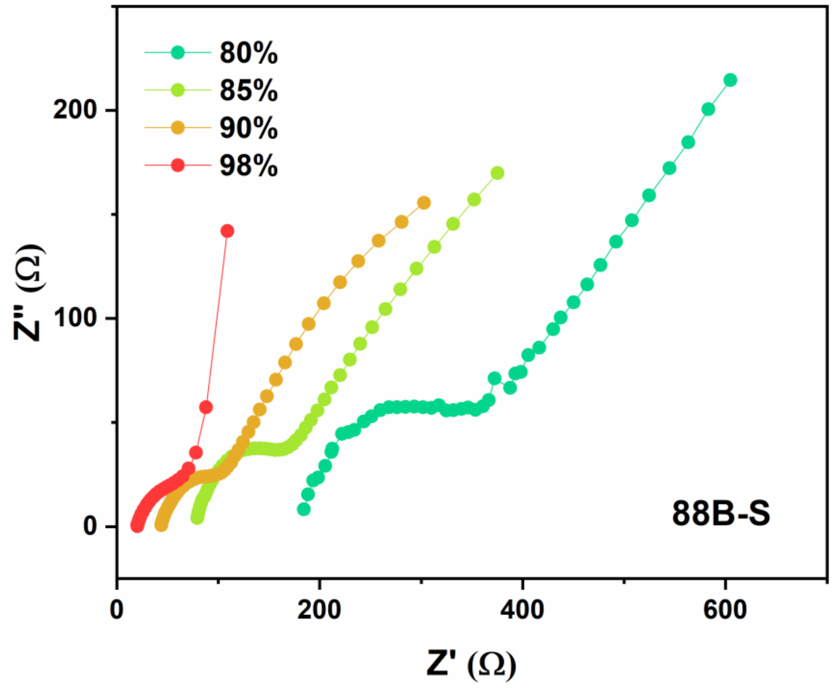

Figure A3.12. Nyquist plots of impedance measurements for **88B-S** at a constant temperature of 45 °C and variable humidity.

Section A3.7. Long term stability test under operational conditions

Consecutive heating-cooling cycles

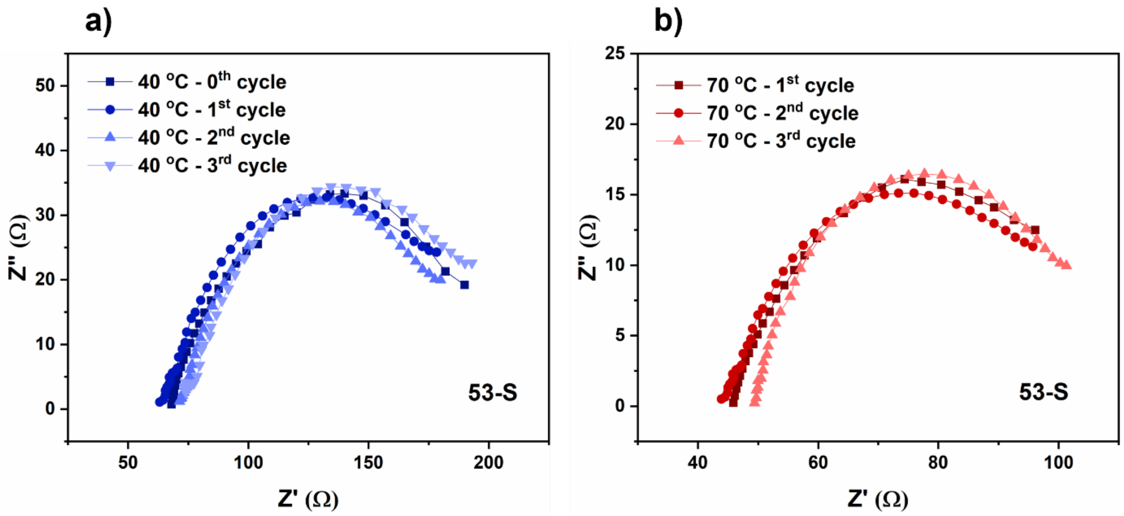

Figure A3.13. Nyquist plots for **53-S** at a constant temperature of a) 40 °C, b) 70 °C and 98% relative humidity.

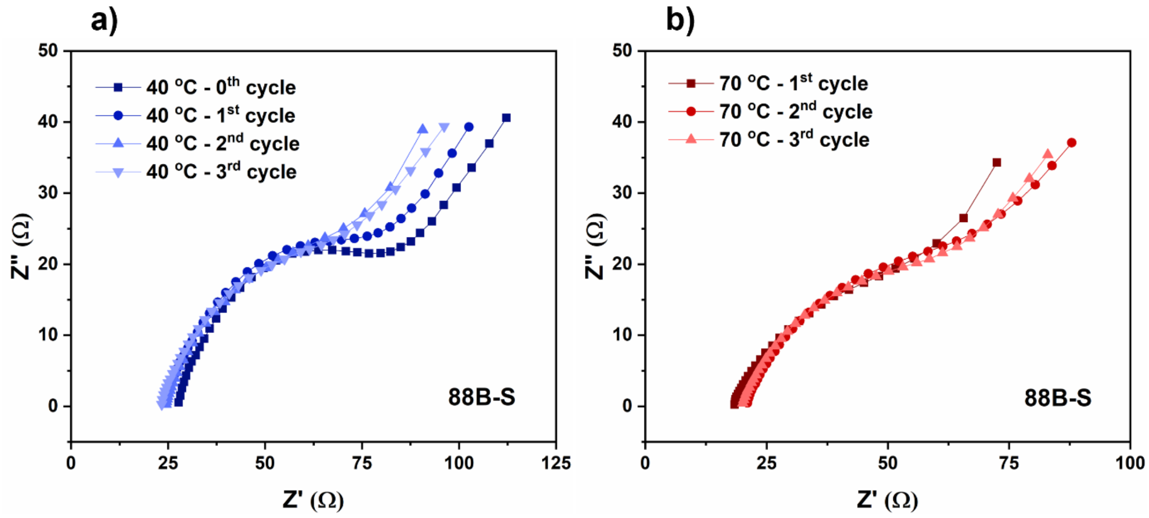

Figure A3.14. Nyquist plots for **88B-S** at a constant temperature of a) 40 °C, b) 70 °C and 98% relative humidity.

Material stability during proton conductivity measurements

In Figure A3.15a and A3.16a, the FESEM images show well-developed spindle-shaped microcrystals of **53-S** and **88B-S**, respectively. After pelletization under high pressure, the crystallites get clubbed together to form bigger particles where there is no distinguishable morphology (Figure A3.15b and A3.16b). Here it is noteworthy that, even after being exposed to high pressure, temperature and humidity, the materials maintained their structural integrity quite well, as inferred from PXRD and FT-IR analysis of the MOFs after pelletization and after impedance measurements.

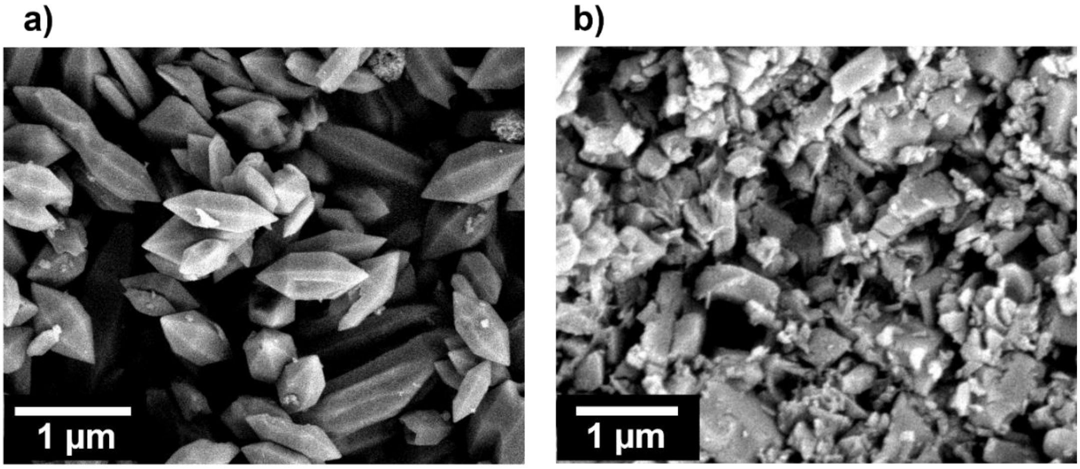

Figure A3.15. FESEM images of **53-S** a) before, and b) after pelletization and impedance measurements.

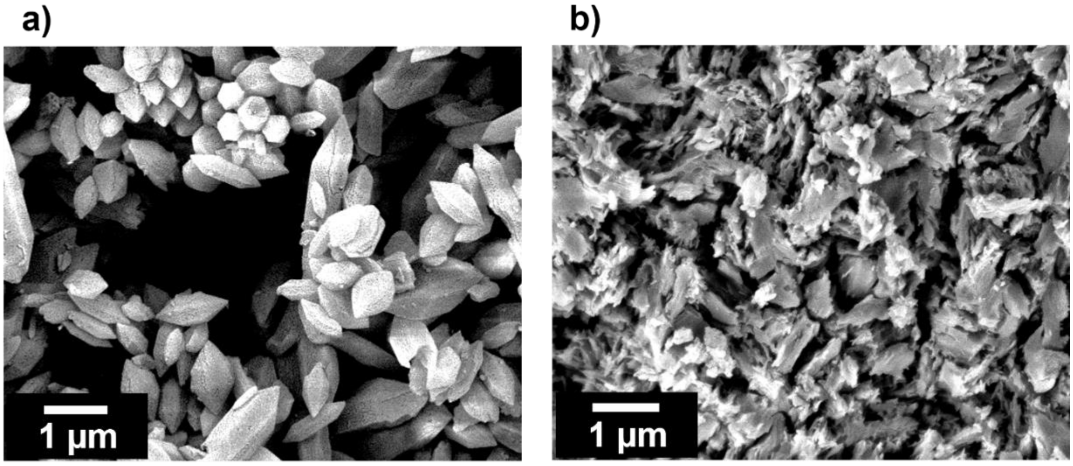

Figure A3.16. FESEM images of **88B-S** a) before, and b) after pelletization and impedance measurements.

The PXRD patterns of **53-S** and **88B-S** measured before and after pelletization and impedance measurements, matched well with each other (Figure A3.17a and A3.18a). Slight broadening of the peaks was observed for pelletized samples, which might have been caused due to the process of pellet making, which involves grinding of the samples into fine powder, and then subjecting them to high pressure to mould it into a pellet. A comparison of the PXRD patterns of **53-S** and **88B-S** pellets after impedance measurements with that of pellets before impedance measurement shows their one-to-one similarity. A comparison of the FT-IR spectra for **53-S** and **88B-S** before and after pelletization and impedance measurements do not show any notable changes (Figure A3.17b and A3.18b). The peaks at ~1037 cm^{-1} and ~1150 cm^{-1} corresponding to the SO_3H functionality of the MOFs, was also found to be intact throughout the process. This proves that the samples are stable during the process of conductivity measurements.

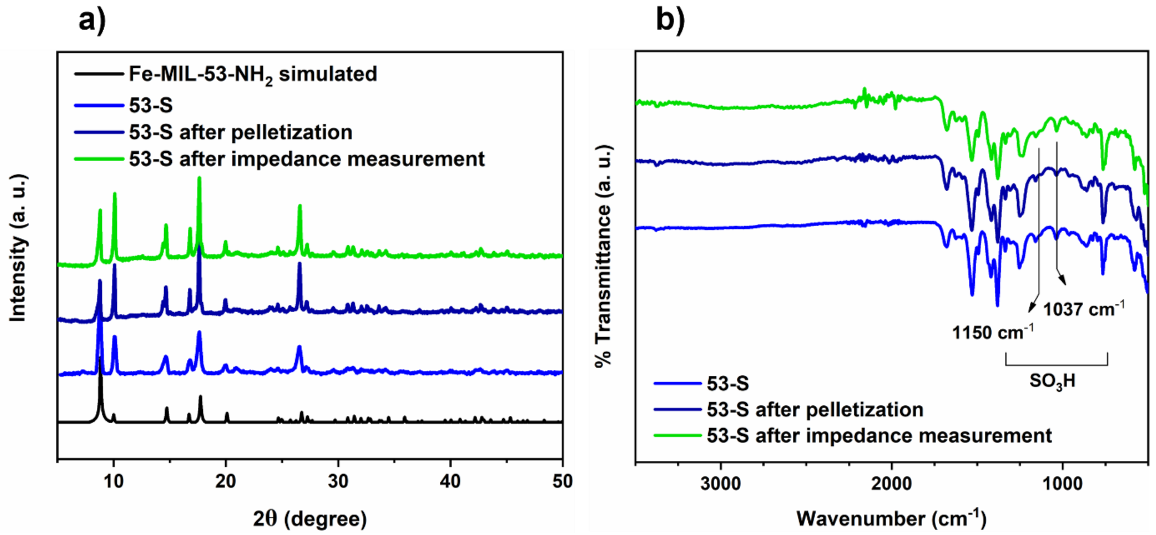

Figure A3.17. a) PXRD patterns and b) FT-IR spectra of **53-S**.

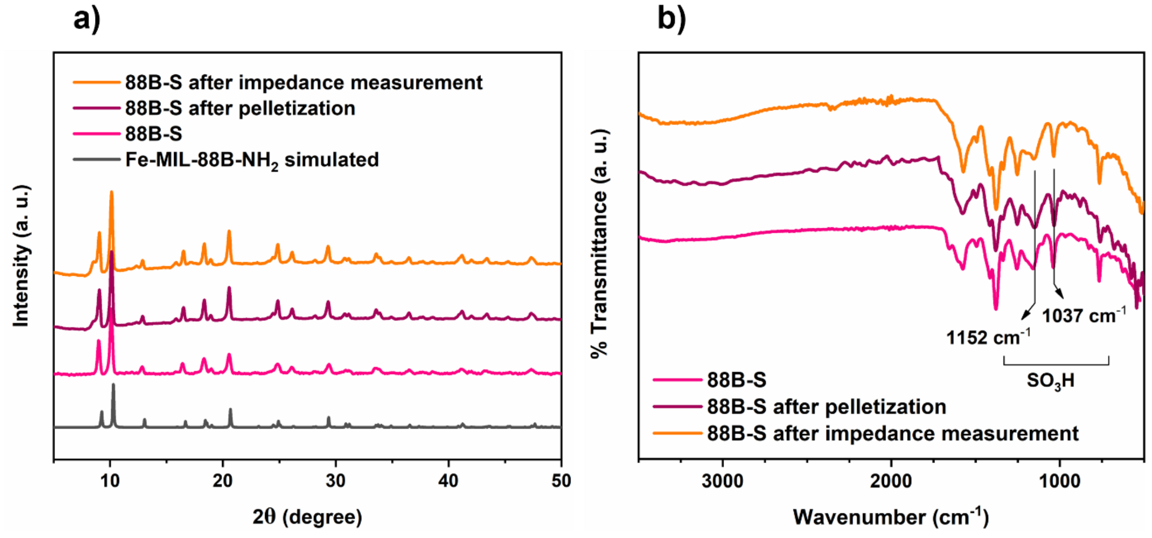

Figure A3.18. a) PXRD patterns and b) FT-IR spectra of **88B-S**.

Section A3.8. Structural analysis of MOFs after treatment with formic acid

To check for the framework stability of the MOFs in formic acid, approximately 300 mg of **Fe-MIL-53-NH2** and **Fe-MIL-88B-NH2** were treated with formic acid for approximately 2 hours. The MOFs were then separated by centrifugation and washed with water thrice. The MOFs were dried in a hot air oven at 70 °C for 48 hours. The formic acid treated **Fe-MIL-53-NH2**, and **Fe-MIL-88B-NH2** MOFs thus obtained, named hereafter as **53-FA** and **88B-FA**, respectively, were studied using PXRD, FT-IR, FESEM and DLS.

The PXRD pattern and FT-IR spectrum of **53-FA** matched well with that of **Fe-MIL-53-NH2**. The FESEM image shows the spindle shaped microcrystals of **53-FA** which resemble the morphology of this MOF before formic acid treatment. From DLS experiments the mean hydrodynamic diameter of the microcrystals in ethanol was found to be approximately 869 nm.

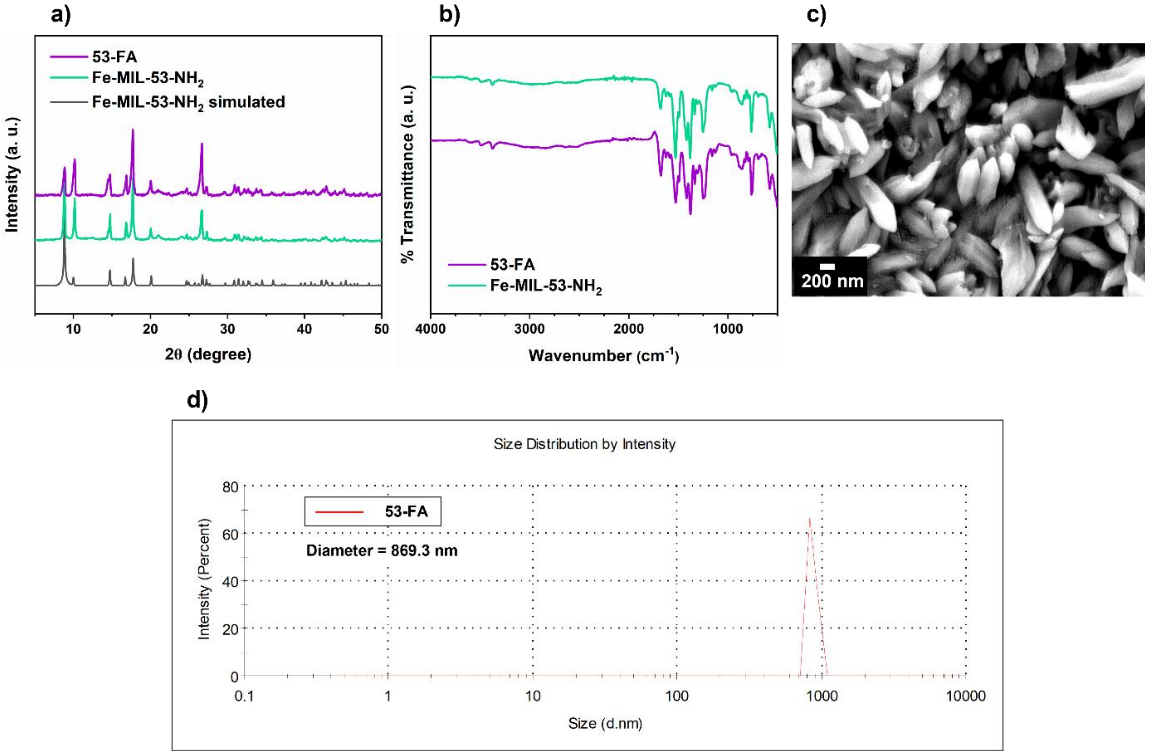

Figure A3.19. a) PXRD patterns and b) FT-IR spectra of **53-FA** and **Fe-MIL-53-NH2**; c) FESEM image of **53-FA**; d) Size distribution of **53-FA** by DLS measurement.

The PXRD pattern of **88B-FA** showed some shift in peak positions from that of **Fe-MIL-88B-NH2**. This phenomenon of shifting of PXRD peaks after introducing MIL-88B MOF to a new solvent or new guest molecules, is a common occurrence and a consequence of the highly flexible framework of MIL-88B.[5] The FT-IR spectrum of **88B-FA** matched well with that of **Fe-MIL-88B-NH_2**. The FESEM image shows the spindle shaped microcrystals of **88B-FA** which is quite similar to the **Fe-MIL-88B-NH_2** morphology. From DLS experiments the mean hydrodynamic diameter of the microcrystals in ethanol was found to be approximately 1087 nm.

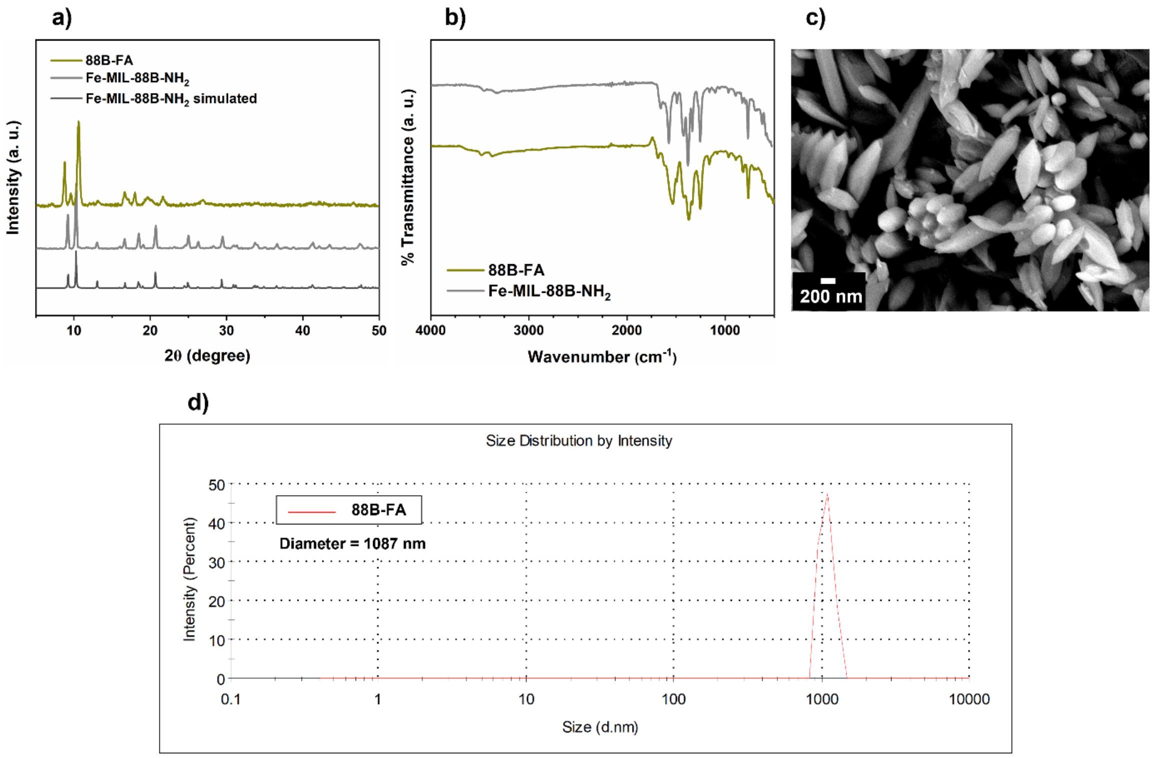

Figure A3.20. a) PXRD patterns and b) FT-IR spectra of **88B-FA** and **Fe-MIL-88B-NH_2**; c) FESEM image of **88B-FA**; d) Size distribution of **88B-FA** by DLS measurement.

Section A3.9. FT-IR analysis of MOF loaded MMMs

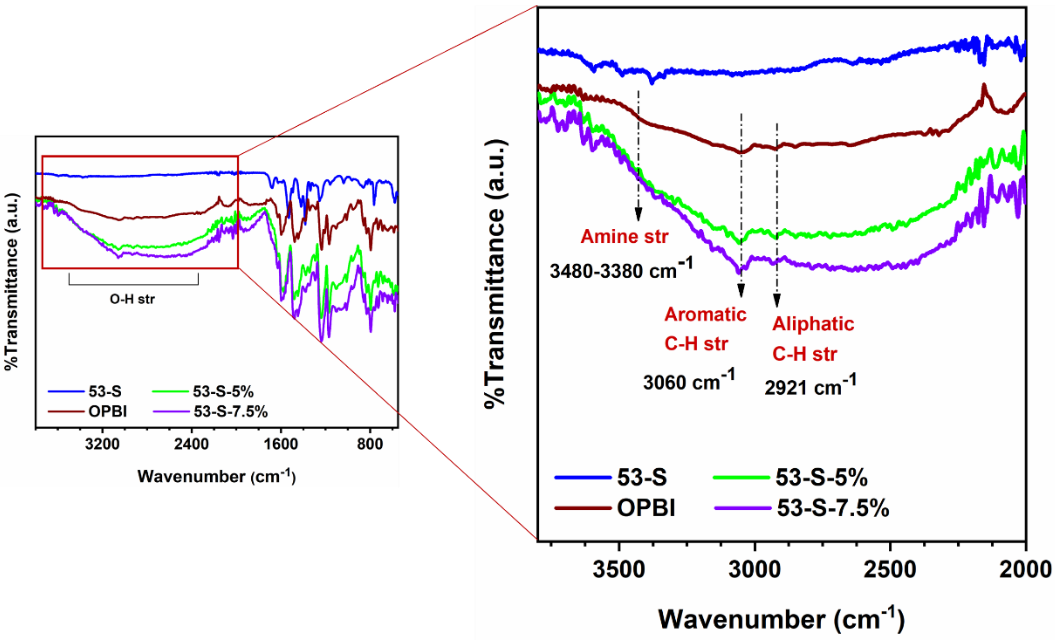

Figure A3.21. FT-IR spectra of **53-S** composite membranes along with **OPBI** and **53-S**.

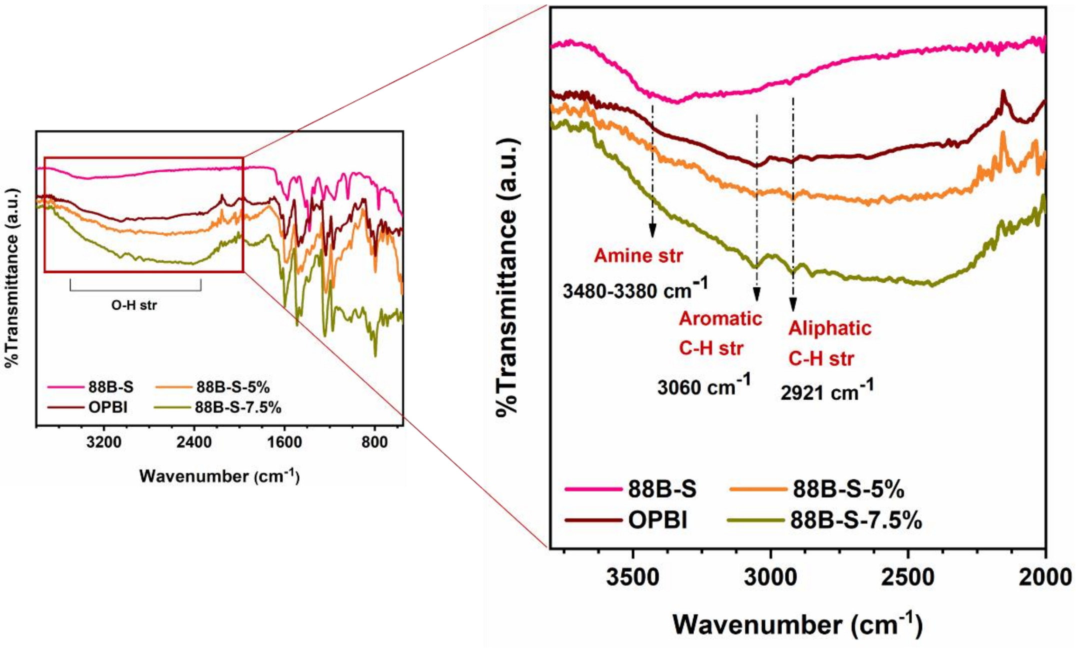

Figure A3.22. FT-IR spectra of **88B-S** composite membranes along with **OPBI** and **88B-S**.

Section A3.10. Morphology of the MOF loaded MMMs

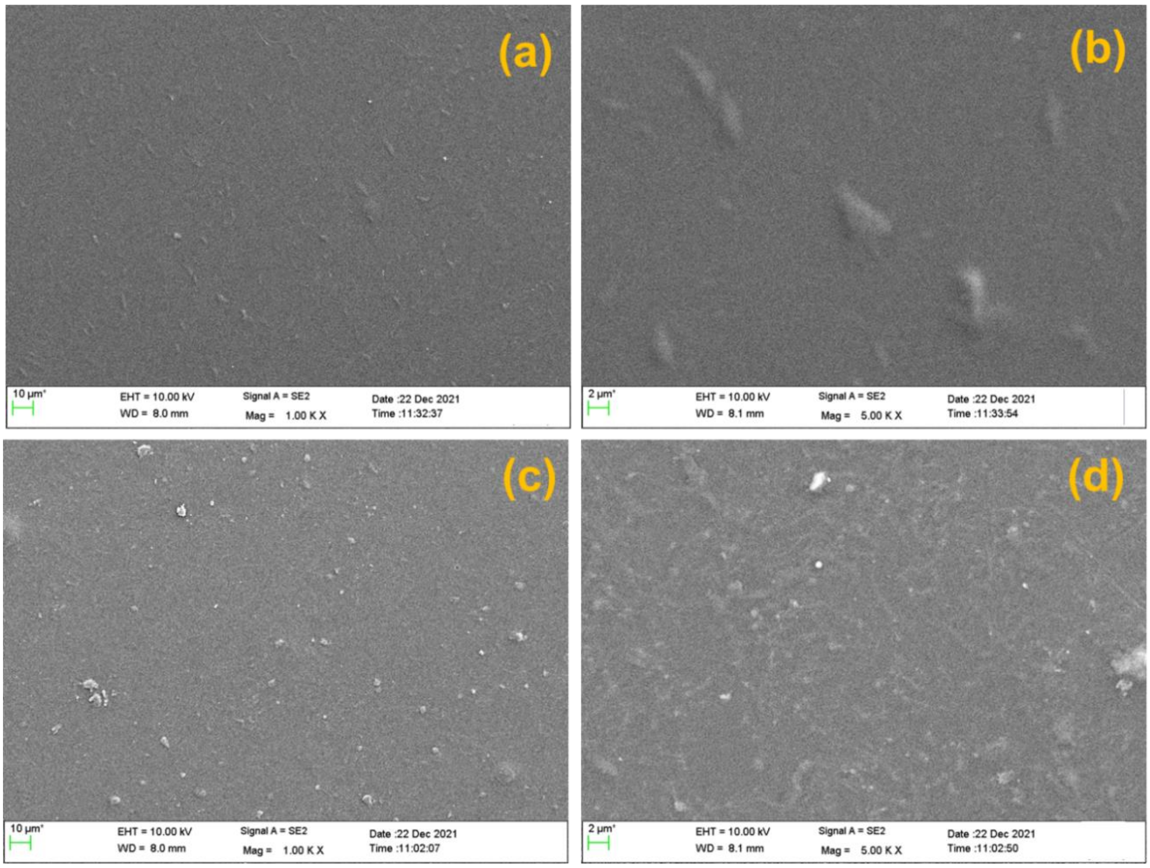

Figure A3.23. (a, b) Membrane surface FESEM image of **53-S-7.5%**, **(c, d)** Membrane surface FESEM image of **88B-S-7.5%.**

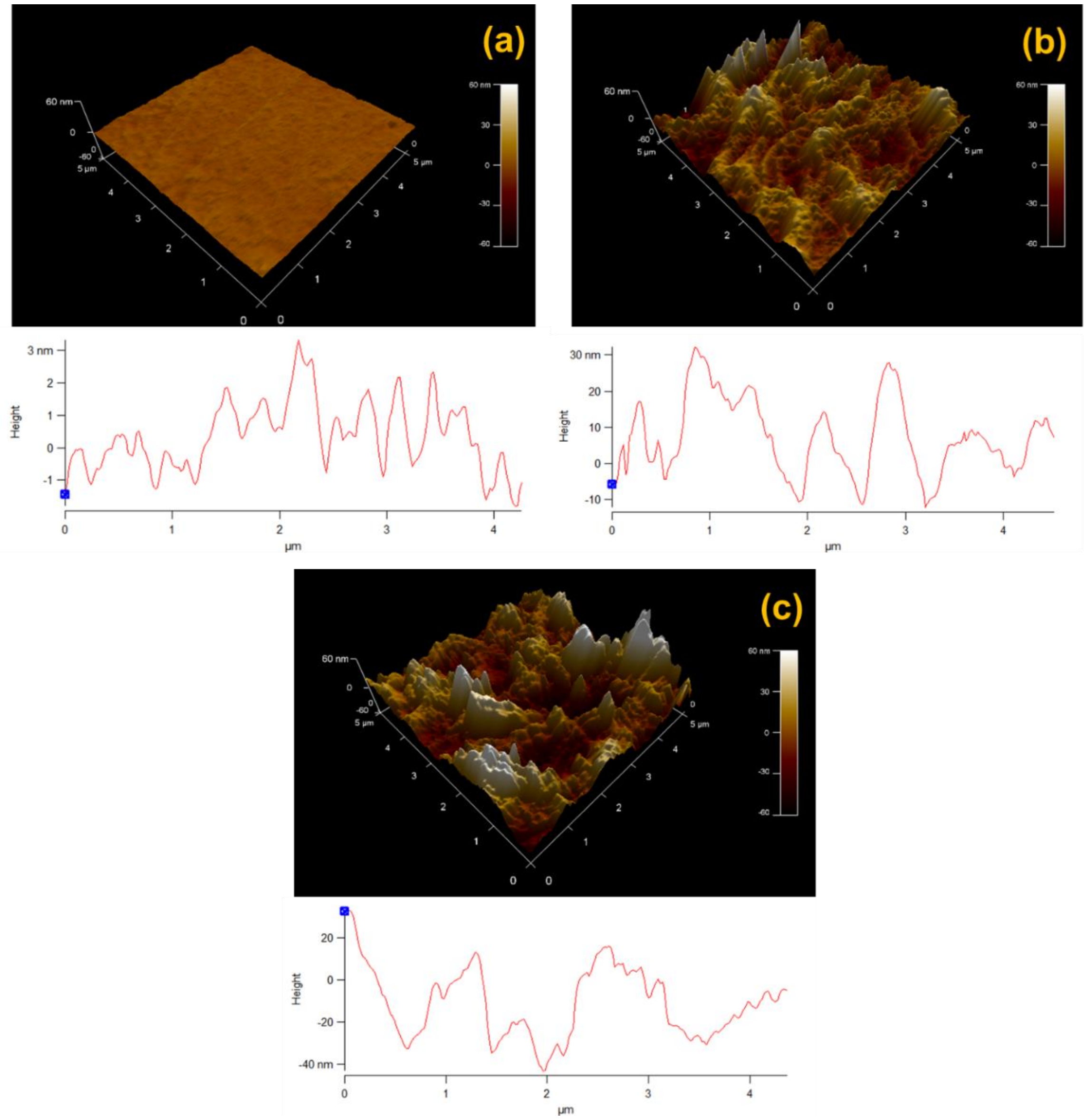

Figure A3.24. (a) Surface morphology (from AFM 3d images) of **(a)** OPBI, **(b) 53-S-7.5%** and **(c) 88B-S-7.5%** membranes. Height profile is also measured (shown below the images) in order to estimate the surface roughness of the membranes.

Table A3.6. Surface roughness of MOF loaded MMMs in a comparison with OPBI.

Sample	**Root mean square roughness (S_q) (nm)**	**Average deviation of roughness (nm)**
OPBI	1.287	1.002
53-S-7.5%	13.828	10.977
88B-S-7.5%	21.253	16.193

Section A3.11. Thermogravimetric analysis (TGA) of MOF loaded MMMs

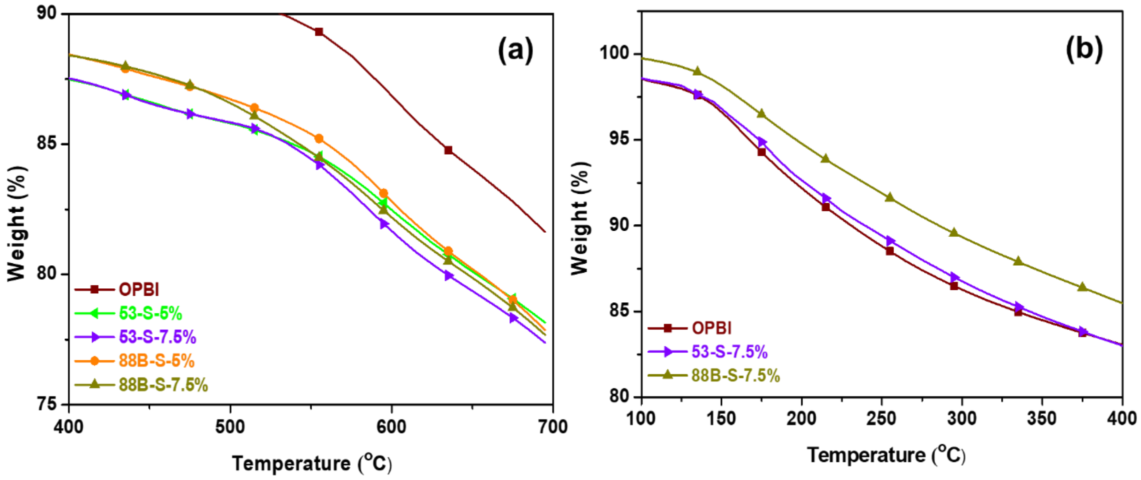

Figure A3.25. (a) Zoomed TGA plots (400 ºC - 700 ºC) of undoped **OPBI, 53-S** and **88B-S** mixed matrix membranes, (b) Zoomed TGA plots (100 ºC - 400 ºC) of PA doped **OPBI, 53-S-7.5%** and **88B-S-7.5%** membranes.

Section A3.12. Ion exchange capacity (IEC) of the membranes.

Table A3.7. Ion exchange capacity (IEC) of the membranes.

Sample name	Ion exchange capacity (meq/g)
OPBI	1.04
53-S-5%	1.68
53-S-7.5%	1.97
88B-S-5%	1.71
88B-S-7.5%	2.09

Section A3.13. Interaction pattern of PA with MOF loaded MMMs.

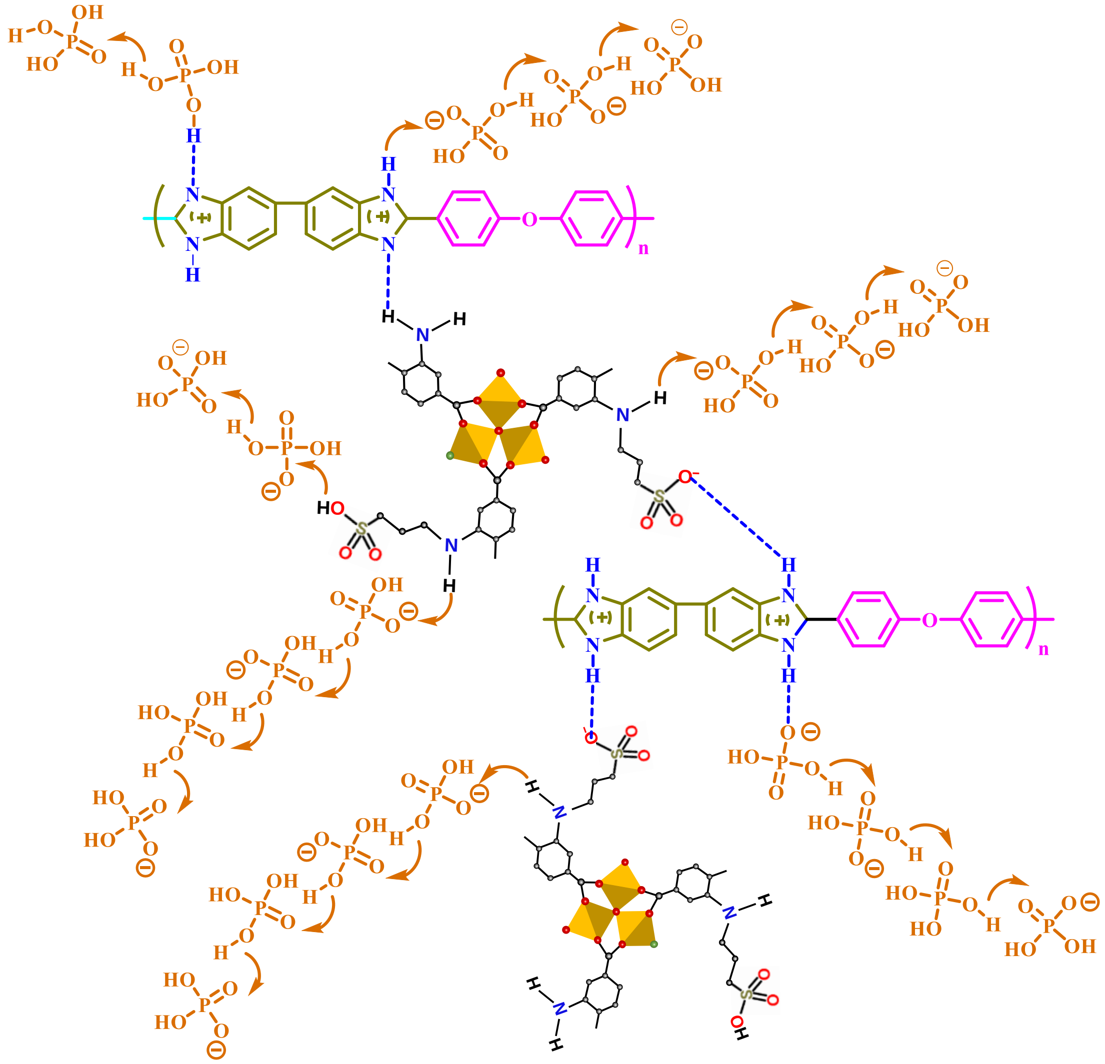

Scheme A3.1. Interaction pattern of PA with MOF loaded OPBI composite membrane matrix. Here, **88B-S** is used as an example, similar interactions are present in case of 53-S MOF loaded MMMs as well.

Section A3.14. Calculation of proton conductivity for the MMMs

Equivalent circuit

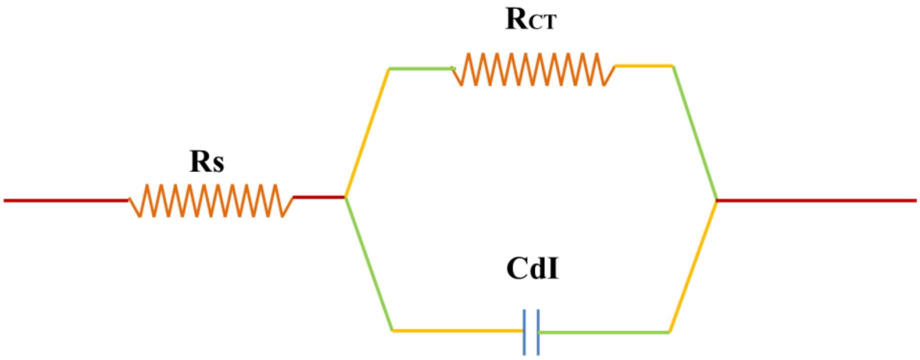

Impedance data were fitted to the most suitable equivalent circuit mentioned above with the help of EC-Lab software. The equivalent circuit is composed of three major components connected to each other in series. The bulk resistance (R_S) connected in series with a parallel combination of charge transfer resistance (R_{CT}) and a capacitor (CdI). Here R_S accounts for the bulk resistance of the membrane while R_{CT} represents the charge transfer resistance existing between the electrodes and the membrane electrolyte. Here, it should be noted that, charge transfer resistance R_{CT} is not associated with the conductivity of the electrolyte. Instead R_S is the crucial factor which quantifies the resistance of the bulk electrolyte. The bulk resistance of electrolyte i.e., R_S is of our primary interest as it represents conductivity of the membrane. R_S depends on (a) intrinsic conductivity of the PA loaded membrane sample, (b) thickness of the membrane and (c) area of cross section of the membrane. Thus, to determine the proton conductivity of the membrane sample from the R_S value, both of the other two factors (*i.e.*, area of cross section and thickness of membrane) should be taken into consideration.

Here we provide the values of R_S, and R_{CT} by fitting the experimentally obtained data points along the curve generated by the equivalent circuit mentioned above.

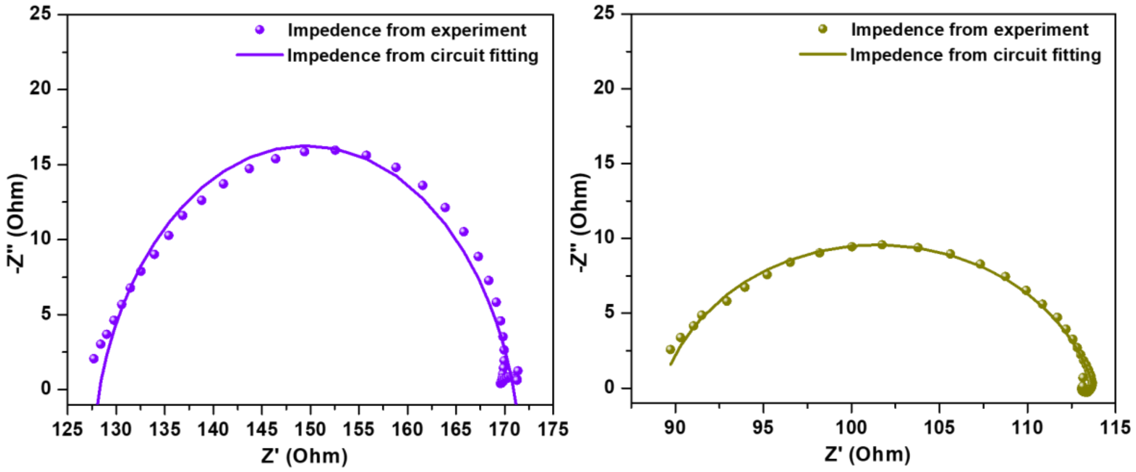

Figure A3.26. (a) Nyquist plot of **53-S-7.5%** and **(b) 88B-S-7.5%** membrane after equivalent circuit fitting at 160 °C**.**

Table A3.8. Fitting parameters to determine proton conductivity of **53-S-7.5%** membrane in various temperatures. (Membrane thickness = 0.010 cm or 0.10 mm)

Temperature (° C)	**Value of R_S (Ohm)**	**Conductivity (Scm^{-1})**
30 °C	417.27	0.079
50 °C	266.58	0.125
60 °C	193.39	0.172
80 °C	174.31	0.191
100 °C	162.60	0.205
120 °C	148.04	0.225
140 °C	138.22	0.241
160 °C	131.34	0.253

Table A3.9. Fitting parameters to determine proton conductivity of **88B-S-7.5%** composite membrane in various temperatures. (Membrane thickness = 0.012 cm or 0.12 mm)

Temperature (º C)	Value of R_S (Ohm)	Conductivity (Scm^{-1})
30 °C	415.38	0.0669
50 °C	211.62	0.131
60 °C	182.5	0.152
80 °C	124.02	0.223
100 °C	113.97	0.243
120 °C	101.73	0.273
140 °C	94.45	0.294
160 °C	91.178	0.304

Table A3.10. Fitting parameters to determine proton conductivity of **53-S-5%** and **88B-S-5%** membranes along with OPBI membrane at 160 °C.

Sample	Value of R_S (Ohm) at 160 °C	Thickness (cm)	Conductivity (Scm^{-1}) at 160 °C
OPBI	424.94	0.012	0.065
53-S-5%	160.58	0.01	0.207
88B-S-5%	123.86	0.011	0.244

Section A3.15. Isothermal proton conductivity of MOF loaded MMMs at 160 ° C.

Isothermal proton conductivities of the **88B-S-7.5%,** and **53-S-7.5%** membranes in a comparison with pristine **OPBI** were measured. The membranes were isothermally kept at 160 °C for 36 h and the conductivity of individual membrane was measured for every 2 h interval up to 36 h. Initially within the first 2-4 h of analysis, a bit decrease of proton conductivity was observed for all the membranes. After the initial period, proton conductivities of the membranes found to be stable up to the entire experimental time range. The PA doped post synthetically modified MOF loaded membranes resulted much less decrement in conductivity compared to **OPBI**. Formation of extensive interfacial H-bonding interactions between the **88B-S/53-S** MOFs functionalities with **OPBI** polymer network resulted enhanced dimensional and mechanical stability of the membranes followed by retention of proton conductivity under long-term isothermal environment at elevated temperature (160 °C).

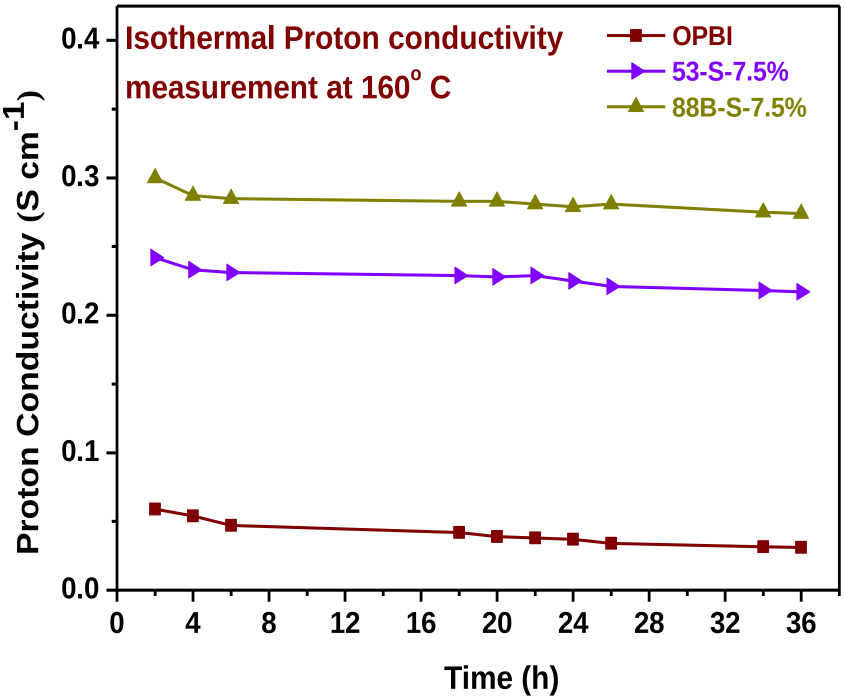

Figure A3.27. Isothermal proton conductivity of **OPBI**, **53-S-7.5%** and **88B-S-7.5%** membranes at 160 ° C for 36 h.

Section A3.16. Storage modulus values and glass transition temperature (T_g) of MMMs. Tensile stress and elongation at break values of the MMMs.

Table A3.11. Temperature dependent storage modulus of MIL based OPBI nanocomposite membranes obtained from DMA.

Sample	E' (MPa) at 100° C	% of increase	E' (MPa) at 400° C	% of increase
OPBI	2079		1096	
53-S-5%	3001	-	1030	-
53-S-7.5%	4946	137.90	2197	100.45
88B-S-5%	3465	-	967	-
88B-S-7.5%	5827	180.27	2206	101.27

The temperature dependent Tan δ plot (Figure A3.28) of all the MMMs display a single relaxation peak and the temperature corresponding to the peak is denoted as the glass transition temperature (T_g). The T_g values, obtained for OPBI and all the other MOF loaded membranes resulted between 280 °C - 370 °C (Figure A3.28, Table A3.11), which is in well accordance with the literature reported PBI based membranes.,[6] The T_g values, obtained from **88B-S** MOF loaded membranes, were found to be significantly higher than pristine OPBI. Presence of ionic crosslinking, certain crystalline ordering along with the formation of widely altered morphology obtained from FESEM, TEM and AFM analysis (Figure 7 of the main article) decreases the free volume fraction of the polymer and therefore requires higher temperature to affect the segmental mobility of the polymer chains.[7] Thus, DMA studies of the MOF loaded membranes dictate that post-synthetic installation of dangling side arm in the sultone modified MIL based MOF materials govern the dispersion pattern of these MOFs into the polymer matrix which in turn resulted in superior quality PEMs with improved mechanical properties.

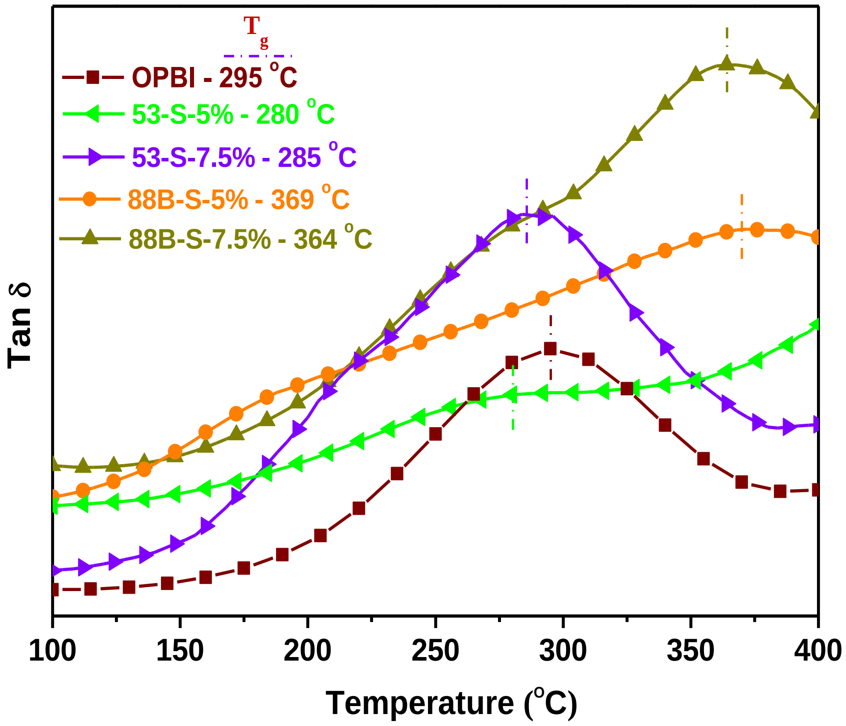

Figure A3.28. tan δ plots of all the 53-S and 88B-S loaded MMMs of different filler loading along with pristine **OPBI**.

Table A3.12. Tensile Stress and Elongation at Break Values of **OPBI**, **88B-S@OPBI** and **53-S@OPBI** Composite Membranes

Sample	Tensile stress at break (MPa)	Elongation at break (%)
OPBI	0.50	79
53-S-5%	0.92	123
53-S-7.5%	1.59	270
88B-S-5%	2.29	244
88B-S-7.5%	2.23	336

Section A3.17. Oxidative stability of the MOF@OPBI composite membranes

To evaluate the efficiency of the **53S@OPBI** and **88B-S@OPBI** membranes towards severe oxidative environment, all the membranes were kept immersed in Fenton's reagent (3% H_2O_2 in 2 ppm $FeSO_4$) for 100 h at 70 °C. The remaining wt% was calculated from the weight differences of the MMMs before and after treating with Fenton's reagent. The oxidative stability of the MMMs was measured as a function of time and plotted in the Figure A3.29. All the MOF loaded MMMs were observed to be superior in terms of chemical stability when compared with bare OPBI polymer. Also the chemical stability of the MMMs maintains proportionality with increase in the **53S** or **88B-S** filler content in the OPBI matrix establishes the fact that the organic functionality of the MOF framework structure restricts the attacks of HO• and HOO• radicals in the polar groups of OPBI. The enhanced oxidative stability is a cumulative effect of H-bonding interfacial interaction between the **53S** and **88B-S** as nanofillers and the OPBI chains. At higher MOF loading, the presence of more interfacial interaction attributed to better shielding of polymer chains, which attributes more chemical stability of the main polymer backbone.

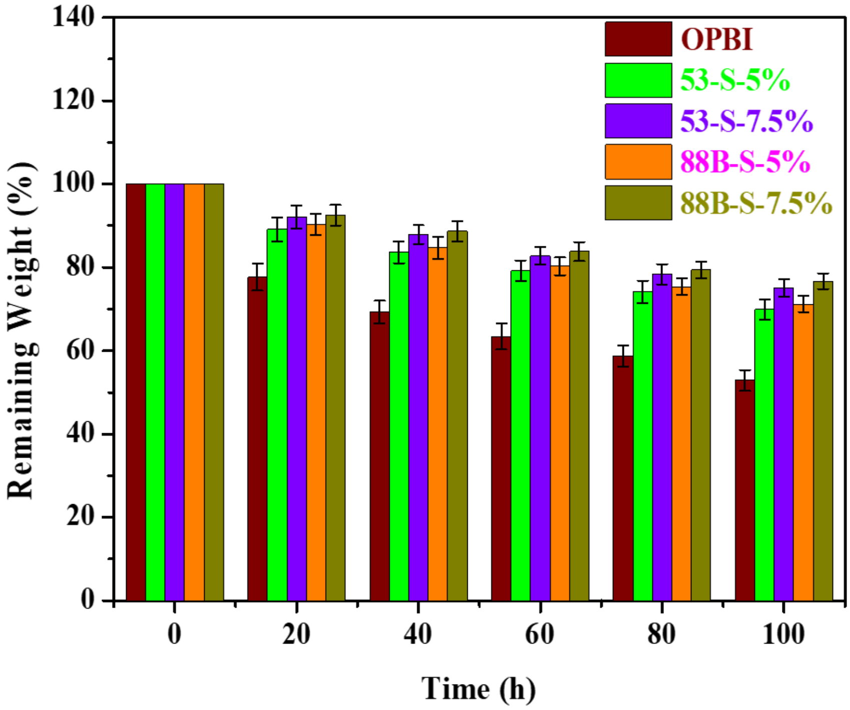

Figure A3.29. Oxidative stability of the MOF@OPBI composite membranes.

Section A3.18. Literature survey of proton conducting MIL-53 and MIL-88B based MOFs and different MOF based polymer composite MMMs (in comparison to our obtained results)

Table A3.13. Proton conductivity values of **53-S** and **88B-S** in comparison with other **MIL-53** and **MIL-88B** based MOF proton conductors operating under humidity.

Sample	**Conductivity (Scm^{-1})**	**Conditions**	**Reference**
MIL-88B			
88B-S	1.687×10^{-2}	80 °C, 98% RH	**This work**
Cr-MIL-88B	6×10^{-3}	100 °C, 85% RH	8
Cr-MIL-88B-PESA	4.50×10^{-2}	100 °C, 85% RH	8
Cr-MIL-88B-PSA	1.58×10^{-1}	100 °C, 85% RH	8
PMNS1	1.52×10^{-1}	80 °C, 100% RH	9
PMNS2	4.68×10^{-2}	80 °C, 100% RH	9
MIL-53			
53-S	1.298×10^{-2}	80 °C, 98% RH	**This work**
MIL-53(Fe)-$(COOH)_2$	7×10^{-6}	80 °C, 95% RH	10
MIL-53(Al)-(OH)	1.9×10^{-6}	80 °C, 95% RH	10
MIL-53(Al)-NH_2	4.1×10^{-8}	80 °C, 95% RH	10
NH_2-MIL-53$(Al)_{it}$	3.0×10^{-5}	80 °C, 26% RH	11

Table A3.14. Recent reports of MOF based polymer composite MMMs

Polymer	**MOF (loading) (%)**	**Additive**	**Proton conductivity (Scm^{-1})**	**Temperature (°C) and Relative Humidity (%)**	**Ref.**
OPBI	**53-S-7.5%**	**H_3PO_4**	**0.253**	**160 °C and anhydrous**	**This work**
OPBI	**88B-S-7.5%**	**H_3PO_4**	**0.304**	**160 °C and anhydrous**	**This work**
Nafion	MIL-101 (12 wt%)	Phytic acid	0.228	100 °C and 100% RH	12
Nafion	HKUST-1 (2.5 wt%)	H_3PO_4	0.018	25 °C and 100% RH	13
Nafion	ZIF-8@GO/Nafion	GO	2.8×10^{-1}	120 °C and 40% RH	14
Nafion	2:1 UiO-66-NH_2: UiO-66- SO_3H (0.6 wt%)	--	0.256	90 °C and 95% RH	15
Nafion	UiO-66-SO_3H (2 wt%)	--	0.17	80 °C and 95% RH	16
SPES	SPES-MOF	--	41×10^{-3}	160 °C and anhydrous	17
SPEEK	SPEEK-7.5 wt% UiO-66-Zr-MOF	--	10.4×10^{-2}	25 °C and 100% RH	18
SPEEK	MIL-101-SO_3H (7.5 wt%)	--	0.306	79 °C and 100% RH	19
SPAEK	IL@MOF-1	--	0.184	80 °C and 100% RH	20
SPEEK	NH_2-MIL-53 (5 wt%)	--	0.017	80 °C and 100% RH	21
SPEEK	SPEEK/HPW@MIL101	--	0.272	80 °C and 100% RH	22
PVA	ZIF-8 (5 wt%)	PAMS	0.134	80 °C and 100% RH	23
PSS	PSS@ZIF-8-9	--	2.59×10^{-1}	80 °C and 100% RH	24
PVP-PVDF	SA/MIL101@PVP-PVDF	--	0.237	160 °C and anhydrous	25

PVP-PVDF	Cu-SAT/PVDF-PVP	--	0.8×10^{-3}	80 °C and 98% RH	26
PVDF	MOF-801 (60 wt%)	--	1.84×10^{-3}	52 °C and 95% RH	27
ILs@MOF	SA-EIMS@MIL-101 MSA-EIMS@MIL-101 PTSA-EIMS@MIL-101	--	1.89×10^{-3} 1.02×10^{-3} 2.78×10^{-3}	150 °C	28
SPPO	Fe-MIL-101-NH_2 (6%)	--	0.25	90 °C	29
Chitosan	CS/H_3PO_4@MIL-101 (8 wt%)	--	0.095	100 °C and 100% RH	30
Chitosan	CS/CF_3SO_3H@MIL-101	--	0.094	100 °C and 100% RH	30
PEI	ZIF-8 (20 wt%) ZIF-67 (20 wt%) 1:1 ZIF-8: ZIF-67 (20 wt%)	TBA TBA TBA	1.9×10^{-3} 1.8×10^{-3} 3.0×10^{-3}	75 °C and 95% RH 75 °C and 95% RH 75 °C and 95% RH	31
PBI	ZIF-8 (5 wt%)	H_3PO_4	3.1×10^{-3}	120 °C and anhydrous	32
PBI	ZIF-67 (5 wt%)	H_3PO_4	0.042	120 °C and anhydrous	32
PBI	1:1 ZIF-8: ZIF-67 (5 wt%)	H_3PO_4	0.092	120 °C and anhydrous	32
OPBI	PSM 1-10%	H_3PO_4	0.290	160 °C and anhydrous	33
OPBI	PSM 2-10%	H_3PO_4	0.308	160 °C and anhydrous	33

References

1. Bauer, S.; Serre, C.; Devic, T.; Horcajada, P.; Marrot, J.; Férey, G.; Stock, N. High-Throughput Assisted Rationalization of the Formation of Metal Organic Frameworks in the Iron(III) Aminoterephthalate Solvothermal System. *Inorg. Chem.* **2008**, *47*, 7568-7576.
2. Taylor, J. M.; Dekura, S.; Ikeda, R.; Kitagawa, H. Defect Control to Enhance Proton Conductivity in a Metal−Organic Framework. *Chem. Mater.* **2015**, *27*, 2286−2289.
3. Yang, F.; Xu, G.; Dou, Y.; Wang, B.; Zhang, H.; Wu, H.; Zhou, W.; Li, J-R. Chen, B. A flexible metal–organic framework with a high density of sulfonic acid sites for proton conduction. *Nature Energy* **2017**, *2*, 877–883.

4. Randviir, E. P.; Banks, C. E. Electrochemical impedance spectroscopy: an overview of bioanalytical applications. *Anal. Methods* **2013**, *5*, 1098–1115.
5. Ma, M.; Bétard, A.; Weber, I.; Al-Hokbany, N. S.; Fischer, R. A.; Metzler-Nolte, N. Iron-Based Metal–Organic Frameworks MIL-88B and NH_2-MIL-88B: High Quality Microwave Synthesis and Solvent-Induced Lattice "Breathing". *Cryst. Growth Des.* **2013**, *13*, 2286–2291.
6. Maity, S.; Jana, T. Soluble Polybenzimidazoles for PEM: Synthesized from Efficient, Inexpensive, Readily Accessible Alternative Tetraamine Monomer. *Macromolecules* **2013**, *46*, 6814–6823.
7. Maity, S.; Singha, S.; Jana, T. Low Acid Leaching PEM for Fuel Cell Based on Polybenzimidazole Nanocomposites with Protic Ionic Liquid Modified Silica. *Polymer.* **2015**, *66*, 76–85.
8. Liu, S-S.; Han, Z.; Yang, J-S.; Huang, S-Z.; Dong, X-Y.; Zang, S-Q. Sulfonic Groups Lined along Channels of Metal−Organic Frameworks (MOFs) for Super-Proton Conductor. *Inorg. Chem.* **2020**, *59*, 396–402.
9. Li, Z-H.; Zeng, H.; Zeng, G.; Ru, C.; Li, G.; Yan, W.; Shi, Z.; Feng, S. Multivariate Synergistic Flexible Metal-Organic Frameworks with Superproton Conductivity for Direct Methanol Fuel Cells. *Angew. Chem. Int. Ed.* **2021**, *60*, 26577–26581.
10. Shigematsu, A.; Yamada, T.; Kitagawa, H. Wide Control of Proton Conductivity in Porous Coordination Polymers. *J. Am. Chem. Soc*. **2011**, *133*, 2034–2036.
11. Liu, J.; Zou, X,; Liu, C.; Cai, K.; Zhao, N.; Zheng, W.; Zhu. G. Ionothermal synthesis and proton-conductive properties of NH_2-MIL-53 MOF nanomaterials. *CrystEngComm*, **2016**, *18*, 525–528.
12. Li, Z.; He, G.; Zhang, B.; Cao, Y.; Wu, H.; Jiang, Z.; Tiantian, Z. Enhanced Proton Conductivity of Nafion Hybrid Membrane under Different Humidities by Incorporating Metal-Organic Frameworks with High Phytic Acid Loading. *ACS Appl. Mater. Interfaces* **2014**, *6*, 9799–9807.
13. Kim, H. J.; Talukdar, K.; Choi, S. J. Tuning of Nafion® by HKUST-1 as Coordination Network to Enhance Proton Conductivity for Fuel Cell Applications. *J. Nanoparticle Res.* **2016**, *18*, 47.
14. Yang, L.; Tang, B.; Wu, P. Metal-Organic Framework-Graphene Oxide Composites: A Facile Method to Highly Improve the Proton Conductivity of PEMs Operated under Low Humidity. *J. Mater. Chem. A* **2015**, *3*, 15838–15842.
15. Rao, Z.; Tang, B.; Wu, P. Proton Conductivity of Proton Exchange Membrane Synergistically Promoted by Different Functionalized Metal-Organic Frameworks. *ACS Appl. Mater. Interfaces* **2017**, *9*, 22597–22603.
16. Donnadio, A.; Narducci, R.; Casciola, M.; Marmottini, F.; D'Amato, R.; Jazestani, M.; Chiniforoshan, H.; Costantino, F. Mixed Membrane Matrices Based on Nafion/UiO-66/SO3H-UiO-66 Nano-MOFs: Revealing the Effect of Crystal Size, Sulfonation, and Filler Loading on the Mechanical and Conductivity Properties. *ACS Appl. Mater. Interfaces* **2017**, *9*, 42239–42246.
17. Anahidzade, N.; Abdolmaleki, A.; Dinari, M.; Firouz Tadavani, K.; Zhiani, M. Metal-Organic Framework Anchored Sulfonated Poly(Ether Sulfone) as a High Temperature Proton Exchange Membrane for Fuel Cells. *J. Membr. Sci.* **2018**, *565*, 281–292.
18. da Trindade, L. G.; Borba, K. M. N.; Zanchet, L.; Lima, D. W.; Trench, A. B.; Rey, F.; Diaz, U.; Longo, E.; Bernardo-Gusmão, K.; Martini, E. M. A. SPEEK-Based Proton Exchange Membranes Modified with MOF-Encapsulated Ionic Liquid. *Mater. Chem. Phys.* **2019**, *236*, 121792.
19. Li, Z.; He, G.; Zhao, Y.; Cao, Y.; Wu, H.; Li, Y.; Jiang, Z. Enhanced Proton Conductivity of Proton Exchange Membranes by Incorporating Sulfonated Metal-Organic Frameworks. *J. Power Sources* **2014**, *262*, 372–379.
20. Ru, C.; Gu, Y.; Na, H.; Li, H.; Zhao, C. Preparation of a Cross-Linked Sulfonated Poly(Arylene Ether Ketone) Proton Exchange Membrane with Enhanced Proton Conductivity and Methanol Resistance by Introducing an Ionic Liquid-Impregnated Metal Organic Framework. *ACS Appl. Mater. Interfaces* **2019**, *11*, 31899–31908.
21. Ahmadian-Alam, L.; Mahdavi, H. A Novel Polysulfone-Based Ternary Nanocomposite Membrane Consisting of Metal-Organic Framework and Silica Nanoparticles: As Proton Exchange Membrane for Polymer Electrolyte Fuel Cells. *Renew. Energy* **2018**, *126*, 630–639.
22. Zhang, B.; Cao, Y.; Li, Z.; Wu, H.; Yin, Y.; Cao, L.; He, X.; Jiang, Z. Proton Exchange Nanohybrid Membranes with High Phosphotungstic Acid Loading within Metal-Organic Frameworks for PEMFC Applications. *Electrochim. Acta* **2017**, *240*, 186–194.
23. Erkartal, M.; Usta, H.; Citir, M.; Sen, U. Proton Conducting Poly(Vinyl Alcohol) (PVA)/ Poly(2-Acrylamido-2-Methylpropane Sulfonic Acid) (PAMPS)/ Zeolitic Imidazolate Framework (ZIF) Ternary Composite Membrane. *J. Membr. Sci.* **2016**, *499*, 156–163.
24. Cai, Y. Y.; Yang, Q.; Zhu, Z. Y.; Sun, Q. H.; Zhu, A. M.; Zhang, Q. G.; Liu, Q. L. Achieving Efficient Proton Conduction in a MOF-Based Proton Exchange Membrane through an Encapsulation Strategy. *J. Membr. Sci.* **2019**, *590*, 117277.

25. Sun, L.; Gu, Q.; Wang, H.; Yu, J.; Zhou, X. Anhydrous Proton Conductivity of Electrospun Phosphoric Acid-Doped PVP-PVDF Nanofibers and Composite Membranes Containing MOF Fillers. *RSC Adv.* **2021**, *11*, 29527–29536.
26. Moi, R.; Ghorai, A.; Banerjee, S.; Biradha, K. Amino- and Sulfonate-Functionalized Metal-Organic Framework for Fabrication of Proton Exchange Membranes with Improved Proton Conductivity. *Cryst. Growth Des.* **2020**, *20*, 5557–5563.
27. Zhang, J.; Bai, H. J.; Ren, Q.; Luo, H. Bin; Ren, X. M.; Tian, Z. F.; Lu, S. Extra Water- and Acid-Stable MOF-801 with High Proton Conductivity and Its Composite Membrane for Proton-Exchange Membrane. *ACS Appl. Mater. Interfaces* **2018**, *10*, 28656–28663.
28. Chen, H.; Han, S. Y.; Liu, R. H.; Chen, T. F.; Bi, K. L.; Liang, J. B.; Deng, Y. H.; Wan, C. Q. High Conductive, Long-Term Durable, Anhydrous Proton Conductive Solid-State Electrolyte Based on a Metal-Organic Framework Impregnated with Binary Ionic Liquids: Synthesis, Characteristic and Effect of Anion. *J. Power Sources* **2018**, *376*, 168–176.
29. Wu, B.; Lin, X.; Ge. L.; Wu, L.; Xu, T. A novel route for preparing highly proton conducting membrane materials with metal-organic frameworks. Chem. Commun. **2013**, *49*, 143-145.
30. Dong, X. Y.; Li, J. J.; Han, Z.; Duan, P. G.; Li, L. K.; Zang, S. Q. Tuning the Functional Substituent Group and Guest of Metal-Organic Frameworks in Hybrid Membranes for Improved Interface Compatibility and Proton Conduction. *J. Mater. Chem. A* **2017**, *5*, 3464–3474.
31. Vega, J.; Andrio, A.; Lemus, A. A.; del Castillo, L. F.; Compañ, V. Conductivity Study of Zeolitic Imidazolate Frameworks, Tetrabutylammonium Hydroxide Doped with Zeolitic Imidazolate Frameworks, and Mixed Matrix Membranes of Polyetherimide/Tetrabutylammonium Hydroxide Doped with Zeolitic Imidazolate Frameworks for Proton. *Electrochim. Acta* **2017**, *258*, 153–166.
32. Escorihuela, J.; Sahuquillo, Ó.; García-Bernabé, A.; Giménez, E.; Compañ, V. Phosphoric Acid Doped Polybenzimidazole (PBI)/Zeolitic Imidazolate Framework Composite Membranes with Significantly Enhanced Proton Conductivity under Low Humidity Conditions. *Nanomaterials* **2018**, *8*, 775.
33. Mukhopadhyay, S.; Das, A.; Jana, T.; Das, S. K. Fabricating a MOF Material with Polybenzimidazole into an Efficient Proton Exchange Membrane. *ACS Appl. Energy Mater.* **2020**, *3*, 7964–7977.

APPENDIX 4

Supporting Data for Chapter 4

TABLE OF CONTENTS

Section A4.1. Powder X-ray diffraction (PXRD) analysis

The PXRD patterns of all the synthesised composites in the series **C_{60}Z-n** (n = A, B, C, D and E are found to be similar to that of ZIF-8.

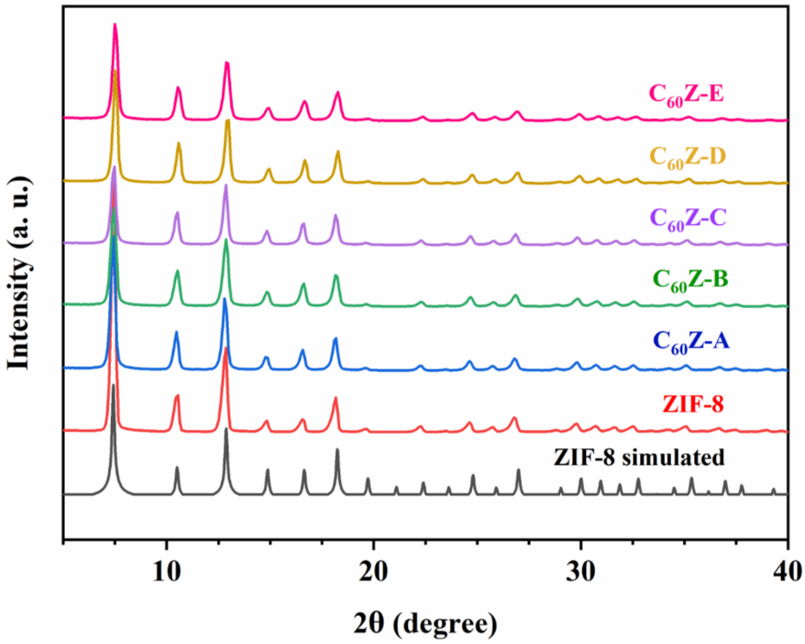

Figure A4.1. PXRD patterns of simulated ZIF-8, ZIF-8 and **C_{60}Z-n** (n = A, B, C, D and E).

Section A4.2. Calculation of C_{60} loading level from CHN analysis

Table A4.1. CHN data of ZIF-8 and $C_{60}Z$.

Name of sample	C	H	N
ZIF-8	41.80	3.89	23.74
C_{60}Z-A	42.63	3.84	23.42
C_{60}Z-B	42.87	3.76	23.24
C_{60}Z-C or C_{60}Z	43.39	3.64	23.09
C_{60}Z-D	43.47	3.62	23.04
C_{60}Z-E	43.44	3.62	23.06

The molecular formula of ZIF-8 is $C_8H_{10}N_4Zn$.
From the CHN data of ZIF-8, the molecular formula comes out to be $C_{8.23}H_{9.20}N_{3.99}Zn$ (taking the amount of N to be standard).

Calculation of loading level of C_{60} in C_{60}Z-A:

Using similar method, from the CHN data of **C_{60}Z-A**, the molecular formula comes out to be $C_{8.49}H_{9.18}N_{3.99}Zn$ (taking the amount of N to be standard).
So, we find that there is an excess of carbon content in **C_{60}Z-A** than in ZIF-8 by ~ 0.26 per formula unit. **… (1)**

Now, each unit cell of ZIF-8 consists of 24 ($C_8H_{10}N_4Zn$) units. 4 Zn ions are situated on each face (total 6 faces) of the unit cell. Thus, each of the Zn is shared between two adjacent unit cells.
Therefore, contribution per Zn = ½.
Effective number of Zn in each unit cell = 24 × ½ =12

Thus, each unit cell has 12 ($C_8H_{10}N_4Zn$) units.
Or, each single cage of ZIF-8 consists of 12 ($C_8H_{10}N_4Zn$) units. **… (2)**

From **(1)** and **(2),** we can calculate that, for each 19 cages of ZIF-8, there is 1 C_{60} molecule in **C_{60}Z-A**.

In a similar way, the loading level of C_{60} in rest of the composites have been calculated. The respective data is presented in a tabular form below (Table A4.2)

Table A4.2. Molecular formula and loading level of C_{60} in C_{60}Z-n (n = A, B, C, D and E).

Name of sample	Molecular formula	1 C_{60} per *x* cages
ZIF-8	$C_{8.23}H_{9.20}N_{3.99}Zn$	----
C_{60}Z-A	$C_{8.49}H_{9.18}N_{3.99}Zn$	$x = 19$
C_{60}Z-B	$C_{8.60}H_{9.04}N_{3.99}Zn$	$x = 14$
C_{60}Z-C or C_{60}Z	$C_{8.75}H_{8.82}N_{3.99}Zn$	$x = 10$
C_{60}Z-D	$C_{8.79}H_{8.80}N_{3.99}Zn$	$x = 9$
C_{60}Z-E	$C_{8.78}H_{8.79}N_{3.99}Zn$	$x = 9$

Section A4.3. Fourier transformed - infrared (FT-IR) spectral analysis

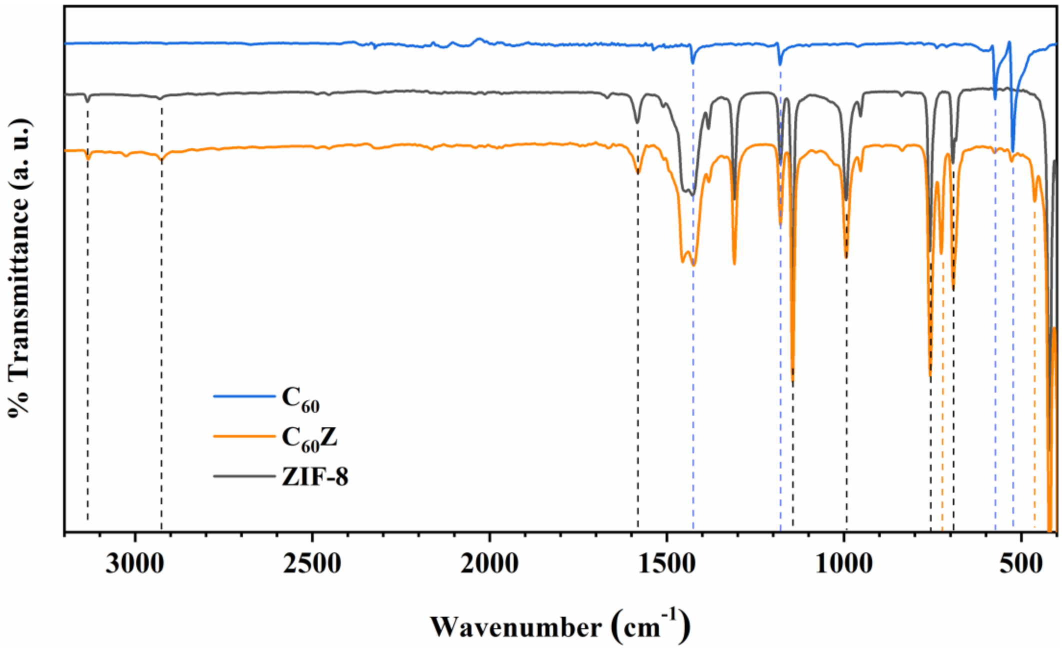

Figure A4.2. FT-IR spectra of C_{60}, ZIF-8 and **C_{60}Z** (400-3000 cm^{-1}).

A comparison of the FT-IR spectra of ZIF-8 and **C_{60}Z-n (n = A, B, C, D and E)** (Figure A4.3) shows that all the composites with different loading of C_{60} in them, have all the prominent features of ZIF-8. The peaks originating due to the presence of C_{60} in the composites, display a gradual increase in intensity going from **C_{60}Z-A** to **C_{60}Z-C** and then become almost constant through **C_{60}Z-D** and **C_{60}Z-E**. This is probably because the loading level of C_{60} in **C_{60}Z-C**, **C_{60}Z-D** and **C_{60}Z-E** is nearly same.

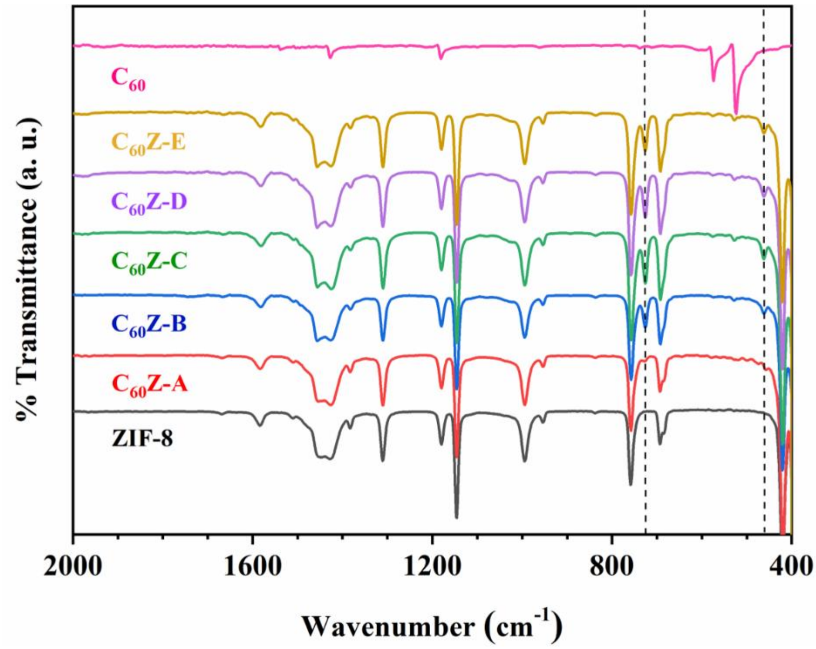

Figure A4.3. FT-IR spectra of C_{60}, ZIF-8 and **C_{60}Z-n** (n = A, B, C, D and E).

Section A4.4. N_2 gas sorption analysis

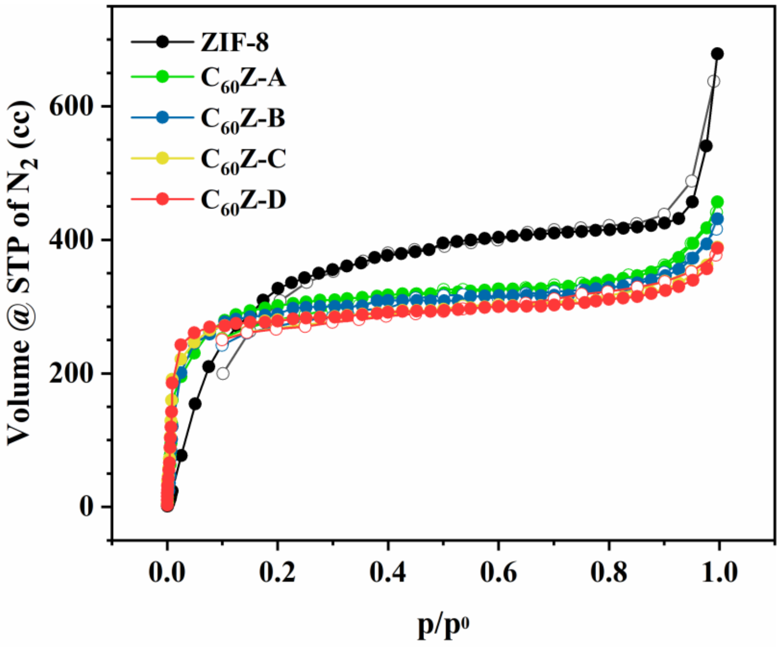

Figure A4.4. N_2 gas sorption isotherms of ZIF-8 and **C_{60}Z-n** (n = A, B, C and D). Filled spheres denote adsorption and hollow spheres denote desorption experimental data points.

According to Brunauer–Emmett–Teller (BET) analysis, the surface area of ZIF-8, **C_{60}Z-A**, **C_{60}Z-B**, **C_{60}Z-C** and **C_{60}Z-D** are found to be 1373.72 m^2/g, 1160.09 m^2/g, 1126.34 m^2/g, 1090.83 m^2/g, and 1081.41 m^2/g, respectively. The lowering of surface area with increasing loading amount of C_{60} indicates the successful encapsulation of the C_{60} molecules.

Section A4.5. Thermogravimetric analysis (TGA)

Both **C_{60}Z** and ZIF-8 started degrading from around 400 °C. By 550 °C, both of them have lost about 60% of their initial weight. The TGA curve for **C_{60}Z** has a slightly higher slope, which might be a result of interaction of C_{60} with the ZIF-8 framework. The residual mass for **C_{60}Z** found to be slightly higher than that for ZIF-8, due to the presence of C_{60}, which has a higher thermal stability (Figure A4.5). The difference in residual weight (~1.24%) can be accounted for the wt% of C_{60} present in the **C_{60}Z** composite.

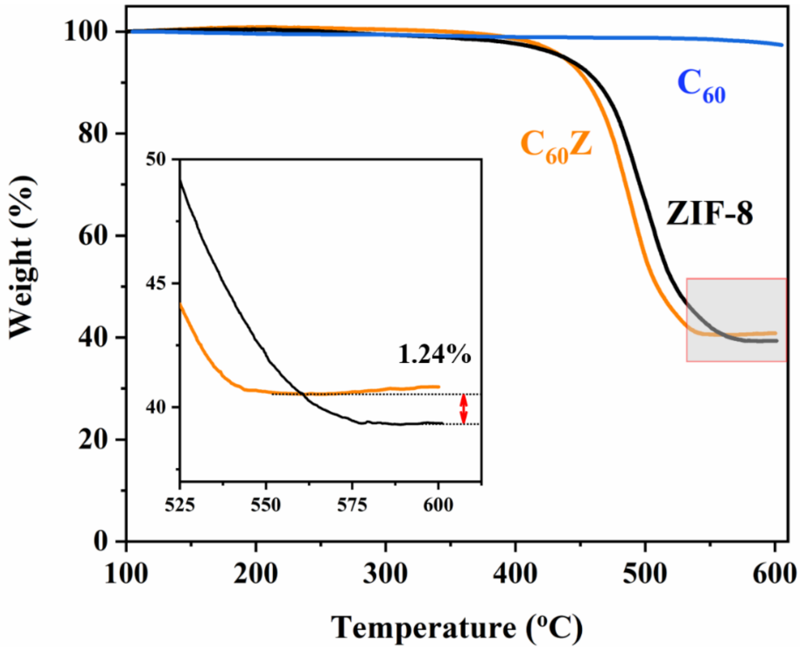

Figure A4.5. TGA of C_{60}, ZIF-8 and **C_{60}Z**. Inset: magnified view of the highlighted region.

Section A4.6. Band gap calculation of C_{60} in C_{60}Z and in dilute solution

The electronic absorption spectra were used for finding the band gap of the samples using the Tauc method. According to this method, it is assumed that absorption coefficient α can be expressed by the following equation:

$$(\alpha h\nu)^n = B(h\nu - E_g) \quad \textbf{… (1)}$$

where h is the Plank constant, v is the frequency of the radiation, B is a proportionality constant and E_g is the band gap energy.[1] For materials having allowed direct transitions, n = 2. Both fullerene C_{60} and ZIF-8 fall under this category of materials and thus for both of them n = 2. The band gap E_g for C_{60} in solution (HOMO-LUMO gap) has been calculated from its absorption spectrum using Tauc method, employing equation 1. The Tauc plot has $(\alpha hv)^2$ on the Y-axis and energy of the photons (hv) on X-axis (Figure A4.6a). The point of intersection of the fitted straight line and X-axis gives the band gap energy. It was calculated to be 1.913 eV.

The band gap for $\mathbf{C_{60}Z}$ has been calculated from its absorption spectrum obtained by Kubella-Munk transformation of the diffused reflectance spectrum (DRS). The reflectance spectrum is converted to absorption spectrum using the following Kubella-Munk function:

$$F(R) = \frac{(1-R)^2}{2R} \qquad \textbf{… (2)}$$

where R is the reflectance. Since $F(R)$ is proportional to the absorption coefficient α, $F(R)$ is substituted in place of α in equation 1 to give:

$$(F(R)hv)^n = B(hv - E_g) \qquad \textbf{… (3)}$$

Using equation 3, the Tauc plot is generated (Figure A4.6b). The band gap E_g for $\mathbf{C_{60}Z}$ is calculated to be 1.959 eV.

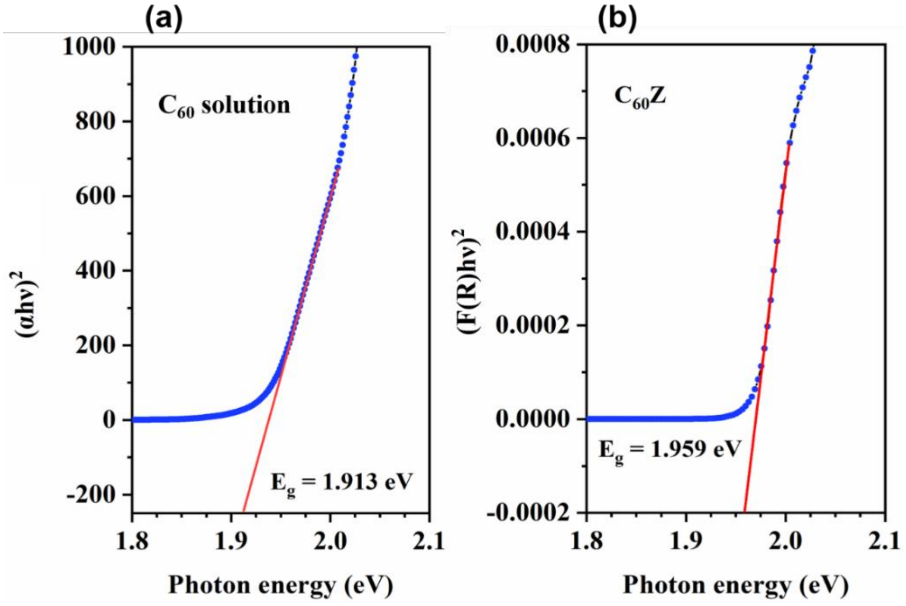

Figure A4.6. Tauc plots of (a) C_{60} in solution and (b) $\mathbf{C_{60}Z}$.

Section A4.7. X-Ray photoelectron spectral analysis

The surface survey of both ZIF-8 and **C$_{60}$Z** displays signals of Au (4f and 4d), C1s, N1s, O1s, and Zn2p core levels.

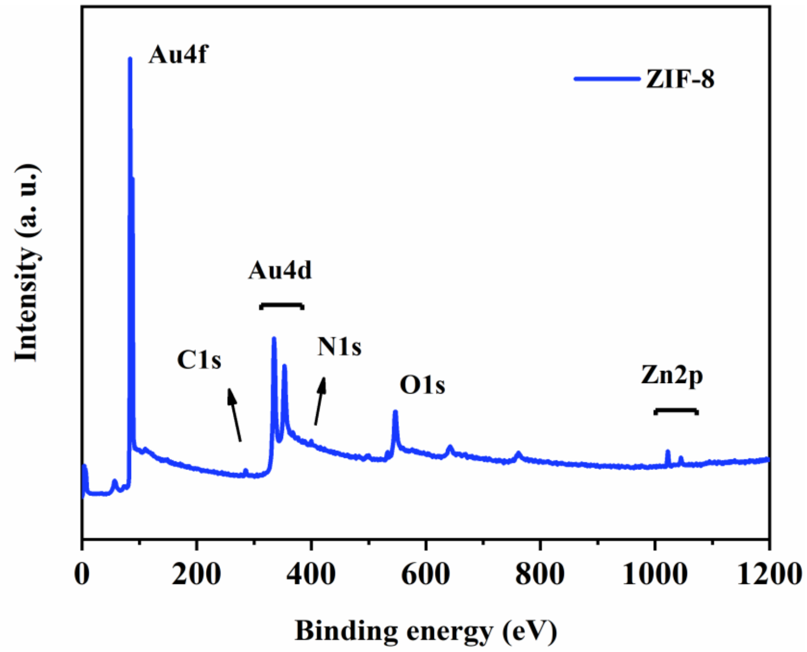

Figure A4.7. XPS surface spectrum of ZIF-8.

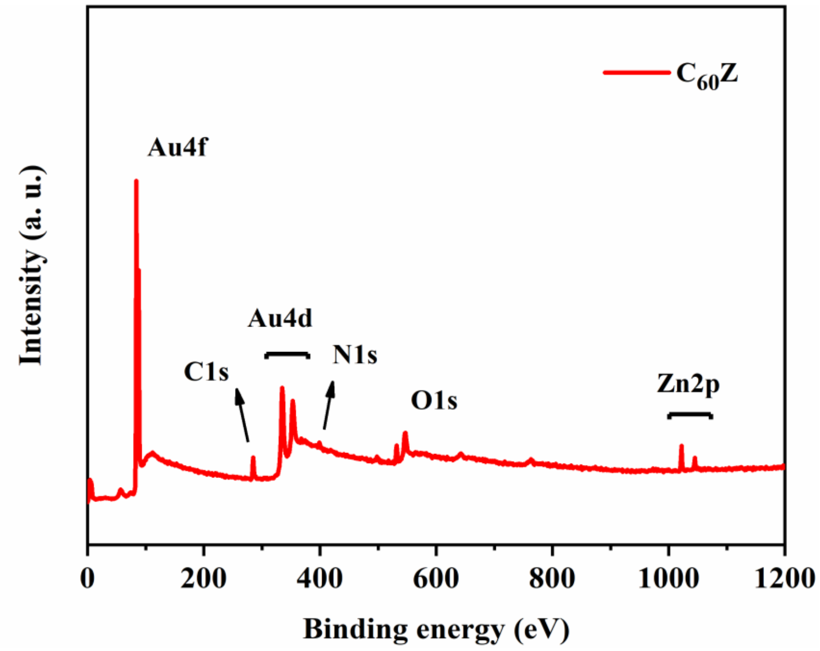

Figure A4.8. XPS surface spectrum **C$_{60}$Z**.

Section A4.8. Electrochemical analysis

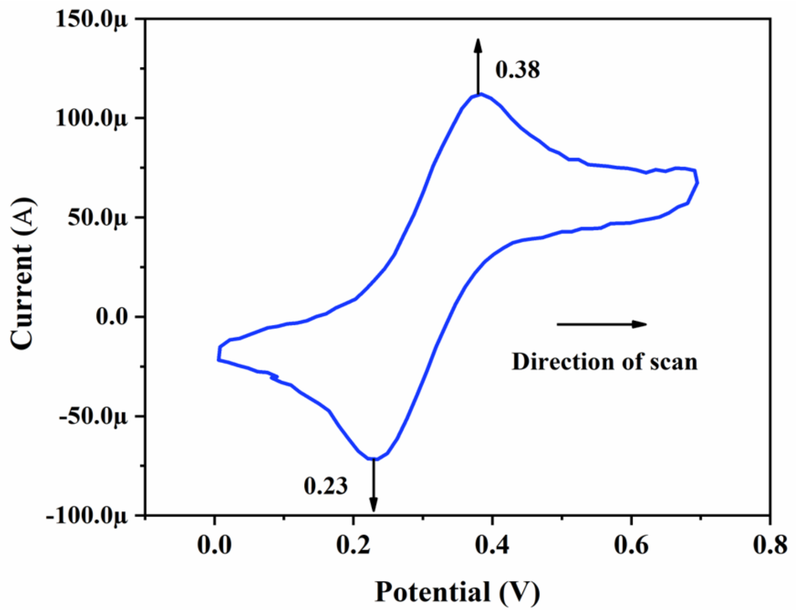

Figure A4.9. Cyclic voltammogram of ferrocene showing the ferrocenium-ferrocene (Fc^+/Fc) couple. The electrochemical measurement was done in 1:2 dry acetonitrile/toluene solvent mixture taking 0.1M tetrabutylammonium perchlorate (TBAP) as the supporting electrolyte, under nitrogen atmosphere at 100 mV s^{-1} scan rate.

Cyclic voltammogram and differential pulse voltammogram for $C_{60}Z$

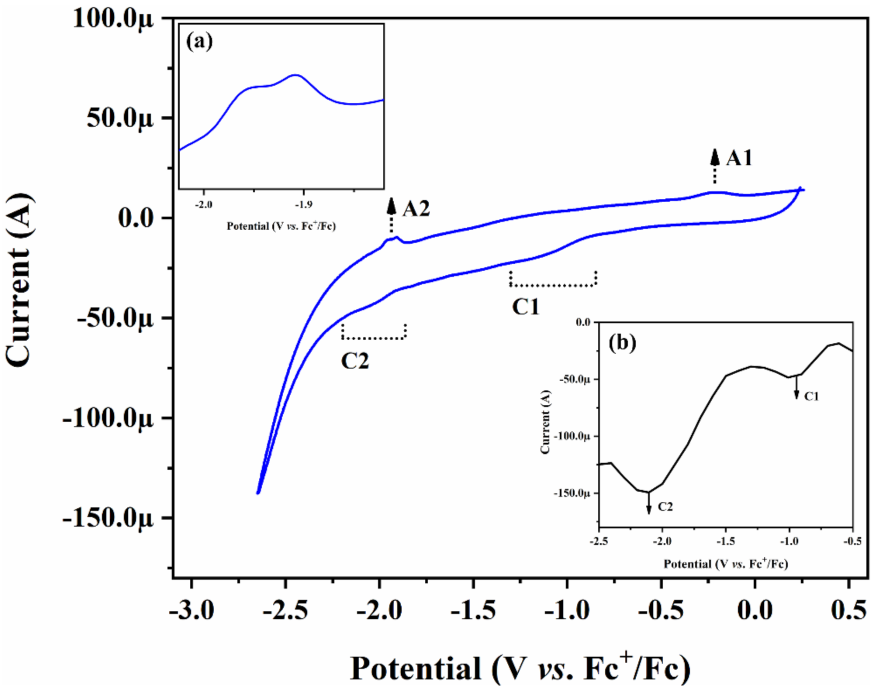

Figure A4.10. Cyclic voltammogram of **$C_{60}Z$** at 10 mV s^{-1} scan rate; inset: (a) magnified view of A2 response in voltammogram; (b) differential-pulse voltammogram of **$C_{60}Z$**. The electrochemical measurement was done in 1:2 dry acetonitrile/toluene solvent mixture taking 0.1M tetrabutylammonium perchlorate (TBAP) as the supporting electrolyte, under nitrogen atmosphere.

The cyclic voltammogram of **C_{60}Z** (Figure A4.10) recorded at 10 mV/s shows two cathodic (C1, C2) and anodic (A1, A2) responses. While A1 had a single hump centered around -0.17 V, A2 showed an overlap of two closely spaced peaks centered around -1.9 V (Figure A4.10, inset), originating from C_{60}. The cathodic responses were broader than the anodic, and therefore differential-pulse voltammogram (DPV) (Figure A4.10, inset) were recorded (Pulse height: 200 mV; pulse width: 0.6 s; scan rate: 50 mV s^{-1}). The DPV clearly showed two cathodic peaks centered around -0.90 V (C1) and -2.10 V (C2).

Cyclic voltammetric and chronoamperometric analysis for C_{60}Z

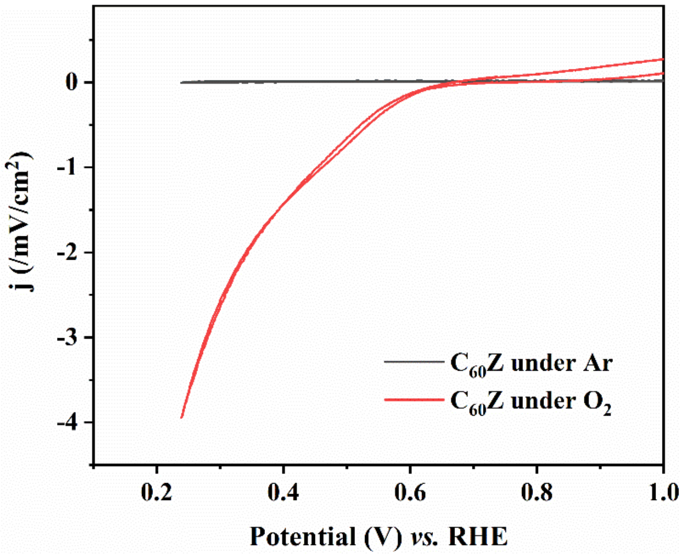

Figure A4.11. Cyclic voltammograms of C_{60}Z (drop cast on glassy carbon working electrode) at 100 mV s^{-1} scan rate.

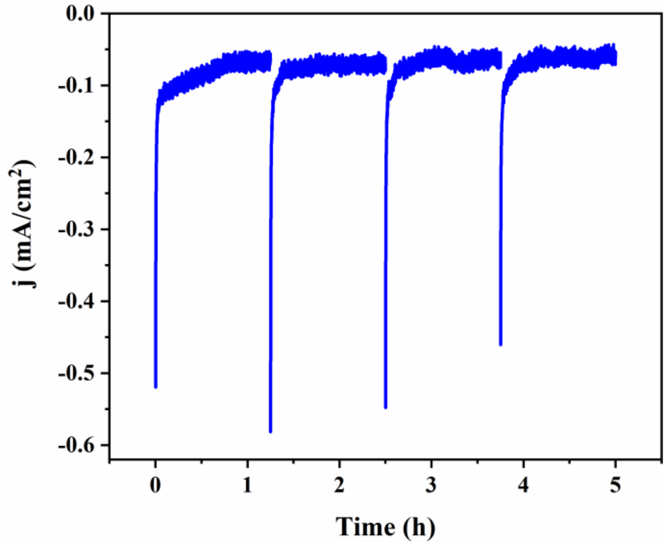

Figure A4.12. Chronoamperometric analysis of **C_{60}Z** at 0.45 V (*vs.* RHE) for a total duration of 5 hours, in 0.1 M KOH. The electrolyte was purged with O_2 for 30 minutes prior to each individual measurement during the 5 h analysis.

Calculation of H_2O_2 selectivity from rotating ring disc electrode (RRDE) experiment

The electron transfer numbers (n_{RRDE}) and H_2O_2 selectivity were calculated using the following relations.[2]

$$n_{RRDE} = \frac{4N_c i_d}{N_c i_d + i_r} \quad \textbf{… (4)}$$

where i_d and i_r denote the disk and ring current, respectively. N_c denotes the collection efficiency of RRDE electrode which was determined to be 0.4182 (or 41.82%).

$$H_2O_2\% = 100 \text{ x } \frac{(4 - n_{RRDE})}{2} \quad \textbf{… (5)}$$

Section A4.9. Controlled experiment with higher C_{60} loaded C_{60}Z composites

Powder X-ray diffraction (PXRD) analysis

The PXRD patterns of the synthesised composites were found to be similar to that of ZIF-8 simulated pattern (Figure A4.13). The position of the peaks matched well but their relative intensities were modified due to C_{60} encapsulation in these high loading samples.[3]

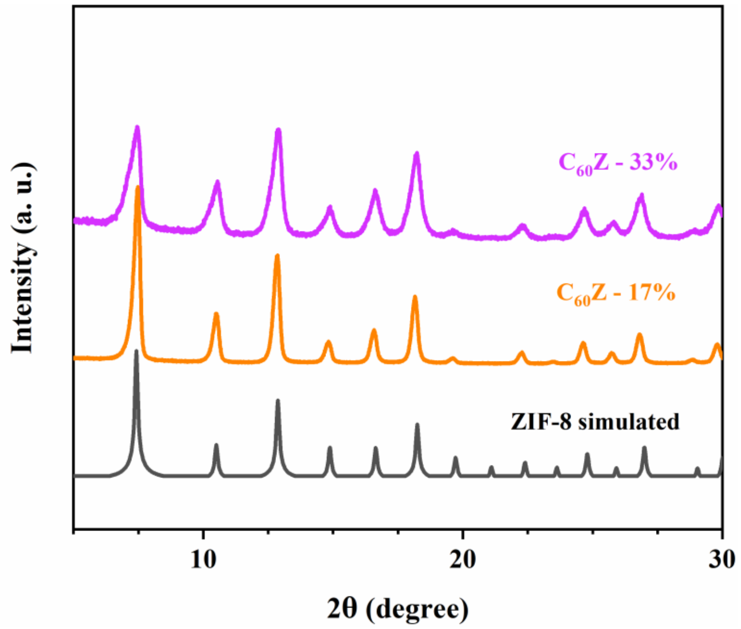

Figure A4.13. PXRD patterns of ZIF-8 simulated, **C_{60}Z – 17%** and **C_{60}Z – 33%**.

Fourier transformed- infrared (FT-IR) spectral analysis

The FT-IR spectra of the composites matched well with the reported data. The spectral feature matched predominantly with that of ZIF-8 and showed gradual increase in peak intensity originating from C_{60}.

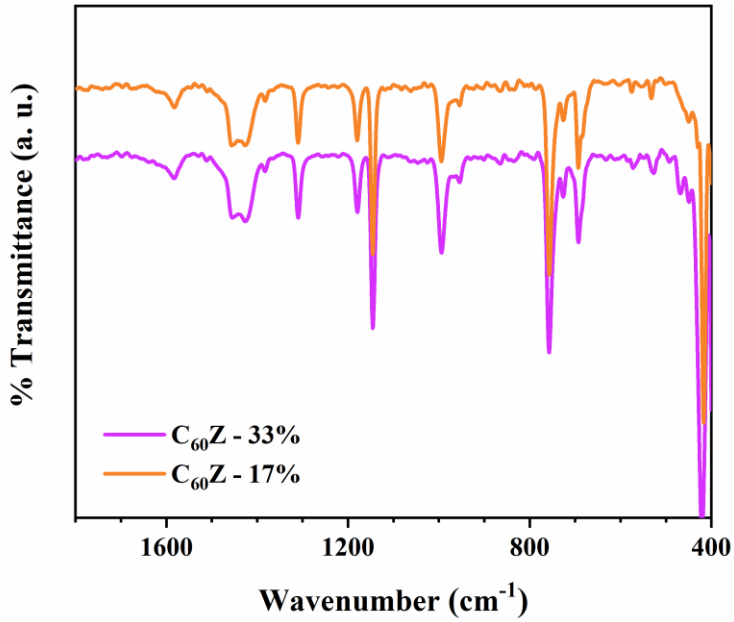

Figure A4.14. FT-IR spectra of **C_{60}Z – 17%** and **C_{60}Z – 33%**.

Calculation of C_{60} loading from CHN analysis

Table A4.3. CHN data.

Name of sample	C	H	N
C_{60}Z – 17%	44.71	4.07	23.05
C_{60}Z – 33%	46.45	3.98	21.81

The loading level of C_{60} in the composites have been calculated using same method as detailed in section A4.2 The respective data is presented in a tabular form below (Table A4.4).

Table A4.4. Molecular formula and loading level of C_{60}.

Name of sample	Molecular formula	1 C_{60} per *x* cages
C_{60}Z – 17%	$C_{9.00}H_{9.84}N_{3.99}Zn$	$x = 6$
C_{60}Z – 33%	$C_{9.91}H_{10.19}N_{3.99}Zn$	$x = 3$

Electrochemical analysis

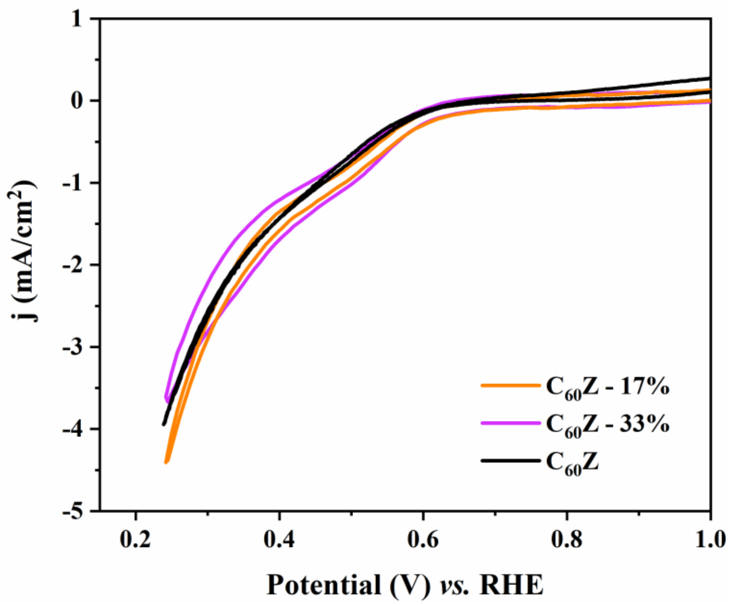

Figure A4.15. Cyclic voltammograms of **$C_{60}Z$**, **$C_{60}Z$ – 17%** and **$C_{60}Z$ – 33%** at 100 mV s^{-1} scan rate. All voltammograms were recorded in O_2 saturated 0.1 M KOH.

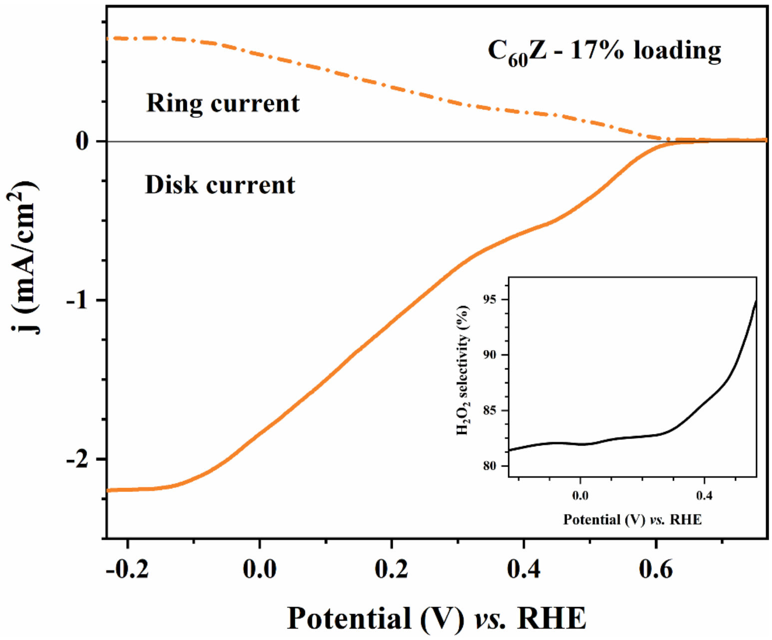

Figure A4.16. Polarization curves of **$C_{60}Z$ – 17%** for oxygen reduction reaction (ORR) and H_2O_2 generation using rotating ring-disk electrode (RRDE) at 1600 rpm, and 10 mV s^{-1} scan rate. The measurements were recorded in O_2 saturated 0.1 M KOH; inset: H_2O_2 product selectivity of **$C_{60}Z$ – 17%** as obtained from the RRDE method.

Section A4.10. Controlled experiments to establish the encapsulation

Powder X-ray diffraction (PXRD) analysis

The PXRD pattern of (C_{60}+ZIF-8) displayed features corresponding to both C_{60} and ZIF-8 (Figure A4.17), as opposed to **C_{60}Z**, whose PXRD pattern matched completely with that of pure ZIF-8.

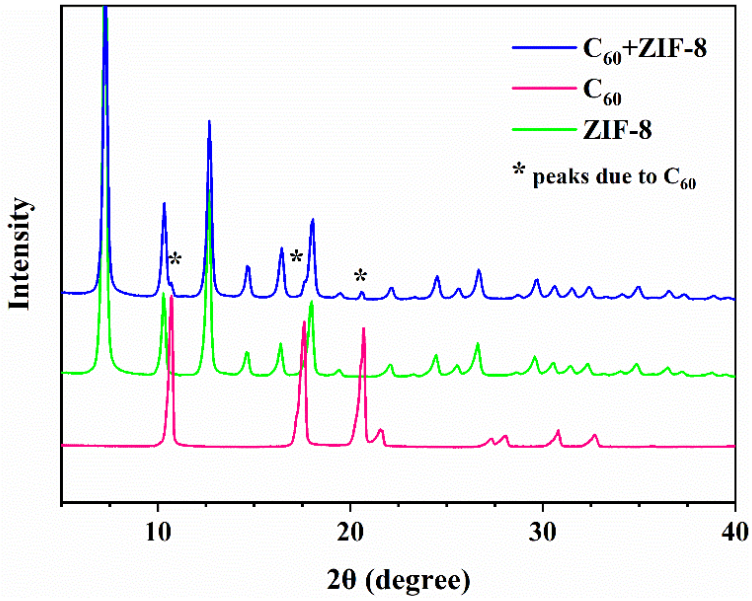

Figure A4.17. PXRD patterns of ZIF-8, C_{60} and (C_{60}+ZIF-8).

Fourier transformed- infrared (FT-IR) spectral analysis

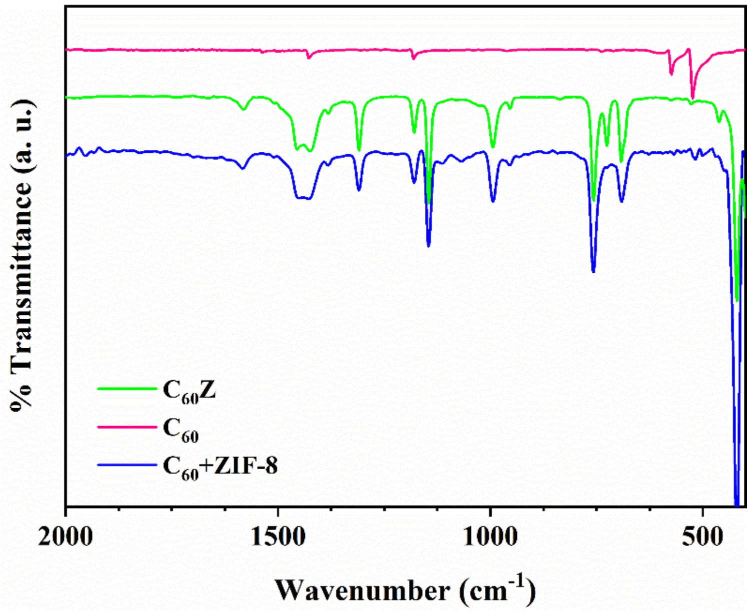

Figure A4.18. FT-IR spectra of solid C_{60}, **C_{60}Z**, and (C_{60}+ZIF-8).

The FT-IR spectra of (C_{60}+ZIF-8) (Figure A4.18) shows all the prominent features of ZIF-8. Due to the low quantity of fullerene C_{60} in (C_{60}+ZIF-8), the peaks at 1184 cm^{-1} and 1428 cm^{-1} corresponding to C_{60}, were masked by the features of ZIF-8. Although the strong peaks at 527 cm^{-1} and 575 cm^{-1} appeared at the same position as non-encapsulated C_{60}. But the new peaks at 725 cm^{-1} and 461 cm^{-1}, originating from the host-guest interaction in **C_{60}Z**, were not found in (C_{60}+ZIF-8). This suggests that the fullerene adsorbed on the ZIF-8 surface of (C_{60}+ZIF-8) do not possess similar strong interaction with the MOF framework, which is present for the encapsulated fullerenes in **C_{60}Z**.

Electronic absorption spectroscopy

The UV-Visible (recorded in diffused reflectance mode) spectrum of the (C_{60}+ZIF-8) was comparable to that of C_{60} solid (non-encapsulated) and was widely different from **C_{60}Z** composite (Figure A4.19). The broad peaks in the 400 nm -700 nm region suggests that the (C_{60}+ZIF-8) cannot provide a molecular level spatial separation for the C_{60} on the surface of ZIF-8. The surface bound C_{60} in this case can interact with each other and behave similar to solid aggregates of C_{60} to some extent. It is well-known that with variation in particle size of fullerene aggregates, the electronic spectrum changes dramatically.[4]

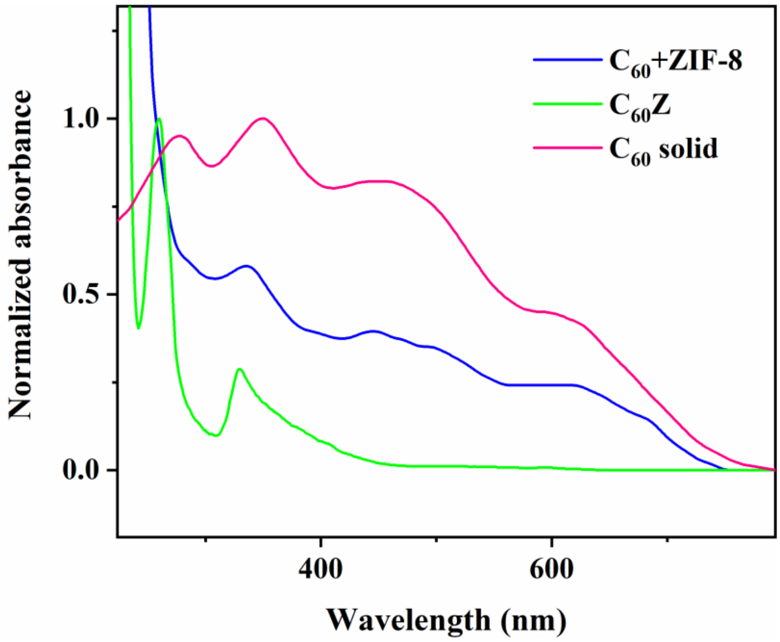

Figure A4.19. K-M converted UV/Vis-DRS spectra of solid C_{60}, **C_{60}Z**, and (C_{60}+ZIF-8).

Calculation of C_{60} content in (C_{60}+ZIF-8) from CHN analysis

Table A4.5. CHN data.

Name of sample	C	H	N
C_{60} + ZIF-8	43.84	4.11	23.19

The content of C_{60} in the physical mixture has been estimated using similar method as detailed in section A4.2 The composition of the mixture is $C_{8.80}H_{9.90}N_{4.00}$. This gives an excess of ~0.57 carbon due to C_{60} per formula unit of ZIF-8, which gives almost same amount of C_{60} content in the physical mixture as compared to **C_{60}Z**.

The above-mentioned XRD, UV-Vis (DRS) and FT-IR spectral analysis along with electrochemical ORR performance of (C_{60}+ZIF-8) physical mixture when compared with that of C_{60} and **C_{60}Z**, it infers the following important information: (1) The (C_{60}+ZIF-8) samples has presence of crystalline planes corresponding to solid C_{60} (Figure A4.17), which further indicates a lack of molecular level spatial separation in the (C_{60}+ZIF-8) physical mixture where the C_{60} species are only adsorbed by the MOF surface; (2) The FT-IR spectrum of (C_{60}+ZIF-8) (Figure A4.18) is basically the summation of FT-IR spectra of C_{60} and ZIF-8 in accordance with their relative abundance in the (C_{60}+ZIF-8) physical mixture; (3) UV-Vis (DRS) spectrum of (C_{60}+ZIF-8) (Figure A4.19) is similar to C_{60} solid and varies widely from **C_{60}Z** indicating a further similarity of (C_{60}+ZIF-8) to the electronic structure of solid C_{60}; a noteworthy point to establish lack of molecular level interaction between the MOF and the surface bound C_{60} species unlike the encapsulated C_{60} species in case of **C_{60}Z**. Thus, it could be inferred that, **C_{60}Z** is not a mere case of surface adsorbed C_{60} onto ZIF-8 surface but a molecular level confinement into the cavity of ZIF-8 to form a host-guest composite material where the ZIF-8 acts as the host and the C_{60} acts as the guest. This inference was further strongly supported by the electrochemical ORR performance of the (C_{60}+ZIF-8) physical mixture (chapter 4). The ORR properties of the (C_{60}+ZIF-8) physical mixture was similar to that of solid C_{60} to some extent and varied widely from that of **C_{60}Z**. With the help of these controlled experiments, it was confirmed that **C_{60}Z** composite was not a case of MOF surface bound C_{60} molecules but is a host-guest composite material.

Section A4.11. Physical characterization of C_{60}Z-PVA membrane

Powder X-ray diffraction (PXRD) analysis

The diffraction pattern of **C_{60}Z-PVA** membrane (Figure A4.20) displays all the features of pure PVA membrane along with some of the prominent peaks of **C_{60}Z**. There were no noticeable changes with respect to broadening or shifting of peaks compared to pure PVA membrane, indicating similar crystallinity even after incorporation of **C_{60}Z** nanofillers.

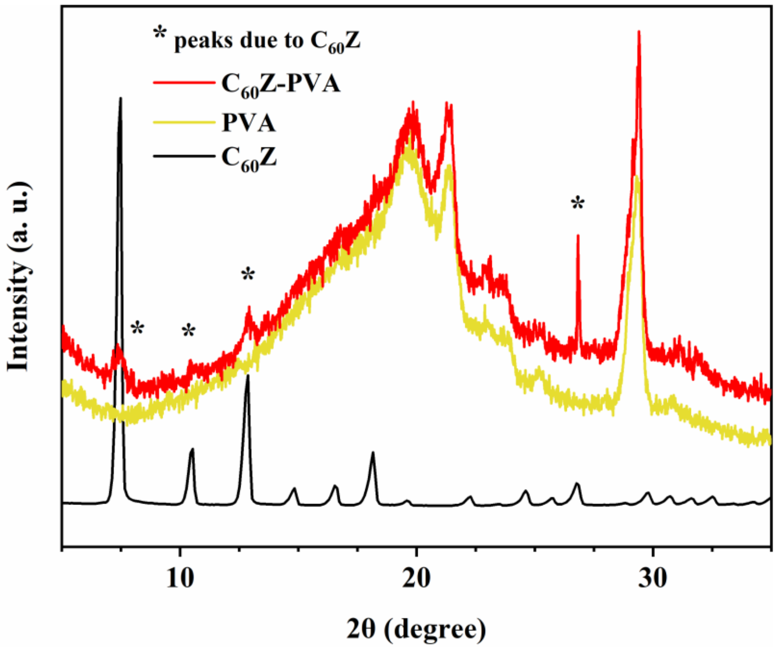

Figure A4.20. PXRD patterns of **C_{60}Z**, **C_{60}Z-PVA** and PVA.

Fourier transformed - infrared (FT-IR) spectral analysis

The FT-IR spectrum of **C_{60}Z-PVA** (Figure A4.21) membrane predominantly consists of the spectral features of PVA polymer. However, several small peaks (marked with *) could be found originating from the **C_{60}Z** nanocomposite. There were no noticeable changes in the position of the peaks, indicating that the molecular structure of **C_{60}Z** was unaltered even after the process of membrane fabrication.

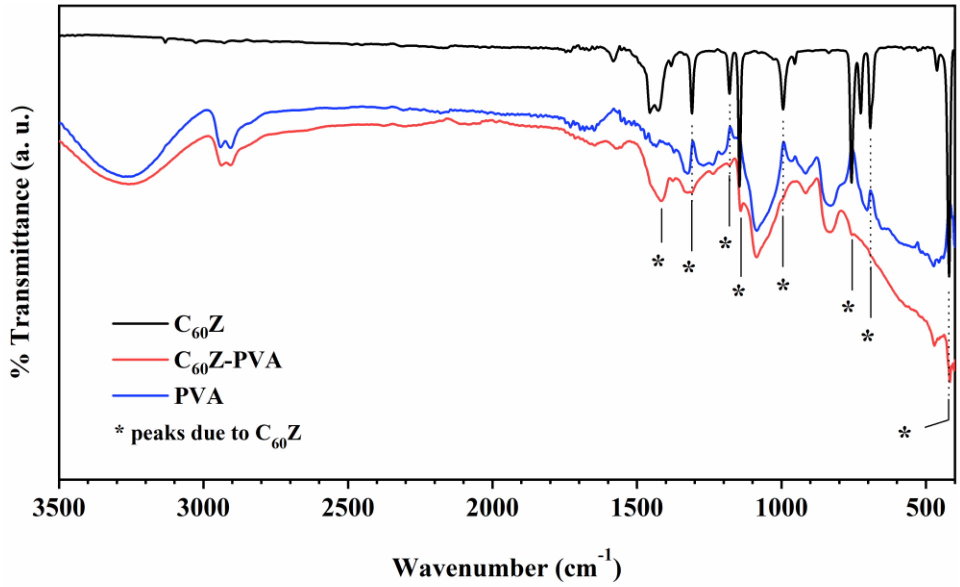

Figure A4.21. FT-IR spectra of **$C_{60}Z$**, PVA and **$C_{60}Z$-PVA**.

FESEM images

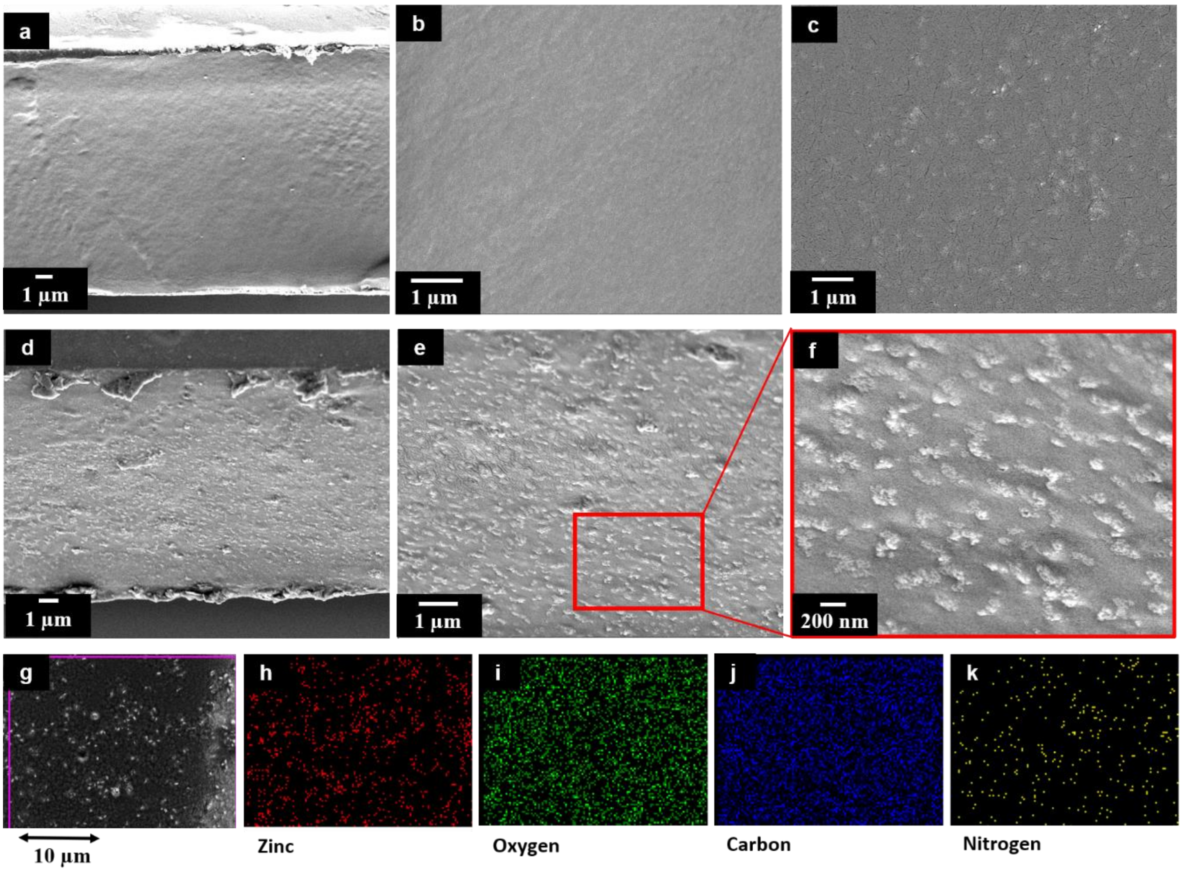

Figure A4.22. FESEM images of (a) PVA membrane cross-section; (b) surface of PVA membrane; (c) surface of **$C_{60}Z$-PVA** membrane; (d) cross-section of **$C_{60}Z$-PVA** membrane; (e) dispersed **$C_{60}Z$** nanofillers in the cross-section of **$C_{60}Z$-PVA** membrane; (f) magnified view of the nanofillers. (g-k) EDX mapping of **$C_{60}Z$-PVA** membrane showing uniform dispersion of **$C_{60}Z$.**

References

1. Makuła, P.; Pacia, M.; Macyk, W. How To Correctly Determine the Band Gap Energy of Modified Semiconductor Photocatalysts Based on UV–Vis Spectra. *J. Phys. Chem. Lett.* **2018**, *9*, 6814-6817.
2. Hasanzadeh, A.; Khataee, A.; Zarei, M.; Zhang, Y. Two-electron oxygen reduction on fullerene C_{60}-carbon nanotubes covalent hybrid as a metal-free electrocatalyst. *Scientific Reports* **2019**, *9*, 13780.
3. Martinez, V.; Karadeniz, B.; Biliškov, N.; Lončarić, I.; Muratović, S.; Žilić, D.; Avdoshenko, S. M.; Roslova, M.; Popov, A. A.; Užarević, K. Tunable Fulleretic Sodalite MOFs: Highly Efficient and Controllable Entrapment of C_{60} Fullerene via Mechanochemistry. *Chem. Mater.* **2020**, *32*, 10628−10640.
4. Lee, J.; Cho, M.; Fortner, J. D.; Hughes, J. B.; Kim, J – H. Transformation of Aggregated C_{60} in the Aqueous Phase by UV Irradiation, *Environ. Sci. Technol.* **2009**, *43*, 4878–4883.

APPENDIX 5

Supporting Data for Chapter 5

TABLE OF CONTENTS

Section A5.1. CHN elemental analysis experimental data for Mo132-R-ED

Table A5.1. CHN elemental analysis experimental data.

Element	Element%
Nitrogen	13.037
Carbon	56.912
Hydrogen	3.074

Section A5.2. Determination of the number of Mo^V centers in Mo132-R-ED

The chemical formula for {Mo132} is $[(NH_4)_{42}\{Mo_{132}O_{372}(CH_3COO)_{30}(H_2O)_{72}\}\cdot$ca.300 $H_2O\cdot$ca.10 $CH_3COONH_4]$.

Out of 132 Mo atoms, 72 are Mo^{VI} and 60 are Mo^V centers.

Now, as described in section 5.2.3.1 (Chapter 5), 50 mg (1.7475×10^{-6} moles) of {Mo132} was titrated against 0.01 M aqueous $KMnO_4$ solution. The oxidant oxidises all the Mo^V to Mo^{VI}.

$$Mo^{5+} \rightarrow Mo^{6+} + e^-$$
$$MnO_4^- + 5e^- \rightarrow Mn^{2+}$$

For pristine {Mo132}, the volume of titrant used was 2.1 mL.

This estimates approximately 1.048×10^{-4} moles of Mo^V in 50 mg of {Mo132}.

Or, ~ 60 Mo^V in one cluster of {Mo132}, which matches perfectly with the theoretical value.

Table A5.2. ICP-OES elemental analysis experimental data for **Mo$_{132}$-R-ED**.

Sample code	Element symbol and Wavelength (nm)	Weight of sample in gms / Volume in ml	Dilution Factor	Concn.in ppm µg/ml (or) mg/litre
Mo$_{132}$-R-ED	Mo 202.031	0.0190g/50ml	1	185.3 mg/L

This means that 19 mg of **Mo$_{132}$-R-ED** sample contains 9.265 mg of Mo.
Or, 50 mg of **Mo$_{132}$-R-ED** contains 24.3815 mg (2.541×10^{-4} moles) of Mo.

For 50 mg of **Mo$_{132}$-R-ED** sample titrated against 0.01 M aqueous $KMnO_4$ solution, the volume of titrant used was 4.75 mL.

This estimates approximately 2.375×10^{-4} moles of Mo^{V} in 50 mg of **Mo$_{132}$-R-ED**.

Or, 2.375×10^{-4} moles of Mo^{V} in total of 2.541×10^{-4} moles of Mo.

Or, 123.3 Mo^{V} centers in one cluster of {Mo$_{132}$} in **Mo$_{132}$-R-ED**.

LIST OF PUBLICATIONS

Thesis chapter publications

1. **Design of Flexible Metal−Organic Framework-Based Superprotonic Conductors and Their Fabrication with a Polymer into Proton Exchange Membranes.**
   Basu, O.; Das, A.; Jana, T.; Das, S. K. *ACS Appl. Energy Mater.* **2022** (DOI: 10.1021/acsaem.2c02972).

2. **Defect Engineering in a Metal−Organic Framework System to Achieve Super-Protonic Conductivity.**
   Basu, O.; Mukhopadhyay, S.; Laha, S.; Das, S. K. *Chem. Mater.* **2022**, *34*, 6734−6743.

3. **Tuning the electrochemical and catalytic ORR performance of C_{60} by its encapsulation in ZIF-8: a solid-state analogue of dilute fullerene solution.**
   Basu, O.; Mukhopadhyay, S.; De, A.; Das, A.; Das, S. K. *Mater. Chem. Front.* **2021**, *5*, 7654–7665.

Other publications

4. **Supramolecular inorganic chemistry leading to functional materials.**
   Basu, O.; Das, S. K. *J. Chem. Sci.* **2020**, *132*, 46. (*Review article*)

5. **Cobalt based functional inorganic materials: electrocatalytic water oxidation.**
   Basu, O.; Mukhopadhyay, S.; Das, S. K. *J. Chem. Sci.* **2018**, *130*, 93–99. (*Perspective*)

6. **Devising a Polyoxometalate-Based Functional Material as an Efficient Electrocatalyst for the Hydrogen Evolution Reaction.**
   Singh, C.; Haldar, A.; Basu, O.; Das, S. K. *Inorg. Chem.* **2021**, *60*, 10302−10314.

7. **Applying the Influence of Conformational Freedom on the Network Topologies Showing Impressive Proton Conductivity.**
   De, A.; Basu, O.; Basu, T.; Mondal, R. *Cryst. Growth Des.* **2021**, *21*, 1461–1472.

8. **ZIF-8 MOF Encapsulated Co-porphyrin, an Efficient Electrocatalyst for Water Oxidation in a Wide pH Range: Works Better at Neutral pH.**
   Mukhopadhyay, S.; Basu, O.; Das, S. K. *ChemCatChem* **2020**, *12*, 5430–5438.

9. **Evolution of metal organic frameworks as electrocatalysts for water oxidation.**
   Mukhopadhyay, S.; Basu, O.; Nasani, R.; Das, S. K. *Chem. Commun*. **2020**, *56*, 11735—11748. (*Feature article*)

10. **Efficient Electrocatalytic Water Oxidation by Fe(salen)–MOF Composite: Effect of Modified Microenvironment.**
    Mukhopadhyay, S.; Basu, O.; Kar, A.; Das, S. K.*Inorg. Chem.* **2020**, *59*, 472–483.

11. **Designing of UiO-66 Based Super Protonic Conductor with the Highest MOF Based Proton Conductivity.**
    Mukhopadhyay, S.; Debgupta, J.; Singh, C.; Basu, O.; Das, S. K. *ACS Appl. Mater. Interfaces* **2019**, *11*, 13423−13432.

12. **Cytochrome c peroxidase activity of heme bound amyloid β peptides.**
    Seal, M.; Ghosh, C.; Basu, O.; Ghosh, S. *J Biol Inorg Chem.* **2016**, *21*, 683−690.

LIST OF PRESENTATIONS

Oral presentation

1. **Defect Engineering in a Metal−Organic Framework System to Achieve Super-Protonic Conductivity.**

   International conference on *modern trends in inorganic chemistry* (MTIC-XIX) at Institute of Science, Banaras Hindu University, India, during 15-17 December 2022.

2. **Tuning the electrochemical and catalytic ORR performance of C_{60} by its encapsulation in ZIF-8: a solid-state analogue of dilute fullerene solution.**

   Chemfest 2022 (In-house symposium) at School of Chemistry, University of Hyderabad, India, during 22-23 April 2022. (*Received best oral presentation award*)

Poster presentation

1. **ZIF-8 MOF Encapsulated Co-porphyrin, an Efficient Bifunctional Electrocatalyst for Water Oxidation and Oxygen Reduction Reaction.**

   International *conference on electrochemistry in advanced materials, corrosion, and radiopharmaceuticals* (CEAMCR-2018) at BARC-Mumbai, India, during 15-17 February 2018.

2. **ZIF-8 MOF Encapsulated Co-porphyrin, an Efficient Bifunctional Electrocatalyst for Water Oxidation and Oxygen Reduction Reaction.**

   Chemfest 2018 (In-house symposium) at School of Chemistry, University of Hyderabad, India, during 9-10 March 2018.

3. **Tuning the electrochemical and catalytic ORR performance of C_{60} by its encapsulation in ZIF-8: a solid-state analogue of dilute fullerene solution.**

   International conference on *modern trends in inorganic chemistry* (MTIC-XVIII) at IIT-Guwahati, India, during 11-13 December 2019.

Designing of Functional Materials for Proton Conduction and Electrocatalysis

by Olivia Basu

Submission date: 28-Apr-2023 10:39AM (UTC+0530)
Submission ID: 2077960399
File name: Olivia_Basu.pdf (9.2M)
Word count: 37113
Character count: 192000

Designing of Functional Materials for Proton Conduction and Electrocatalysis

ORIGINALITY REPORT

64%	16%	58%	6%
SIMILARITY INDEX	INTERNET SOURCES	PUBLICATIONS	STUDENT PAPERS

PRIMARY SOURCES

1	Olivia Basu, Anupam Das, Tushar Jana, Samar K. Das. "Design of Flexible Metal–Organic Framework-Based Superprotonic Conductors and Their Fabrication with a Polymer into Proton Exchange Membranes", ACS Applied Energy Materials, 2022 Publication	24%
2	Olivia Basu, Subhabrata Mukhopadhyay, Subhajit Laha, Samar K. Das. "Defect Engineering in a Metal–Organic Framework System to Achieve Super-Protonic Conductivity", Chemistry of Materials, 2022 Publication	14%
3	Olivia Basu, Subhabrata - Mukhopadhyay, Avik De, Anupam Das, Samar K Das. "Tuning electrochemical and catalytic ORR performance of C60 by its encapsulation in ZIF-8: a solid-state analogue of dilute fullerene solution", Materials Chemistry Frontiers, 2021 Publication	13%

S.K.Das

Prof. Samar K. Das
School of Chemistry
University of Hyderabad
Hyderabad-500 046., INDIA
skdas@uohyd.ac.in

S.K.Das

Prof. Samar K.
School of Chem
University of Hy
Hyderabad-500
skdas@uo

S.K.Das

Prof. Samar K. Das
School of Chemistry
University of Hyderabad
Hyderabad-500 046., INDIA.
skdas@uohyd.ac.in

4	www.rsc.org Internet Source	5%
5	Submitted to University of Hyderabad, Hyderabad Student Paper	2%
6	Olivia Basu, Subhabrata Mukhopadhyay, Avik De, Anupam Das, Samar K. Das. " Tuning the electrochemical and catalytic ORR performance of C by its encapsulation in ZIF-8: a solid-state analogue of dilute fullerene solution ", Materials Chemistry Frontiers, 2021 Publication	1%
7	www.researchgate.net Internet Source	1%
8	link.springer.com Internet Source	<1%
9	www.ias.ac.in Internet Source	<1%
10	dspace.ncl.res.in:8080 Internet Source	<1%
11	eprints.gla.ac.uk Internet Source	<1%
12	hdl.handle.net Internet Source	<1%

S.K.Das

Prof. Samar K. Das
School of Chemistry
University of Hyderabad
Hyderabad-500 046., INDIA
skdas@uohyd.ac.in

S.K.Das

Prof. Samar K.
School of Chemi
University of Hyde
Hyderabad-500 04
skdas@uohy

S.K.Das

Prof. Samar K. Das
School of Chemistry
University of Hyderabad
Hyderabad-500 046., INDIA.
skdas@uohyd.ac.in

13	Submitted to Indian Institute of Technology Roorkee Student Paper	<1 %
14	qdoc.tips Internet Source	<1 %
15	gyan.iitg.ernet.in Internet Source	<1 %
16	coek.info Internet Source	<1 %
17	Dirk Volkmer, Alexander Du Chesne, Dirk G. Kurth, Heimo Schnablegger, Pit Lehmann, Michael J. Koop, Achim Müller. " Toward Nanodevices: Synthesis and Characterization of the Nanoporous Surfactant-Encapsulated Keplerate (DODA) (NH) [(H O) ⊂Mo O (CH COO) (H O)] ", Journal of the American Chemical Society, 2000 Publication	<1 %
18	Lijuan Zhang, Zonghai Shi, Lihui Zhang, Yunshan Zhou, Sadaf ul Hassan. "Fabrication and optical nonlinearities of ultrathin composite films incorporating a Keplerate type polyoxometalate", Materials Letters, 2012 Publication	<1 %
19	Lan Sun, Qiaomei Luo, Zhengfei Dai, Fei Ma. "Material libraries for electrocatalytic overall	<1 %

	water splitting", Coordination Chemistry Reviews, 2021 Publication	
20	conservancy.umn.edu Internet Source	<1%
21	Nanostructure Science and Technology, 2016. Publication	<1%
22	scholarbank.nus.edu.sg Internet Source	<1%
23	elib.uni-stuttgart.de Internet Source	<1%
24	ir.lib.uwo.ca Internet Source	<1%
25	www.mdpi.com Internet Source	<1%
26	Submitted to 於2012-04-12提交至Eastern Illinois University Student Paper	<1%
27	You, Bo, Nan Jiang, Xuan Liu, and Yujie Sun. "Simultaneous H2 Generation and Biomass Upgrading in Water by an Efficient Noble-Metal-Free Bifunctional Electrocatalyst", Angewandte Chemie International Edition, 2016. Publication	<1%
	cris.bgu.ac.il	

28	Internet Source	<1 %
29	www.slideshare.net Internet Source	<1 %
30	"Affordable and Clean Energy", Springer Science and Business Media LLC, 2021 Publication	<1 %
31	"Core-Shell and Yolk-Shell Nanocatalysts", Springer Science and Business Media LLC, 2021 Publication	<1 %
32	Chandani Singh, Atanu Haldar, Olivia Basu, Samar K. Das. "Devising a Polyoxometalate-Based Functional Material as an Efficient Electrocatalyst for the Hydrogen Evolution Reaction", Inorganic Chemistry, 2021 Publication	<1 %
33	Submitted to Western Washington University Student Paper	<1 %
34	patents.google.com Internet Source	<1 %
35	es.scribd.com Internet Source	<1 %
36	Huazhen Sun, Beibei Tang, Peiyi Wu. "Rational Design of S-UiO-66@GO Hybrid Nanosheets for Proton Exchange Membranes with	<1 %

Significantly Enhanced Transport Performance", ACS Applied Materials & Interfaces, 2017
Publication

---

37 mafiadoc.com
Internet Source
<1%

---

38 Chandani Singh, Subhabrata Mukhopadhyay, Samar K. Das. "Polyoxometalate-Supported Bis(2,2'-bipyridine)mono(aqua)nickel(II) Coordination Complex: an Efficient Electrocatalyst for Water Oxidation", Inorganic Chemistry, 2018
Publication
<1%

---

39 Submitted to Imperial College of Science, Technology and Medicine
Student Paper
<1%

---

40 Liang Chu, Junzhen Guo, Zhi Huang, Haibin Yang, Mu Yang, Ge Wang. "Excellent catalytic performance over acid-treated MOF-808(Ce) for oxidative desulfurization of dibenzothiophene", Fuel, 2023
Publication
<1%

---

41 Yongyi Jiang, Ming Hou, Jinkai Hao, Baolian Yi, Zhen Wang, Wei Song, Zhigang Shao. "Enhanced durability of sulfonated poly (ether ether ketones)-based polymer electrolyte membranes by a multi-layer composite technology", Solid State Ionics, 2017
<1%

	Publication	
42	dspace.uohyd.ac.in Internet Source	<1 %
43	opus.lib.uts.edu.au Internet Source	<1 %
44	patentimages.storage.googleapis.com Internet Source	<1 %
45	res.mdpi.com Internet Source	<1 %
46	Camila Canales, Galo Ramírez. "Glassy carbon electrodes modified with supramolecular assemblies generated by π-stacking of Cobalt (II) octaethylporphyrins. A 4 electrons-dioxygen reduction reaction occurring at positive potentials", Electrochimica Acta, 2015 Publication	<1 %
47	Hanguang Zhang, Sooyeon Hwang, Maoyu Wang, Zhenxing Feng et al. "Single Atomic Iron Catalysts for Oxygen Reduction in Acidic Media: Particle Size Control and Thermal Activation", Journal of the American Chemical Society, 2017 Publication	<1 %
48	Submitted to University of Aberdeen Student Paper	<1 %
49	s-space.snu.ac.kr Internet Source	

		<1 %
50	summit.sfu.ca Internet Source	<1 %
51	Erich Boeck. "Chapter 4 Vorgänge in elektrischen Leitern", Springer Science and Business Media LLC, 2022 Publication	<1 %
52	Hongwei Zhang, Pei Kang Shen. "Recent Development of Polymer Electrolyte Membranes for Fuel Cells", Chemical Reviews, 2012 Publication	<1 %
53	Rambabu Koyilapu, Suchismita Subhadarshini, Shuvra Singha, Tushar Jana. "An in-situ RAFT polymerization technique for the preparation of poly(N-vinyl imidazole) modified Cloisite nanoclay to develop nanocomposite PEM", Polymer, 2021 Publication	<1 %
54	Submitted to University of Sheffield Student Paper	<1 %
55	tsukuba.repo.nii.ac.jp Internet Source	<1 %
56	www.frontiersin.org Internet Source	<1 %

57	Junyuan Xu, David Aili, Qingfeng Li, Erik Christensen et al. "Oxygen evolution catalysts on supports with a 3-D ordered array structure and intrinsic proton conductivity for proton exchange membrane steam electrolysis", Energy & Environmental Science, 2014 Publication	<1 %
58	Xuechuan Gao, Manjue Zhai, Weihua Guan, Jingjuan Liu, Zhiliang Liu, Alatangaole Damirin. "Controllable Synthesis of a Smart Multifunctional Nanoscale Metal–Organic Framework for Magnetic Resonance/Optical Imaging and Targeted Drug Delivery", ACS Applied Materials & Interfaces, 2017 Publication	<1 %
59	www.nature.com Internet Source	<1 %

Exclude quotes	On	Exclude matches	< 14 words
Exclude bibliography	On		